Innovative aerosol-based synthesis of nanostructured catalysts for the direct upgrading of glycerol

MARGOT VAN DER VERREN

SEPTEMBRE 2023

Thèse présentée en vue de l'obtention du grade de docteur en sciences agronomiques et ingénierie biologique

Faculté des bioingénieurs

UCLouvain

Examining board:

Prof. Damien Debecker (UCLouvain)	Supervisor
Prof. Carmela Aprile (UNamur, Belgium)	Supervisor
Prof. Jean-François Gohy (UCLouvain)	Chairperson
Prof. Benjamin Elias (UCLouvain)	Secretary
Dr. Karen Leus (UGent, Belgium)	
Dr. Cédric Boissière (Sorbonne Université, France)	

REMERCIEMENTS

Au moment d'écrire les conclusions de ces quatre années de recherche, je tiens à exprimer mes plus sincères remerciements à toutes les personnes qui ont contribué de près ou de loin à la réalisation de ce manuscrit.

Tout d'abord, je souhaite adresser mes plus chaleureux remerciements à mes deux promoteurs, Pr. Damien Debecker et Pr. Carmela Aprile, pour leur expertise et leur inestimable soutien. Leurs conseils avisés aux travers de nos nombreuses réunions mais aussi pendant les discussions de couloir ont guidé mes quatre années de thèse et je leur en suis profondément reconnaissante. Je tiens également à remercier Damien pour la confiance qu'il m'a accordée en me donnant la chance de faire cette thèse à la suite de mon mémoire.

Mes remerciements s'étendent également aux membres de mon jury, le Dr. Karen Leus, le Pr. Benjamin Elias, le Dr. Cédric Boissières et le Pr. Jean-François Gohy, pour leurs précieuses contributions, leurs conseils éclairés et leurs remarques constructives durant la pré-défense qui ont grandement contribué à l'amélioration de ce travail.

Je tiens à exprimer ma reconnaissance toute particulière à François Devred, sans qui nombre de mes expériences n'auraient pu être menées à bien. Merci pour ton aide mais également pour ta bonne humeur au quotidien. Merci à ceux qui m'ont également permis de mieux comprendre des résultats parfois complexes, notamment Pierre Eloy et Corry Charlier. Votre patience et vos explications ont été essentielles à l'accomplissement de cette thèse. Je tiens également à remercier Jean-Charles Godefroid pour son expertise technique. Je ne peux oublier de mentionner l'aide précieuse de Françoise Somers au début de ma thèse, qui m'a guidée à travers la jungle administrative, ainsi que l'aide inestimable de Nathalie Blangenois.

Je voudrais également adresser mes remerciements aux stagiaires et mémorants que j'ai eu l'occasion d'encadrer, Sophie, Laurent, Johan et Kachia, ainsi qu'à Guillaume pour notre collaboration courte mais fructueuse ! Je suis reconnaissante pour leur dévouement et leur travail acharné qui m'ont apporté une aide précieuse.

Un très grand merci à mes collègues du C3 et du C2 (anciens et nouveaux), pour la bonne humeur et la convivialité toujours présente qui ont

contribué à la bonne ambiance constante au sein de l'équipe. Merci particulièrement à Marty, Denis, Hippolyte, Fanny pour les weekends à la mer et en Ardennes, les nombreux jeudredi, sans vous je ne suis pas sûre que le covid n'aurait pas eu raison de ma santé mentale ! Merci à Giovanni et Marty, qui ont toujours mis l'ambiance dans le bureau, sans oublier François, Cédric, Vincent, Isaac pour les nombreux verres à la cabane (RIP l'Onlywood), les mots croisés et sudoku du Metro et les fous rires du midi à la cafétaria qui ont rendu cette aventure encore plus mémorable.

Sur un plan plus personnel, mes parents et Jérémy, occupent une place spéciale dans mes remerciements. Merci du fond du cœur pour votre soutien indéfectible dans tout ce que j'entreprends et vos encouragements constants. Vous avez été des piliers essentiels tout au long de cette aventure académique de pas moins de 9 ans !

Je remercie également le gang Maurice (Manon et Louise) pour les fous rires partagés autour d'un Spritz ou d'un thé, les aventures mémorables, les séances de sport pour se défouler, mais surtout pour leur soutien et leur présence en toute circonstance ! Sans oublier Céline, Clémence, Camille et Pauline, Laurent, Arthur, les oenopotes Marie, Madleen, Paul, Flo et Amélie, merci pour les nombreux moments quali partagés. Je suis reconnaissante de tous vous avoir à mes côtés.

Enfin, Denis, je te remercie pour ta patience à toute épreuve mais aussi et surtout de m'avoir supportée dans les moments de stress (et ils sont nombreux !), de doute (tout aussi nombreux) et d'avoir cru en moi quand je n'en étais pas capable. Je te remercie pour tout, pour ton aide au labo, les relectures de chapitres (c'est quand même pratique de travailler ensemble), les soirées et weekends détente loin de la thèse et tous tes encouragements au quotidien.

ABSTRACT

Fossil fuels' scarcity, expense, and environmental hazards necessitate sustainable alternatives. Biofuels, like biodiesel, derived from organic materials, offer promising renewable energy options with low environmental impact. Biodiesel production has significantly grown and is projected to reach 46 billion liters by 2030. The main by-product, crude glycerol, poses a waste issue, but its valorization into high-value chemicals can enhance biodiesel production's value chain. Alkyl lactates offer versatile applications, especially for synthesizing biopolymers such as polylactic acid from bio-based sources like sugars and glycerol. The catalytic transformation of glycerol to alkyl lactates relies on a multistep process involving noble metal nanoparticles and Lewis acid sites. Green chemistry principles emphasize developing heterogeneous catalysts, combining different catalysts in one reactor, or creating multifunctional catalysts to efficiently run the reactions. However, combining different catalytic sites on one unique material can be challenging as multi-steps synthesis can damage the pre-existing active sites, be time-consuming and produce many wastes. This thesis addresses the existing challenges in the current research on synthesizing bifunctional catalysts.

On the one hand, new types of supported gold nanoparticles are prepared in one-pot with their support by the aerosol-assisted sol-gel technique, and investigated with a particular focus on the control of the nanoparticles formation and avoiding their sintering. Upon optimization of the synthesis parameters, small gold nanoparticles embedded on a silica support is successfully prepared and this novel synthesis protocol was successfully extended to other metals. These materials are exploited for the selective oxidation of glycerol to dihydroxyacetone.

On the other hand, the synthesis of bifunctional catalysts, and more precisely combining supported metal nanoparticles and Lewis acid sites is investigated. These catalysts promote the direct conversion of glycerol to lactates, converting rapidly the intermediate (dihydroxyacetone) and minimizing the formation of side-products. The benefit to run the cascade reaction with a bifunctional material as compared to mechanical mixtures is demonstrated.

TABLE OF CONTENT

LIST OF ABBREVIATIONS

Preparation methods

NP	Nanoparticles
AASG	Aerosol-assisted sol-gel
EISA	Evaporation induced self-assembly
DP	Deposition-precipitation

Chemicals

DHA	Dihydroxyacetone
EtOH	Ethanol
GLY	Glycerol
ML	Methyl lactate
MPTMS	Mercaptopropyl trimethoxysilane
TEOS	Tetraethyl orthosilicate
TBASCN	Tetrabutylammonium thiocyanate
OAm	Oleylamine
TBAB	Tetrabutylammonium bromide

Characterization technique

BET	Brunauer-Emmet-Teller
BJH	Barret-Joyner-Halenda
PSD	Pore size distribution
S_{BET}	BET Specific surface area [$m^2.g^{-1}$]
V_p	Pore volume [$cm^3.g^{-1}$]
D_p	Pore diameter [nm]
TSE	Tensile strength effect
DR	Diffuse reflectance
FT-IR	Fourrier-transform infrared
XRD	X-Ray diffraction
2θ	Bragg's angle [°]
FWHM	Full width at half maximum
XPS	X-Ray photoelectron spectroscopy
TGA	Thermogravimetric analysis
TEM	Transmission electron microscopy
FID	Flame ionization detector
BE	Binding energy [eV]
GC	Gas chromatography
TOF	Turn-over frequency

GENERAL INTRODUCTION

This section settles the context in which the present thesis was conducted. Then, a literature review is proposed so as to bring and explain the key notions that will be discussed throughout the document. Finally, the objectives are defined and the strategy is exposed.

GENERAL CONTEXT

In recent years, the global research community has been confronted with the pressing need to address global challenges, such as climate change and fossil fuel resources scarcity. The heavy reliance on fossil fuels has led to a marked surge in greenhouse gas emissions, ecosystem degradation, and depletion non-renewable resources. As the urgency to address these issues intensifies, the field of chemistry should improve its processes towards more sustainable and greener routes to produce chemicals while reducing or limiting the use or generation of hazardous substances (i.e. in line with the green chemistry principles).[1]

In this context, catalysts play a crucial role in modern chemistry by accelerating chemical reactions while themselves remaining unchanged. Heterogeneous catalysts, in particular, offer remarkable advantages due to their solid-state nature. Unlike homogeneous catalysts, which are typically dissolved in the reaction medium, heterogeneous catalysts can be easily separated, reused, and do not contaminate the final products. This property enhances the sustainability of the chemical processes and contributes to reducing waste generation. The use of heterogeneous catalysts also eliminates the need for harsh reaction conditions, leading to reduced energy consumption and minimal waste generation. Their cost-effectiveness and wide applicability across diverse chemical processes make them indispensable in the pursuit of greener chemistry.

The growing imperative to transition away from petro-based chemistry has led the scientific community to explore alternatives such as renewable bio-based feedstocks. Biomass, derived from organic sources such as agricultural residues, wood, and algae, emerges as a promising alternative to fossil fuels. Biomass is sustainable, abundantly available, and its utilization reduces carbon dioxide emissions, making it an environmentally friendly choice. While biomass represents a promising alternative as a renewable feedstock, its unique composition presents distinct challenges in catalysis. Biomass usually contains highly oxygenated compounds, such as sugars, lignin, and cellulose, which have complex structures and reactivity patterns. Conventional catalysts, which are often tailored for petro-based chemistry, may not be effective in converting biomass feedstocks into the high-added value desired products. Therefore, there is a critical need to develop new types of catalysts that can effectively tackle the intricacies of biomass valorization. These catalysts must be designed to cope with the high oxygen content, diverse functional groups, and complex molecular structures inherent to biomass,

ensuring efficient and selective conversion into valuable chemicals and fuels. To transform these biomass molecules into desired products, a series of chemical transformations must often be carried out. These multi-steps reactions, known as cascade reactions, require the presence of multiple active sites to facilitate each step of the conversion process. The development of efficient and selective catalytic processes for the cascade transformation of bio-based glycerol to alkyl lactate is a rapidly evolving field that has the potential to make a significant impact on the chemical industry as a whole.

As chemistry progresses towards green and sustainable practices, it becomes increasingly essential to minimize waste during chemical processes. Conducting multi-step reactions in a single reactor reduces the amount of energy and resources required, leading to more sustainable and economically viable processes. In light of this, the concept of developing bifunctional catalysts has gained significant attention in the scientific community. Multifunctional catalysts possess more than two active sites that can simultaneously catalyze different reactions involved in cascade processes. This unique characteristic offers the potential to enhance reaction efficiency and selectivity, thus paving the way for more sustainable and effective biomass valorization. The development of such catalysts is highly desirable, but is also associated with considerable challenges (i.e. to keep the intrinsic properties of each active sites, avoid hindering of one active specie by the second one). Innovative catalyst preparation methods need to be implemented to tackle these challenges.

Recently, aerosol processes have gained significant interest as a method for synthesizing heterogeneous catalysts. The technique allows for precise control over particle size, morphology, and composition, leading to enhanced catalytic performance. Moreover, the aerosol process offers advantages such as high purity, uniform distribution of active sites, and scalability, making it a promising avenue for catalyst development in various industrial applications. As research continues to advance, the aerosol process holds great promise for revolutionizing catalysis and contributing to sustainable chemical processes. Following these developments, the current thesis proposes a new strategy to target the synthesis of bifunctional catalysts with tailored properties able to reach high selectivity in the production of alkyl lactates from bio-based glycerol, with good stability and recyclability, leveraging on the aerosol process.

STATE OF THE ART

1.Glycerol upgrading

1.1. Challenge and opportunities for the chemical industry

Glycerol (1,2,3-propane triol), is one of the most important bio-based platform chemical owing to its appealing properties: renewable, non-toxic, biodegradable, edible, highly functionalized and therefore reactive. It is emerging as one of the most important feedstocks of the modern industry due to its high availability, low cost and its potential to be transformed into numerous valuable chemicals.

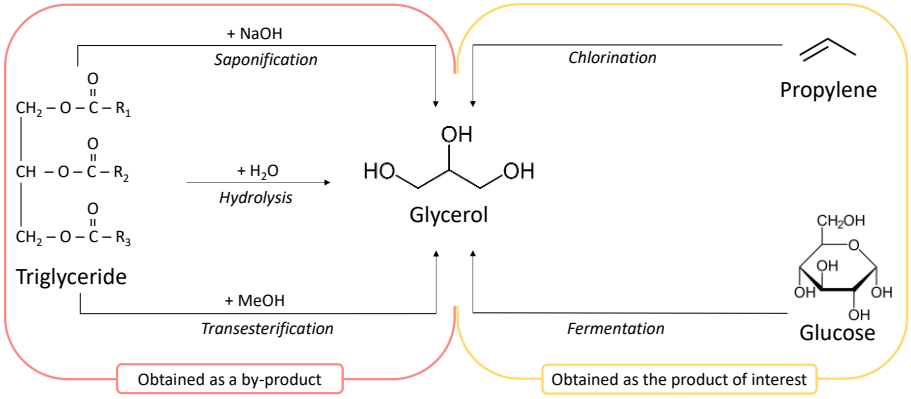

Figure I.1. Different chemical pathways to produce glycerol

Glycerol can be produced by several different chemical routes using different starting materials: (i) via the chlorination of (petro-based) propylene (to first form allyl chloride, then glycerine dichlorohydrine which is subsequently hydrolyzed by caustic soda to form synthetic glycerin), (ii) as a by-product from vegetable oil or animal fat saponification, (iii) as a by-product of biodiesel production, (iv) from the hydrolysis of oils and (v) from the fermentation of sugars such as glucose and sucrose (Figure I.1).[2] Glycerol obtained from natural fats and oils is called natural glycerol.[3] Currently, glycerol is derived from various sources, with ~10% being obtained through hydrolysis, ~12% through the saponification of natural oils, and 50-80% through the production of biodiesel by oil transesterifcation, while the fermentation route to produce glycerol is not used industrially[4,5] Biodiesel

process is currently the main mechanism responsible for the global production of glycerol.

1.1.1. Glycerol synthesis from the biodiesel production

Biodiesel is a renewable biofuel produced from biomass, and more precisely from vegetable edible oils (such as rapeseed, palm and soy oils), animal fat, used cooking oils (UCO), and algae oils. However, the economic viability of producing biodiesel from edible oils is currently challenged by the competition with the food supply, resulting in an increase of the biodiesel prices. Consequently, there has been recent development on the production of biodiesel from non-edible plant oils (jatropha, karanja, castor, and others).[6,7]

Biodiesel shows similar properties to traditional fuels, but interestingly it degrades more rapidly and, when combusted, it emits lower amounts of contaminants (CO, toxic nanoparticles, aldehydes, SO_2) into the atmosphere.[8,9] It is also nontoxic, renewable, and biodegradable which makes it more environmentally friendly and sustainable than fossil fuels. Currently, biodiesel is rarely used in its pure form – as most of combustion engines are not 100% compatible. It is therefore used as an add-in fuel, with a ratio of 5-20% of biodiesel blended with diesel.

Biodiesel is produced through a transesterification process, which involves the reaction of vegetable oils or animal fats with a primary alcohol (such as methanol or ethanol) in the presence of a catalyst (Figure I.2). The transesterification reaction actually converts the triglycerides present in vegetable oils or animal fats into fatty acid alkyl esters (i.e., biodiesel) and glycerol, the main by-product of this process (~ 10 wt.% of the process). While heterogeneous catalysts can perform the reaction,[10] industrially, the reaction is typically carried out in the presence of a strongly basic homogeneous catalyst, such as sodium or potassium hydroxide. The reaction is carried out at moderate temperature (333-338 K).[11] After the reaction is complete, the mixture is separated into two phases, with the biodiesel layer on top and the glycerol layer at the bottom. The phase containing glycerol is usually further processed to extract pure glycerol, while the biodiesel layer undergoes additional purification steps such as washing, drying, and filtration to remove the impurities and the homogeneous catalysts before it can be used as fuel.

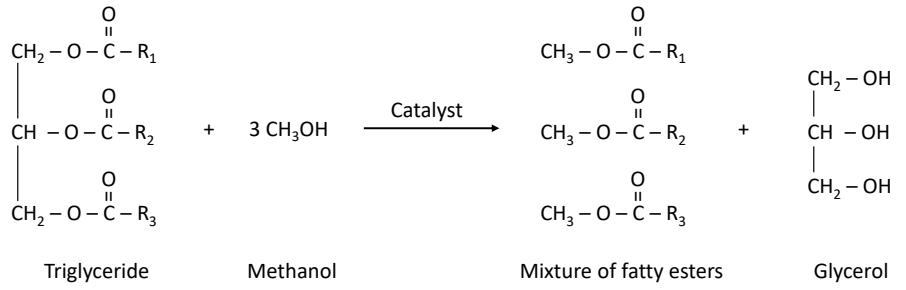

Figure I.2. Transesterification reaction for biodiesel production.

As already stated, a large amount of glycerol is generated by the biodiesel industry as it accounts for 10 wt% of biodiesel production. The glycerol obtained – called crude glycerol – exhibits a 60-80% of purity. Impurities include the excess of alcohol, water, soap, inorganic salts and fatty acids.[4] The composition and purity of crude glycerol can vary depending on the nature of the catalyst, the transesterification efficiency and the source of the oil used in the biodiesel production. It is important to note that the impurities found in crude glycerol may also have economic value. Methanol or ethanol, for instance, can be recovered through distillation and reused in the biodiesel production process, leading to a decrease in the overall production costs. While the separation of the impurities may be considered (by vacuum distillation in inert atmosphere), it is typically only feasible for large-scale biodiesel producers with sufficient capital for the necessary investments.[12] The purification of crude glycerol to recover the pure glycerol is indeed a costly process and generates a lot of waste, making it less appealing.[13]

The use of biodiesel has emerged as an important transition strategy to minimize the fossil fuel dependence. The transport sector accounts for 20% of the global energy demand and for 25% of the carbon dioxide emissions.[14] Indeed, the environmental impact of using fossil fuels encouraged the scientific community to find new bio-based energy sources such as biodiesel. Government policies were implemented in this direction; the European Union's targeted a 20% of renewable energy consumption by 2020, including a 10% of liquid biofuels for transportation. As a result, the biodiesel market has grown significantly in recent years, and is expected to continue to grow. Biodiesel production is projected to increase from 36 Mm^3 in 2017 to 39 Mm^3 by 2027,[15] with Europe leading biodiesel production and consumption.[14,16,17]

Along with the increasing production of biodiesel, glycerol has been over supplied on the market, decreasing its cost in the meantime.[2,18]

The surplus of glycerol raises question on the sustainable use of biodiesel. The use and conversion of crude glycerol into high-value products has therefore become a priority in the biodiesel industry to enhance its economic and environmental competitiveness.[19,20] An efficient and economical utilization of the glycerol produced would greatly improve the economics and the sustainability of the biodiesel production.

1.1.2. Glycerol uses and transformation

Glycerol is a versatile molecule that can be used in a wide range of applications with its main utilization in 2020 depicted in Figure I.3. Currently, the most important use of glycerol is in the pharmaceutical industries where it is used as an emollient, humectant, solvent an lubricants for the production of toothpaste, mouthwashes and soaps, but also in creams and ointments to prevent their drying.[21] In the food industry, glycerol can be used as a sweetener, thickening agent and emulsifier and preservative as it's a nontoxic compound. It is also used as a raw material for the production of surface coatings, inks, resins, cellulose films and adhesives, or to prevent the disintegration due to dryness in the tobacco industry. Furthermore, glycerol has received a great attention as a 'green solvent' in synthetic organic chemistry because of its physical and chemical properties.[22]

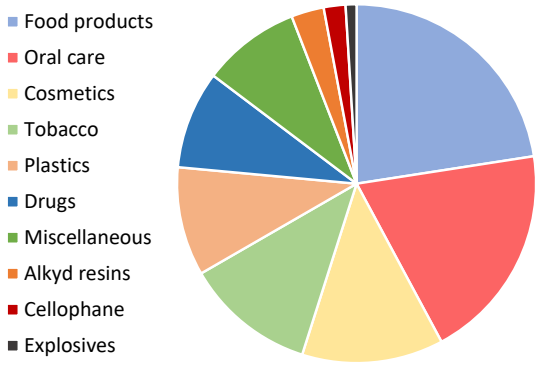

Figure I.3. Main use of glycerol in 2020. From Liu *et al.*, *RSC Adv.*, (2022)[23]

The wide range of industrial applications for glycerol and its high availability from the biodiesel production has boosted the glycerol market. However, the current traditional uses do not absorb its growing production. Therefore, new routes for enhancing its use, such as its chemical transformation into high-added value product is an appealing alternative. Following this idea, the derivatization of low-cost glycerol into added-value compounds has become a hot topic in the research community and highly attractive from an industrial point of view.[2,24,25] Indeed, with a current price of glycerol on the US market approximated at 0.73€ per kg,[26] it is an interesting and cost-effective starting material for further conversion into valuable chemicals. Moreover, the idea to use bio-based chemicals to replace fossil-based chemicals is also of great importance in the current context.

The high degree of oxygen content of glycerol makes it a building-block chemical that can be catalytically converted through various reactions including oxidation, polymerization, dehydration, carboxylation, esterification, reduction, etherification (Figure I.4).[27–33] Numerous products can be obtained including polymers, ethers and fine chemicals valuable for the cosmetic, pharmaceutical, chemical and food industries. More specifically, a lot of glycerol derivatives are building blocks (monomers) to further form polymers.[34] Resulting from the hydrogenolysis of glycerol, 1,3-propanediol is for example used as an important monomer in the production of biodegradable polyesters (such as polypropylene terephthalate – PPT) valuable in the textile industry and carpet manufacturing.[35] The production of acrolein via the catalytic dehydration of glycerol is also of great interest as it is a crucial intermediate in the industrial production of acrylic acid and methionine.[36] Similarly, glycerol carbonate and polyglycerols – obtained respectively by the carboxylation and the etherification of glycerol – are gaining more interest in the recent years for their wide range of uses as biofuel or food additives and as raw materials for the production of plasticizers.[37,38]

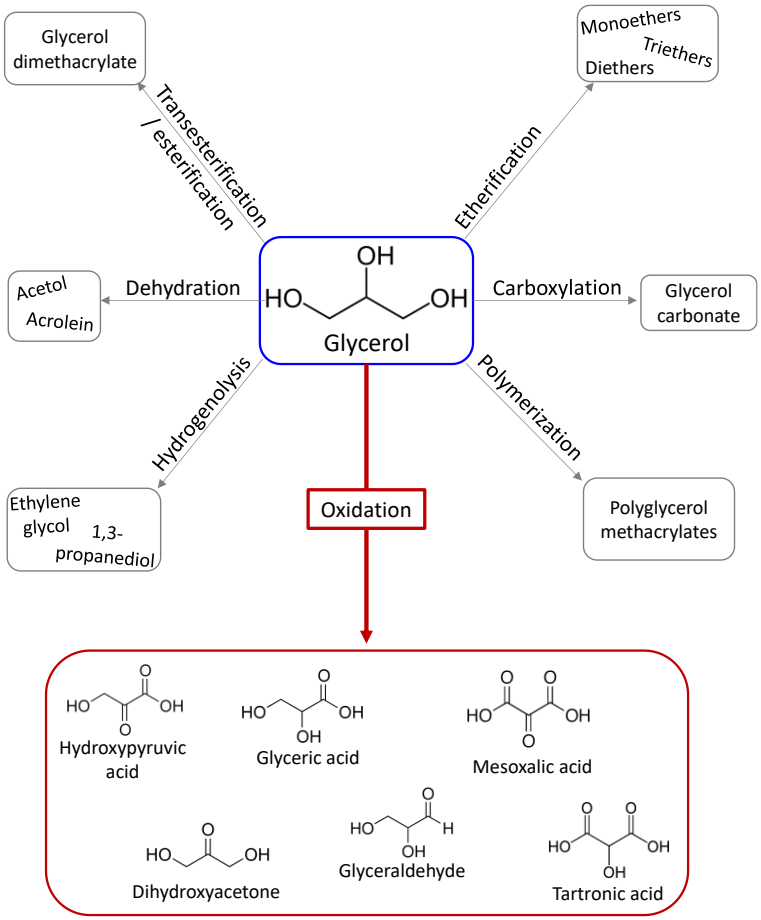

Figure I.4. Scheme of the different transformations possible for upgrading glycerol to valuable compounds, with a focus on oxidation routes.

The glycerol oxidation is one of the most interesting reaction pathways to produce valuable chemicals such as dihydroxyacetone, glyceric acid, glyceraldehyde, etc. Owing to the presence of two different types of hydroxyl groups – primary and secondary – in the glycerol molecule, its partial oxidation primarily produces either glyceraldehyde (GLA) or dihydroxyacetone (DHA) (Figure I.5). The latter is mostly used as an active ingredient in self-tanning lotions in which it produces a brown pigment when reacting with keratin on the skin surface.[39] It is also used in the alcohol, wine, and beverages industries.[5] Dihydroxyacetone is an added-value chemical and the global

dihydroxyacetone market reached the value of 173.95 million USD in 2021.[40] Currently, DHA is produced via the microbial fermentation of glycerol by *gluconobacter oxydans*, which has low productivity because of the low substrate concentration and the long fermentation time.[41] The use of a solid catalyst for the heterogeneous process of selectively oxidizing glycerol to DHA is a highly appealing approach for both academic exploration and practical utilization in industry.

The numerous products resulting from glycerol oxidation highlight the complexity of performing the selective oxidation to a desired product. The main challenge lies in controlling the catalytic selectivity towards the primary or secondary hydroxyl groups of glycerol and in avoiding the consecutive oxidation reactions which can ultimately lead to low value product such as oxalic acid or even carbon dioxide.[42,43] Figure I.5 displays the different products that can form through the oxidation of glycerol. Experimental results showed that the reaction conditions and the nature of the catalyst are key parameters to ensure a good control on the selectivity.[14]

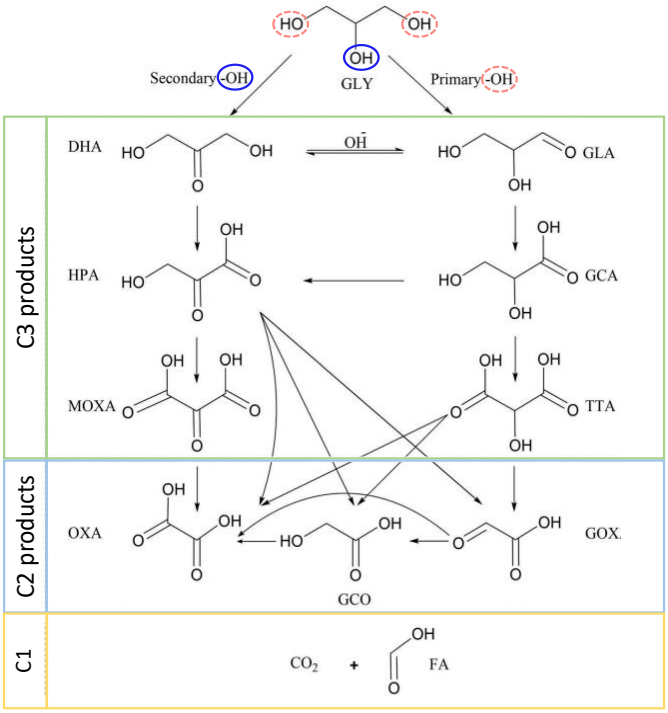

Figure I.5. Glycerol oxidation different pathways. Nomenclature: GLY = glycerol; DHA = dihydroxyacetone; GLA = glyceraldehyde; GCA = glyceric acid; HPA = hydroxypyruvic acid; TTA = tartronic acid; MOXA = mesoxalic acid; GOXA = glycoxylic acid; OXA = oxalic acid; GCO = glycolic acid. Figure adapted from Walgode *et al.* (2020)[14]

1.2. Glycerol oxidation to DHA

It was previously stated that the control on the level of oxidation of glycerol is a major challenge, especially due to the possibility to oxidize the primary and secondary hydroxyl groups of glycerol and the possible (usually unwanted) consecutive oxidation reactions. The following section aims at understanding the reaction mechanism, the key parameters to form and enhance the selectivity to dihydroxyacetone and to discuss the catalytic systems developed in the literature that achieved the best results so far. The readers looking for a more detailed and extensive study on the different catalysts developed over the years can turn to the comprehensive review on

aerobic glycerol oxidation processes using heterogeneous catalysts for the production of DHA, published by Walgode *et al*.[14]

The first catalytic studies on glycerol oxidation were carried out in aqueous basic medium. It is reported that the addition of NaOH (essentially OH^-) plays a crucial role and promotes the oxidation by abstracting one proton from one of the three hydroxyl groups, thereby activating glycerol.[44–48] Supported Au nanoparticles (NPs) or immobilized Au colloids have frequently been employed as active catalysts in the glycerol oxidation reaction.[48–51] However, significant glycerol conversions could only be achieved in a basic medium.[52,53] In the presence of a base, the oxidation of the terminal (primary) hydroxyl group in glycerol is favored, driving the reaction toward very high selectivity to glyceric acid (GLA) rather than dihydroxyacetone (DHA). Another drawback of using basic medium is the formation of organic salts during the reaction. To obtain the desired product, additional separation and processes involving neutralization and acidification are necessary. These additional steps are not environmentally friendly – due to the production of large amounts of salt waste – and expensive. Also, intermediate compounds may strongly adsorb onto the catalyst, thereby hindering the active sites for further uses. Moreover, the addition of a base enhances C-C bond cleavage, leading to an increase of C2 and C1 products, and therefore a decreased DHA yield.[54] From the industrial point of view, it is preferable to directly produce the free products in neutral/acidic reaction conditions.

Therefore, numerous studies have been focusing on the possibility to perform the glycerol oxidation under base-free conditions, in which the formation of DHA is preferred. The base-free catalytic oxidation of glycerol is usually performed using noble metals such as Au, Pt and Pd or bimetallic catalysts based on these noble metals. Due to their great resistance to oxidation, even when exposed to high temperatures, they are highly suitable for the oxidation of alcohols. The reaction is usually carried out with low-cost, non-toxic oxidizing agent such as molecular oxygen or hydrogen peroxide. Due to the versatility of compounds resulting from the glycerol oxidation, the reaction is described as “structure sensitive”, meaning that the characteristics of the catalyst such as the surface nature, the metal nanoparticles size or the support used affect the catalytic performance and more importantly the selectivity toward DHA. To obtain DHA rather than glyceraldehyde, the oxidation of the secondary (central) hydroxyl group must be favored, and further oxidation should be avoided. Consequently, a fundamental challenge is to rationally design advanced heterogeneous catalysts that can offer high selectivity toward DHA at high glycerol conversion.

Meng *et al.* focused on understanding the mechanism of glycerol oxidation at a molecular level by performing density functional theory (DFT) calculations.[18] Figure I.6 (left) shows the two possible pathways to perform glycerol oxidation on gold nanoparticles. The reaction is initiated by the adsorption of molecular O_2 at the Au nanoparticle surface, where the O-O bond is stretched. The adsorbed O_2 can abstract an H atom from the central or terminal C-H bond to form an adsorbed OOH group, which subsequently abstracts an H atom from central or terminal O-H bond to form H_2O_2 and corresponding oxygenates. Notably, the C-H bond cleavage possesses the highest activation energy, serving as the rate determining step. The activation energy for C-H bond cleavage to from DHA (red line; 112.3 kJ mol^{-1}) is much lower than that to form glyceraldehyde (black line; 169.2 kJ mol-1), indicating that, in base-free conditions, the oxidation of central hydroxyl group is thermodynamically favorable. It is also demonstrated by DFT that the stretched O-O bond plays a significant role in the C-H bon cleavage, so in the absence of oxygen, it is much more difficult to activate the C-H bond. Therefore, the activity of Au nanoparticles could be enhanced if the oxygen activation is improved. The presence of water can also benefit the oxygen activation on Au suface.[52]

The oxygen activation can be enhanced by the metal oxide support. Meng *et al.* employed the stretch of O-O bond and the adsorbed O_2 charge as activity descriptors to predict which support are more suitable for Au NPs (Figure I.6, right).[18] They showed that the stretch of the oxygen bond was linearly correlated with the charge measured in adsorbed O_2 and confirmed that O_2 was actually activated through the electron donation of Au into the O_2 π*orbital, resulting in an elongated O-O bond similar to that of the superoxo-like (O_2^-) adsorbate state. Based on their calculations, Zn and Cu oxides were the best supports for AuNPs with a high O-O stretch indicating a good oxygen activation. They also experimentally confirmed those results in the oxidation of glycerol to DHA. Au/ZnO and Au/CuO exhibited the highest TOF (respectively 229 and 211 h^{-1}) as compared to the AuNPs on the other supports ($TOF_{Au/TiO2}$ h^{-1} = 20, $TOF_{Au/SiO2}$ = 0 h^{-1}).

Similarly, Yuan *et al.* showed that the surface acidity/basicity of the supporting material ($MgO-Al_2O_3$ in their work) is a key to control the selectivity of Au NP in the base-free conversion of glycerol in water.[55] The $MgO-Al_2O_3$ support with the highest acidity and lowest basicity exhibited the greatest activity for activating glycerol and producing DHA with the highest selectivity. Conversely, enhancing the surface basicity or reducing the acidity of the $MgO-Al_2O_3$ support resulted in an increase in selectivity for glyceric acid but a

decrease in selectivity for DHA formation. Similarly, Wang *et al.* used Cu-Zr mixed oxide to show that the presence of a large number of basic sites would lead to a decreased glycerol conversion.[56]

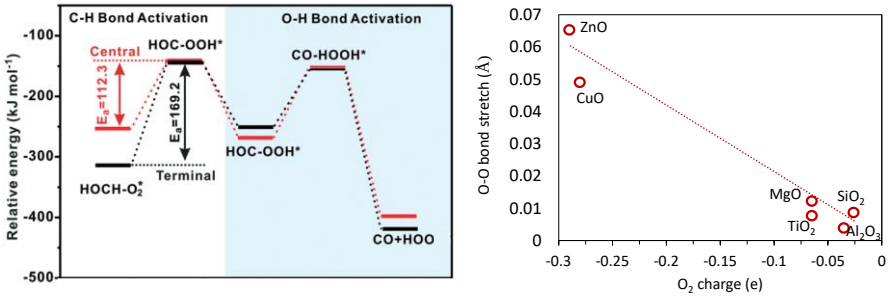

Figure I.6. (Left) Energy changes for the oxidation of central hydroxyl group (red line) or of terminal hydroxyl group (black line) of glycerol on Au (111). (Right) O_2 charge and O-O bond stretch on 2-layer Au supported on different oxides.[18]

As mentioned previously, the majority of studies in the literature employ catalysts based on noble metals such as Pt, Pd, Au, and Ag, which have shown to be highly effective in selectively oxidizing glycerol through aerobic processes.[14] Kimura *et al.* were the first to report the glycerol oxidation to DHA using an active carbon-supported 1%Bi-5%Pt/C catalyst. The highest DHA yield reached 20% with a 30% conversion of glycerol under acidic conditions (pH 2-4); 323 K and 0.1 MPa air atmosphere.[57,58] They showed that the addition of bismuth to supported Pt enhanced the selectivity of the secondary hydroxyl group oxidation to from DHA. Further investigations were performed on Pt-promoted catalysts. Various carbon supported bimetallic PtM (M = Sn, Mn, Fe, Cu, Ni, Zn) were synthesized and tested in glycerol oxidation.[59] These catalysts demonstrated higher activity compared to monometallic catalyst, resulting in a better production of DHA, although with a relatively low selectivity ranging from 10% to 15%. Such beneficial effects were not observed for Pd-based catalysts promoted with non-noble metals. Actually, the addition of Bi as a promoter to Pd did not enhance the selectivity to DHA or GCA; on the contrary, it led to a reduction in catalytic activity.[60] Pd-based catalyst are generally poorly active in base-free conditions,[61] but once combined with Au[62–64] or Ag[65], the catalytic performance can be improved. With PdAg/AC, the DHA selectivity reached 82% with a 10% glycerol conversion.[66] After optimization of the reaction conditions, DHA yield reached 44% at 52% glycerol conversion over PdAg/C.[65] This is the best DHA yield

achieved by both Pd and Ag-based catalyst. The alloy phase is believed to be responsible for the enhanced activity and selectivity toward DHA.

The main drawback observed with Pt- and Pd-based catalyst is that they are prone to deactivation by oxidation or by-product poisoning during the liquid phase glycerol oxidation.[67,68] Therefore DHA selectivity with these catalysts was generally limited as the oxidation of the primary alcohol group could not be fully avoided.[69,70] Gold was therefore considered as a more attractive catalyst thanks to its high resistance toward oxygen poisoning, allowing to work under higher oxygen pressure. Prati *et al.* obtained good results using supported Au catalysts for the oxidation of various alcohols.[71] Liu *et al.* were the first to report the synthesis of DHA under base-free conditions with an Au(2%)/CuO catalyst and reached a 80% DHA yield at 98% glycerol conversion.[47] In their work, the impact of different supports (Al_2O_3, TiO_2, ZrO_2, NiO, and CuO) on monometallic Au catalysts was investigated under mild conditions (in water, 50°C, GLY/Au of 50, P_{O2} = 20 bar), and, among the supports studied, CuO was found to be the most effective. Au(2%)/CuO catalyst demonstrated the highest level of activity and DHA was the primary product of glycerol oxidation. To the best of our knowledge, this is the highest reported yield of DHA for glycerol catalytic aerobic oxidation in a batch process.

The choice of reaction conditions and catalysts can have a significant impact on the selectivity and yield of the desired product. The effect of these conditions should be carefully considered to achieve the desired product selectivity and yield. As mentioned earlier, the pH has a major impact on the selectivity of glycerol oxidation. Although the conversion of glycerol is enhanced under basic conditions, the production of DHA is not favored. Moreover, catalyst deactivation by metal leaching was reported under basic conditions.[58,60,68] Therefore base-free conditions should be employed to ensure high DHA selectivity. For most of the catalysts discussed above, increasing the temperature led to higher glycerol conversion while the DHA selectivity was usually not changed.[47] The oxidation of glycerol into DHA is exothermic, with a standard enthalpy of reaction at 25°C = -139 kJ mol^{-1}.[72] The influence of temperature on the reaction mechanism, however, is unclear. Thus, optimization of temperature for specific catalysts is necessary. The catalyst performance during glycerol oxidation should also be affected by the oxygen pressure. When the oxygen pressure is increased, the concentration of oxygen in the liquid phase also increases, potentially leading to a higher overoxidation reaction rate. However, it was found that with Au(2%)/CuO, increasing the oxygen pressure from 5 to 30 bar actually decreased the DHA

selectivity and led to the formation of CO_2.[47] In the case of catalysts based on Pt and Pd, the catalytic performances were even poorer due to catalyst overoxidation.[73] Table I.1. summarizes the different key points presented above.

Aside from reaction conditions, the properties of the catalyst itself – such as the metal particle size, the preparation method, the dispersion, the nature of the support – can greatly influence the catalyst activity, stability, and product selectivity in glycerol oxidation. These parameters are critical for achieving high catalyst activity and selectivity towards the desired product. The influence of these parameters will be discussed in the following section 1.3 of this introduction, focused on the preparation of heterogeneous catalysts.

It is interesting to note that selective synthesis of DHA from glycerol has also been achieved through electro- and photo-oxidation methods.[74–76] Glycerol electro-oxidation provides the ability to adjust the oxidizing conditions through the modification of the electrode potential, therefore allowing a better control of the reaction rate and the product selectivity. However, it has been reported that maintaining high DHA selectivity becomes challenging as glycerol conversion increases. Nevertheless, this was recently overcome by utilizing a Bi- and Sb- promoted Pt/C electrode, although long reaction times of approximately 10 hours were required.[77,78]

Glycerol oxidation has been extensively studied in water (all the studies presented in this section were performed in aqueous medium),[14,48,52,55,56,79–82] and there are very few reports of this oxidation process taking place in methanol. The group of Taarning performed the reaction in methanol over supported gold catalysts and sodium methoxide. The formation of dimethyl mesoxalate was reported with a 89% selectivity at full conversion (T°=373 K, 5 bar of O_2).[83] DHA and glyceraldehyde were not detected during the test. It is assumed that it was directly converted to the next products of oxidation. To the best of our knowledge, no successful upgrading of glycerol into DHA has been reported using alcohols as the solvent. Reaction in a solvent (in particular methanol) is however very relevant to the present thesis work in the perspective of the cascade upgrading of glycerol to lactates (see below, section 3 of the introduction).

Table I.1. Summary of the catalysts developed for the base-free oxidation of glycerol to DHA in water.

Catalyst	Comments	Ref
Supported Au	DFT calculations to better understand the impact of the support on Au nanoparticles activity in the glycerol oxidation. It showed that glycerol's central -OH oxidation via with Au catalysts under base free conditions was thermodynamically favorable. While CuO and ZnO are the best supports, on SiO_2 the catalytic activity is highly reduced.	18
Au/MgO-Al_2O_3	Study of the influence the acidity/basicity of the support on the catalytic activity of Au nanoparticles. Increasing the acidity increases the selectivity toward DHA while increasing the basicity leads to larger amount of glyceric acid.	55
1%Bi-5%Pt/C	Investigation on the effect of the addition of a promoter such as Bi on Pt metal nanoparticles. The presence of Bi increases the selectivity toward the oxidation of the second hydroxyl group to form DHA. The catalytic performance of the BiPt nanoparticles are better than the ones of the monometallic.	57
PdAg/AC	Pd nanoparticles are less active in the glycerol oxidation, but once alloyed with Au or Ag the catalytic performances are improved. The formation of alloy favors the oxidation of the second hydroxyl group to form DHA.	66
2%Au/CuO	Highest DHA yield reported in a base-free medium reported in the literature (XGLY = 98%, Y_{DHA} = 80%). Several supports tested (Al_2O_3, TiO_2, ZrO_2, NiO, CuO). Optimized the reaction conditions (T, $P(O_2)$, reaction time, GLY/Au, presence/absence base) for DHA production. Increasing the pressure from 5 to 30 bar resulted in a decrease of the production of DHA in favor of the formation of CO_2.	47

1.3. Supported metal nanoparticles synthesis for glycerol oxidation

Metal nanoparticles (NPs) are of great interest due to their unique properties that differ from their bulk counterparts.[84,85] When materials are reduced to the nanoscale, their properties generally undergo changes due to the size-induced metal-insulator transition, also called the quantum size effect. As the material size decreases in the nanometer range, the proportion of atoms on its surface also becomes more significant, in other words, the surface-to-volume ratio increases. Metal nanoparticles with a small size distribution have attracted significant attention in both scientific research and industrial applications due to their unique properties, rising from their large surface-to-volume ratios.[86] This, in turn, impacts the material's surface-related properties. However, due to their high surface area, dispersions of small NPs are thermodynamically and intrinsically unstable and therefore, if not stabilized, they tend to sinter and aggregates quite easily. Therefore, there is a need to stabilize the metal nanoparticles during their synthesis and immobilization.

In catalysis applications, metal nanoparticles have a significant impact, particularly those with a high surface area and abundant active sites that promote faster reactions and enhance product yield. They can be used as colloidal metal nanoparticles, with the presence of capping ligands to stabilize the particles,[87] or they can be supported on various metal oxides.[88] Considering the ease to recover NPs when they are immobilized on a support – as compared to colloids – the vast majority of metal nanoparticles-based catalysts are in fact supported catalysts. This section will focus on the properties of supported metal nanoparticles in general, and on their preparation methods. This overview will be essential to understand the original approach that we propose in the framework of this PhD research to design metal-based catalysts for the oxidation of glycerol.

1.3.1. Metal NPs characteristics

Supported metal nanoparticles are generally classified into two main categories: noble-metal-supported nanoparticles (such as Au, Pt, Ag, Pd, Ru, Rh, etc.) and non-noble-metal-based nanoparticles (including Fe, Cu, Ni, Co, etc.). A series of parameters govern the level of catalytic performance: the shape and the size of particles, the nature of the metal and the support, the interactions between the support and the metal NP and the preparation

method. Those different parameters will be discussed in more details in the following paragraphs.

The shape of NPs has an important effect on catalytic activity as the shape determines the surface atomic arrangement and coordination. The catalytic activity of metal nanoparticles is enhanced when they possess a high-density of atoms in step edges, and kinks (Figure I.7). These sites are commonly recognized as being crucial to perform catalytic processes.[89] Depending on the shape of the nanoparticles, the number of atoms in these positions vary. The size of the nanoparticles is also very important parameters to control as it affects the surface properties which dictates the catalytic behavior. Nanoparticles possessing larger surface areas can increase the number of active sites, thereby reducing the activation energy required for catalytic reactions.[90] Haruta and coworkers were the first to observe the relationship between the turnover frequency (TOF) of CO oxidation and the size of gold nanoparticles.[91] They showed that when the size of Au NP increased from 2.5 to 6 nm, the apparent activation energies changed from 1.7 to 5 kcal.mol^{-1}. The highest TOF was obtained when gold nanoparticle had an average size of 3 nm. Since then, it is known that obtaining small metal nanoparticles is of paramount importance to develop high catalytic performance.

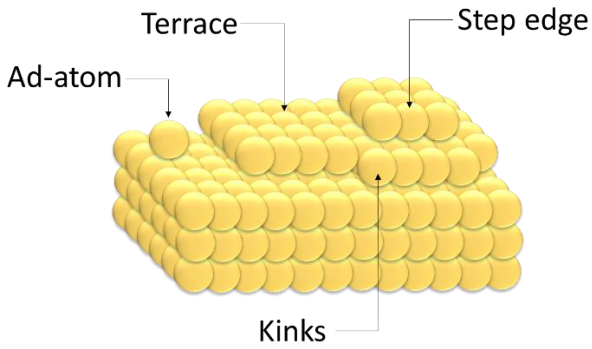

Figure I.7. Model of metal surface indicating the different features: terrace, step, kink and ad-atom (inspired from Farias *et al.*[92]).

1.3.2. Metal NPs deactivation

The main reason leading to catalyst deactivation is the particle growth, also called sintering. It can be understood in terms of two mechanisms: the Ostwald ripening or the particle diffusion and coalescence (Figure I.8).[93] Ripening refers to the process of larger particles growing at the expense of smaller particles due to differences in surface free energy, which involves interparticle transport of mobile species. On the other hand, particle migration involves the Brownian motion of nanoparticles, which can lead to coalescence when particles come into close proximity.[94] It is commonly accepted that sintering proceeds in 3 steps: (i) Ostwald ripening is favored and is responsible for the rapid loss of activity due to the disappearance of the smallest nanoparticles, (ii) once the smallest particles have disappeared and a combination of Ostwald ripening and coalescence occurs and (iii) the particles have now grown large and their mobility is highly reduced.[93] Small particles tend to have a higher mobility than large particles and sintering slows down as particles grow in size. These phenomena are influenced by the environment of the NPs and are triggered by elevated temperature. The Tammann temperature (0.5 $T_{melting}^{bulk}$ [K]) is defined as the temperature where surface atoms become mobile and this mobility at the surface constitutes the mechanism for particle mobility.[94,95] At this temperature, sintering can occur. It was also reported that when gold nanoparticles had a size under 10 nm, their melting temperature decreases, implying that the Tammann temperature is also lower, explaining why very small nanoparticles tend to have a higher mobility. For instance, gold Tammann temperature is estimated at 395°C, but under a diameter of 2 nm, reached only about 150°C.[96]

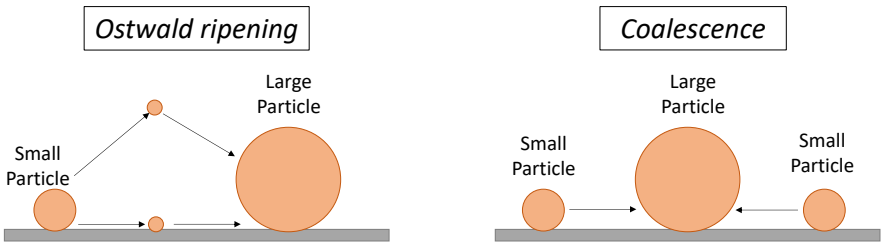

Figure I.8. Scheme of the different mechanisms of particle growth

1.3.3. Influence of the support

The dispersity, the size and the shape of the active metals are greatly influenced by the nature of the support and the preparation method used to deposit/form these nanoparticles at the surface. Indeed, the properties of the support can significantly affect the activity and the chemical properties of the supported metal particles.

Metal oxides are often used as supports of finely dispersed active metal nanoparticles in catalysis. The metal oxides present specific properties such as acidity (Lewis or/and Brønsted types), basicity, redox features (when transition metal ions are present), which lead to specific catalytic properties. They can be divided into two main classes depending on their chemical properties: (i) nonreducible oxides (*e.g.* SiO_2, Al_2O_3) and reducible oxides (*e.g.* (TiO_2, CuO, Fe_2O_3).[97] Nonreducible oxides are materials that exhibit resistance to losing oxygen, due to the intrinsic resistance of the metal cations to oxidation state changes. These oxides possess a large band gap, typically greater than 4-5 eV, separating the conduction band from the valence band. Whenever oxygen is removed from the material, the remaining excess electrons become trapped in specific sites, such as oxygen vacancies, resulting in the creation of new defect states in the band gap. This process is energetically very costly, and therefore these as-prepared materials are highly stoichiometric, stable, and chemically inert. In contrast, reducible oxides have the capacity to exchange oxygen relatively easily. Consequently, they tend to have semiconductor character, with band gaps below 4 eV. When oxygen is removed from reducible oxides, the excess electrons are redistributed to the cation empty levels, causing their oxidation state to change.

Numerous reports have focused on the catalytic properties of metal oxide to use them as support for NPs, including oxides of Si, Al, Ti, Zr, Cu, Ca, Mg and Zn. When used as supports, nonreducible metal oxide usually have a negative impact on the dispersion and size of the metal nanoparticles (i.e. producing rather large particles), while reducible supports have a positive impact and tend to improve NP dispersion.[98] It is noteworthy that the support can also actively affect the catalytic behavior of the metal nanoparticles. Depending on the support and the nature of the metal precursors, the affinity between the surface and the metal and their interactions can vary, leading to different range of size of nanoparticles.

Among them, Si oxides are versatile, inert and cheap supports showing a high chemical and thermal stability and a tunable texture. These properties makes it an attractive material, especially to study more in detail the catalytic activity of the metal NPs without the influence of the support.[99–101] Moreover, silica is a very versatile material that serves as the starting point for the preparation of various heterogeneous catalysts that are not based on metal nanoparticles (*e.g.* metallosilicates, *vide infra*). The silica surface can also be easily functionalized and modified to change its properties. These materials are synthesized easily by sol-gel chemistry, template-assisted and microwave assisted techniques.[102] However, silica tends to negatively influence the dispersion of metal NPs and to increase sintering. On the silica surface, metal nanoparticles usually have a high mobility and the nanoparticles tend to sinter and form large particles, rather poorly active in catalysis. Therefore, the deposition of metal NPs on silica materials is usually challenging and great efforts are made in the research community to find solutions to obtain small metal NPs highly dispersed on silica.[99,103] Gold has for instance a very poor affinity with silica's surface and conventional methods of synthesis – such as impregnation or deposition-precipitation methods – therefore often lead to large gold particles with size above 20 nm.[104]

Thus, sintering is significantly influenced by the interaction between the metal and the support, which is determined by the relative strengths of the metal-metal and metal-support bond energies.[105] There are some strategies proposed in the literature to improve the affinity between a support and the metal NPs. The functionalization of the surface support with different groups (*e.g.* thiol, amine) has been widely used over the last decades. This way, the point of zero charge (PZC) of silica – which is relatively low (~2) – is modified and the affinity between the support surface and the metal precursors is increased. Similarly, the compounds used to functionalize the surface can also be used to anchor the NPs at the surface of the support so that their sintering is prevented. Working with porous materials with a periodic pore structure of similar diameters (*e.g.* SBA-15) also can be useful to mitigate the sintering as the nanoparticles can be confined in the pores. Sintering and particle aggregation is then inhibited by the pore size.[106,107] Fore example, Pan *et al.* reported that confining metals particles inside carbon nanotubes could effectively prevent metal sintering.[106] Gabaldon *et al.* showed that silica which displays tortuous 1-D pores with limited connectivity hampered the sintering via the Ostwald ripening.[108] The gold nanoparticles incorporated on this support exhibited small and narrow size distribution, leading to good catalytic performance in the oxidation of CO. Another strategy found in the literature to limit the sintering is to add a second component (as in a bimetallic) or another porous oxide phase applied as an overcoat on the primary support.[109,110] For

instance, the addition of a small amount of titania on silica or silica on titania led to an improved stability of supported gold nanoparticles.[108,111]

1.3.4. Metal NPs synthesis on mesoporous silica

Within the field of nanomaterials in general and catalysis in particular, the green chemistry principles are of great importance. Ideally, metal nanoparticles should be synthesized using less toxic precursors, in environmentally benign solvents like water or ethanol, with minimal use of reagents, at or close to room temperature, and the synthesis through a single synthetic step (one-pot reaction) should be favored, while minimizing the generation of by-products and waste. Additionally, the nanoparticles should be well dispersed on the support surface and highly active in their catalytic applications.

There are a wide variety of methods for preparing catalytically active supported nanoparticles. Typically, two main approaches are used for the production of NPs: the top-down approach, which involves breaking a solid into smaller particles, and the bottom-up approach, which produces NPs from molecular precursors, salts, or complexes, through chemical vapor deposition, sol-gel process, chemical reduction, or co-precipitation methods.[112,113] The bottom-up approach has become more popular due to its ability to provide better control of particle size compared to the top-down approach. Among them, the different preparation methods can be divided into physical and chemical routes.

Chemical routes are widely used for their ease of implementation with different metals and different support. These techniques are depicted in Figure I.9 and will be explained in the following part. The deposition-precipitation which involves the precipitation of a metal precursor – by the addition of a precipitating agent (such as urea) – onto the surface of a suspended material, allows obtaining relatively small nanoparticle sizes with a good distribution of the metal at the surface of the support.[114–119] Impregnation methods (dry and wet impregnations) have long been the mainstay to incorporate metal on silica surface. It is based on the wetting of the support by a controlled volume of solution (= pore volume of the catalyst support in the case of dry impregnation, in excess in the case of wet impregnation) containing the metal precursors and on the subsequent drying, leading to the deposition of the metal at the support surface. A subsequent reduction step is then performed to obtain the metal particles.[120–122] These methods are easy but suffer from a poor control

on the nanoparticles size and dispersion, especially with silica-based support. In the case of silica-based supports, the difficulty is indeed related to the specific conditions of the deposition of the metal precursor. At pH higher than 2, the surface of silica is negatively charged, making it very difficult to interact with the metal anions (for instance $[AuCl_4]^-$ when $HAuCl_4$ is used as a precursor), resulting in poor dispersion of the salt and in the formation of large metal particles. In order to obtain a better dispersion, the silica surface can be functionalized to modify the point of zero charge and improve the affinity with the metal anions.[123–125] The surface modification process can either occur after silica support synthesis (post-synthesis grafting) or during the hydrolysis and condensation process when the silica walls form (in situ co-condensation). Post-synthesis grafting is more commonly used as it allows a better control of the level of grafting at the surface of the synthesized material. Factors including the nature of the functional group, solution pH, and thermal treatment conditions affect the size of formed metal nanoparticles.[126] More recently, ionic liquids have also been employed as modifying groups to trigger the nucleation of metal nanoparticles.[127,128] Finally, sol immobilization, on the other hand, relies on the pre-formation of metal nanoparticles with a controlled size to subsequently immobilize them on a support.[129–131] Through such colloidal route, the support is submerged in suspension of nanoparticles that adsorb at its surface. Functionalization can also facilitate the immobilization and dispersion of the pre-formed nanoparticles. Various structures can be obtained via these synthesis routes: surface supported metal nanoparticles, core-shell structure, wall intercalated metal nanoparticles.[126] All these methods implies multi-steps routes (synthesis of the support or the pre-formed nanoparticles, functionalization, deposition/immobilization of the NPs, with all the thermal treatment between the different steps) which are somewhat unattractive from an industrial point of view.

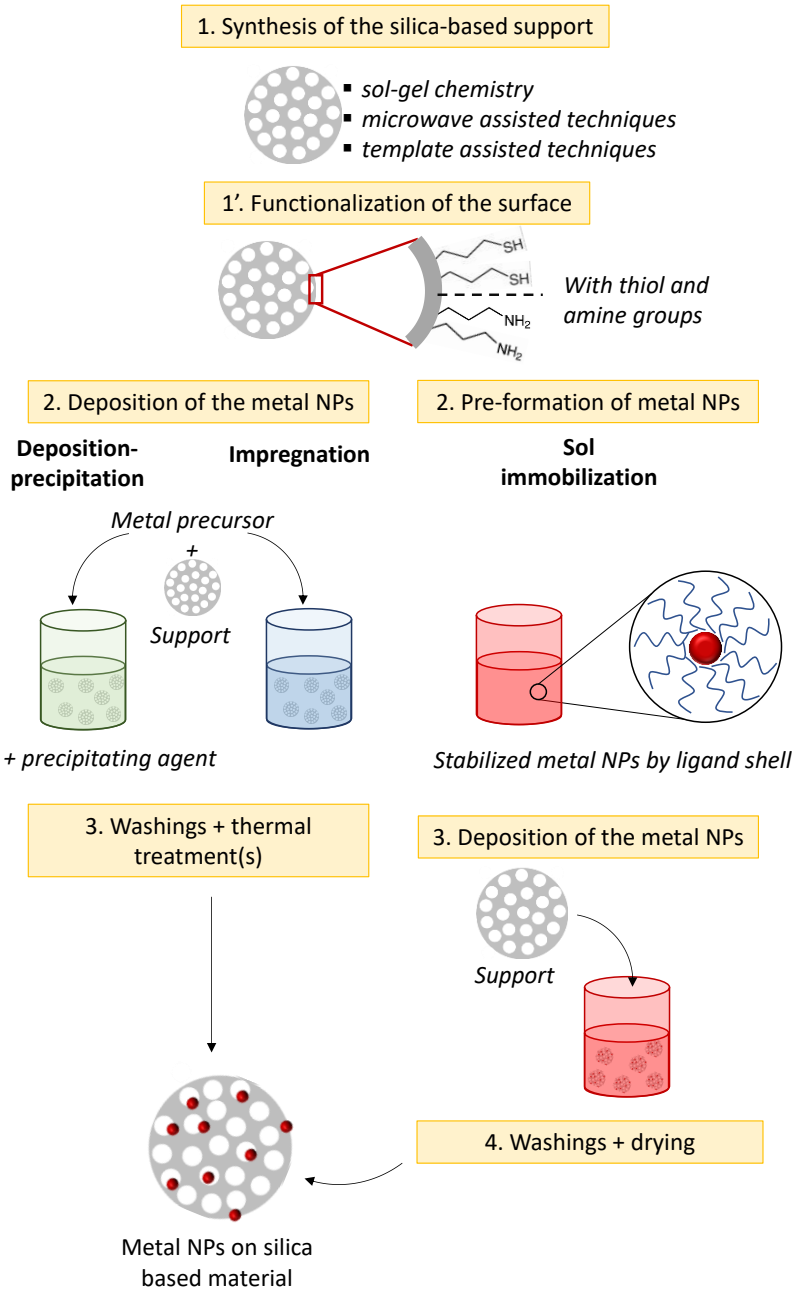

Figure I.9. Schematic of the different chemical routes to immobilize metal NPs on silica-based materials

Physical routes to prepare supported metal NPs are also less extensively studied and developed. They include sonication,[132] microwave irradiation,[133] supercritical fluids,[134] laser ablation,[135] and plasma synthesis.[136] Although most of these techniques allow controlling the size and dispersion of the NPs and are usually environmentally friendly, they often involve costly specialized equipment that limit their throughput and their widespread use. Therefore, these methods will not be discussed in this work but there are various reviews describing them more extensively.[137–139]

1.3.5. Summary and considerations

A challenge when working with supported metal nanoparticles, especially when they're small – which is usually desirable for catalysis – is to improve their stability and avoid their sintering and aggregation, which would lead to a loss of active sites and catalytic activity.

There have been major developments on the synthesis methods to use silica materials as a support for metal NPs. In this matter, there are two pathways to improve their preparation: (i) via the synthesis of the silica support itself (i.e. the functionalization of the surface or the control of the porosity) and (ii) via the synthesis of the NPs on the support (i.e. the synthesis parameters). Nevertheless, although small gold nanoparticles can be obtained, such synthesis routes are generally time- and resource-consuming due to their multistep approach, which makes them less attractive for industrial applications. In the present dissertation, we will turn our attention to an innovative alternative synthesis method (*vide infra*) to combine metal NPs and silica-based materials in a simple, direct pathway involving a limited number of steps while managing to disperse and obtain small metal NPs.

2. Towards lactates

2.1. Industrial significance of lactates

Lactic acid holds significant interest across various industries due to its versatile properties and wide range of applications. Lactic acid (LA) is currently the most commercially used hydroxycarboxylic acids[140] In the food and beverage industry, lactic acid acts as a natural preservative, flavor enhancer, and pH regulator. It is widely used in dairy products, baked goods, beverages, and pickled foods. More importantly, lactic acid serves as a precursor for the production of biodegradable polymers, such as polylactic acid (PLA), which finds applications in packaging materials, disposable cutlery, and textiles. PLA is a promising biodegradable polymer showing excellent biological compatibility and good recyclability. As it is the most promising substitute to fossil-based polymers such as polyethylene and polypropylene, there have been many studies to improve its properties and synthesis.[141,142]

Currently, over 90% of the lactic acid is produced by glucose microbial fermentation. In Belgium, Galactic is now known as one of the world's leading producers of lactic acid and its derivatives through sugar fermentation process. Although it offers eco-friendly synthesis conditions (low temperature, low consumption of energy), biological processes are characterized by low product yield, lack of stability, long processing time and relatively large amount of salts produced.[143] A purification step is also required to remove the impurities and obtain a polymer-grade lactic acid, highly desirable for PLA synthesis. However, it is still cumbersome to recover lactic acid from the fermentation broth. The current method used implies several steps. In the traditional procedure, LA is transformed into calcium lactate via the addition of calcium carbonate. The heated and filtered fermentation broth is then concentrated to allow crystallization or precipitation of calcium lactate, followed by addition of sulfuric acid to remove the calcium in form of calcium sulphate (gypsum) and recover lactic acid.[144] To further obtain highly pure LA (99% wt.), additional steps are required: (ii) the esterification of impure lactic acid to form an alkyl lactate (AL, usually methyl lactate ML) which can be separated more easily by distillation[145–147] followed by (ii) the hydrolysis of the lactate into high-purity lactic acid, which can be further transformed to PLA. This multistep process is energy-, time- and waste consuming. The separation and final purification steps accounts for 50% of the production costs.[140] The high cost of the processes to synthesize highly pure LA constitute a barrier to widespread PLA use and therefore, alternative methods are currently being sought to limit its cost.[148]

The direct utilization of lactates for PLA production has sparked significant interest over the last decade. However, their current synthesis primarily depends on the LA formation through its esterification which is associated with numerous disadvantages stated above. Hence, the development of new approaches for lactate synthesis has become a prominent and exciting research topic.

2.2. Lactates in biorefineries

Recently, novel approaches have been proposed for synthesizing lactic acid and alkyl lactates using trioses, such as glyceraldehyde (GLY) and dihydroxyacetone (DHA), as starting materials. It is actually considered as an attractive pathway to reduce the tedious process of lactic acid production in fermentation and waste management.[149] The production of alkyl lactates from trioses has attracted much attention in the field of research as they are platform molecules widely used in the industry as green solvents and starting materials for the synthesis of biodegradable polymers.[150] For these reasons the research for catalysts able to catalyze the efficient conversion of DHA to AL is a highly active topic.[117,151]

The transformation of DHA to alkyl lactates is performed by acid catalysts, involving the combination of Brønsted and Lewis acid sites. Mechanistic studies were performed by several groups to understand how the conversion of DHA to alkyl lactates (and more precisely methyl lactate) proceeds (Figure I.10).[151–154] They showed that the reaction includes two steps: (1) the successive keto-enol tautomerization and dehydration of the primary hydroxyl group to form pyruvic aldehyde (PA), catalyzed by weak Brønsted acid sites; (2) the rehydration of PA followed by a 1,2-hydride shift and a nucleophilic addition of the alcohol molecule to the carbonyl carbon atom of the aldehyde. This step is catalyzed by Lewis acid sites and leads to the formation of methyl lactate. The presence of strong Brønsted acid sites should be avoided to prevent the formation of acetals as major by-products.[155]

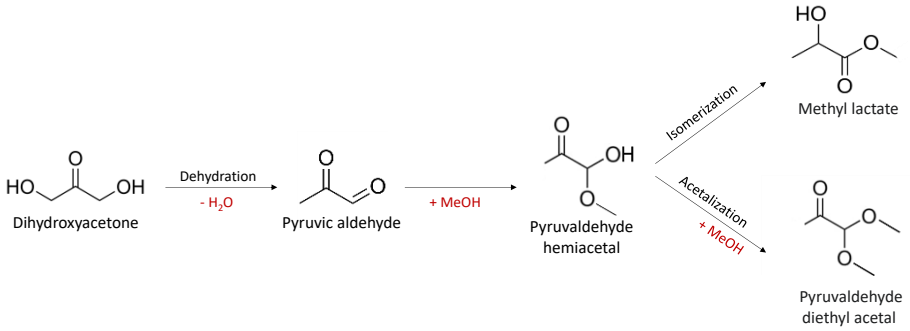

Figure I.10. Proposed reaction pathway for converting dihydroxyacetone to methyl lactate

Homogeneous catalysts, such as $ZnSO_4$,[156] have been investigated, but their use was limited due to harsh conditions (high temperature and pressure) and the use of toxic and corrosive catalysts. Hayashi and Sasaki investigated the use of metal salts as homogeneous catalysts for the conversion of trioses to alkyl lactates and showed that tin catalysts ($SnCl_2$ and $SnCl_4 \cdot 5H_2O$) were the most active catalysts[157] as tin exhibits a high Lewis acidity compared to other transition metals.[158] Moreover, tin has the unique ability to activate the carbonyl group which brings a high selectivity toward alkyl lactates.[159] Indeed, a methyl lactate yield of 82% was achieved using $SnCl_4 \bullet 5H_2O$ at 90°C, although large amount of salts were needed. Importantly, however, as mentioned earlier, homogeneous catalysts are difficult to remove from the reaction mixture.

Therefore, based on these results, many tin-containing heterogeneous catalysts were developed to improve the recyclability of the material. A review published recently extensively summarizes all the heterogeneous catalysts developed for the synthesis of methyl lactate and lactic acid from sugars and their derivatives.[153] Among them, tin-containing zeolites (such as Sn-USY[160,161], Sn-Beta[83], SnFAU[162]) showed excellent performance (ML yield > 99%).[83,153,163] The active site of Sn-beta is found to have notably stronger acidity compared to the other examined catalysts, which likely accounts for its superior catalytic performance at low temperatures during the conversion of triose sugars to methyl lactate.

Hydrothermal crystallization can be used to synthesize certain types of tin-containing zeolites.[164] However, this process is challenging and time-consuming, leading to limited metal loadings and the formation of large zeolite

particles that can restrict diffusion inside the pores.[165] An alternative method is post-synthetic zeolite metalation, which involves two steps: dealumination and/or desilication of the starting zeolite to create vacancies in the crystal framework, followed by metalation to fill these vacancies with metal species.[166,167] This method is simpler than hydrothermal crystallization and can be completed easily for tin-containing zeolites, but it is also time-consuming as the synthesis is performed in several steps.

It was found that mesoporous structured materials bearing Lewis acid sites such as Sn-MCM-41 and Sn-SBA-15 can also be very active and selective in the conversion of DHA to alkyl lactates.[83,83,151,155,168,169] Indeed their superior performance compared to microporous solids like zeolites is due to reduced limitations in the diffusion of reactants and products. By adjusting the size and arrangement of mesopores, the diffusivity of these materials can be further controlled. Although the yield toward methyl lactate is significantly better using the Sn-BEA catalyst at low temperature (40°C), the tin-based mesoporous structured materials (such as Sn-MCM-41 or Sn-SBA-15) can achieve similar yields (> 80%) if the temperature is increased (120°C).[170] Li *et al.* demonstrated that decreasing the size of mesoporous particles to form extra-small (XS) Sn-MCM-41 particles with diameter ranging from 20 to 140 nm improved the conversion of DHA as compared to conventional Sn-MCM-41 (64% compared to 32%). However, the selectivity was also reduced at higher conversion.[168]

The use and development of Sn mesoporous silicates has been optimized to find a perfect balance between activity, accessibility, dispersion and stability to the selected reaction conditions (that imply the possible reuse in consecutive cycles). The successful incorporation of isolated tetrahedrally coordinated Sn into the silica framework – which provide the acid sites required for the reaction – is the key to obtain an active catalyst.[168] It was shown that the incorporation of Sn in the framework also better promotes the formation of Brønsted acid sites, especially when compared to materials prepared via Sn-doping of MCM-41 catalysts. In their work, Kim *et al.* reported that in the conversion of DHA, a lower Brønsted/Lewis acid sites ratio resulted in higher selectivity toward lactates.[155] Based on this finding, the optimized catalyst developed in their work (Sn-MCM-41) provided a 100% yield toward lactates during the catalytic conversion of DHA within a reaction time of 30 minutes at 65°C.

2.3. Incorporation of Lewis acid sites in mesoporous materials

Mesoporous structured materials bearing Lewis acid sites (i.e. Sn-MCM-41, Sn-SBA-15, among others) were reported as active materials in the conversion of DHA to alkyl lactates. The acidity and porosity are the most important parameters to control to ensure good selectivity and to reach excellent yield to the targeted product.[171] Mesostructured silica-based materials were already described as attractive for their morphology, the size and shape of the pores can be controlled to improve the accessibility to the active sites and therefore the catalytic performance.

Mesoporous silica-based materials such as SBA-15, MCM-41 and "aerosol SiO_2" (*vide infra*) have high surface area, adjustable pore volume and good thermal stability. However, they have almost no acidity, limiting their applications in catalysis. Heteroatoms can be incorporated to tune the acidic properties of the material. On the one hand, the incorporation of trivalent atoms (such as Al) in tetrahedral coordination in the framework causes an excess of negative charge, giving rise to Brønsted acidity. On the other hand, the addition of tetravalent atoms such as Zr, Sn, Hf and Ti in the silica framework results in the presence of Lewis acidic properties.[172]

Kilos *et al.* reported that the location of the metal (i.e. if it is inserted in the framework or extra-framework), the texture, morphology and the final acidity of the resulting material were strongly dependent on the nature of the metal and its loading in the material.[173] For instance, they incorporated Nb, V, and Mo in SBA-15 and it was showed that Nb-oxide would mostly be located in the extra-framework while Mo oxide was almost fully located inside the framework. The nature of the metal, and more precisely the size of the heteroatom is an important feature to look at. Obviously, heteroatom with a size similar to the one of silicon have a better ability to enter the silicon matrix and to incorporate the framework.[174]

Sn-based materials have shown outstanding catalytic performance that remains unsurpassed in the transformation of DHA to alkyl lactates. Two strategies can be envisaged for the production of stannosilicate catalysts: (i) a bottom-up approach, which involves adding a Sn precursor to the catalyst synthesis gel (*e.g.,* through hydrothermal procedures), and (ii) top-down strategy (referred as post-synthesis strategies in the following), which entail depositing Sn onto an existing silica structure. The selection of a specific strategy can result in the formation of distinct catalytic active sites (*e.g.* hydrated or dehydrated, framework species or extra-framework oxides), ultimately influencing the activity, selectivity, and stability of the resulting materials. Achieving atomically dispersed Sn sites is the most critical

parameter to control during the synthesis of tin silicates that show good activity in the conversion of DHA to alkyl lactates. The formation of condensed SnO_x phases should be avoided for they are less in this reaction. Indeed, in the most common oxide form of Sn (SnO_2) the tin metal is octahedrally coordinated to six –O–Sn, which corresponds to tin in its highest coordination state. As a result of the absence of open coordination sites, Sn cannot interact with reactants and is inactive. Ideally, catalytically active Sn species have four (tetrahedral) or fewer bonds with the support structure to enable coordination with electron-donating groups of the substrate, such as carbonyls. Depending on the synthesis technique and conditions, the formation of Sn oxide species can be prevented or minimized.

Bottom-up approaches to synthesize Sn-containing materials are attractive to obtain stannosilicates in one pot. The introduction of tetrahedrally coordinated framework Sn in the mesoporous silica structure was successfully accomplished by the direct addition of the tin precursor ($SnCl_4$•$5H_2O$) in the synthesis gel of a silica-based material.[175–177] The incorporation of high loading of Sn (up to ~15%) have been reported with this strategy. However, the formation of extra framework SnO_x species could not be avoided for such high metal loading. Moreover, tin was partially buried in the amorphous silica walls rather and on the surface, lowering its accessibility for catalysis.[178,179] This synthetic approach typically involves several steps (hydrolysis, aging, etc.), sometimes spanning several days. Combined with the difficulty to scale-up the process, this preparation route can be considered unappealing.[180]

Post-synthetic strategies are usually preferred as they imply shorter and easier protocols while assuring higher accessibility of Sn atoms. Different strategies exist: chemical vapor deposition (CVD) of $SnCl_4$, grafting of alkyl Sn salts (liquid and gas) and impregnation of tin precursor ($SnCl_4$•$5H_2O$).[181,182] Among them, liquid grafting is particularly interesting as it allowed the controlled introduction of Sn tetrahedral sites homogeneously at the surface of the framework. The silanol groups present at the surface of the material can be used as anchoring groups for the grafting of the tin alky salt. These strategy usually involves the preparation of the alkyl tin salt through a multi-step procedure, followed by the grafting and the chemical exchange of the ligands to afford the active tin species.[183] Advantageously, Wang *et al.* showed that SBA-15 grafted with tetrabutyltin exhibited a better hydrothermal stability, most probably due to the reduced amount of silanol groups at the surface resulting in a higher hydrophobicity of the surface and a higher resistance toward water.[182] Similarly, Nishiyama *et al.* reported an enhanced thermal stability of the catalyst when comparing the MCM-41 post synthetically treated with $SnCl_4$ vapor and Sn-free MCM-41.[184] Although impregnation method is easy to implement and widespread, it often results in less homogeneous

incorporation of tin compared to the other methods, with the presence of hexacoordinated tin in the material.[182]

These methods are widely spread and used. However, they either rely on multi-steps synthesis which are for obvious reasons time-consuming and waste-intensive, or their use results in extra framework tin species, poorly active in catalysis. The dissertation turns to alternative synthesis strategies (see next section of the Introduction), with the aim to limit the number of steps while ensuring a homogeneous incorporation of tin in tetrahedral coordination in the silica framework.

3. From glycerol to lactate: an integrated process

3.1. The cascade reaction: Glycerol to methyl lactate

Considering the potential of methyl lactate for the biopolymer and chemical industries and the limitations of its current production (see section 2.1 above), alternative synthesis routes are considered. More specifically, the conversion of bio-based glycerol – a green renewable feedstock – to alkyl lactates is extremely appealing, in particular using methanol as a solvent to form methyl lactate as methanol is already presented in the crude glycerol produced from biodiesel, as mentioned in section 1.1.1 of this introduction[185] This approach eliminates the need for an additional esterification step, which is required for the production of high-quality polylactic acid. The production of methyl lactate starting from glycerol has therefore attracted increasing interest in the scientific community over the last decade, with an increasing number of papers tackling this matter. Such transformation involves the two reactions (thereafter called “steps”) describes in the sections above: oxidation to DHA and rearrangement to methyl lactate.

The development of greener processes involving limited number of steps is highly desirable from an industrial point of view. In this perspective, integrating multiple catalytic steps within one system (to therefore perform cascade reactions) is an elegant example of process intensification, aiming to achieve direct transformation while minimizing resource consumption. This approach is characterized by its ability to achieve more with less, promoting sustainability and efficiency in chemical processes. Cascade reactions offer several advantages and have garnered significant interest in the field of catalysis.[186–188] Performing multiple reactions in a single reactor eliminates the need for intermediate purification steps. Indeed, in traditional multi-reactor setups, intermediate products are often isolated and purified between each reaction step, leading to increased costs, time, and potential loss of valuable intermediates. In a cascade reaction, however, the direct transfer of intermediates between catalytic sites allows for seamless progression without the requirement for isolation or purification. More importantly, the proximity of different catalysts may facilitate rapid transfer of intermediates, reducing the loss of reactive species and enhancing reaction efficiency, thereby leading to higher yields of the desired product.

Great efforts have been made to develop catalytic systems to perform the direct upgrading of glycerol to methyl lactate in one unique reactor. Several reports have been released, showing efforts to design heterogeneous catalysts to perform the cascade reaction. Based on the works reviewed in the previous sections on each step, the catalytic systems for the valorization of

glycerol to methyl lactate should combine two types of active sites: (i) a noble metal for the oxidation step and (ii) Brønsted and Lewis acidity for the triose isomerization (Figure I.11). While many research groups have successfully developed catalytic systems for converting glycerol to lactic acid using water as a solvent,[189–193] there have been relatively few reports on the upgrading of glycerol to methyl lactate in methanol, especially working in base-free conditions. Controlling the level of glycerol oxidation to produce trioses selectively presents a challenge, as these intermediate compounds are prone to further oxidation, which can result in the formation of predominantly highly oxidized compounds.[43] Fast and selective transformation of the intermediates is crucial as the lactic acid/alkyl lactate produced is more stable than the trioses under the reaction conditions. Hence, careful design of the catalytic system, including the noble metals and solid acid functions, and their relative amounts, is essential.[194,195]

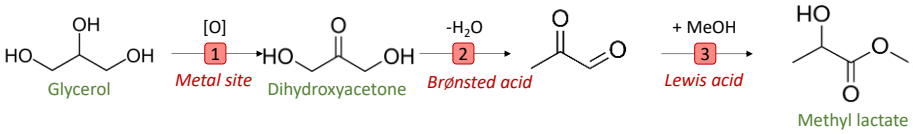

Figure I.11. Cascade reaction from glycerol to methyl lactate with the different steps of the reaction and the catalytic species required.

3.2. Mechanical mixture for the cascade reaction

Few groups reported the catalytic transformation of glycerol to methyl lactate with a mechanical mixture of two catalysts (one for each step of the cascade reaction). The group of Pescarmona first demonstrated that a mechanical mixture of 2%Au/CuO and Sn-MCM-41-XS could reach a 95% glycerol conversion with a ML yield up to 62% in 10.5h at 140°C.[196] Extra small Sn-MCM-41 particles were selected for their moderate Brønsted acidity (compared to zeolite catalysts) which is more favorable for the second step of the cascade reaction. Indeed, Sn-MCM-41-XS exhibited a much better selectivity compared to USY in the isomerization step. Based on these first results they focused their effort in designing a better catalytic system for the first step of the cascade reaction.[197] The use of bimetallic nanoparticles tuning the electronic properties, stability and morphologies of the nanoparticles was studied. The optimal ratio Au:Pd was found at 1:1 and deposited on carbon

nanotubes. The support was functionalized with different functions to ensure the best anchoring of the metal nanoparticles. The developed catalyst gave 85% yield of methyl lactate at 96% conversion of glycerol after 9 h at 140 °C, which is the best catalytic performance reported so far in the literature for base-free systems. The use of bimetallic Au–Pd nanoparticles was shown to lead to higher activity compared to the monometallic systems (either Au or Pd alone), proving the synergy between Au and Pd. The turn-over frequency TOF) of these systems was calculated based on the initial glycerol conversion and the loading of gold introduced in the reaction ($mol_{GLYconverted}.mol_{Au}^{-1}.h^{-1}$). The two catalytic systems exhibited good TOF (Table I.2, entry 5-6).

Based on the results obtained by Pescarmona and collegues, Zhou *et al.* used an Au/CuO catalysts combined with Sn-Beta zeolites as a mechanical mixture to perform respectively the oxidation and isomerization to form ML.[198] Similarly, CuO was selected as the best among a series of metal oxides to support gold NPs and enhance their catalytic performance The reaction was tested under low temperature (90°C). The best Sn loading in the Beta zeolites was found at 2 wt.%, due to the formation of inactive extra framework species at higher loadings. The one-pot conversion of glycerol to ML was successfully executed over the mixture of Au/CuO and Sn-Beta, with a 85% glycerol conversion and 60% ML yield after 4 hours at 90°C. Increasing the glycerol concentration up to 4 times led to decrease the glycerol conversion to 54% and the ML yield to 34%, mostly due to DHA overoxidation. Although this report showed great potential while working at low temperature, the resulting catalytic system still showed poorer performance when calculating the TOF (Table I.2, Entry 7), as the high amount of catalysts engaged during the reaction was relatively high.

3.3. Development of bifunctional catalysts

Moving forward, with the idea to improve the sustainability of the transformations, efforts are made to intensify the processes, for example by developing multifunctional catalysts bearing different catalytic species, able to run cascade reactions in a unique reactor.[199] Strong boost of the catalytic performance in multifunctional catalysts are often observed due to the synergistic effect brought by the active site proximity.[200–204] Also, from a chemical engineering perspective, it is attractive to handle only one type of solid particles instead of two or more, as it facilitates the optimization of

handling, stirring, recovery, etc. The challenge, however, is to combine two or more types of functional sites – such as acid and metallic – on the same solid particles in a way that they both preserve their intrinsic activity, and to make them work cooperatively in a reactor to perform the one-pot cascade reaction.

The group of Heeres was the first to report the direct conversion of glycerol to methyl lactate using methanol as a solvent with a material bearing two active sites. Their pioneering work was based on the combination of gold nanoparticles supported on USY zeolites.[194] In this system, the Lewis acid sites are brought by the USY-600 zeolites. The bifunctional catalyst was synthesized following a multi-step procedure. Colloidal gold was first synthesized using PVA as a protecting agent and $NaBH_4$ as a reducing agent to form Au^0 sol. The nanoparticles were then immobilized on the zeolite support. The gold nanoparticles size displayed rather large distribution with diameter ranging from 3 to 15 nm. The catalytic conversion reached 95% after 10h at 160°C with a yield approximated at 73% to ML. The direct conversion of DHA into ML enabled them to highlight the minimal occurrence of overoxidation products. At 90°C, the glycerol conversion was significantly decreased to only 5%. In their work, they also tested different support (USY-720, Al_2O_3, H-Mordenite) and showed that the highest ML yield was achieved when zeolites contained a significant proportion of extra-framework Al species, indicating the importance of Lewis sites in this reaction. The catalytic system developed in this work exhibited very high TOF (calculated based on the glycerol conversion and gold loading, see Table I.2, Entry 1).

Moving further Lu *et al.* worked on the introduction of tin in less acidic USY zeolites. This way, the amount of Lewis acid sites can be precisely controlled and studied in the isomerization of trioses.[205] In their work, a hierarchical Sn-USY, active at room temperature, was synthesized to fully convert DHA to ML with an excellent yield (95%). The Sn-USY zeolites were obtained by a first step of dealumination followed by dry impregnation of tin. On this modified zeolite, preformed Au nanoparticles were immobilized by a colloidal deposition method (as it was described above). The interaction between those two active sites and their properties (i.e. the surface electronic properties of gold and the acidity of tin) were also investigated. Interestingly, they showed that the gold nanoparticle size was positively impacted by the presence of tin. Indeed, when tin was absent of the zeolites, large nanoparticles of 18.7 nm were obtained with a large particle size distribution ranging from 8 – 32 nm. The incorporation of tin in the USY, with loading from 1 to 4 wt. % gradually decreased the nanoparticles size from 9.4 to 5.5 nm. They evidenced that the presence of extra-framework Sn species (Sn reacting with Si-OH to form SnO_x) at high tin

loadings was responsible for this size decrease. The gold nanoparticles were preferentially located near the extra framework species and interacted by transferring some electrons into the SnO_x species, hindering the further growth and aggregation of the nanoparticles (Figure I.12). Leveraging on the positive interactions between Au and extra-framework Sn, they worked with a 3 wt.% Sn loading to obtain nanoparticle of 6.2nm. The resulting catalyst displayed good catalytic activity. They were the first to report such a high ML selectivity (~90%) with a high yield (>75%) after 10 hours of reaction, at 160°C. The mechanical mixture of the two separate catalysts showed poorer conversion (~ 40%) with a ML yield of only 12%. It is unclear if the improved catalytic performance observed with the bifunctional catalyst are the result of (i) the significantly smaller gold nanoparticles or (ii) the proximity of the two active sites. Their work evidenced the complexity of synthesizing bifunctional materials, even when using intricate multistep procedures. Importantly, the gold nanoparticles size could not be controlled independently from the Sn loading, Also, the amount of Lewis and Brønsted acid sites were also affected by the parameters used to immobilize the gold.

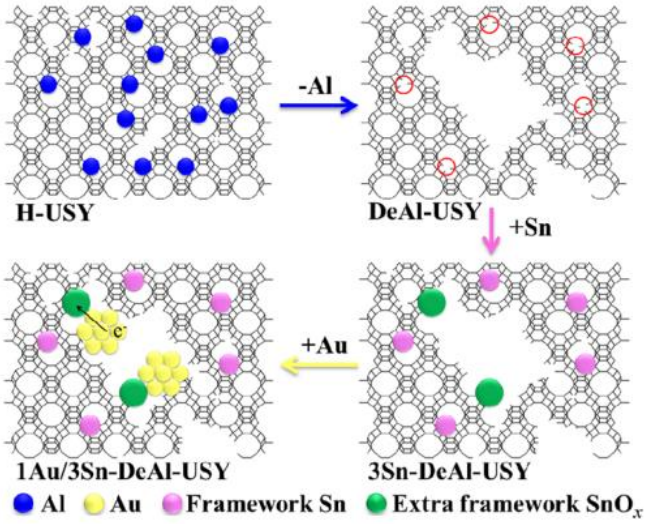

Figure I.12. Schematic representation of the synthesis of the Au/3Sn-DeAl-USY catalyst from Lu *et al.* (2014).[205]

Later on, Li *et al.* developed a tin-exchanged montmorillonite (Mt), a low-cost material with high surface area, a tunable acidity and a great ability to exchange cations, such as metals cations.[185] In their paper, up to 25 wt.% of tin was successfully incorporated in the Mt using an ion exchange method.

The gold nanoparticles were also deposited on the support surface as preformed Au^0. The best catalyst contained 20% of tin and 1% of gold (Au/Sn(20)-Mt). In the conversion of glycerol to methyl lactate, at 150°C and after 6h, only 35% of conversion and less than 5% of ML yield was obtained. Better catalytic performances were however obtained when increasing the temperature to 210°C, with a maximum conversion of 78% and a methyl lactate yield of 54%. Impressively, the developed catalyst showed the best TOF found in the literature (Table I.2, Entry 3-4). As it was already observed in the work of Lu *et al*., they reported in this work that the average gold nanoparticle size was impacted by the tin loading, but with an opposite effect. The incorporation of Sn into the materials led to a noticeable increase in the size of gold nanoparticles, growing from 3.5 nm without tin to 6.1 nm when the tin loading reached 25 wt.%. The authors suggested that the introduction of tin into the Mt altered the surface properties of the support, negatively impacting the anchoring of Au particles and promoting their aggregation upon immobilization. Low-angle and wide-angle XRD patterns both showed a reduced crystallinity owing to the partial delamination of the Mt structure in the acidic solution containing the tin precursor. After the further deposition of gold nanoparticle, the Mt layered structure completely collapsed. Furthermore, a decrease in the overall acidity of the material (while maintaining a constant L:B acidity ratio) was observed after gold deposition on the support. These observations emphasize the challenged encountered when preparing a bifunctional catalyst, particularly in terms of preserving the integrity of the starting material and the already formed active site during the subsequent incorporation of each additional active site.

Similar results were obtained by the group of Perscarmona when trying to deposit gold nanoparticles and Sn-MCM-41-XS. The synthesis of the bifunctional catalyst proceeded in two steps: (i) the synthesis of Sn-MCM-41-XS particles, (ii) the loading of gold nanoparticles at the surface MCM using the deposition-precipitation method. Unfortunately, the alkaline conditions of this second step resulted in the deterioration, the partial dissolution of the support material MCM-41-XS and a significant loss of tin sites (~30%) and thus of Lewis acidity. As a result, low ML yield were reached (35%) at rather high conversion (76%), with a higher amount of overoxidation side product. The synthesis of bifunctional materials can be a complex endeavor, as active sites may be lost during multi-step processes. Preserving and incorporating these active sites effectively is essential to ensure the desired functionality and maximize the catalytic potential of the material.

More recently, a bifunctional catalyst was synthesized leveraging on the idea to anchor gold nanoparticles on hierarchically ordered core-shell Snβ@mesoporous silica composites.[206] The catalyst was synthesized in three steps: (i) the synthesis of the Snβ zeolites – the core, (ii) the deposition of the mesoporous silica (MS) around the crystals – the shell and (iii) the deposition-precipitation of gold nanoparticles on the Snβ@MS. In this work, they managed to create a unique sandwich-like structure in which the gold nanoparticles are located at the junction of the Snβ surface and the mesoporous silica wall. As a result, the obtained gold nanoparticles (size distribution of 1.3-3.9 nm) are protected from sintering. The resulting catalyst exhibited good catalytic results with a glycerol conversion of 98% and a ML yield of 92% at 140°C after 4 hours. However, those results were obtained working with a very high catalyst loading (Au/glycerol molar ratio) compared to other works and the resulting TOF of the catalytic system in this work was actually found to be the lowest (Table I.2, Entry 8).

As it was demonstrated through the various aforementioned examples, synthesizing bifunctional materials represents a challenge for it usually involves multistep synthesis processes in which the addition of an active species on a preformed (active) material can modify its morphology or texture, can affect the nature of chemical surface species, and can hinder the availability of catalytic sites. However, the synthesis of bifunctional material is highly desirable to perform a cascade reaction, especially the transformation of glycerol to ML because the proximity of the two active sites may enhance the rate of the reaction and increase the yield of desired products – while preventing side reaction leading to the decomposition of the intermediate (DHA). Therefore, it appears pertinent and imperative to develop innovative synthesis strategies that minimize synthesis steps while preserving the intrinsic properties of each catalytic species.

Table I.2. Catalytic systems already developed in the literature and their catalytic performance for the glycerol conversion to methyl lactate

Entry	Catalysts	T (°C)	t (h)	P (bar)	$C_{Glycerol}$ (M)	Au / AuPd loading (wt%)	Molar Gly/Au ratio	Sn loading (wt%)	X_{Gly} (%)	Y_{ML} (%)	TOF[a]	Summary	Ref
1	Au/USY-600	160	5	30 (air)	0.25	0.35	1407	/	81	60	228	1st work to report the cascade reaction, lower overoxidation product during the one-pot cascade, extra framework Al needed for the 2nd step	194
2	Au/Sn-USY	160	0.5	5 (O_2)	0.2	1	98.5	3	59	48	116	Introduction of Sn for a better control of the Lewis acidity, the presence of extra framework Sn stabilize the gold NP during their formation	205

3	Au/Sn(20) Mt	210	0.5	30 (air)	0.25	1	1407	20	62	62	1745	Mt a very good support to incorporate Sn (up to 25%), the deposition of the AuNp leads to the partial collapse of the structure and a loss of acidity	[185]
4	Au/Sn(20) Mt	150	0.5	30 (air)	0.25	1	1407	20	29	~0	816		[185]
5	2Au/CuO + SnMCM-41-XS	140	4.5	30 (air)	0.25	1.79	985	3	65	62	142	Mechanical mixture better than bifunctional, Sn-MCM-41-XS for a better selectivity than zeolites, CuO best support for Au	[196]
6	PdAu/C + SnMCM-41-XS	140	2.5	30 (air)	0.25	1 (1:1)	692.5	3	47	42	130	Better catalytic performance in the first step with bimetallic than monometallic	[197]
7	Au/CuO + Snβ	90	0.5	15 (air)	0.1	1	49.2	2	47	25	46	Catalysts successfully working at the lowest temperature reported, increasing	[198]

8	Au/SnβMS	140	1	5 (air)	0.2	1	98.5	4	31	30	30	the concentration of glycerol decreases the conversion AuNPs protected from sintering thanks to a unique sandwich-like structure	206

[a] Turn-over frequency, calculated on amount of glycerol transformed and the amount of gold introduced ($mol_{GLYconverted}.mol_{Au}^{-1}.h^{-1}$).

4. The aerosol-assisted sol-gel process

As showed above, the concomitant dispersion of small and stable metal NP onto silica, and incorporation of metal sites into the silica matrix remains challenging, and existing synthetic procedures suffer from various types of limitations. In this context, it is interesting to turn to alternative preparation routes that may offer potential advantages.

Sol-gel routes are known to offer wide synthetic options, in particular for the preparation of heterogeneous catalysts.[207] Sol-gel syntheses are widely used to produce metal oxides, especially silica, titania, alumina, zirconia, etc. Usual hydrolytic sol-gel methods involve two main reactions: (i) the hydrolysis of the metal organic precursors (such as alkoxides and salts) in acid or basic medium to form reactive species and (ii) the polycondensation of the hydrolyzed products through oxolation (in the case of silica) (Figure I.13). Sol-gel chemistry – as a "chimie douce" approach[208] – offers a handy toolbox for blending different precursors and obtaining mixed oxides, for creating tailored porosity, and for introducing surface functionalities. All of these aspects are crucial for the preparation of heterogeneous catalysts.

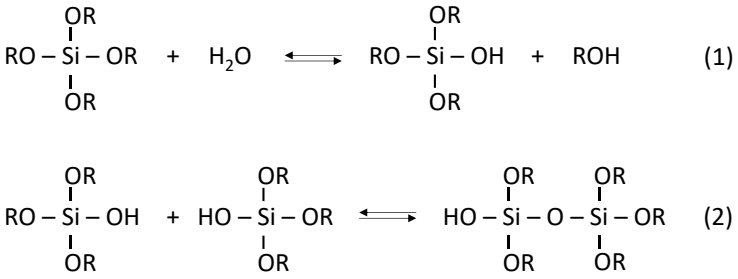

Figure I.13. Typical sol-gel chemistry with a Si alkoxide with (1) the hydrolysis and (2) the condensation via oxolation reaction. R = alkyl chain ($-CH_2CH_3$ for TEOS).

Aerosol processes are versatile methods to produce dry powders. They rely on the atomization of a liquid sample and on the rapid evaporation of a volatile solvent from a liquid mixture to obtain powders. When drying a suspension of preformed solid particles, it referred to as "spray drying". The utilization of aerosol processes has found wide applications in industries such

as pharmaceuticals, chemicals, polymers, and food, primarily due to its economic viability, continuous operation, scalability, and rapid powder production capabilities.[209,210] Notably, one of the remarkable advantages of aerosol processing is the precise manipulation of particle characteristics, including shape, size, and density, which can be achieved through meticulous control of the aerosol operating conditions. In the field of catalysts synthesis, continuous aerosol processes are primed to solve some synthesis challenges such as time- and resource- consuming issues, as they involve a very limited number of preparation steps and allow producing various kinds of advanced heterogeneous catalysts with a fine control of the catalyst particle shape, size, surface chemistry and textural properties.[211]

Interestingly, coupling sol-gel chemistry with particular processing strategies, can offer an extended toolbox to control the final materials properties.[212] In particular, sol-gel chemistry can be combined with aerosol processing. This has been coined as the “aerosol-assisted sol-gel” process, AASG. In this case, the atomization is not exploited simply to dry a preformed solid, but instead liquid droplets are used as micro-reactors into which the solid material is being synthesized during processing. A stable and homogeneous solution of (pre-hydrolyzed) precursor(s) is atomized to form a mist of droplets which have all the same composition (Figure I.14). The droplets are subsequently dried under relatively mild conditions which initiates the evaporation of the solvent and the inorganic polycondensation reactions. Pore-generating agents are often used to generate the desired porosity in the material. It can either be pre-formed particles, such as polymer or biopolymer beads, or surfactant molecules which undergo evaporation-induced self-assembly (EISA) to form micelles that are trapped in the inorganic framework during the drying step. The aerosol-assisted sol-gel process is frequently accompanied by subsequent thermal or chemical treatments to eliminate the templating agent, thereby create the porosity.[211]

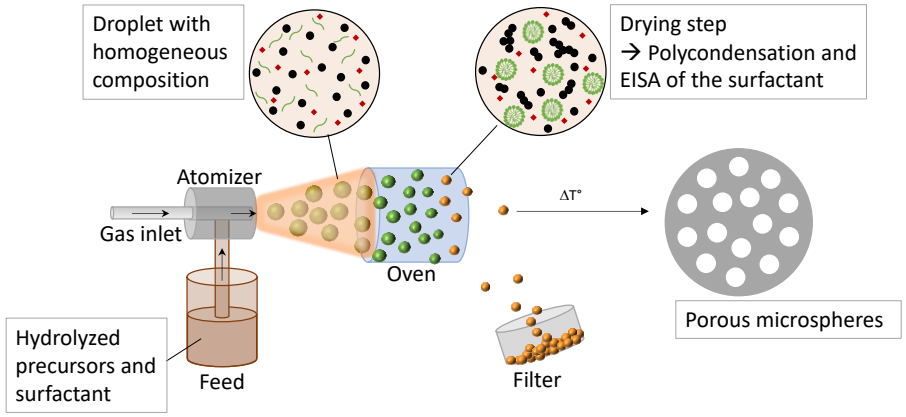

Figure I.14. Schematic view of the aerosol-assisted sol-gel process to synthesize catalysts.

A key feature of the AASG process is that the solid particles are formed very rapidly (in the order of 1 to a few seconds). Thus, unreactive or less reactive species (such as metal nanoparticles, salts, complexes), can be confined by "brute force" in the matrix of the forming inorganic oxide, even if the natural affinity between the species is poor. Also, sol-gel precursors of different nature, which would tend to react at very different rates under the classical (slow) sol-gel chemistry conditions (leading to highly inhomogeneous mixed oxides), will here be statistically mixed in a homogeneous way. This effect is referred to as the "kinetic quenching".

AASG process was shown to give access to a variety of mesostructured oxides and mixed oxides successfully employed as catalysts or catalyst supports.[213–216] Indeed, this technique is currently emerging as versatile method for the production of tailored heterogeneous catalysts with tailored properties (texture, composition, dispersion, surface functionality).[211] Various types of catalysts were prepared in our group leveraging on this synthesis method, including $SnSiO_2$ mesoporous mixed oxides,[217] hierarchically porous Ti-SiO_2 mixed oxides,[214] mesoporous TiO_2 supports for Ru-based catalysts,[215] $NaAlO_2$ microspheres,[218] Mo- and W- based catalysts[216] and many others inorganic catalysts. It was also recently used to prepare hybrid chemoenzymatic heterogeneous catalysts combining TS-1 zeolites and glucose oxidase enzyme.[219,220]

Mesoporous silica particles obtained by AASG have already been used as supports for Au nanoparticles incorporated in a second step by deposition-precipitation.[221] However, gold tended to form large nanoparticles blocking the pores of the silica. Interestingly, the direct (one-step) preparation of nanostructured metal-based catalysts was also demonstrated with various supports. Kan *et al.* first showed that adding pre-formed Au, Pt and Pd nanoparticles in the aerosol feed allowed to embed small gold nanoparticles in an alumina or ceria support.[222] Initially, a suspension of nanoparticles with size ~ 2 nm was prepared through the reduction of metal salt with $NaBH_4$ in the presence of a capping agent such as CTAB, which is expected to prevent the sintering of the metal nanoparticles. The suspension was then mixed with a solution of precursor (either for alumina or for ceria) and a templating agent. The resulting solution was atomized and spray dried at 480°C, causing the precursor condensation, micelles formation and oxide polycondensation. The metal nanoparticles were trapped in mesoporous Al_2O_3 or CeO_2 microspheres. The resulting catalysts displayed metal nanoparticles with diameter slightly increased of 5 nm and were active in the hydrogenation of 4-nitrophennol.

Moving further, the group of Geng used an efficient synchronous spray-pyrolysis deposition route (SPDR) working at high temperature to prepare Pt/TiO_2 and Pd/TiO_2 catalysts.[98,223] To do so, they directly added the metal precursor (H_2PtCl_6 or $Pd(NO_3)_2$) in a solution containing the titania precursor (tetrabutyl titanate, TBT) and a templating agent (F127). The precursors were hydrolyzed with HCl and mixed with ultrasonic assistance. Finally, the mixture was sprayed into a tube furnace at 600 °C. They managed to obtain single-atom (by introducing metal precursor) and/or nanoparticles (by introducing pre-formed NPs). They observed in both work that there is a synergistic effect between single sites and metal nanoparticles to obtain better catalytic performance in the CO oxidation (for Pt samples) and ketone/aldehydes hydrogenation (for Pd samples). They also investigated the effect of the support by performing the same synthesis using an “inert” support (Al_2O_3) with Pd/Pt nanoparticles. Both the dispersion and therefore the catalytic performance were negatively affected when working with Al_2O_3.

Similarly, Hampsey *et al.*, reported a direct synthesis of $Pd\text{-}SiO_2$ catalysts by adding the metal precursor in the feed of the aerosol together with the Si alkoxides and the templating agent.[224] Depending on the nature of the Pd precursors (and therefore on the nature of their interactions with the silicate matrix), Pd nanoparticles of different sizes could be obtained, ranging from 15 to 25 nm (i.e. relatively large). They also showed that the metal NPs size can

be controlled by varying the amount of metal salt in the precursor solution. Indeed, adding higher amount of palladium resulted in an increased nanoparticles size (Figure I.15).

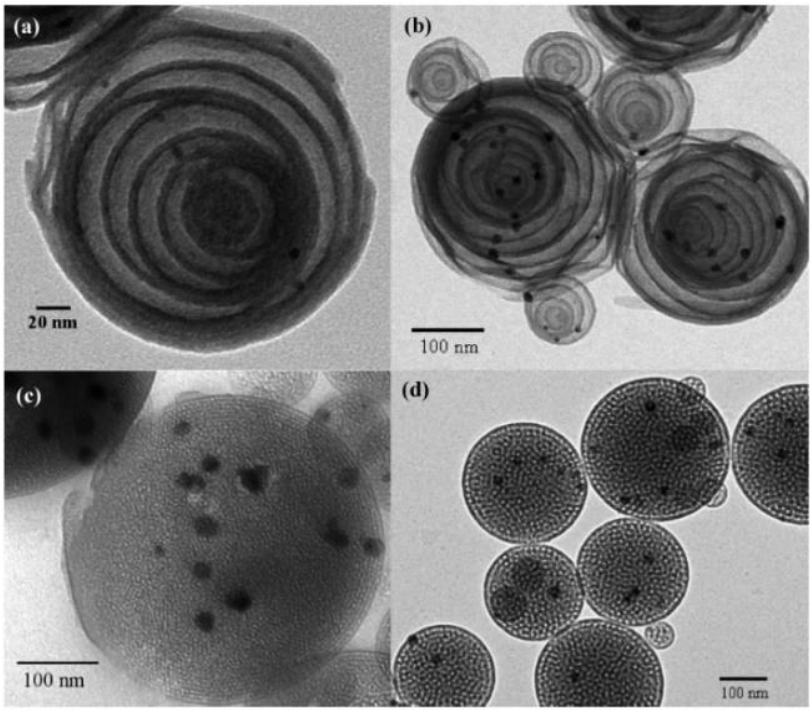

Figure I.15. TEM micrographs of 2% Pd-SiO_2 mesoporous particles prepared with (a, b) P123, (c) Brij-58, and (d) F127 surfactants. From [224].

It is interesting to notice that different types of pore morphologies (onion-like, interconnected) with variable size can be obtained depending on the surfactant used. Surfactant molecules can actually form different phases, depending on their chemical composition (the hydrophobic/hydrophobic ratio and length), the nature of the solvent, but also the conditions that are used (temperature, concentration). P123 and F127 are for example both composed of PEO (polyethylene glycol) and PPO (polypropylene glycol) units (Figure I.16), but the ratio PEO/PPO is different, bringing different properties to the two surfactants. Depending on these different parameters, the surfactant can assemble into different types of micelle structure (lamellar, spherical, worm-like, inverted micelles).[225] The control of the pore morphologies through the

micelles self-assembly usually relies on a thermodynamic equilibrium. However, due to the kinetic quenching occurring during the AASG process, such equilibrium cannot be reached. Instead, the formation of the micelles is induced by the rapid evaporation of the solvent and the formation of the silica framework sets their structure. Thus, the conditions in the aerosol must be optimized to reach the desired porosity.

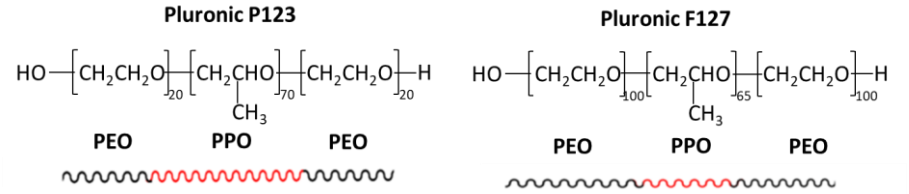

Figure I.16. Chemical composition of the two surfactants P123 and F127.

Although the addition of Pt and Pd in the aerosol process has already been demonstrated, only large nanoparticles could be obtained when working with an inert support, such as silica. Gold, on the other hand, has almost not been tested in the aerosol. Jin *et al*. first reported in 2015 the direct addition of Au precursor ($HAuCl_4$) in the AASG process with Al_2O_3/TiO_2 or ZrO_2 precursors.[226] Although the gold nanoparticles obtained were homogeneously dispersed in the support oxides, they exhibited rather large particle diameters ranging from 10 to 30 nm. As a consequence, the catalytic performance – tested in the liquid-phase reduction of 4-Nitrophenol – of these materials were very poor. Similar results were obtained by Kan *et al.* when synthesizing Au supported on Al_2O_3 by one-pot leveraging on the aerosol. The sample displayed very large nanoparticles (20 – 25 nm) and poor thermal stability with important sintering.[222] However, they established that the best support to enhance the affinity gold – support was ceria. Based on this, Jia *et al.* focused their work on the synthesis of Au/CeO_2 with loading from 1 to 5 mol.%. Still, the size ranged from 15 nm (1 mol.%) to 21 nm (5 mol.%). The only successful synthesis of small supported gold nanoparticles using the aerosol process was achieved when gold nanoparticles are pre-formed as mentioned earlier. Currently, the direct one-pot synthesis of small supported gold nanoparticles with diameter below 10 nm has never been reported. Moreover, the direct synthesis of small noble metal (Pd and Pt) nanoparticles has never been achieved successfully using inert support such as silica.

Recently, a series of Cu-SiO_2 catalysts was prepared via a one-pot preparation by the AASG in our group, showing high activity in the CO_2-to-methanol reaction.[227] $Cu(NO_3)_2$ was directly added to the solution of the aerosol, and CuO particles were then formed upon calcination. The CuO nanoparticles reached a size of 11 nm, which increased to 37 nm when the calcination temperature was increased from 350 to 750°C. The copper surface concentration also increased with the increasing calcination temperature, indicating that the copper progressively migrates at the surface of the particles (a phenomenon called “exsolution”) and sinters as the temperature increases.

Although the synthesis of supported metal nanoparticles using the aerosol-assisted sol-gel process has then been investigated by few groups, the direct addition of the metal precursors in the synthesis with a non-reducible support (such as silica) usually leads to the formation of rather large particles, especially in the case of gold which is unstable. The temperature of synthesis in the aerosol process, the metal loading, the temperature of calcination, the nature of the metal precursor are key parameters that need to be studied to have a better understanding of the formation of the nanoparticles in the aerosol process, and how to control their formation to target small nanoparticles (ideally below 5 nm).

The aerosol-assisted sol-gel preparation strategy recently proved to be highly relevant to prepare mesoporous mixed-oxides particles (*e.g.* Ti-silicate,[228] Zn-silicate,[227] Ga-silicates,[229] and Sn-silicates[213,217]). Such catalysts displayed interesting features, including a large surface area, open and calibrated mesoporosity and the different metals were successfully incorporated in the silica framework, with the insertion of the metals predominantly as single site in tetrahedral coordination. The catalysts showed excellent catalytic activity in their respective reactions. For example, mesoporous tin silicates produced by the AASG method demonstrated good catalytic performance with a conversion of DHA reaching 34% and a lactate yield of 12% at low temperature (90 °C). The latter catalyst's turnover number attained a value close to previously reported reference catalysts.

To conclude on the potentialities of the AASG process, it is well established that it can produce silica-based materials with an excellent control on texture, with the insertion of transition metal oxides inserted in the silica matrix, and incorporating metal nanoparticles (although facing some challenges especially regarding the size).

TOWARD THE OBJECTIVES OF THE THESIS

Considering the current context and the latest developments in the field of biomass upgrading, this thesis focuses on the valorization of glycerol – the main byproduct of the biodiesel production – to target the synthesis of methyl lactate, a valuable chemical that can be used to produce polylactic acid. To intensify the process, we aim to perform this cascade reaction involving two steps, in one unique reactor.

Therefore, we ambition to explore the preparation of bifunctional catalysts that would allow to step forward in the design of an integrated (intensified) cascade reaction, to directly upgrade glycerol towards the desired lactates. More precisely, we aim to design, in a limited number of steps, catalysts displaying highly dispersed noble metal nanoparticles (gold, palladium or platinum) – as they are known to be highly active in oxidation reaction – supported on a catalytically active tin-silicate showing good Lewis acidity. To achieve this goal, we first need to address the development of a synthesis strategy to obtain noble metal nanoparticles with a narrow size distribution supported on silica to selectively convert glycerol to dihydroxyacetone, the intermediate of the cascade reaction.

As mentioned in the state of the art, the remaining challenges to meet these goals are (1) carefully controlling the formation of the noble metal nanoparticles during synthesis, (2) creating strong interactions between the noble metal nanoparticles and its silica support, (3) demonstrating that both types of active species can be obtained on one unique support, and coexist without hindering or deactivating each other and (4) find suitable conditions for both active sites to maintain their catalytic performance. Therefore, a special attention will be given to these objectives.

By achieving these objectives and overcome the different challenges, this thesis aims to provide valuable insights into the design and optimization of supported noble metal and bifunctional catalysts for the oxidation of glycerol and the subsequent cascade reaction to produce methyl lactate.

STRATEGY

As mentioned, the AASG process is a quite versatile, cost- and time-effective technique, and protocols are amenable to further complexify the formulations. In the context described above, we hypothesized that this method could prove highly interesting for the preparation of supported metal catalysts (for the oxidation of glycerol) and of metallosilicate catalysts for the rearrangement of DHA to lactates. Moving further we believe that this preparation method could be suitable to combine the two catalysts into one bifunctional material. The general strategy developed is articulated around four parts described below. In each part of this study, a cyclic strategy is implemented in which (i) the catalysts are synthesized by the aerosol process (ii) the materials are characterized using various techniques such as XRD, N_2 physisorption, TEM, ICP, XPS and other methods to provide valuable insights into the structural and chemical properties of the catalyst before and after thermal treatment and (iii) then, they are tested in their respective reactions to evaluate their catalytic performance.

In a first chapter, we will investigate the synthesis of supported gold nanoparticles-silica catalysts following a two-steps procedure. In a first step, colloidal gold nanoparticles with a controlled size and structure will be synthesized. These particles will then be directly added in the AASG process alongside the silica precursor and the templating agent. The effect of aerosol processing and calcination on the nanoparticles size will be studied. The interactions between the nanoparticles and the silica will be also studied and hopefully improved by investigating different ligands to stabilize the colloidal gold during the aerosol synthesis.

In the second chapter of this work, the focus will be put on the study and development of a one-pot synthesis strategy (still relying on the AASG process) of Au-SiO_2 catalysts. To do so, the Au precursors will be directly added in the precursor solution right before the aerosol processing. This way, we expect to incorporate them homogeneously into the silica matrix, taking advantage of the kinetic quenching of the aerosol synthesis. The parameters of synthesis (such as the gold loading, the temperature of synthesis and calcination, etc) will be intensively investigated to target the formation of small nanoparticles. Once the parameter of the synthesis will be optimized, it will be expanded to other noble metals such as Pt and Pd.

The third and fourth chapters will mainly focus on the synthesis of bifunctional materials, combining gold, palladium, platinum or bimetallic nanoparticles and tin-silicate. To do so, the one-pot strategy developed in the

previous chapter will be implemented and studied in the design of bifunctional catalysts. These will be extensively studied to assess if the intrinsic properties of each catalytic species are maintained or if they actually interfere with each other. Regarding the cascade reaction, a significant part of the research will focus on investigating the kinetics of the sequential reaction and the impact of reaction variables (amount of noble metal, temperature, O_2 pressure, etc.) on the active sites. This exploration aims to fine-tune the performance of the bi-functional catalysts.

The methods and materials developed in this project will have industrial appeal due to the ease of scaling-up of aerosol processes for industrial use, and their potential for adaptation to other catalytic systems.

EXPERIMENTAL SECTION

This section describes the main characterization techniques used jointly in all chapters of the thesis. The preparation of the different materials, as well as the catalytic testing procedures that is different in each chapter are described in separate experimental sections at the beginning of the said chapters.

1. Materials

Tetraethyl orthosilicate (TEOS, >97%), dodecane (>99%), (3-mercaptopropyl)-trimethoxysilane (MPTMS, >96%) and 1,3 – Dihydroxyacetone dimer (DHA, >96%) were purchased from TCI. Methanol (HPLC Grade, 99.8+%) and urea (ACS, 99-100%) were purchased from Alfa Aesar. Methyl DL-lactate (ML, >97%), Pluronic® F-127, Pluronic® P-123, hydrochloric acid (37%), palladium (II) chloride ($PdCl_2$, 5 wt. % in HCl), ammonium tetrachloroplatinate (II) ($(NH_4)_2PtCl_4$, 99%), borane tert-butylamine complex (97%), sodium tetrafluoroborate ($NaBF_4$, 99%), tetrabutylammonium bromide (TBAB, >98%), tetrabutylammonium thiocyanate (TBASCN, 98%), chloroform (ACS reagent, >99.8%) and tin (IV) chloride pentahydrate ($SnCl_4 \cdot 5H_2O$, 98%) were all purchased from Sigma-Aldrich. Glycerol (Pure, 99%+), oleylamine (OAm, approximate C18 content 80-90%), 1,2,3,4-tetrahydronaphtalene (tetralin, 98+ %) and chloroauric acid trihydrate ($HAuCl_4 \cdot 3H_2O$, ACS reagent) were purchased from Acros Organics. Absolute ethanol (ACS reagent) was purchased from VWR Chemicals. N-hexane (ACS reagent) and phenylethyl mercaptan (PEM, >99%) were purchased from Merck. Ammonium thiocyanate (NH_4SCN, 98+ %) was purchased from Alfa Aesar.

2. Material preparation

The aerosol syntheses followed protocols already developed by our group.[213,217] Due to the variety of materials synthesized, the synthesis procedures will be described in each chapters.

3. Characterization of the catalysts

3.1. Bulk composition

The metals bulk content was measured by inductively coupled plasma – optical emission spectrometry (ICP-OES) on an ICP 6500 instrument (Thermo Scientific Instrument) after dissolution of the samples by sodium peroxide fusion. The experiments were carried out at the MOCA platform if Earth and

Life Institute (ELI) of the UCLouvain. Elodie Devos and Hélène Dailly are acknowledged for performing the ICP-OES experiments. The samples have been prepared by sodium peroxide (Na_2O_2) / sodium hydroxide (NaOH) fusion (30 mg of sample + 1 g Na_2O_2 + 1 g NaOH) and then dissolved in 200 mL H_2O Milli-Q and 30 mL HCl (37%) and finally brought to 500 mL. The wavelengths used for Au are 197.819 / 208.209 / 242.595 / 267.595 nm (Axial) and for Si 212.412 / 221.667 / 251.611 / 288.158 (Axial and radial). The calibrations were performed in the same composition (Na_2O_2 / NaOH) with Au concentration 0.1-0.2-0.4-1-2 ppm and Si concentration 1-2-4-10-20-40 ppm. Samples were diluted twice before analysis.

3.2. Surface composition

The surface composition was investigated by X-ray photoelectron spectroscopy (XPS). The experiments were carried out with an SSX-100/206 spectrometer (Surface Science Instruments, USA) equipped with a monochromatized Al-Kα radiation operated at 10 kV and 20 mA. The calibration of the binding energy scale was performed on the Si 2p peak at 103.5 eV.1 The data obtained were processed with CasaXPS from Casa Software Ltd, UK. More precisely, the quantification of surface Au (performed by XPS) was based on the 4f peak ($4f_{5/2}$ and $4f_{7/2}$) at 87.5 and 84.0 eV. The quantification via X-ray photoelectron spectroscopy (XPS) experiments of Pt was based on the $4f_{7/2}$ peak (~71 eV), the one of Pd on the $3d_{5/2}$ (335.8 eV)[230] peak and the one of Sn was based on the $3d_{5/2}$ peak (486.5 eV). The calibration of the binding energy scale was performed on the Si 2p peak at 103.5 eV. The data obtained were processed with CasaXPS from Casa Software Ltd, UK. Pierre Eloy is acknowledged for his help during the XPS analysis and the data analysis.

3.3. X-Ray diffraction

The crystallite size of metal nanoparticles was determined by X-Ray diffraction (XRD) patterns using the Scherrer equation. The diffraction patterns were measured at room temperature with a Bruker-D8 Advance diffractometer (Bragg-Brentano geometry) using Cu Kα radiation operated at 40 kV and 30 mA. Diffractograms were collected from 5° to 100° (2θ) with a step size of 0.05° (2θ) and a time step of 1.5 second. All samples were analyzed using a Bruker holder PMMA ring with a diameter of 25 mm. The resulting data were processed using Winplotr to integrate each peak, determine the full width at half maximum, and to calculate the nanocrystallite size via Scherrer equation.

3.4. Nitrogen physisorption

Nitrogen physisorption analyses were carried out at 77.4 K using a Tristar 3000 instrument (Micromeritics, USA) to determine the textural properties of the different samples. Prior to analysis, the samples were degassed overnight at 200°C. The specific surface area was determined by the *Brunauer-Emmett-Teller* (BET) method in the 0.05-0.30 relative pressure range. The total pore volume (V_p) was measured at p/p_0 = 0.98. The pore size distribution was obtained from the adsorption part of the isotherm using the *Barrett-Joyner-Halenda* (BJH) method. The microporous specific surface area was evaluated by the t-plot method in the thickness range of 3.5 to 5.0 Å.

3.5. Thermogravimetric analysis

TGA-MS analysis was performed to follow the decomposition of the sulfur and the organic moieties. The apparatus was operating under air (100 mL.min^{-1}) from 25 to 850°C at a heating rate of 10°C.min^{-1}.

3.6. Diffuse reflectance UV visible spectroscopy

Diffuse reflectance UV/Vis spectra were measured for the tin-containing powders with a UV-vis spectrophotometer (UV-3600i Plus, Shimadzu) from λ = 200 nm to λ = 500 nm.

3.7. Transmission electron microscopy

The particle morphology and size were investigated using transmission electron microscopy. Two different equipment were used:

- A transmission electron microscope FEI Tecnai F20 (FEI, Eindhoven, The Netherlands) equipped with a field emission gun source, a 4k CCD camera (FEI Eagle) and operated at 200 kV was used for sample visualization (collaboration with Brno, Department of Chemistry, Mazaryk University). STEM-EDS measurements were performed on a FEI Titan Themis instrument with a combination of a spherical aberration image (Cs) corrector, a monochromator system, sensitive ChemiSTEM technology, and a high-end GATAN GIF Quantum energy filter for EELS and EFTEM with a new enhanced piezo stage, FEI and GATAN software, and a FEI Ceta 16-megapixel CMOS camera. Vit Vykoukal is acknowledge for performing the TEM analysis on this apparatus.

- Transmission electron microscopy (TEM) was performed using a Philips Tecnai 10 or 20 microscope operating at 80 kV. Corry Charlier is acknowledged for his help to obtain the TEM images.

3.8. Pyridine adsorption FTIR spectroscopy

Acidity was studied by pyridine adsorption. The FTIR spectra were recorded on a Bruker Equinox 55 spectrometer (Transmission mode), performing 256 scans from 4000 to 500 cm^{-1} with a resolution of 4 cm^{-1}. Catalysts were pelleted and degassed for 2 hours at 350 °C. The pyridine adsorption was carried out at room temperature for 30 minutes. After stabilization, the pyridine was desorbed at 150 °C for 2 hours. The FTIR spectra of the pellet was then measured and the peak of interest integrated with the software OPUS. The amount of Lewis acid sites was calculated based on the following equation:

$$n_L = \frac{A_L C_d}{\varepsilon_L m}$$

Where n_L is the number of micromoles of Lewis acid site per gram of catalyst, A_L the integrated absorbance of the ~1450 cm^{-1} peak on the FTIR spectra (cm^{-1}), C_d the cross-sectional area of the wafer (cm^2), ε_L the extinction coefficient (= 2.22 $cm.\mu mol^{-1}$)[231] and m the mass of the wafer (g).

3.9. Gold titration

Gold dispersion was deduced from a titration experiment, with phenylethyl mercaptan (PEM).[232] Briefly, 50 mg of catalyst was contacted with 10 mL of a 0.1 mM PEM solution in hexane. The PEM concentration was measured by subtracting the absorbance at 258 nm to the absorbance at 273 nm of a solution of PEM in hexane (using a UV-vis spectrophotometer, UV-3600i Plus, Shimadzu) before and after being contacted with the catalyst. By difference, the amount of PEM adsorbed on gold can be deduced. Dispersion is calculated considering a stoichiometric factor of 1 PEM molecule for each Au accessible on the surface. Gold dispersion (%) is defined as the proportion of Au atoms present in the catalysts that are accessible to titration (i.e. surface Au atoms).

3.10. Solid NMR

The coordination of Sn atoms was measured by static ^{119}Sn Nuclear Magnetic Resonance (NMR). The spectra were recorded at room temperature on a Varian VNMRS-400 spectrometer operating at 9.4 T using a 5 mm wideline probe. The sample was packed in a 5 mm glass tube and studied in static condition. Static NMR was selected based on previous experiments. Luca Fusaro from UNamur is acknowledged for performing the experiments.

3.11. X-Ray absorption near edge (XANES) and X-ray adsorption fine structure (EXAFS)

X-ray absorption spectra at the Au L_3-edge were recorded on the B18 beamline at the DIAMOND synchrotron (Oxfordshire, UK). The samples, in form of powder, was diluted with polyvinylpyrrolidone (PVP) and pressed to form a pellet. Due to the low concentration of absorbing atom the data were collected in fluorescence mode at room temperature, using a Si(311) monochromator. The monochromator energy scale was calibrated using a Au, Pd or Pt reference foil. The data of the sample were collected simultaneously to those of the foil, placed after the fluorescent detector, measuring the transmitted intensity via an ionization chamber. The data analysis was performed using the ATHENA and ARTEMIS software.[233] With ATHENA, the absorption edge, E_0, was determined, and the absorption due to the isolated atom was subtracted, by fitting the pre-edge and post-edge regions, to obtain the EXAFS interference functions, χ(k), and the normalized XANES spectra. The Fourier Transforms of the EXAFS interference functions were corrected for phase shift, using the phase shifts calculated using ARTEMIS.

4. Catalytic testing

The catalytic tests are described in each chapter of the thesis. In order to evaluate the catalytic performance of each material, the catalytic results are expressed in terms of conversion, selectivity and yield as follow:

$$Conversion(\%) = \frac{(n_{i0} - n_i)}{n_{i0}}\ x\ 100$$

Where n_{i0} is the initial molar concentration of reactant i and n_i the molar concentration of reactant at a given reaction time.

$$Selectivity\ (\%) = \frac{n_j}{(n_{i0} - n_i)} x\ 100$$

Where n_j is the molar concentration of the product of interest formed at a given reaction time, n_{i0} is the initial molar concentration of reactant "i" and n_i the molar concentration of reactant at a given reaction time.

$$Yield\ (\%) = \frac{n_j}{n_{i0}}$$

CHAPTER 1.
Colloidal route to support gold on silica

Abstract

In recent years, supported gold catalysts have gained prominence in heterogeneous catalysis for their efficacy in selective oxidation reactions. Precise control of gold particle formation (<5 nm) is crucial for catalytic activity. Among the possible catalyst silica shows attractive features such as a high stability, a tunable porosity and surface. However, gold usually form large nanoparticles poorly dispersed on silica due to its low affinity between with the silica surface. Here, we report the synthesis of mesoporous gold-silica catalysts using a two-steps one-pot synthesis route based on the synthesis of colloidal gold with a controlled size (~ 2 nm) and their incorporation in the aerosol-assisted sol-gel process. Three different ligands were tested (oleylamine, TBASCN and MPTMS) to stabilize the gold nanoparticles. The MPTMS was incorporated first in the synthesis of silica and then used as an anchoring point for the impregnation of gold NPs in a second step. We show that the presence of the different ligands was not sufficient to protect the gold nanoparticles from sintering during the aerosol, reaching a diameter of ~10 nm. Further thermal treatment to remove the surfactant increased even more their size to ~15 nm, indicating a poor thermal stability. TEM and XPS analyses showed a rather inhomogeneous dispersion of the nanoparticles in the silica microspheres. These results lead to materials that are poorly catalytic active in the glycerol oxidation to DHA. On the other hand, we demonstrated that introducing MPTMS as a silica precursor (and therefore thiol functions anchoring points), the gold nanoparticles showed a high resistance toward sintering, with a diameter of 3 nm after calcination, a better dispersion in the microspheres and therefore, improved catalytic performance (X_{Gly}= 24 % S_{DHA} = 60%).

This work was performed in collaboration with Dr. Guillaume Gouget (Rennes Institute of Chemical Sciences, France), in the framework of a short research stay he did in our group. Guillaume Gouget was mostly in charge of preparing the stabilized gold colloids with the different ligands.

1.1. Introduction

In recent years, the synthesis of metal nanoparticles has gained considerable attention due to their unique physical and chemical properties, making them highly promising materials for various applications, particularly in catalysis. Among the various metal nanoparticles, gold nanoparticles (AuNPs) have gained significant interest owing to their exceptional catalytic performance and tunable reactivity.[234] The fine control of the size and morphology of the gold nanoparticles is a key parameter in order to obtain catalysts with a high level of catalytic activity.[119,235]

Colloidal gold synthesis (AuNPs) has emerged as a versatile technique to precisely engineer nanoparticle size, shape, and surface properties. The ability to control these parameters is of great importance, as they significantly influence the catalytic activity, selectivity, and stability of AuNPs. Colloidal particles are more commonly synthesized by chemical reduction,[236] but other techniques such as UV irradiation,[237] sonochemical[238] and sonoelectrochemical[239] methods exist. The synthesis of colloidal gold by chemical reduction typically is based on two major elements: (i) the reduction of the gold ion (Au^{3+} to Au^{0}) by a reducing agent and (ii) the stabilization of the gold nanoparticles using ligands to avoid their aggregation.[240]

While colloidal gold nanoparticles are renowned for their catalytic activity, they are accompanied with certain drawbacks, including a relatively limited stability (depending on the pH and the ionic strength of the medium)[241] and limitations in terms of both handling and reusability. To overcome these drawbacks, immobilizing colloidal gold nanoparticles on a support to form stable heterogeneous catalysts easily recoverable should be favored.[242,243] As mentioned in the introduction, silica is a cheap, with an easily tunable porosity and surface, relatively inert to allow to study the size effect of the metal nanoparticles.[99] However, to avoid gold nanoparticles sintering, the interactions between the colloidal gold and the support surface should be ameliorated. In this perspective, leveraging the nature of the ligand used to stabilize the colloidal gold to also improve their interactions with the silica surface is highly relevant.

Colloidal gold nanoparticles are usually immobilized on a pre-formed support. Such process relies on multi-steps time-consuming procedure poorly attractive from industrial point of view. Taking a side step, we propose a to synthesize silica-supported gold nanoparticles supported on silica in one-pot via the aerosol-assisted sol-gel process. The aerosol method offers several advantages (see section 4 of the Introduction) and is expected to lead to a uniform distribution of nanoparticles on or possibly in the silica matrix. Such strategy was already investigated by Kan *et al*. In their work, they show that adding pre-formed Au nanoparticles in the aerosol feed allowed embedding

small gold nanoparticles in an alumina or ceria support.[222] The resulting catalysts displayed slightly larger metal nanoparticles displaying a diameter of 5 nm and were active in the hydrogenation of 4-nitrophennol.

In this context, this first chapter aims to explore a “two steps – one-pot” route combining the synthesis of colloidal gold with a targeted size (< 5 nm) and its incorporation in the aerosol process to synthesize Au@SiO_2 catalysts. A particular focus is placed on optimizing the affinity between the stabilized gold nanoparticles and the silica to achieve the higher gold dispersion and the best catalytic performance for the glycerol oxidation to DHA. More precisely, we investigated the influence of various ligands on the resulting AuNP size, distribution, and stability in the final material.

1.2. Experimental section

The reader is directed to the EXPERIMENTAL SECTION (p. 54-59) for general procedures of characterization. Here, only the methods specifically implemented in this chapter are presented.

1.2.1. Catalyst preparation

Gold nanoparticles (AuNPs) synthesis

The gold nanoparticles were synthesized following a protocol from the literature to obtain 2 nm gold nanoparticles.[244] The gold precursor solution was obtained by mixing 10 mL of tetralin, 10 mL of oleylamine (OAm) and 0.1 g of $HAuCl_4 \cdot 3H_2O$ at room temperature. The solution was put under N_2 flow and stirred for 10 minutes at 38°C. A reducing solution made of 0.5 mmol of TBAB, 1 mL of OAm and 1 mL of tetralin was mixed by sonication and injected into the precursor solution. The reduction was instantaneously initiated and the orange precursor solution turned to purple within 5 seconds. The mixture was stirred for 1 hour at 38°C and then, 60 mL of acetone was added to induce the precipitation of the gold nanoparticles (Au NPs). The gold nanoparticles were collected by centrifugation (8500 rpm, 5 minutes) and washed with acetone. The AuNPs were then dispersed in hexane and kept under stirring for further use. The nanoparticles obtained consist of gold nanoparticles stabilized by OAm ligands. Before using the AuNPs, the solvent in which they are dispersed is exchanged by centrifugation and redispersion of the AuNPs, with chloroform to ensure a better stability over time.

Ligand exchange

One other ligand was investigated to stabilize the gold nanoparticles pre-formed: TBASCN. The ligand exchange was performed following a protocol from the literature.[245] In a typical ligand exchange, the amount of gold nanoparticles desired was dispersed in 1 mL of hexane. Then, 0.5 mL of the ligand solution (130 mM) in acetone was added to the AuNPs solution and stirred for 1 minute. The flocculation of the gold particles is quickly observable and they are recovered by centrifugation (8500 rpm, 1 minute). 1 mL of acetone is added and the solution is stirred for another minute. The AuNPs are separated from the supernatant by centrifugation (8500 rpm, 1 minute). 1 mL of chloroform is added to the pellet and the mixture was stirred until the particles were fully dispersed.

Incorporation of gold NPs into silica via aerosol

The protocol followed for the synthesis of the gold catalysts of this chapter followed a protocol already developed by our group.[213,217] Briefly, two solutions were prepared consisting of 20 g aqueous HCl (0.01 M) and 12 g TEOS (solution A) and 45 g absolute ethanol, 8 g deionized water and 3.88 g F127 (Solution B). The two solutions were kept stirring overnight. Solution A was added to solution B and stirred for another 30 minutes. The AuNPs colloidal suspension was then added dropwise to the mixture of solution A+B right before the aerosol processing. The amount of suspension is controlled to obtain a 1 wt.% loading in the final calcined material. A preliminary test was performed to ensure the stability of the resulting mixture. The sol was stable for 1 hour before becoming very viscous with a heterogeneous composition. The mixture was atomized with a 6-Jet 9306A atomizer from TSI (operating at 30 psi) and the droplets formed were dried by passing through a tubular quartz tube heated at 350 °C. The powder was recovered on a cellulose nitrate filter (pore size: 0.45 µm). The resulting sample was calcined under static air at 550°C for 6 h (1°C/min) and is here denoted **Au-x@SiO_2** where ‘x’ is the nature of the ligand (Figure 1.1).

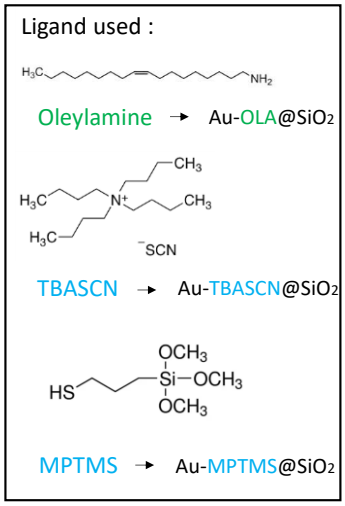

Figure 1.1. Structure of the ligands used in this chapter and notation of the resulting material.

For the second aerosol strategy of synthesis tested in this chapter, (3-Mercaptopropyl)trimethoxysilane (MPTMS) was added at different stages of the aerosol synthesis: (i) in solution A, so that the MPTMS is hydrolyzed overnight with the TEOS (95 mol.% TEOS + 5 mol.% MPTMS) or (ii) in the AuNPs solution (0.53 g) before its addition to the mixture A+B. The amount of gold is controlled to obtain a 1 wt.% loading in the final calcined material. The resulting sample was calcined under static air at 550°C for 6 h (1°C/min) and is here denoted **Au-MPTMS$_{hydrolyzed}$@SiO$_2$** when MPTMS is hydrolyzed in solution A overnight or **Au-MPTMS$_{ligand}$**@SiO$_2$ when the MPTMS is added in the AuNPs solution.

1.2.2. Catalytic oxidation of glycerol

Catalytic tests were performed in a 160 mL Parr stainless steel autoclave reactor equipped with a Teflon liner and a magnetic stirrer. A solution of glycerol in methanol (0.25 M, 20 mL) was loaded with 68 mg of dodecane (used as GC internal standard) and 200 mg of Au-based catalyst. The reaction was performed under 30 bar of air (used as oxidant) under vigorous stirring at 140°C. After 4 hours, the reactor was cooled down in a cold bath and the reaction mixture was centrifuged to separate the catalyst. The supernatant was analyzed by gas chromatography (Scion Instruments 456-GC) equipped with a Restek Stabilwax column (30-meter length, 0.53 mm ID, 0.25 µm d_f) and a FID detector.

1.3. Results and discussion

In this first chapter, we explored a first synthesis strategy to synthesize gold nanoparticles supported on silica, leveraging on a two steps procedure.

In a first step, the AuNPs were synthesized as a colloidal suspension of gold nanoparticles using a protocol found in the literature.[244] The use of a ligand is crucial during the synthesis to control the size distribution of the nanoparticles and prevent their sintering.[246] The AuNPs were first synthesized using OAm as a ligand. In a typical procedure, the gold precursor ($HAuCl_4 \cdot 3H_2O$) was mixed with OAm, before adding TBAB to reduce the gold and induce the formation of the gold nanoparticle. Their diameter was measured by TEM and reached the value ranging from 2 to 3 nm (Figure 1.2). This is consistent with what was expected following the synthesis protocol used.[244]

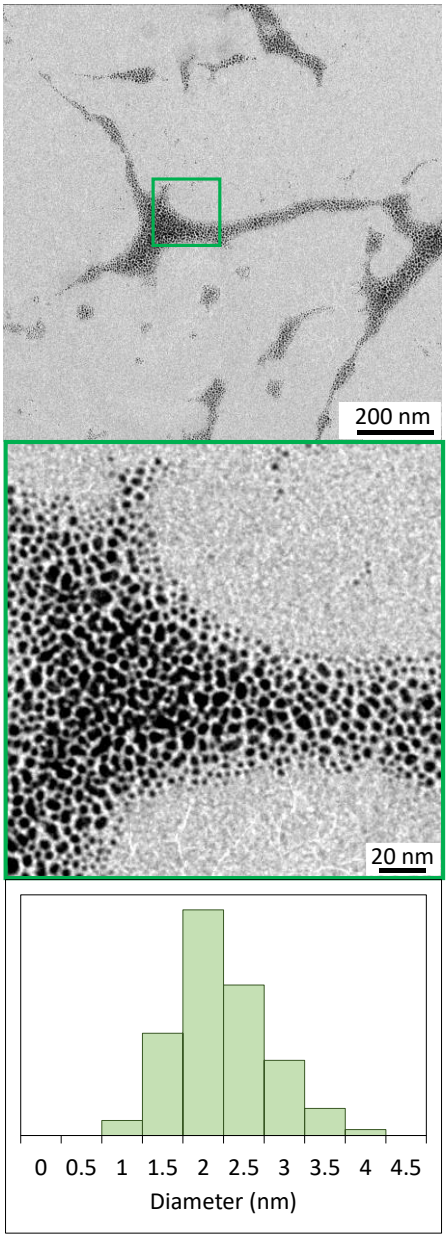

Figure 1.2. TEM images of **AuNPs-OAm** solution with the particle size distribution of the AuNPs. The sample was prepared on a carbon coated copper grid. The particle size distribution was calculated on 200 nanoparticles.

As the stability of the gold nanoparticles and their interactions with the silica support might depend on the ligand used, two different ligands were investigated: the oleylamine (OAm) and tetrabutylammonium thiocyanate (TBASCN). In a second step, the resulting AuNPs solution was added to the feed of the aerosol process (containing the silica precursor – TEOS – and the surfactant – F127) to synthesize in one-pot the gold catalysts (Figure 1.3). The precursors solutions are processed (dried) at 350°C and the resulting materials are calcined at 550°C for 6 hours to remove the surfactant and release the porosity. The catalysts are denoted as **Au-x@SiO_2** where "x" is the ligand used during the aerosol synthesis (**Au-OAm@SiO_2** or **Au-TBASCN@SiO_2**)

Owing to the excellent affinity between thiol functions and gold atoms reported in the literature,[232,247–250] we decided to also investigate the use of a thiolated silica precursor ((3-Mercaptopropyl)trimethoxysilane (MPTMS)) in the synthesis, first as a ligand to stabilize the gold nanoparticles (**Au-$MPTMS_{ligand}$@SiO_2**), and then as a silica precursor (95 mol.% TEOS and 5 mol.% MPTMS) to possibly serve as an anchoring point for the gold nanoparticles (stabilized with OAm) at the silica surface (**Au-$MPTMS_{hydrolyzed}$@SiO_2).** Indeed, numerous researches have reported enhanced stability and affinity of the gold nanoparticles after the functionalization of the silica surface using MPTMS prior the gold deposition.[251–253]

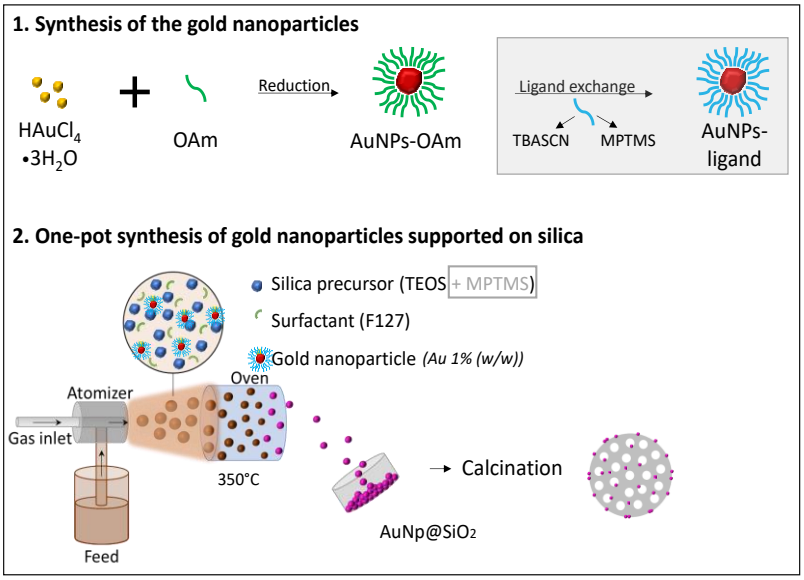

Figure 1.3. Scheme of the two steps synthesis of the gold catalysts. The ligand exchange step is not always used as well as the addition of MPTMS as a silica precursor, which is why they are underlined in grey.

The textural properties of the silica-supported gold materials were investigated by N_2-physisorption (Figure 1.4). A pristine mesoporous silica was also synthesized by aerosol without gold, and used as a benchmark. All the materials exhibited a type IV isotherm with a clear hysteresis characteristic for pores with an ink bottle shape (Figure 1.4 A) and a narrow pore size distribution around 8-10 nm (Figure 1.4 B). The addition of the different AuNPs-ligand did not have an impact on the shape of the isotherms, the pore size distribution, or the pore volume, although an increase of the BET surface area is observed when compared to the pure **SiO_2** (Table 1.1). In the particular case of **Au-TBASCN@SiO_2**, a higher increase of the surface is observed. Similarly, the micropore volume was also increased in this sample, while it remained constant for the other samples. This could be attributed to a particular interaction of the AuNPs-TBASCN incorporated in the synthesis and the surfactant (F127). The catastrophic desorption observed at p/p_0 ~ 0.45 in each sample was caused by the tensile strength effect (TSE) phenomenon. The hysteresis loss actually arises from the instability of the hemispherical meniscus when capillary evaporation occurs within pores having diameters less than approximately 4.0 nm.[254] The presence of 'forced closure' in the isotherm shape might indicate the existence of pores with diameters smaller than 4.0 nm. This could further lead to diffusion limitations during catalytic testing and furthermore affect the selectivity of the reaction.

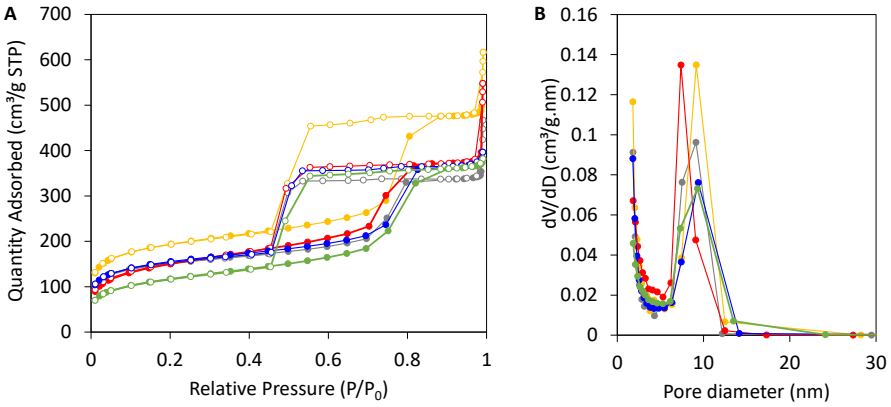

Figure 1.4. (A) Nitrogen adsorption (plain symbols) and desorption (empty symbols) isotherms of pristine SiO_2 (●), **Au-OAm@SiO_2** (●), **Au-TBASCN@SiO_2** (●), **Au-MPTMS$_{ligand}$@SiO_2** (●) and **Au-MPTMS$_{hydrolyzed}$@SiO_2** (●). (B) BJH pore size distribution analysis obtained from the adsorption isotherm.

The size of the gold nanocrystallites in the different materials were measured by XRD applying the Scherrer equation on the 2θ = 38° peak. The size was measured after spray drying (on the fresh catalyst) to primary study

the impact of the aerosol on the aggregation of the NPs and after calcination to further monitor the impact of thermal treatment.

Table 1.1. Textural properties of silica and the AuNPs@SiO_2 catalysts

	BET surface ($m^2.g^{-1}$)	BJH adsorption pore size (nm)	Pore volume ($cm^3.g^{-1}$)	Micropore volume ($cm^3.g^{-1}$)
SiO_2	400	6	0.6	0.05
Au-OAm@SiO_2	490	8	0.5	0.11
Au-TBASCN@SiO_2	620	8	0.7	0.14
Au-$MPTMS_{ligand}$@SiO_2	510	8	0.6	0.08
Au-$MPTMS_{hydrolyzed}$@SiO_2	500	7	0.6	0.11

The diffractograms of the different samples are displayed in Figure 1.5. The broad peak observed at 2θ~22° corresponds to the diffuse scattering of the amorphous silica.[255] Except in **Au-$MPTMS_{hydrolyzed}$@SiO_2**, the sharp peaks of metallic gold are observable in each samples, confirming the incorporation of the gold nanoparticles in the silica during the synthesis. In those samples, the aerosol synthesis actually leads to the severe aggregation of the AuNPs, which are shown to grow from 2 nm in the as-prepared gold NPs colloidal suspension to ~10 nm in the freshly prepared catalyst (Table 1.2). The Tammann temperature – defined as the temperature at which atoms in the bulk of a solid can diffuse to the surface – for gold is estimated at 396°C.[256] When the size of gold nanoparticles is reduced to less than 10 nm, their melting temperature decreases, leading to a lower Tammann temperature. For instance, a 2 nm diameter gold nanoparticle has a melting temperature of 327°C, indicating an approximate Tammann temperature of around 150°C.[257] This explains the quick sintering of the ~3nm nanoparticles in the aerosol synthesis (performed at 350°C).

The calcination further increased the size of the gold nanoparticles, most probably due to a combination of the high mobility of the gold nanoparticles at high temperature and the complete decomposition of the ligand and therefore the loss of stabilization of the gold nanoparticles. As mentioned in the introduction (1.3.3. Influence of the support) the gold nanoparticles have a very low affinity with the silica surface, favoring their sintering. Actually, the metal-metal bond between the gold nanoparticles are much stronger than the metal-hydrogen bonds to the substrate (2.87 eV vs. 0.1 eV). However, the sintering caused by the calcination was slightly lowered when using MPTMS as a ligand, suggesting that the thiol function is a better stabilizer – i.e. is possibly more resistant toward calcination – than the others.

When the MPTMS was hydrolyzed overnight with the silica precursors and the gold NPs only added to the mixture right before the aerosol processing, only a small broad peak of metallic gold at 2θ~38° was observable by XRD, even after calcination at high temperature. The size of the nanocrystallites in this material was maintained at ~3 nm after calcination, which is very close to the size of the AuNPs suspension. It is believed that the hydrolyzed MPTMS plays two roles in this material: (i) a ligand that stabilize the gold during the aerosol processing and (ii) an anchoring point at the silica surface. This latter is very interesting, as it appears to prevent the phenomenon of sintering during calcination observed for the other materials. We conclude that the thiol function increases the metal-support bond and hinder the mobility of Au NPs.

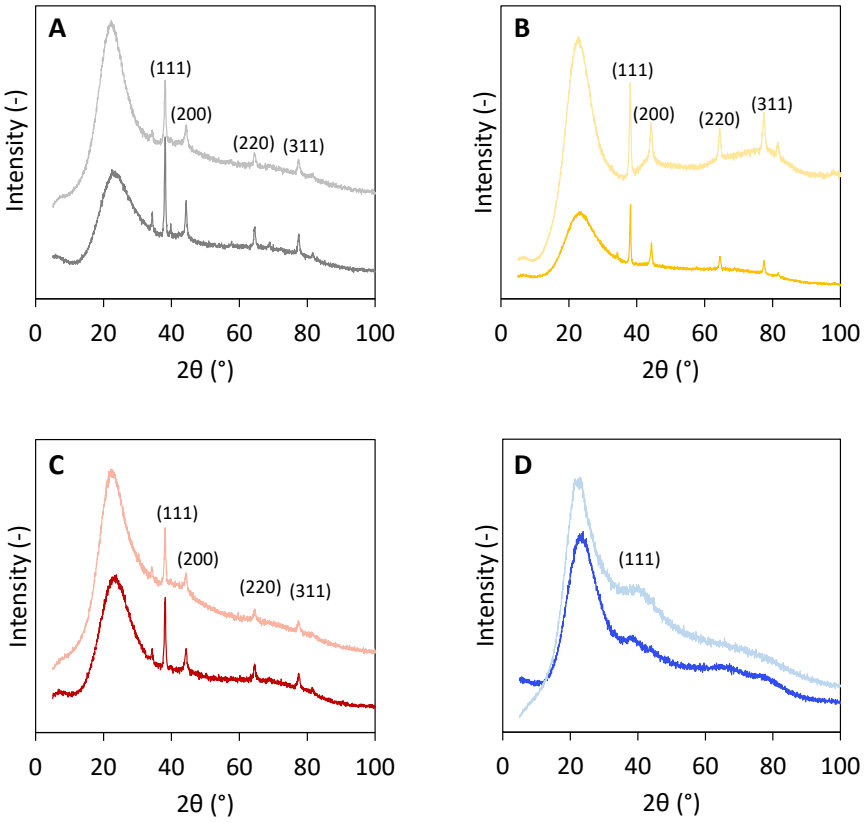

Figure 1.5. X-ray diffractograms highlighting the metallic gold peaks of (**A**) **Au-OAm@SiO_2**, (**B**) **Au-TBASCN@SiO_2**, (**C**) **Au-MPTMS$_{ligand}$@SiO_2** and (**D**) **Au-MPTMS$_{hydrolyzed}$@SiO_2**. The light color corresponds to fresh catalysts while the darker one corresponds to the calcined material. The different facets of metallic gold are shown on the diffractograms.

Table 1.2. Crystallites size and surface content of the gold nanoparticles in the aerosol samples and catalytic activity.

	AuNPs size fresh catalyst[a] (nm)	AuNPs size calcined catalyst[a] (nm)	Surface Au content[b] (wt.%)	Glycerol conversion (%)
Au-OAm@SiO_2	10.6	14.6	0	0
Au-TBASCN@SiO_2	9.9	14.8	0	0
Au-$MPTMS_{ligand}$@SiO_2	9.6	11.1	0.3	0
Au-$MPTMS_{hydrolyzed}$@SiO_2	/	~3	0.2	24

[a] The size was measured with the Scherrer equation on the 2θ = 38°.
[b] Measured by XPS.

X-Ray photoelectron spectroscopy was also performed to check the surface composition of the gold catalysts. Only Si, C, O and Au were detected in each sample with no remaining traces of the ligands. Surprisingly, for all samples without MPTMS (ligand or hydrolyzed), no trace of gold was detected at their surface (Figure 1.6, Table 1.2). This indicates that the gold nanoparticles are mostly buried inside the silica microspheres during the aerosol process rather than at their surface. It can also hint at a poor dispersion of gold. On samples prepared in the presence of MPTMS, gold was detected at their surface, but in very low amount (< 1%) (Figure 1.6, Table 1.2).

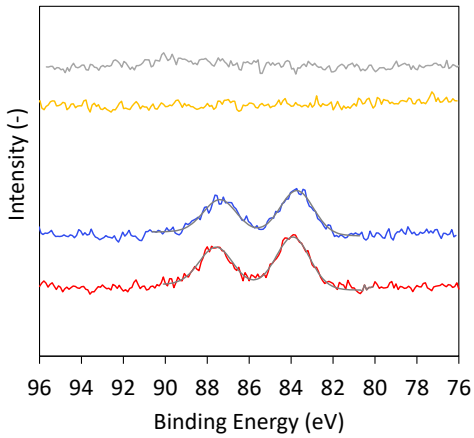

Figure 1.6. XPS spectra from top to bottom: **Au-OAm@SiO_2** (●), **Au-TBASCN@SiO_2** (●), **Au-$MPTMS_{hydrolyzed}$@SiO_2** (●) and **Au-$MPTMS_{ligand}$@SiO_2** (●).

While synthesizing the catalyst, the pre-formed gold nanoparticles had the tendency to block the aerosol atomizer, likely due to their aggregation in the aerosol feed. Indeed, a clear change of color of the aerosol solution was observable when removing the solution after ~1 hour of synthesis (from red to blue/purple). As a consequence, the synthesis yielded only a limited amount of catalyst. Unfortunately, due to this low yield, it was not possible to perform ICP analysis to determine the elemental composition. Despite being unable to fully confirm the complete incorporation of pre-formed AuNPs in the final material, the presence of gold peaks in XRD and XPS results (especially for MPTMS containing materials) indicates that at least part of it is incorporated in the materials.

Transmission electron microscopy was employed to gain a deeper insight into the catalyst's morphology. The analysis focused on the samples: **Au-OAm@SiO_2**, **Au-MPTMS$_{Ligand}$@SiO_2** and **Au-MPTMS$_{hydrolyzed}$@SiO_2** (Figure 1.7). In the case of **Au-OAm@SiO_2** and **Au-MPTMS$_{Ligand}$@SiO_2**, the images revealed the presence of large gold nanoparticles unevenly dispersed within the microspheres. On **Au-MPTMS$_{Ligand}$@SiO_2**, it was evidenced that some of the gold nanoparticles were located on the surface of the microspheres. These results are in good agreement with XRD and XPS results previously discussed. Interestingly, the bottom image of Au-MPTMS$_{Ligand}$ clearly shows the accumulation of gold nanoparticles in one unique microsphere. We reckon some aerosol droplets are loaded with gold NPs while some others are actually gold free at the moment of the droplet formation. This underlines the lack of homogeneity of the precursor solution during the synthesis of gold-silica material when utilizing pre-formed gold nanoparticles in the aerosol process. It is presumably due to a tendency of the Au NPs to aggregate, despite the presence of stabilizing ligands. However, when MPTMS was hydrolyzed, in **Au-MPTMS$_{hydrolyzed}$@SiO_2**, only small nanoparticles were observed, highlighting the successful stabilization of the gold nanoparticles.

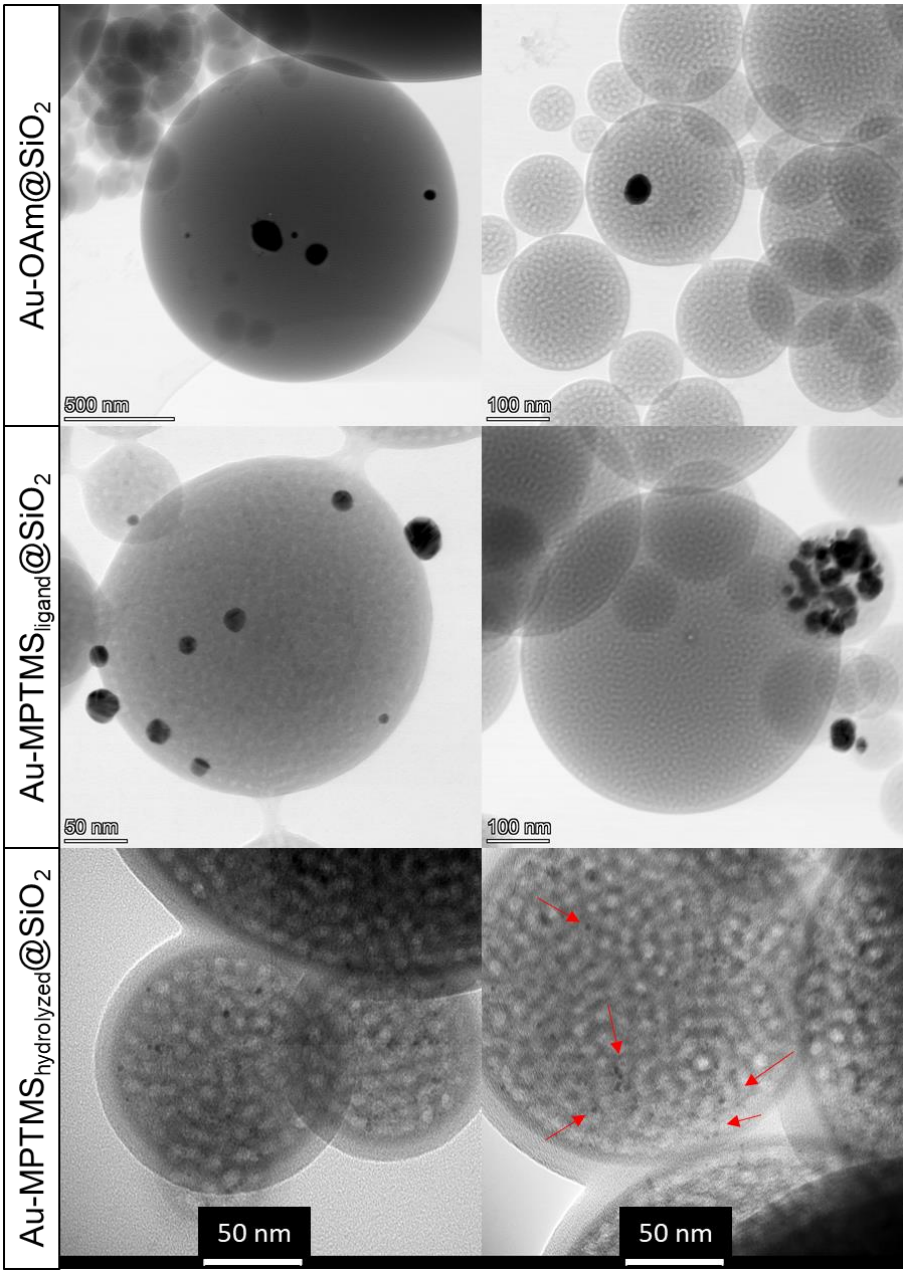

Figure 1.7. TEM images of **Au-OAm@SiO_2**, **Au-$MPTMS_{ligand}$@SiO_2** (measured with a FEI Tecnai F20) and **Au-$MPTMS_{hydrolyzed}$@SiO_2** (measured with a Phillips Tecnai 20). Red arrows show small Au NPs.

The catalysts were tested in the catalytic oxidation of glycerol to dihydroxyacetone. The reaction was carried out at 140°C, under 30 bar or air (used as the oxidant) for 4 hours. Except for **Au-MPTMS$_{hydrolyzed}$@SiO$_2$**, no catalytic activity was observed. This is attributed to (i) the absence of gold at the surface of the microsphere and (ii) the presence of large nanoparticles (> 10 nm), known to be poorly active in catalysis. On the other hand, when MPTMS was used as a silica precursor (and therefore hydrolyzed before the addition of Au NPs and aerosol processing) small nanoparticles were obtained, leading to a catalytically active material in the oxidation of glycerol to DHA. The glycerol conversion reached 24% with a good DHA selectivity of 60% after 4 hours (Y_{DHA} = 14%) (Table 1.2). While the glycerol conversion showed a moderate level, the selectivity towards DHA was quite good. Unfortunately, these results could not be compared to others in the literature due to the fact that under base-free conditions, the glycerol oxidation always performed in water. No leaching of gold nanoparticles was detected during the reaction.

1.4. Conclusion

In this first chapter, we proposed a two-steps strategy to obtain gold nanoparticles embedded in mesoporous silica. Leveraging on a colloidal synthesis route, gold nanoparticles with diameter of ~2 nm were synthesized and were incorporated in the aerosol-assisted sol-gel process to obtain gold-silica catalyst. Different ligands were tested to study their effect on the stability of the pre-formed gold nanoparticles. Despite the different nature of the ligands tested, the coalescence of the gold nanoparticles during the aerosol processing could not be avoided, resulting in nanoparticles diameter above 10 nm, buried in the silica microspheres and therefore not available or not active in catalysis. The challenges of working with gold nanoparticles and silica arise from the difficulty of stabilizing gold at the silica, often leading to sintering, particularly at high temperatures, due to the high mobility of the gold nanoparticles on the silica surface. On the other hand, interestingly, the direct stabilization of gold nanoparticles could be demonstrated when MTPMS was used as an anchoring point (i.e. replacing a small fraction of TEOS, as a silica precursor). The resulting catalyst displayed small nanoparticles (~ 3 nm) with a high resistance toward sintering, homogeneously dispersed throughout the silica microspheres and displaying some catalytic activity in the oxidation of glycerol to DHA (X_{Gly}= 24 % S_{DHA} = 60%). The results obtained in the first chapter – in particular this beneficial effect of the thiolated alkoxide precursor – provide valuable information for the next stages of this work, as we further exploit the aerosol-assisted sol-gel process to prepare highly active gold-silica catalysts.

CHAPTER 2.
Airborne preparation of small gold nanoparticles dispersed on mesoporous silica for the catalytic oxidation of glycerol to dihydroxyacetone

Abstract

Supported gold nanoparticles play a fundamental role in modern material science, and particularly in heterogeneous catalysis. Such catalysts are known to be excellent catalysts, not only for the total oxidation of various pollutants (CO, VOCs), but also for the selective oxidation of bio-based platform molecule (such as glycerol) to added-value chemicals (dihydroxyacetone, glyceric and glycolic acid). However, as it was illustrated in the first chapter, controlling their fine dispersion however remains a challenge, especially when using silica supports. We report in this second chapter a simple one-pot aerosol route to mesoporous Au-SiO_2 catalysts featuring small gold nanoparticles (~3 nm). To achieve this, we rely on the strong interactions between gold and the thiol function of a mercapto-silane demonstrated previously. The addition of this gold-stabilizer during synthesis enhances the stability of the gold precursor and is the key to control the formation of small gold nanoparticles. The dispersion of gold in the material reaches 21 % (compared to 3 % without the stabilizer). The selective oxidation of glycerol to dihydroxyacetone was employed as a test reaction, of importance in the context of sustainable chemistry. The highly dispersed catalyst obtained via gold stabilization outcompetes benchmark catalysts, reaching a glycerol conversion of 59 % after 8 hours (vs. 5 % without stabilization). Finally, we show that such new synthesis strategy can be extended to other metal.

The results presented in this chapter were published in

Airborne preparation of small gold nanoparticles dispersed on mesoporous silica, Margot Van der Verren, Vit Vykoukal, Ales Styskalik, Ali Shan Malik, Carmela Aprile, Damien P. Debecker*, **ACS Applied Nano Materials**, 5 (2022) 18977-18985.

2.1. Introduction

Owing to their unique optical, physical, and chemical properties gold nanoparticles are ubiquitous in many fields of nanotechnology, such as sensing, labelling, imaging, (photo)thermal therapy, and catalysis.[234] In heterogeneous catalysis gold nanoparticles are known to be highly efficient for the total oxidation of various pollutants (CO, VOCs).[258–260] Supported gold nanoparticles are also attractive in biorefining scenarios for the selective oxidation of bio-based platform molecules to obtain added-value chemicals such as the selective oxidation of glycerol to value-added compounds (dihydroxyacetone, glyceric and glycolic acid).[50,261,262] Unlike Pd and Pt, gold is highly resistant against oxygen poisoning, allowing to perform oxidation reactions with higher efficiency under higher O_2 pressure.[263] As explained in the introduction, catalysis on gold, is strongly structure-sensitive,[119] so that gold particles formation should be finely controlled; in general their size should remain below 5 nm.[235] Supporting gold on various materials – TiO_2, CuO, ZrO_2, SiO_2, NiO – can be considered to obtain gold nanoparticles effectively dispersed. [118]

SiO_2 is a versatile and cheap support material showing a high stability and a tunable texture. These properties makes it an attractive support for catalysis.[99] However, silica is also one of the most challenging support to combine with gold nanoparticles. Owing to the poor affinity of gold for the silica surface, conventional methods of synthesis – such as impregnation or deposition-precipitation method – often lead to gold particle size above 20 nm.[104] To improve the affinity between the silica surface and gold, silica can be modified with an organic linker.[264–266] Although it allows a better control on the sintering of the gold nanoparticles, diameters still remains above 10 nm. Alternative routes to small and dispersed gold nanoparticles include microwave induced synthesis,[267,268] physical vapor deposition technique (such as magnetron sputtering),[269] and sonochemical approaches.[270] Although small gold nanoparticles can be obtained, such synthesis routes are generally time- and resource-consuming due to their multi-steps approach which makes them less attractive for industrial applications. Moreover, once formed, gold nanoparticles tend to aggregate (due to their high mobility on silica) when exposed to harsh reaction conditions, leading to the deactivation of the catalyst.[242]

To overcome these issues, one-pot sol-gel syntheses of gold nanoparticles embedded in mesoporous silica were developed by few groups.[126,271–273] These syntheses are based on the direct addition of the gold precursors in a

mix of the pre-hydrolyzed silica precursors and a templating agent followed by the aging of the gel and its calcination. The materials exhibit small gold nanoparticles (~ 2–4 nm) very resistant to sintering thanks to their entrapment either in the pores or in the walls of the silica framework. However, it is unclear what fraction of gold is catalytically accessible in these materials and part of it might be trapped in the silica matrix.

Continuous aerosol processes are also primed to solve such synthesis challenges, as they involve a very limited number of preparation steps and allow producing various kinds of advanced heterogeneous catalysts with a fine control of the catalyst particle shape, size, surface chemistry and textural properties.[211] In particular, the aerosol-assisted sol-gel (AASG) process led to a variety of mesostructured oxides and mixed oxides successfully employed as catalysts or catalyst supports.[213–216] In this method, a solution of reactive precursors is atomized (possibly in the presence of sacrificial pore-generating agents) in the form of small droplets which undergo a rapid reactive drying. Mesoporous silica particles obtained by AASG have already been used as supports for Au nanoparticles incorporated in a second step by deposition-precipitation.[221] However, gold tended to form large nanoparticles blocking the pores of the silica.

In this second chapter, we disclose a modified aerosol process which gives access to highly dispersed gold on mesoporous silica, in one-step and with a fine control on the gold particle size, thereby boosting their catalytic performance. Such modified aerosol process was then extended to other metals to further investigate its potential interest in supported nanoparticles synthesis.

2.2. Experimental section

The reader is directed to the EXPERIMENTAL SECTION (p. 54-59) for general procedures of characterization. Here, only the methods specifically implemented in this chapter are presented.

2.2.1. Catalysts preparation

Synthesis by deposition-precipitation

A first reference catalyst was prepared by the method of deposition-precipitation with urea (DP urea) described elsewhere.[116,120] Briefly, a solution of $HAuCl_4$ was prepared by dissolving a determined amount of $HAuCl_4 \cdot 3H_2O$ (final loading = 1 %) in 100 mL of deionized water. Urea was then added to this solution to reach a concentration 100 times higher than the one of $HAuCl_4$. 1 g of mesoporous silica support synthesized by aerosol (see section next paragraph) was then added to the mixture and the suspension was stirred and heated at 80°C in a closed vessel protected from light for 16 h. The solid was recovered by centrifugation, washed several times with deionized water and dried under vacuum at 25°C for 2 h. The solid was calcined in flowing air (50 mL min^{-1}) at 300 °C for 4 h (2 °C min^{-1} from 50 °C to 300 °C). The resulting sample is denoted **Au/SiO_2 DP**.

Synthesis by AASG

Typically, solution A was prepared by mixing 11.38 g TEOS and 0.58 g MPTMS with 20 g of acidified water (HCl, 0.01M). In a second vessel, 3.88 g of Pluronic F127 was dissolved in 45 g of absolute ethanol and 8 g of deionized water. The two solutions were kept overnight under stirring at room temperature. Then, chloroauric acid trihydrate (HAuCl4·3H2O) was added to solution A in order to have a nominal gold loading of 1 wt.% in the final Au-SiO_2 catalyst. The resulting solution was stirred for 10 minutes and afterward added to solution B and stirred for 30 minutes. The mixture was atomized with a 6-Jet 9306A atomizer from TSI (operating at 30 psi) and the droplets formed were dried by passing through a tubular quartz tube heated at 350 °C. The powder was recovered on a cellulose nitrate filter (pore size: 0.45 µm) and then dried at 80 °C overnight. The powders were calcined under static air during 6 h at temperature ranging from 350 to 750 °C. Those samples are denoted **$AuSiO_2$-MPTMS-x**, where 'x' is the calcination temperature. The synthesis was also performed with 100 % of TEOS and in the absence of MPTMS following the exact same protocol. Those samples are then denoted **$AuSiO_2$-x**, where 'x' is the calcination temperature. The synthesis without the addition of gold and MPTMS results in a simple silica support calcined under static air at 550°C for 6 h (1 °C min−1) and is here denoted **SiO_2** (used as the support for the synthesis of **Au/SiO_2-DP**, see previous paragraph).

The strategy was afterward extended to other noble metals (Pd and Pt) using their respective precursors ($PdCl_2$ and $(NH_4)_2PtCl_4$ and an equimolar mixture of $PdCl_2$ and $HAuCl_4 \cdot 3H_2O$) in the aerosol process exactly as described for gold, also targeting a theoretical loading of 1 wt.%. The same conditions were used during the synthesis and the calcination.

2.2.2. Catalytic oxidation of glycerol

A solution of glycerol in methanol (0.25 M, 20 mL) was loaded with 68 mg of dodecane (used as GC internal standard) and 200 mg of Au-based catalyst. The reaction was performed under 30 bar of air (used as oxidant) under vigorous stirring at 140°C. After a desired time, the reactor was cooled down in a cold bath and the reaction mixture was centrifuged to separate the catalyst. Reusability test conditions were performed keeping a GLY/Catalyst (w/w ratio) = 4.6 during the different cycles. The reaction was stopped after 3.5 h. After each cycle, the catalyst was recovered by centrifugation, washed with methanol three times, dried overnight at 40°C under vacuum and calcined at 450°C (1°C/min) under flowing air (100 mL/min) for 1 hour. The leaching test was performed under the same reaction conditions. After 1h, the catalyst was recovered by centrifugation and the supernatant was then allowed to react 7 h. The glycerol conversion was evaluated by GC after removing the catalyst (1h) and at the end of the test (8h).

2.3. Results and Discussions

2.3.1. The gold catalysts

The aerosol process relies on the rapid evaporation of a volatile solvent from a liquid mixture to produce dry powders. Briefly, the reactive medium containing the different precursors (here, silicon and gold precursors) and the templating agent (here, Pluronic F127) is atomized into small droplets. Each droplet has the same composition. The aerosol droplets are then dried by passing through a heated zone where the solvent evaporates, the surfactant self-assembles into micelles, and inorganic precursors undergo polycondensation reactions to form an oxide matrix. Finally, the dried particles are recovered on a filter and calcined to eliminate the surfactant and create the porosity.[211]

Here, as a reference, a pristine mesoporous silica support was first prepared by AASG (see textural properties in Table 2.1), and then loaded with Au using a deposition-precipitation (DP) with urea.[120] The resulting catalyst exhibits a purple color after deposition (Figure 2.1 a-b).

Figure 2.1. Photographs of the different powders synthesized in this work. a) SiO_2 support used for the deposition – precipitation of gold; b) **Au/SiO_2 DP**; c-f) **AuSiO_2-x**; g-m) **AuSiO_2-MPTMS-x**. The calcination temperature of each sample is mentioned in each image.

The gold loading was verified by ICP (1.47 wt.%, see Table 2.2). This catalyst – denoted **Au/SiO_2 DP** – exhibited a mesoporous texture, with a typical type-IV isotherm showing a characteristic H2 hysteresis loop (Figure 2.2 A). Its specific surface area reached 240 $m^2.g^{-1}$ with a pore volume of 0.4 $cm^3.g^{-1}$ and an average pore size of 9 nm (Table 2.1).

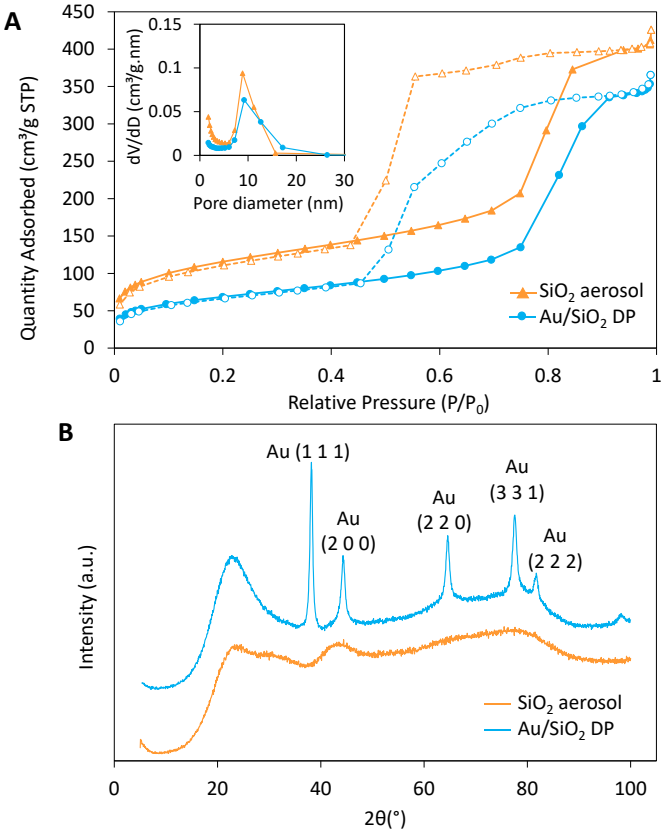

Figure 2.2. (A) Nitrogen adsorption (plain symbols) and desorption (empty symbols) isotherms of **SiO_2** (▲) and **Au/SiO_2 DP** (●). Inserts show BJH pore size distribution analysis obtained from the adsorption isotherms. (B) X-ray diffractogram of **SiO_2** and **Au/SiO_2 DP**. The broad signal at 23° is attributed to the amorphous silica.

In agreement with the N_2-physisorption observations, TEM micrographs (Figure 2.3) showed that **Au/SiO_2 DP** consisted of spherical SiO_2 particles with interconnected pores of ~8 nm. The spherical shape of the microspheres is the result of the formation of the aerosol droplets from which the solvent evaporates during the drying step. The uniform pore size comes from the thermal removal of the structure directing agent (F-127 surfactant) which forms uniform micelles. Gold nanoparticles are found on the microspheres surface with a size estimated in the 10-80 nm range (estimated with TEM measurements).

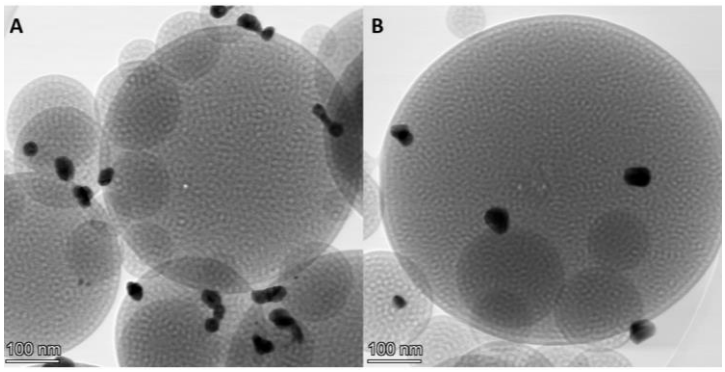

Figure 2.3. TEM images of (A) **Au/SiO_2 DP** and (B) **AuSiO_2-550**. These images were measured with a FEI Tecnai F20 microscope.

XRD pattern revealed the characteristic diffractions for metallic gold (Figure 2.2 B).[274] The gold crystallites size, calculated with the Scherrer equation applied on the 38.1° peak, reached the average value of 10 nm. Thus, TEM and XRD results confirm the formation of relatively large gold nanoparticles up to 80 nm resulting from the aggregation of crystallites of 10 nm outside of the silica microspheres (Figure 2.3 and 2.4). XPS analyses confirmed the presence of metallic gold on the material surface ($Au4f_{7/2}$ binding energy centered at 84.1 eV, Figure 2.5).[275,276] The external surface composition determined by XPS shows a relatively high Au/Si atomic ratio, accounting for gold preferentially located at the surface of the material (Table 2.2). However, gold dispersion – as measured by titration with phenylethyl mercaptan (PEM) – was low for **Au/SiO_2 DP** (6 %). Indeed, the poor affinity between the silica support and the gold nanoparticles implies a high mobility of Au (during calcination); the formation of large and poorly dispersed gold nanoparticles was favored.

Table 2.1. Textural properties of the different materials synthesized

		BET surface ($m^2.g^{-1}$)	BJH adsorption pore size (nm)	Pore volume ($cm^3.g^{-1}$)
SiO_2		400	6	0.6
Au/SiO_2 DP		240	9	0.4
$AuSiO_2$-	350	460	6	0.6
	550	300	8	0.5
	750	200	8	0.4
$AuSiO_2$- MPTMS -	350	590	5	0.6
	550	440	5	0.5
	750	270	6	0.4

Table 2.2. Physicochemical properties of the different materials synthesized

		Bulk Au content (wt.%)[a]	Surface atomic ratio[b] Au/Si (%)	Surface Au content[b,*] (wt.%)	Au crystallite size[c] (nm)
SiO_2		-	-	-	-
Au/SiO_2 DP		1.47	0.56	1.8	10
$AuSiO_2$-	350	1.02	0.21	0.63	12
	550		0.18	0.53	13.7
	750		0.24	0.79	13.8
$AuSiO_2$- MPTMS -	350	0.79	0.04	0.11	2
	550		0.04	0.13	3.7
	750		0.07	0.25	5.7

[a] Determined by ICP-OES analysis,
[b] Determined by XPS analysis
[c] Measured by XRD with Scherrer equation on the peak 2θ = 38.1°. * Calculated based on the surface atomic ratio of O, Si and Au. ** Theoretical atomic ratio Au/Si = 0.32%.

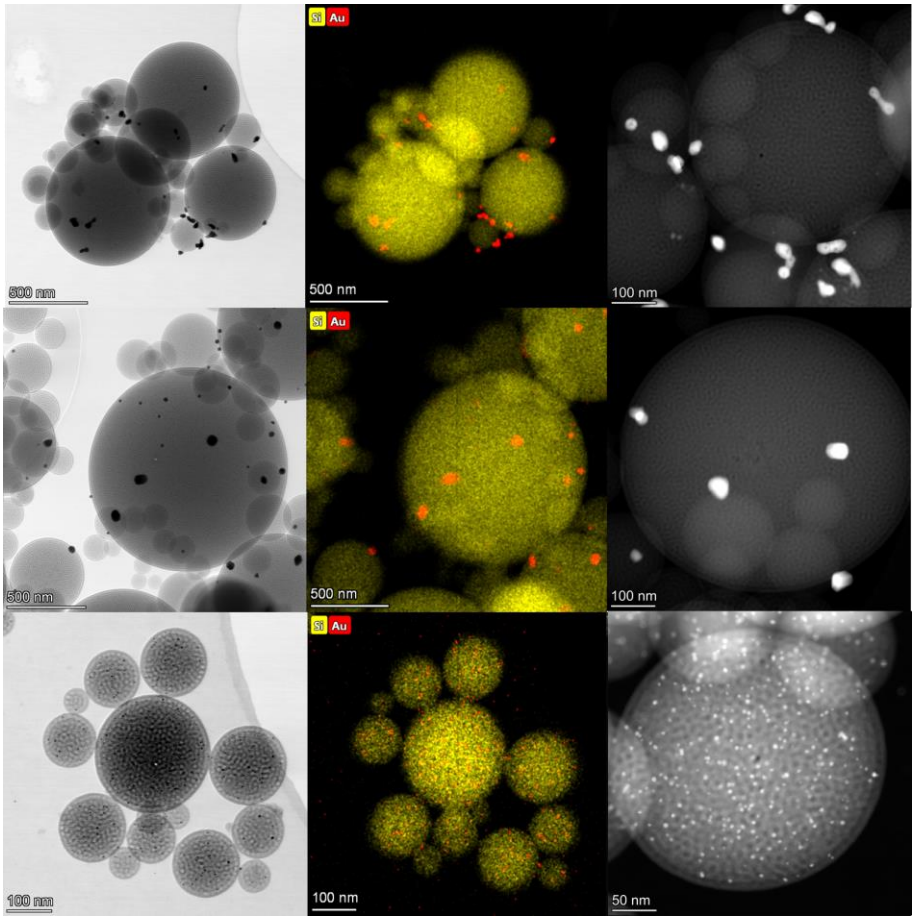

Figure 2.4. Transmission electron microscope analysis. Respectively from top to bottom: **Au/SiO_2 DP**, **AuSiO_2-550**, **AuSiO_2-MPTMS-550**; from left to right: STEM, STEM-EDX, HAADF. These images were measured with a FEI Tecnai F20 microscope.

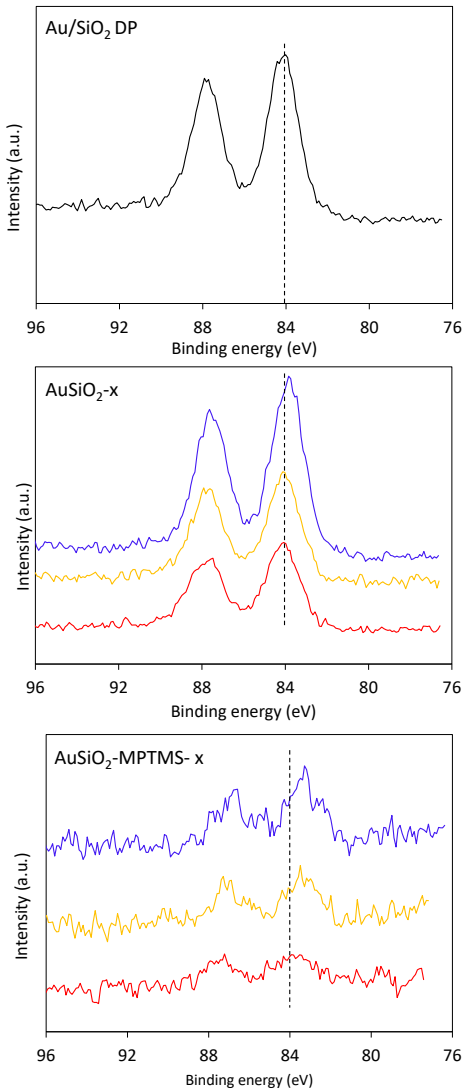

Figure 2.5. XPS spectra of the Au4f region of the different samples synthesized. The color of the curve for **$AuSiO_2$-x** and **$AuSiO_2$-MPMTS-x** depends on the calcination temperature; 350°C (●), 550°C (●), 750°C (●).

With the idea to overcome these challenges, a one-pot aerosol synthesis was investigated. The gold precursor ($HAuCl_4 \cdot 3H_2O$) was directly added to the aerosol precursors solution before atomization, resulting in a yellow transparent solution. The as-synthesized gold-silica powder was calcined at 3 different calcination temperatures: 350, 550 or 750°C to investigate the

formation of gold nanoparticles. The catalysts are denoted **$AuSiO_2$-x**, where x is the calcination temperature.

The obtained powders all exhibited a pink color after calcination, providing clear evidence that metallic gold was formed (Figure 2.1).[277] Solids synthesized by this method showed type-IV isotherms with characteristic H2-hysteresis (Figure 2.6 A). Increasing the calcination temperature caused a gradual decrease of the BET surface area and pore volume due to the gradual smoothening of the roughness. (Table 2.1).

ICP analyses confirmed that gold was effectively incorporated in the material via the one-pot syntheses with an Au wt.% of 1.02 % (1 % targeted). Similar to Au/SiO_2 DP, the binding energy of Au4f7/2 for each **$AuSiO_2$-x** sample (~84 eV, Figure 2.5) is attributed to bulk metallic gold.[275,276] The external Au/Si surface ratio measured by XPS was slightly lower. Importantly, this ratio remained similar for the different calcination temperatures (Table 2.2), meaning that the calcination temperature did not affect significantly the distribution (in the bulk or at the surface) or the dispersion (sintering) of the gold nanoparticles. This contrasts with the case of $Cu\text{-}SiO_2$ catalysts, where a migration of Cu towards the external surface was observed, together with a progressive sintering, when calcination temperature was increased.[227] Here, the relatively low Au surface concentration suggests that the gold NP remain partly trapped in the mesoporous silica matrix.

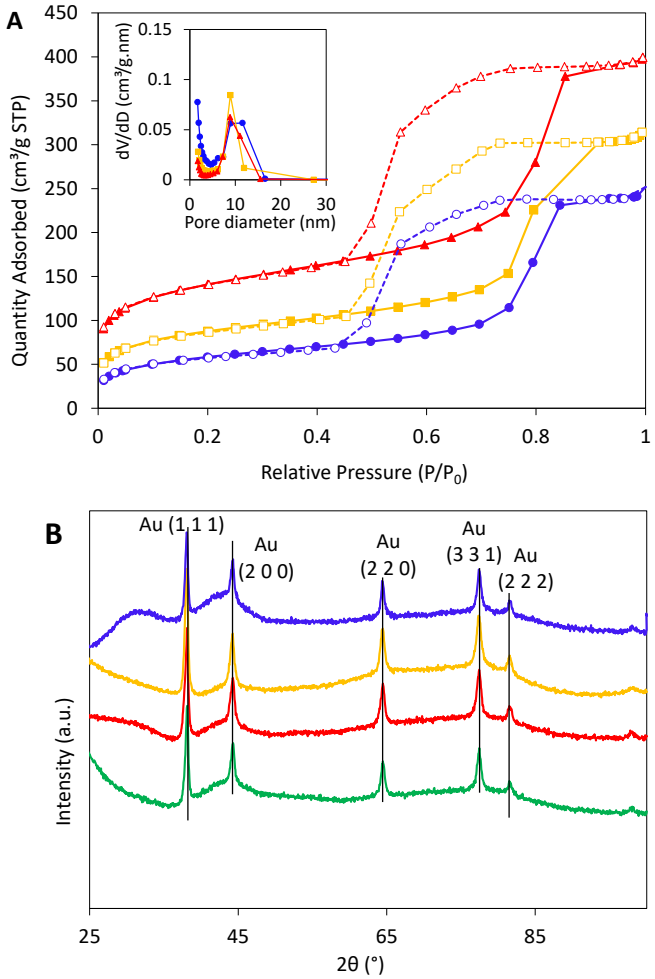

Figure 2.6. (A) Nitrogen adsorption (plain symbols) and desorption (empty symbols) isotherms of **AuSiO$_2$-x**. Inserts show BJH pore size distribution analysis obtained from the adsorption isotherms. (B) X-ray diffractogram of **AuSiO$_2$-x**. The color of the curve depends on the calcination temperature; before calcination (green), 350°C (▲), 550°C (■), 750°C (●).

The gold particle size of each sample was also evaluated by X-ray diffractometry. All catalysts obtained via this one-pot strategy featured similar gold particles sizes, above 10 nm of diameter, independently of the calcination temperature (Figure 2.7). Surprisingly, analyzing the freshly prepared catalyst right after aerosol processing and before any thermal treatment, we also found

the diffraction patterns of metallic gold crystallites (Figure 2.6 B) with a size of about 13.7 nm of diameter.

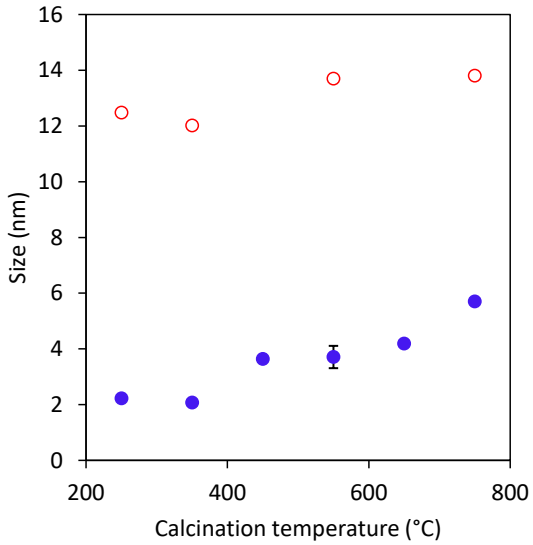

Figure 2.7. Crystallite diameter of **$AuSiO_2$-x** (empty symbols) and **$AuSiO_2$-MPTMS-x** (plain symbols) at calcination temperature ranging from 250 to 750°C. The error bar was calculated on three different batch of **$AuSiO_2$-MPTMS-550,** showing that the difference of size between the different samples is significant.

This clearly shows that gold nanoparticles were already formed during AASG process, most probably by the thermal decomposition of $HAuCl_4 \cdot 3H_2O$ in the drying furnace.[278] Lowering the aerosol processing temperature or the gold loading did not allow us to avoid the formation of these relatively large Au nanoparticles (Figure 2.8), indicating that their formation occurs very easily during the aerosol processing.

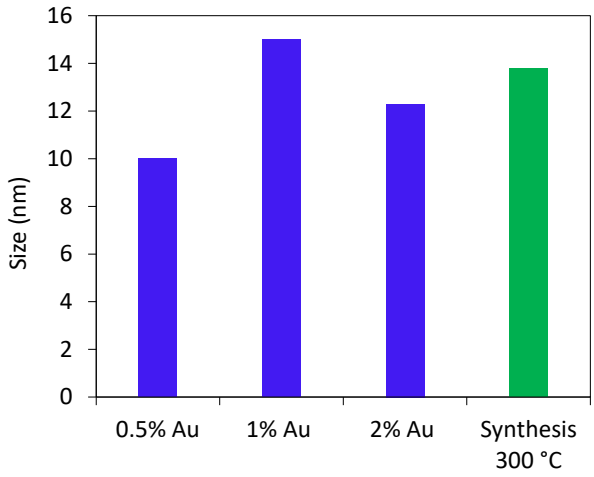

Figure 2.8. Gold particles size of fresh **$AuSiO_2$** synthesized with the tubular oven set at 350°C with wt.% loadings from 0.5 to 2% (blue), or synthesized with the tubular oven set at 300°C with 1%Au (green).

$AuSiO_2$-550 was selected to conduct TEM measurements and EDX mapping. The sample consisted of microspheres of 200-300 nm with large gold nanoparticles ranging from 10-100 nm and interconnected pores (Figure 2.3, Figure 2.9). Consistently, the dispersion measured for this sample was as low as 4 %, owing to the formation of large particles and possibly to the partial entrapment of gold in the silica walls.

These observations prompted us investigate a means to stabilize the gold precursors in the silica matrix during the aerosol synthesis.[279,280] Ligands such as (3-mercaptopropyl)-trimethoxysilane (MPTMS), a thiol based molecule, are often used as stabilizers for the synthesis of colloidal gold particles.[281] Inspired by this, we replaced a small fraction of TEOS by of MPTMS (5 % of the molar content of Si) in the synthesis. MPTMS was pre-hydrolyzed together with TEOS before adding the gold precursor so that the silicon moiety is integrated in the silica walls. While in the absence of MPTMS the precursor solution turned yellow after the addition of the gold precursor, in the presence of MPTMS, a clear solution was obtained, attesting for the stabilization of the precursor. The catalysts are denoted **$AuSiO_2$-MPTMS-x**, where x is the calcination temperature.

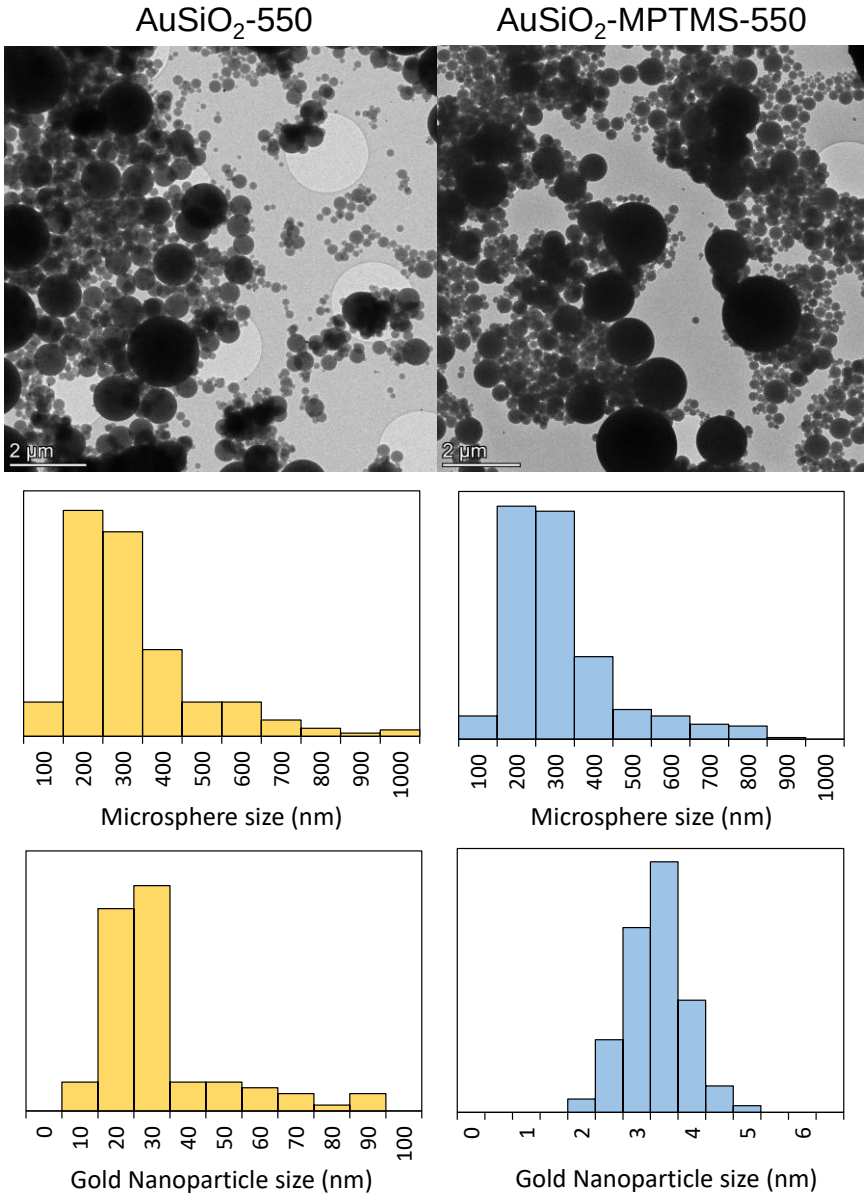

Figure 2.9. TEM images (left), microsphere size distribution (middle) and gold nanoparticles size distribution (right) of **$AuSiO_2$-550** and **$AuSiO_2$-MPTMS-550**. The microsphere size distribution was measured on 400 particles of whole catalyst while the nanoparticle size distribution was measured on 100 gold particles.

The samples consist of powders of different shades of pink depending on the calcination temperature (Figure 2.1). The textural properties (Figure 2.10 A, Table 2.1) and microspheres size distribution (Figure 2.9) were not affected by the addition of MPTMS in the synthesis. Similar to **$AuSiO_2$-x**, the porosity tended to decrease when increasing the calcination temperature. Gold was successfully incorporated in the **$AuSiO_2$-MPTMS** sample with a Au wt.% of 0.79 %. Strikingly, however, the corresponding surface ratio (determined by XPS) was very low (0.04 %). This is true regardless of the calcination temperature (Table 2.2). XPS analyses showed that the $Au4f_{7/2}$ was shifted to lower binding energy (~83 eV, Figure 2.5). This corresponds to surface Au atoms and is explained by the lower coordination number of surface atoms in small nanoparticles.[275] This result suggests the formation of very small gold nanoparticles in **$AuSiO_2$-MPTMS-x** samples. No traces of sulfur (from MPTMS) were detected in XPS analysis, suggesting the complete removal of MPTMS during calcination. Indeed, TGA-MS analyses confirmed that thiol moieties were completely decomposed at 350°C (ANNEX 1, Figure A.1.1).

Unlike the freshly prepared **$AuSiO_2$**, the freshly prepared **$AuSiO_2$-MPTMS** (before calcination) did not show any gold diffraction peak (Figure 2.10 B). Undoubtedly, the addition of MPTMS in the synthesis process prevented the formation of large metallic gold nanoparticles during aerosol processing and the powder of the fresh $AuSiO_2$-MPTMS remained white (Figure 2.1). Gold nanoparticles formation was only induced by calcination, as small and broad diffraction peaks were detected (Figure 2.10 B). Overall, the catalysts prepared in the presence of MPTMS displayed small crystallites size, which moderately increased from 2.2 nm to 5.7 nm when calcination temperature was increased (Figure 2.7). TEM measurements on **$AuSiO_2$-MPTMS-550** confirmed the marked influence of the addition of MPTMS. Gold nanoparticles were homogeneously dispersed in the microspheres and exhibited diameters between 3 and 5 nm, consistent with the size of the crystallites detected in XRD (Figure 2.4, Figure 2.9). Moreover, gold dispersion in **$AuSiO_2$-MPTMS-550** reached 21%, which is considered as an excellent dispersion. Indeed, based on the mathematical model proposed by Bergeret et al.,[282] the maximum dispersion possible for gold nanoparticles of 3.7 nm is 33%. This result, combined with XPS analyses and TEM measurements, highlighted that gold nanoparticles were dispersed throughout the microspheres and at least partly pointing towards the empty pores (i.e. accessible) rather than embedded in the pore walls. We suggest that the forced entrapment of gold in the thiol-functionalized silica microparticles not only prevented the formation of large nanoparticles during aerosol processing, but also impeded sintering upon calcination.

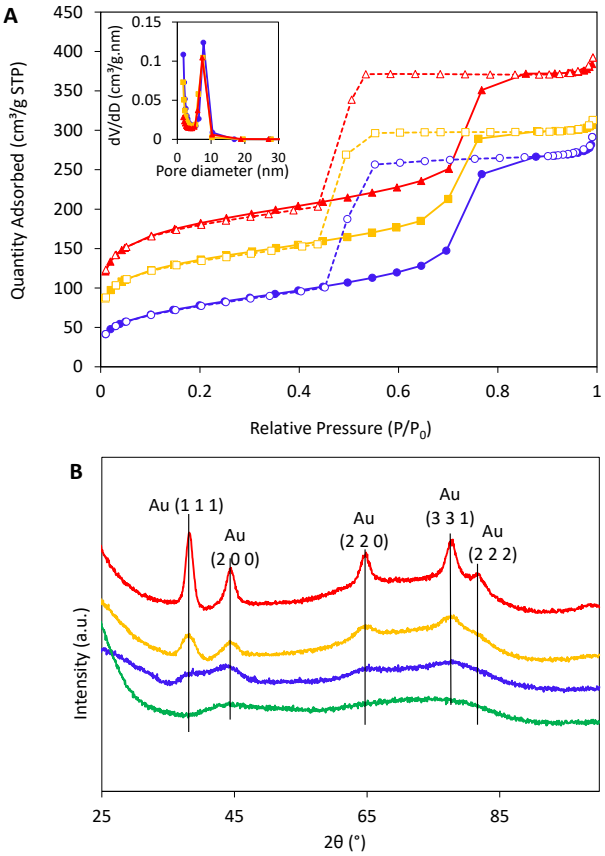

Figure 2.10. (A) Nitrogen adsorption (plain symbols) and desorption (empty symbols) isotherms of **AuSiO$_2$-MPTMS-x**. Inserts show BJH pore size distribution analysis obtained from the adsorption isotherms. (B) X-ray diffractogram of **AuSiO$_2$-MPTMS-x**. The color of the curve depends on the calcination temperature; before calcination (green), 350°C (▲), 550°C (■),750°C (●).

Au/SiO$_2$ DP, **AuSiO$_2$-550** and **AuSiO$_2$-MPTMS-550** were tested in the catalytic oxidation of glycerol to dihydroxyacetone.[196] The reaction was performed using methanol as the solvent, in a stainless-steel autoclave reactor at 140°C under 30 bar of air for 8 hours. Poor activity was observed for **Au/SiO$_2$ DP** (17% conversion and 30% selectivity, see Table 2.3) consistent with the presence of large gold nanoparticles catalytically inert. Glycerol conversion with **AuSiO$_2$-550** was even lower (5 %), probably

attributable to the poor availability of the nanoparticles entrapped in the silica walls and the rather large size of gold nanoparticles. At such a low conversion level, selectivity to DHA expectedly remained high (DHA is the first product of glycerol oxidation and further oxidation does not take place, in particular on poorly active large Au particles). On the other hand, the **AuSiO$_2$-MPTMS-550** catalysts – which featured highly dispersed gold nanoparticles below 5 nm in the catalyst microspheres – allowed reaching much higher glycerol conversion (59 %). The DHA yield reached 18 % in these reaction conditions, while the other catalysts yield 5% or less. Here, the DHA that is produced in large quantities in the early stage of the reaction can be further oxidized into other by-products (glyceric acid, tartronic acid or oxalic acid)[14], leading to a moderate selectivity value. Arguably, the optimization of the reaction conditions could lead to further improvement of the DHA yield. Alternatively, as it will be demonstrated in the Chapter 3 of this PhD dissertation, the coupling with the effectively-catalyzed second reaction (rearrangement of DHA toward lactates) could be a way to sort this issue of selectivity. At this stage, the results of this test reaction clearly showed the decisive role of MPTMS in the preparation of an effective silica-supported gold catalyst, whose catalytic performance is governed by the dispersion of the active metal nanoparticles.

Table 2.3: Catalytic results of the oxidation of glycerol by Au/SiO$_2$ DP, AuSiO$_2$-550 and AuSiO$_2$-MPTMS-550

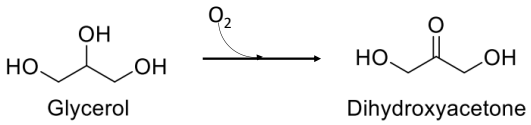

Glycerol Dihydroxyacetone

	Glycerol conversion (%)	DHA selectivity (%)	DHA Yield (%)
Au/SiO$_2$ DP	17	30	5
AuSiO$_2$-550	5	100	4
AuSiO$_2$-MPTMS-550	59±7	30±7	18±2

Catalytic test condition: 140°C, p_{air} = 30 bar, 8h, 460 mg of glycerol in 20 ml of methanol, 200 mg catalyst. Tests were repeated three times for AuSiO$_2$-MPTMS-550.

Among the $AuSiO_2$-MPTMS-x series, **$AuSiO_2$-MPTMS-550** exhibited the best catalytic performance (Table 2.4). Catalysts calcined at low temperature (250-350°C) showed no activity. This can either be the results of a low accessibility of the gold nanoparticles caused by the uncomplete decomposition of the surfactant or the appearance of quantum size effects associated with the very small size of the particles. The existence of an optimal particle size was already reported with a sudden drop of activity below 2-3 nm.[283,284] From 650°C, the catalytic conversion of glycerol decreases as the gold nanoparticles size increases above 4 nm. Further catalytic experiments were carried out with **$AuSiO_2$-MPTMS-550**. The kinetic profile of the glycerol conversion and the DHA yield are shown in Figure 2.11 A. After 2 hours, the DHA yield is slightly decreasing. This is attributed to the subsequent oxidation of DHA to other products. After 4 h, the activity seems to level off, indicating a possible catalyst deactivation. However, XRD and TEM measurements were performed on the spent catalyst after 4 h, and indicated that the crystallite size remained stable (3.8 nm) and the microspheres were intact (Figure 2.12).

Table 2.4. Catalytic performance of **$AuSiO_2$-MPTMS-**x samples.

		Glycerol conversion (%)	DHA selectivity (%)	DHA Yield (%)
$AuSiO_2$-MPTMS-	250	0	-	-
	350	0	-	-
	450	12.3	58.5	7.2
	550	16.5	55.1	9.1
	650	8.3	100	8.3
	750	8	89.7	7.2

Catalytic test condition: 140°C, p_{air} = 30 bar, 1h, 460 mg of glycerol in 20 ml of methanol, 100 mg catalyst.

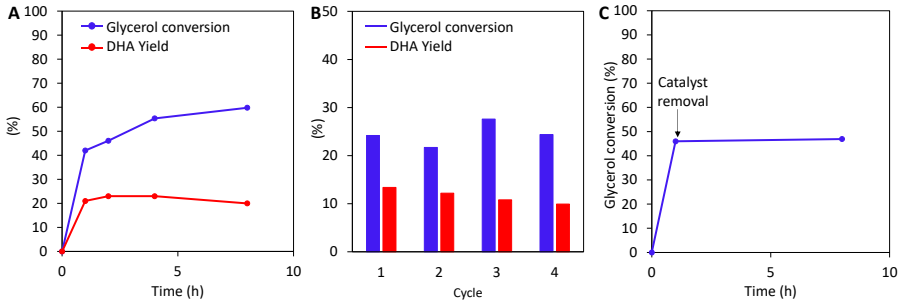

Figure 2.11. (A) Kinetic study, (B) reusability tests and (C) leaching test performed on **$AuSiO_2$-MPTMS-550**. Catalytic conditions: 140°C, p_{air} = 30 bar, 0.25 M glycerol in methanol, GLY/Catalyst ratio = 2.3 (w/w). For the reusability test, the GLY/Catalyst = 4.6 (w/w ratio) and the tests were carried out for 3.5h.

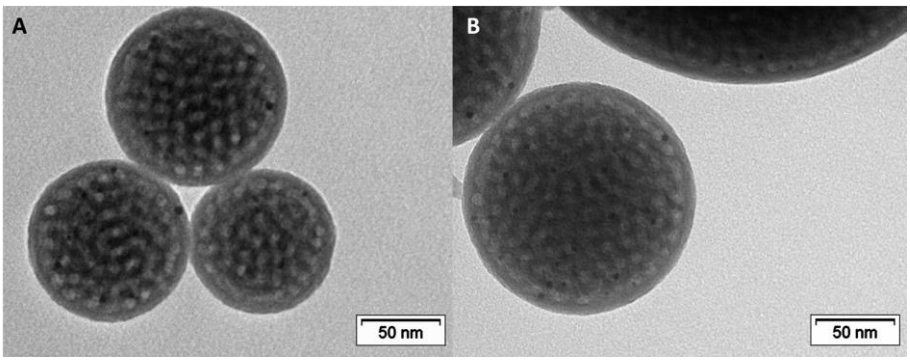

Figure 2.12. TEM images of **$AuSiO_2$-MPTMS-550** before(A) and after (B) the catalytic test. Small gold nanoparticles are observable even after the reaction, showing that their size is not impacted by the reaction conditions. These images were measured with a Phillips Tecnai 20 microscope.

Reusability tests were carried out to evaluate the occurrence of deactivation by product adsorption. For this purpose, the reaction conditions were adapted to target the initial rate of the reaction (see caption Figure 2.11). After a simple procedure of washings and drying catalytic performance dropped already after 1 cycle. A possible mechanism for the deactivation (also observed in the kinetic study) is the adsorption of one of the by-products on the catalyst active site. It was already reported that methyl glycerate (that can be obtained through the oxidation of glycerol)[285] may act as a strong chelating agent for noble metals such as gold, directly hindering the active site of the

glycerol conversion.[286] Therefore, an additional regeneration step was performed at 450°C (1°C/min, and dwell for 1 hour) under flowing air (100 mL/min). Here, the catalytic activity (conversion) of **$AuSiO_2$-MPTMS-550** was maintained, but the selectivity was slightly lowered over each cycle (Figure 2.11 B). This can be rationalized by the fact that the regeneration procedure induced a progressive structure change of the gold nanoparticles, which grow from 3.7 nm for the freshly calcined catalyst to ~ 4.5 nm after the 4th cycle of use.

A hot filtration test was performed in order to prove the catalyst stability during the reaction (Figure 2.11 C). The glycerol conversion was evaluated after 1 h of reaction (46% conversion) and the catalyst was removed by centrifugation. The supernatant was allowed to further react in the absence of the solid catalyst under the same reaction conditions for another 7 h. The final glycerol conversion remained unchanged (47% after 8 h), showing that no active species was leached.

2.3.2. Extending the scope of the strategy developed for gold to other metals

As a follow-up on the work presented above (and published in [287]), we attempted to extend the one-pot aerosol synthesis route aided by MPTMS to other metals. We targeted various metals, including transition metals such as Ni, Co, and Cu (see ANNEX 2). In the scope of this thesis, we focus of noble metals such as Pd and Pt as they are also active in the oxidation of glycerol.[14] Different materials were synthesized, containing 1 wt.% or 2wt.% of Pd or Pt, embedded on silica support. For each targeted composition, the synthesis was carried out either with (5 mol.% of the Si content) or without MPTMS. Interestingly, as it was already observed during the synthesis of the gold catalysts, the color of the solution precursor was impacted by the presence of MPTMS. For Pd, the solution turned from red to yellow with the addition of MPTMS while for Pt, a clear change from yellow to orange was observed.

From a qualitative point of view, as it was already observed for gold, the fresh samples with identical metal and loadings clearly exhibited distinct colors depending on whether they contained MPTMS or not (Figure 2.13). This observation indicated that MPTMS may interact with the metal precursor. The colors observed for the fresh catalysts containing MPTMS resembled the color of the precursor used in the aerosol, suggesting that the metal had not yet formed nanoparticles and was still in the precursor form. Conversely, in the

absence of MPTMS, the fresh powder displayed a color similar to that of the calcined powders, implying the possible formation of metal nanoparticles during the aerosol process.

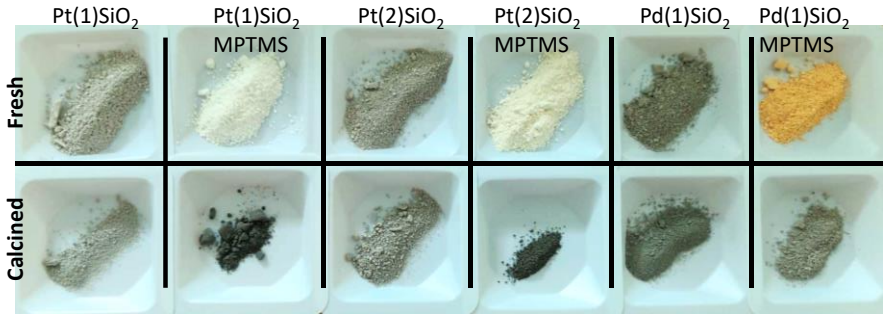

Figure 2.13. Photographs of the fresh and calcined Pt and Pd catalysts with and without MPTMS.

The textural properties (Table 2.5) of the different materials synthesized remained overall similar to what was observed with gold (Table 2.1). The shape of the isotherms was however impacted by the presence of the different noble metal precursors (both for Pt and Pd) with a change in the shape of the hysteresis loop of these materials (**Pt(1)SiO$_2$**, **Pt(2)SiO$_2$** and **Pd(1)SiO$_2$**) (Figure 2.14). This was attributed to a small modification of the pore shape or the presence of two populations of mesopores in these materials. Indeed, although the type of hysteresis remained the same (H2 type – characteristic for interconnected pores with bottleneck shape), the phenomena observed in these materials was possibly caused by a broader neck width distribution,[288] as confirmed by the BJH pore size distribution analysis. Interestingly, in the presence of MPTMS, the hysteresis loop returned to what was usually observed when synthesizing silica-based catalyst via the AASG process and in the conditions used in this work. This observation strongly suggested that the possible interactions between the silica matrix and the metal precursor observed in the absence of MPTMS was prevented in the presence of MPTMS, most probably due to MPTMS-metal interactions. The isotherms of **Pt(1)SiO$_2$ MPTMS** was be measured but it was expected that the results should be close to the ones of **Pt(2)SiO$_2$ MPTMS**.

Table 2.5. Textural properties of Pd- and Pt- silica catalysts.

	BET surface area ($m^2.g^{-1}$)	BJH pore size (nm)	Pore volume ($cm^3.g^{-1}$)	Micropore volume ($cm^3.g^{-1}$)
$Pd(1)SiO_2$	540	8	0.74	0.09
$Pd(1)SiO_2$ MPTMS	450	8	0.54	0.07
$Pt(1)SiO_2$	350	7	0.51	0.05
$Pt(2)SiO_2$	370	9	0.51	0.07
$Pt(2)SiO_2$ MPTMS	490	7	0.57	0.07

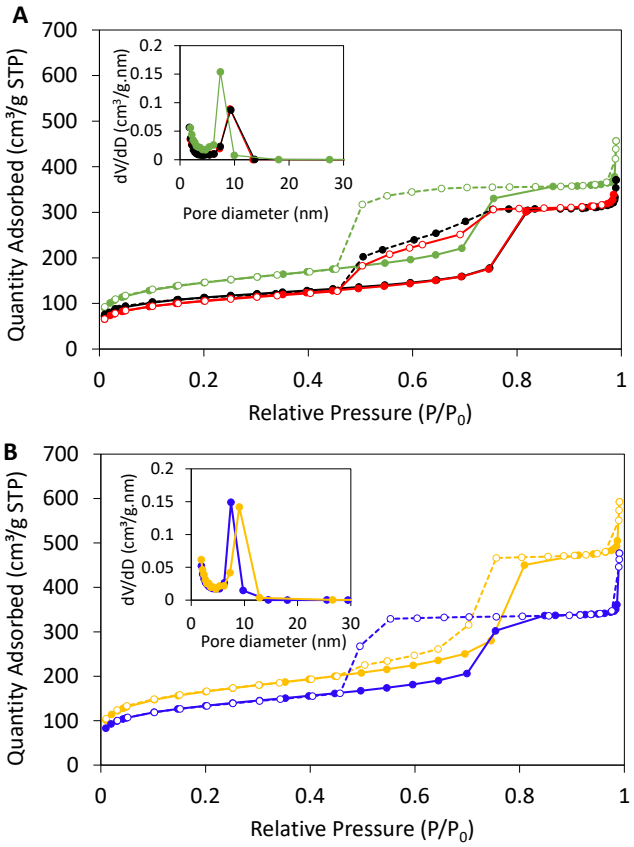

Figure 2.14. Nitrogen adsorption (plain symbols) and desorption (empty symbols) isotherms of (A) Pt catalysts: **$Pt(1)SiO_2$** (●), **$Pt(2)SiO_2$** (●) and **$Pt(2)SiO_2$ MPTMS** (●); and (B) Pd catalysts: **$Pd(1)SiO_2$** (●) **and $Pd(1)SiO_2$ MPTMS** (●). Inserts show BJH pore size distribution analysis obtained from the adsorption isotherms.

As for the gold, Pt and Pd were successfully incorporated in the materials as shown by ICP analysis (Table 2.6). The experimental content of Pt and Pd reached close values to the targeted ones. The surface composition was then investigated by XPS analysis. The peak of $Pd3d_{5/2}$ in the Pd-based catalysts was centered at ~334.5 eV (Figure 2.15 A). As the theoretical binding energy of Pd^0 is 335.4 ± 0.9 eV, we can conclude that metallic Pd nanoparticles were formed in these samples. Similarly, the presence of metallic Pt was confirmed with a $Pt4f_{7/2}$ peal centered at 74.1 in the Pt catalysts (Figure 2.15 B). The amount of metal at the surface was calculated based on these results (Table 2.6). The presence of MPTMS in the Pt catalysts led to a lower amount of Pt found at the surface – as it was already observed for gold – while without MPTMS the amount was close to the experimental bulk content. As the nanoparticles in all these samples exhibited very small diameter (< 3 nm), the differences observed in the surface composition could only be attributed to the location of the Pt nanoparticles. In the Pd catalysts, the opposite trend was observed, with a lower amount of Pd at the surface of **$Pd(1)SiO_2$** than on **$Pd(1)SiO_2$ MPTMS**. This result could be correlated to the size of the Pd nanoparticles that were larger in **$Pd(1)SiO_2$**.

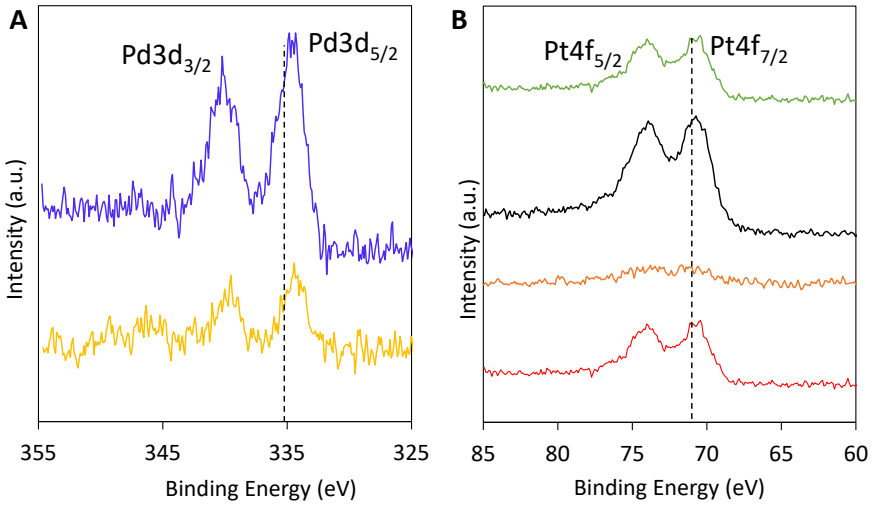

Figure 2.15. XPS spectra of (A) the Pd3d region of Pd catalysts: **$Pd(1)SiO_2$** (●) and **$Pd(1)SiO_2$ MPTMS** (●) and (B) the Pt4f region of Pt catalysts: **$Pt(1)SiO_2$** (●), **Pt(1)SiO2 MPTMS** (●), **$Pt(2)SiO_2$** (●) **and $Pt(2)SiO_2$ MPTMS** (●). The theoretical binding energy of Pd^0 and Pt^0 is shown by the black dotted line in the different spectra.

Table 2.6. Chemical composition and nanoparticles size.

	Bulk Pd or Pt content (wt.%)[a]	Surface Pt or Pd content (wt.%)[b]	Nanoparticle size (nm)[c]
Pd(1)SiO_2	1.3	0.37	7.6
Pd(1)SiO_2 MPTMS	1.4	0.54	2.6
Pt(1)SiO_2	0.8	0.66	2.5
Pt(1)SiO_2 MPTMS	0.8	0.14	Not measurable
Pt(2)SiO_2	1.7	2.15	2.6
Pt(2)SiO_2 MPTMS	1.7	0.83	Not measurable

[a] Measured by ICP analysis
[b] Measured by XPS and calculated based on the surface atomic ratio of O, Si and Pt or Pd
[c] Measured by the Scherrer equation on the X-ray diffractograms

The diffractograms of the different samples are displayed on Figure 2.16. The size of the nanoparticles was estimated with the Scherrer equation on the first peak (2θ = 39.8 ° for Pt; 2θ = 40.15 ° for Pd) (Table 2.6). As previously noted in the case of the gold material, the fresh **Pd(1)SiO_2** without MPTMS (represented by the blue curve) showed characteristic peaks corresponding to metallic Pd. This confirmed the formation of nanoparticles during the AASG process, indicating the thermal decomposition of the chloride and suggesting a lack of control over the particle formation during synthesis. Upon calcination, the peaks became sharper, attesting for an increase in the particle size (from 4.8 to 7.6 nm). On the contrary, when MPTMS was used in the synthesis, the fresh catalyst diffractogram did not exhibit any peaks; they only appeared after the thermal treatment. The use of MPTMS stabilized the metal precursors and allowed to form very small nanoparticle (~2.6 nm) after calcination.

For the Pt catalysts without MPTMS, no peaks were observable for the fresh catalyst (although slightly visible for the 2%). This was attributed to a greater stability of the Pt precursor under the specific aerosol conditions employed. After calcination, however, the characteristic peaks of metallic Pt clearly appeared, confirming the formation Pt nanoparticles. Their diameter, however, remained very small (~2.5 nm), even with the 2% loading. In this particular case, unlike it was observed for Pd and Au, the aggregation of the nanoparticles was very limited, even after calcination, showing a good stability of the metal nanoparticles formed. As for the catalysts containing MPTMS, the fresh catalysts diffractograms did not exhibit any peaks. Even after thermal treatment at 550°C, the peaks were almost not visible. In these samples, the formation of the nanoparticles was prevented and the stabilization of the

nanoparticles was even strong enough to avoid their severe sintering after calcination. These results, similarly to the ones presented previously for the gold materials, clearly demonstrated the impact of MPTMS on the formation and stabilization of the metal nanoparticles.

It is noteworthy to mention that these different results are in good agreement with the visual aspect of the powder described previously (Figure 2.13). When comparing the results obtained for Pd and Pt with the ones described in the previous section for Au, we can conclude that MPTMS played an important role in stabilizing the three different noble metals. In the absence of MPTMS, however, gold was prone to form larger nanoparticles (> 10 nm) while for Pd, and especially for Pt, sintering was limited (7.6 nm and 2.6 nm respectively). This is explained by their Tammann temperature, which is as follows: Au < Pd < Pt (396°C <.644°C < 741°C).[289] Gold nanoparticles have a higher mobility at lower temperature, hence increasing the sintering phenomena. As calcination is performed at 550°C, sintering is somewhat limited for Pd and strongly hindered for Pt. While the intensity of the stabilization effect brought by MPTMS is different for the three noble metals (as a function of theirr intrinsic (in)stability), the trend is consistent: MPTMS allows stabilizing smaller metal nanoparticles because it enhanced the interaction with the surrounding silica matrix and hinders metal mobility, minimizing sintering.

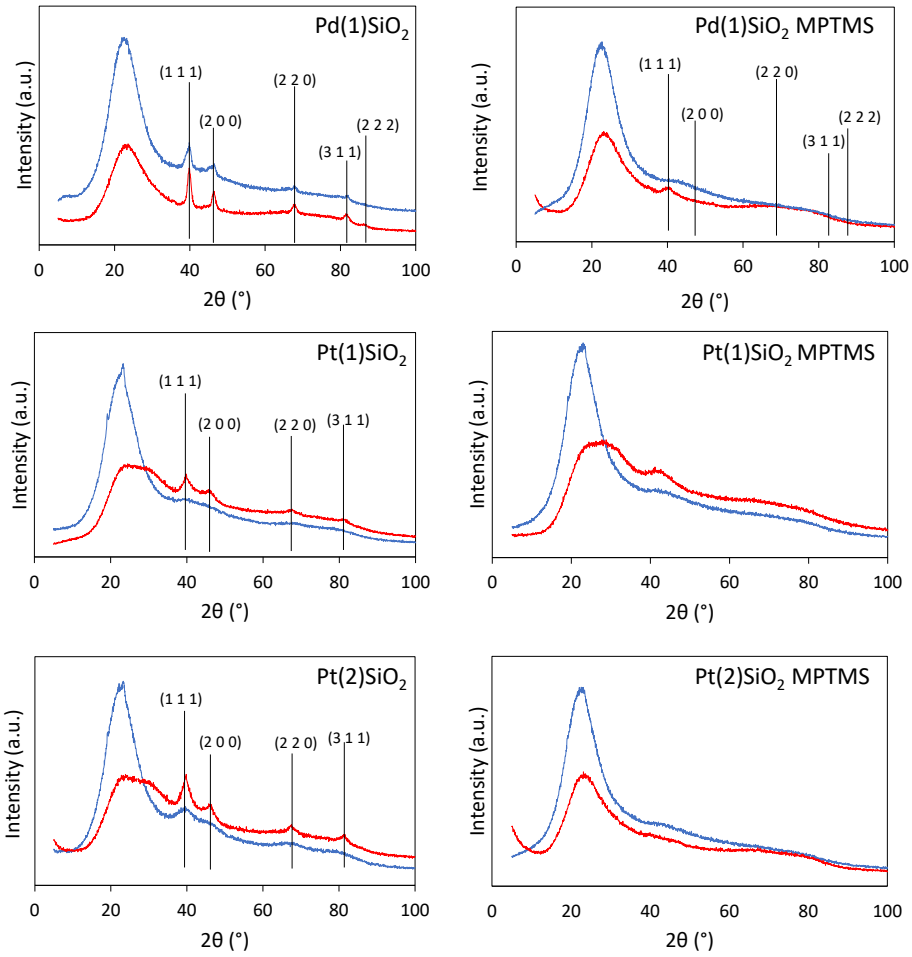

Figure 2.16. X-ray diffractograms of the different Pt and Pd catalysts with and without MPTMS. The blue curve corresponds to the fresh catalyst and the red curve the calcined material. The peaks corresponding to the facets of metallic Pt and Pd are identified by the dark lines.

The different catalysts were tested in the glycerol oxidation to DHA following the same procedure as used before (described in the 2.2. Experimental section). The reaction was stopped after 4 hours of reaction and the reaction media were analyzed by GC.

All catalysts were active in the glycerol oxidation (Figure 2.17). Notably, the 2% loading of Pt exhibited higher conversion than its counterpart with 1%, indicating that increasing the number of active sites might be advantageous for the reaction. The nature of the noble metal did not significantly influence the catalytic performance. Surprisingly, when comparing catalysts with and without MPTMS, the catalytic performance showed no significant impact and remained quite similar for each pair of catalysts. No correlation could be made between the size nanoparticles and the catalytic performance in the glycerol oxidation. Given the results obtained with gold and the significant reduction in nanoparticle size observed by XRD when MPTMS is used, we initially expected to observe enhanced catalytic activity with the MPTMS-based catalysts. Unfortunately, it is possible that the 4h reaction time is already too long for making a rigorous comparison (conversion is already relatively high, possibly approaching the activity plateau, see Figure 2.11 A for gold catalysts). It is suggested that the activity survey should be repeated by stopping the test after 1 or 2 hours, to allow a comparison based on the initial reaction rate.

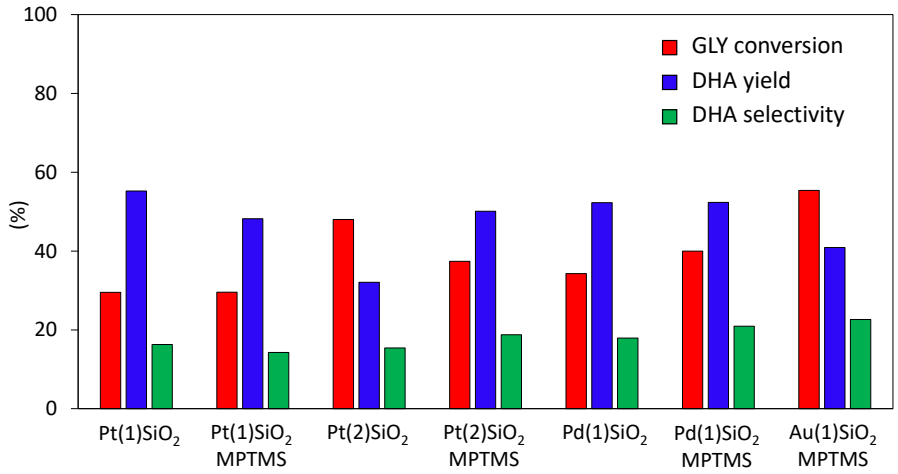

Figure 2.17. Comparison of the catalytic performance of the Pd and Pt catalyst. The “M” at the end of the material name stands for “MPTMS”. Reaction conditions: 200 mg of catalyst, 20 mL of 0.25 M glycerol in MeOH, 140°C, p_{air} = 30 bar, 4h.

2.4. Conclusions

In this second chapter, we disclosed an innovative synthesis strategy to synthesize mesoporous noble metal-silica catalysts with highly dispersed and accessible gold nanoparticles, in one-pot. Leveraging on the aerosol-assisted sol-gel process, metal nanoparticles embedded on SiO_2 catalysts can be obtained in a facile and continuous manner. Importantly, however, the uncontrolled gold nanoparticles formation during aerosol processing must be avoided, as it leads to large particles with poor activity in the selective oxidation of glycerol to DHA. We demonstrate that the in-situ stabilization of the gold precursor during the aerosol-assisted sol-gel synthesis using MPTMS suppresses nanoparticles formation and further hampers gold sintering during calcination, leading to accessible and small (~3.7 nm) gold nanoparticles, homogeneously dispersed in the porous silica support. The corresponding catalyst is very active for the oxidation of glycerol to DHA markedly outcompeting the benchmark catalyst prepared by deposition-precipitation or by aerosol processing in the absence of MPTMS. Moreover, we demonstrated that such synthesis strategy can be extended to other noble metals (Pd and Pt) active in the glycerol oxidation to DHA, but also to other non-noble metals (Ni, Cu, Co). The results obtained in this second chapter are considered as highly valuable in the field of supported metal nanoparticles synthesis, possibly paving the way to the synthesis of various supported metal-based catalysts of various nature and for various applications. In the framework of the current dissertation, these results constitute the starting point to move on to the cascade reaction study in Chapter 3 and 4.

CHAPTER 3: Bifunctional Au-Sn-SiO_2 catalysts promote the direct upgrading of glycerol to lactates

Abstract

Valuable alkyl lactates can be obtained from (waste) glycerol, through a two-step process that entails (i) the oxidation to dihydroxyacetone (DHA) and (ii) a rearrangement of DHA with an alcohol. While the latter reaction is effectively catalyzed by Sn-based heterogeneous catalysts, the former reaction can be carried out with Au-based catalysts. The overall process, however, is penalized by a limited selectivity of supported gold nanoparticles in the first reaction, which strongly restrains the overall lactate yield. To avoid transitional purification steps, it appears interesting to run the process as a cascade reaction, in one step, and ideally with bifunctional catalysts. The preparation of such catalysts, however, remains a challenge. Here, bifunctional catalysts are prepared in one step, through a straightforward aerosol-assisted sol-gel route. The catalysts feature small Au nanoparticles (3-4 nm) embedded at the surface of mesoporous Sn-doped silica microspheres. The preparation successfully leads to insert both active sites in their most active forms, and in close proximity. With the bifunctional catalysts, the selectivity for the final product of the cascade reaction (methyl lactate) is higher than the DHA selectivity when only the first reaction is carried out. This highlights a beneficial substrate channeling effect which helps avoiding side reactions. Interestingly, the bifunctional catalysts also markedly outcompeted mechanical mixtures of the corresponding Au- and Sn-based catalysts. Thus, the spatial proximity between the two active sites in bifunctional catalysts is identified as a key to stir the cascade reaction towards high yield for the final lactate product.

The results obtained in this chapter have been submitted for publication and are available as a preprint:

Bifunctional Au-Sn-SiO_2 catalysts promote the direct upgrading of glycerol to lactates, Margot Van der Verren, Anna Corrias, Vit Vykoukal, Ales Styskalik, Carmela Aprile, Damien P. Debecker, ChemRxiv, preprint, DOI: 10.26434/chemrxiv-2023-2qdvc

3.1. Introduction

The development of efficient catalytic processes for the valorization of (waste) biomass is now clearly identified as a key priority to unlock the path toward a more sustainable chemical industry. As an abundant and renewable resource, biomass is a promising alternative to the existing petro-based technologies and is also economically attractive.[143,290] In the up-and-coming biorefinery schemes, the upgrading of bio-based compounds into valuable chemicals usually relies on multistep process, where separate reactions are carried out in different reactors, using different catalysts.

Robust chemical pathways to synthesize alkyl lactates from (waste) bio-based sources have to be developed, and glycerol is an attractive starting point. As it was discussed in the introduction, the upgrading of glycerol to lactates is typically achieved in two steps: (1) glycerol is oxidized to dihydroxyacetone (DHA) and (2) DHA is further transformed via a rearrangement either to lactic acid when working in water or to alkyl lactate when working in an alcohol.[197] In the first reaction, controlling the level of glycerol oxidation to selectively produce the targeted trioses represents a challenge, as these compounds are prone to further oxidation, which can result in the formation of predominantly highly oxidized compounds (Figure 3.1).[43]

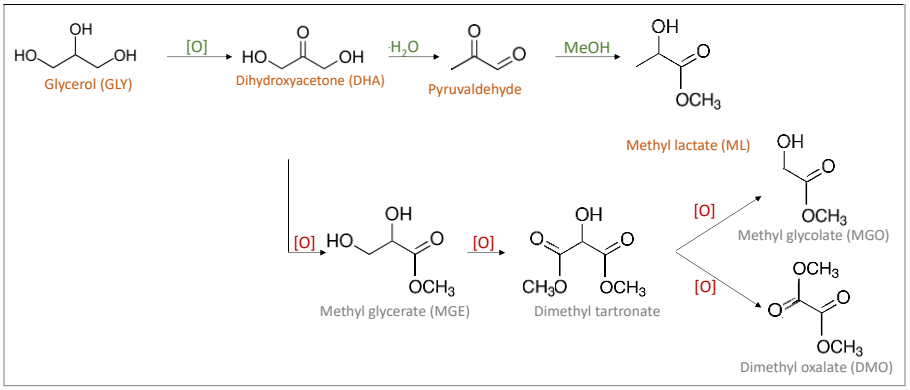

Figure 3.1. Transformation of glycerol to methyl lactate via the formation of dihydroxyacetone (DHA), with the possible side products from the overoxidation of DHA in grey.

Considering such two-step processes, it is important to realize that poor selectivity in the first reaction will unavoidably imply either (i) even lower overall selectivity (and yield) for the whole transformation as the second

reaction occurs in the presence of a complex mixture of intermediates, or (ii) costly purification transitional steps to allow operating the second reaction in clean conditions.

In this perspective, the one-pot cascade reaction of glycerol to lactates is highly attractive, as it might allow boosting the selectivity of the process towards the desired target. Yet, as it was the section 3.2 and 3.3 of the introduction, a few research groups have addressed this possibility.[185,194,196–198] Moving forward, with the idea to improve the sustainability of the transformations, efforts are made to further intensify the processes, by developing multifunctional catalysts bearing different catalytic species, able to run cascade reactions in a unique reactor.[199] A strong boost in the catalytic performance was sometimes observed with multifunctional catalysts due to the synergistic effect brought by the active site proximity.[200–204] Specifically, to perform a cascade reaction such as the transformation of glycerol to ML, effective bifunctional catalysts would be highly desirable because the proximity between the two active sites might favor the rapid channeling of the unstable intermediate (DHA) towards completion of the second step of the cascade reaction thus decreasing the possibility of side reactions. In this way, higher overall yields could be obtained.

As it was extensively discussed in the section 3.3 in the introduction, the synthesis of such materials can be challenging as they usually rely on multistep synthesis processes in which the addition of an active specie on a preformed (active) material can modify its morphology or texture, affect the nature of chemical surface species, and hinder the availability of catalytic sites. [196]

In this chapter, we propose a one-pot strategy, relying on the aerosol-assisted sol-gel process, for the preparation of a new type of bifunctional heterogeneous catalysts for the upgrading of glycerol to methyl lactate. The aerosol process provides easy access to heterogeneous catalysts with tailored properties (texture, composition, dispersion, surface functionality) in a limited number of preparation steps.[211] This technique relies on the rapid thermally-induced evaporation of a solution containing the different precursors (alkoxides or salts) and a templating agent to form dry particles with homogeneous composition and controlled porosity. Various catalysts including porous oxides, metal and metal alloys or even hybrids catalysts were synthesized using this technique.[216,218–220,229,291–296] The catalysts developed in this work consist of small Au nanoparticles highly dispersed on a mesoporous Sn-Si mixed oxide. We demonstrate how combining the two active sites on the same solid particles allow us to boost the overall catalytic

performance of the cascade and to lower the formation of over-oxidized by-products.

3.2. Experimental section

The reader is directed to the EXPERIMENTAL SECTION (p. 54-59) for general procedures of characterization. Here, only the methods specifically implemented in this chapter are presented.

3.2.1. Catalyst preparation

Tin catalyst

The mesoporous Sn-SiO_2 catalyst was synthesized following a protocol already developed by our groups.[213,217] Typically, solution A was prepared by mixing 12 g of TEOS with 20 g of acidified water (HCl, 0.01M). In a second vessel, 3.88 g of Pluronic F127 was dissolved in 45 g of absolute ethanol and 8 g of deionized water (Solution B). The two solutions were kept overnight under stirring at room temperature. Then, tin (IV) chloride ($SnCl_4 \cdot 5H_2O$) was added to solution A in order to have a nominal Si/Sn ratio equal to 74. This ratio was selected based on a previous study on the optimization of the activity of $SnSiO_2$ in the conversion of DHA to ethyl lactate.[217] The resulting solution was stirred for 10 minutes and then added to solution B and stirred for another 30 minutes. The mixture was atomized with a 6-Jet 9306A atomizer from TSI (operating at 30 psi) and the droplets formed were dried by passing through a tubular quartz tube heated at 350°C. The powder was recovered on a cellulose nitrate filter (pore size: 0.45 µm) then dried at 80°C overnight. The resulting sample was calcined under static air at 550°C for 6 h (1°C/min) and is here denoted $SnSiO_2$.

Gold catalyst

The synthesis of the Au-SiO_2 catalyst featuring small gold nanoparticles is based on the stabilization of the gold precursors by MPTMS developed in the previous chapter of this thesis (see Chapter 2, 2.2.1. Catalysts preparation).

Bifunctional catalyst

Bifunctional catalysts were synthesized combining the syntheses described above. Solution B is the same. In solution A, three gold loadings were investigated: 0.5, 1 and 2% (w/w). The gold precursor was added to the pre-hydrolyzed silica precursors (MPTMS and TEOS) (Solution A), stirred for

10 minutes. Then, tin precursors (Si/Sn = 74) was added and the solution was stirred for another 10 minutes. Solutions A and B were mixed and further stirred for 30 minutes. Then the mixture is atomized as explained above and the recovered powder is calcined in the same conditions. The catalysts are named Au(x)SnSiO2, where x corresponds to the gold loading.

3.2.2. Catalytic studies

The catalytic transformation of glycerol to either DHA (with $AuSiO_2$) or to methyl lactate (with the bifunctional catalyst, $AuSnSiO_2$) were performed in a 160 mL Parr stainless steel autoclave reactor equipped with a Teflon liner. In a typical experiment, a solution of glycerol in methanol (0.25 M, 20 mL) was loaded with 68 mg of dodecane (used as GC internal standard) and a chosen amount of catalysts. The reaction was performed under 30 bar of air (used as oxidant) under vigorous stirring at the desired temperature. After a selected time, the reactor was cooled down in a cold bath and the reaction mixture was centrifuged to separate the catalyst. The solution was analyzed by gas chromatography (Scion Instruments 456-GC) equipped with a Restek Stabilwax column (30-meter length, 0.53 mm ID, 0.25 µm df) and an FID detector. Investigations on the reaction conditions were performed by changing the temperature, the glycerol concentration and the air pressure. Reusability tests were performed keeping a constant glycerol/catalyst molar ratio during the different cycles. The reaction was stopped after 2 h. After each cycle, the catalyst was recovered by centrifugation, washed with methanol three times, dried overnight at 40°C under vacuum and then calcined at 450°C (1°C/min) under flowing air (100 mL/min). The leaching test was performed under the same reaction conditions. After 1 h, the catalyst was recovered by centrifugation and the supernatant was then allowed to react for 7 h. The glycerol conversion was evaluated by GC after removing the catalyst (1 h) and at the end of the test (8 h).

The catalytic tests for the conversion of dihydroxyacetone to methyl lactate were performed in the same reactor. In a typical experiment, 360 mg of dihydroxyacetone was dissolved in 20 ml of methanol with 68 mg of dodecane at 45°C for 15 minutes. Then the clear solution was loaded in the reactor with 200 mg of catalyst. The reaction was performed in the same conditions described above. After 4 hours of reaction, the reactor was cooled down in a cold bath and the catalyst was separated by centrifugation. The solution was analyzed by GC.

3.3. Results and Discussion

3.3.1. Mono-functional $AuSiO_2$ and $SnSiO_2$ catalysts

To achieve a good dispersion of Au nanoparticles onto the mesoporous silica material, we relied on the aerosol-assisted sol-gel process and on the strong interactions between gold and the thiol function of a mercapto-silane.[287] The addition of this gold-stabilizer during synthesis was shown to be the key to control the formation of small gold nanoparticles (in the absence of MPTMS, large Au particles form readily during aerosol processing, see Chapter 2). **$AuSiO_2$** (referred as $AuSiO_2$-MPTMS-550 in the previous chapter) (catalyst consists of mesoporous microspheres with calibrated mesoporosity (5-7 nm) and homogeneously dispersed Au nanoparticles of about 3-5 nm in size (Figure 3.2 A-C). The pores result from the removal of F127 micelles, after calcination.

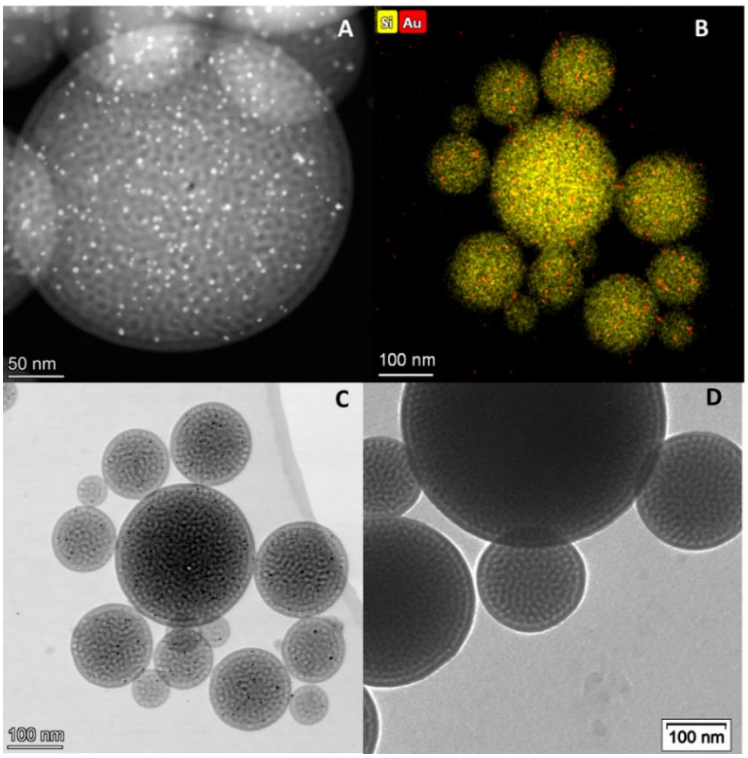

Figure 3.2. Transmission electron microscope analysis of (A,B,C) **$AuSiO_2$** and (D) **$SnSiO_2$**. Respectively from left to right: HAADF, STEM-EDX, STEM. Images A to C were measured with a FEI Tecnai F20 microscope while image D was measured with a Phillips Tecnai 10.

Textural properties were investigated by N_2-physisorption. The type IV isotherm with H2 hysteresis loop demonstrated the presence of ink-bottle neck mesopores (Figure 3.3 A). Overall, the catalyst displayed advantageous textural properties (SSA = 440 $m^2.g^{-1}$; V_p = 0.47 $cm^3.g^{-1}$; D_p = 5 nm) (Table 3.1, Figure 3.3 B). The gold content was verified by inductively couple plasma optical emission spectroscopy (ICP-OES) and was very close to the nominal loading (=1%) (Table 3.2). The surface composition was measured by XPS. No sulfur was detected after calcination, proving that the calcination applied to remove the surfactant also leads to the decomposition of mercaptopropyl moieties. XPS analyses showed that the gold present in the sample was in metallic Au^0 state. $Au4f_{7/2}$ was shifted to relatively low binding energy (~83 eV). This corresponds to surface Au atoms and is explained by the low coordination number of surface atoms in small nanoparticles.[275] This suggests the formation of very small gold nanoparticles in **$AuSiO_2$**. The crystallite size was estimated by X-ray diffraction, applying the Scherrer equation on the 2θ = 38.1° peak (Figure 3.3 C). This sample displayed 3.7 nm diameter crystallite (this measure has systematically a standard error of ± 0.1 nm), consistent with TEM (Figure 3.2) and XPS that pointed to small Au nanoparticles. In good agreement with the N_2-physisorption analysis, TEM shows the presence of 5-7 nm interconnected pores. The gold dispersion measured by thiol titration reached a value of 21%, accounting for a high proportion of gold available in the pores of the microspheres, and therefore available for catalysis.

Table 3.1. Textural properties of the mono- and bifunctional catalysts

	BET surface area ($m^2.g^{-1}$)	BJH pore size (nm)	Pore volume ($cm^3.g^{-1}$)	Micropore volume ($cm^3.g^{-1}$)
$AuSiO_2$	440	5	0.47	0.09
$SnSiO_2$	330	5	0.34	0.07
$Au(0.5)SnSiO_2$	410	5	0.41	0.10
$Au(1)SnSiO_2$	440	5	0.45	0.11
$Au(2)SnSiO_2$	400	5	0.38	0.10

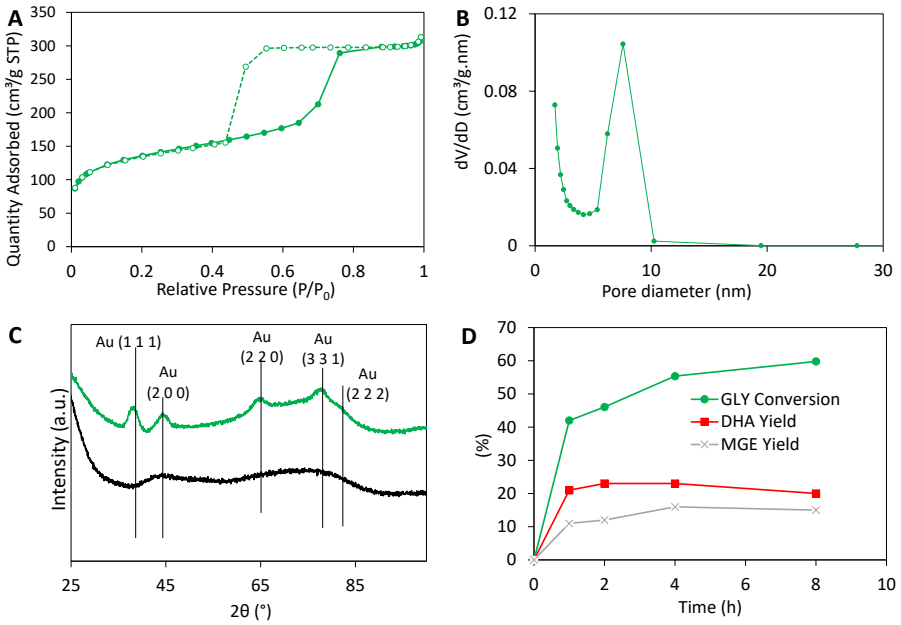

Figure 3.3. (A) Nitrogen adsorption (plain symbols) and desorption (empty symbols) isotherms of **$AuSiO_2$** . (B) BJH pore size distribution analysis obtained from the adsorption isotherm. (C) X-ray diffractogram of fresh **$AuSiO_2$** (●) and calcined **$AuSiO_2$** (●). (D) Kinetic study of the oxidation glycerol (GLY) to dihydroxyacetone (DHA) and methyl glycerate (MGE) with **$AuSiO_2$.** Reaction conditions: T = 140°C, p_{air} = 30 bar, 0.25 M glycerol in methanol, and GLY/Catalyst ratio = 2.3 (w/w).

$AuSiO_2$ was tested in the oxidation of glycerol at 140°C, under 30 bar of air and vigorous stirring. After 4 hours, glycerol conversion reached 55% and the DHA selectivity reached 40% (Figure 3.3 D). By-products such as methyl glycerate (S_{MGE} = 28%) and traces of dimethyl oxalate (Scheme 3.1) were also detected during the reaction. During the 4 hours of reaction, glycerol was quickly consumed to form DHA and methyl glycerate (MGE), resulting from the further oxidation of DHA. Increasing the reaction time to 8 hours slightly increased the glycerol conversion to 60% with similar selectivity MGE (= 28%) and to DHA (=38%). These results are in good agreement with the mechanism already reported by previous studies and with the known relative instability of DHA, prone to overoxidation.[14]

A mesoporous **$SnSiO_2$** catalyst was also prepared by the one-pot aerosol-assisted sol-gel process, using the same templating agent (F127) and targeting a Si/Sn molar ratio of 74. This formulation was selected because it

was reported in a previous work as being very active for the conversion of DHA to ethyl lactate. Other Si/Sn ratio were also tested in this previous study and the ratio of 74 was shown to have the best TON.[217] TEM shows that the morphology and texture of $SnSiO_2$ is very similar to $AuSiO_2$ (Figure 3.2 D). The mesopores, clearly visible in TEM, are confirmed by textural analysis (Figure 3.4 A-B and Table 3.1). Type-IV isotherm showed the same H2 hysteresis observed for **$AuSiO_2$** and the BJH analysis also highlighted a narrow pore size distribution centered on 5 nm. The BET surface area was slightly lower than for $AuSiO_2$ (330 $m^2.g^{-1}$). Tin was successfully incorporated in the material as evidenced by elemental analysis (ICP) which closely fits with the nominal composition (Table 3.2).

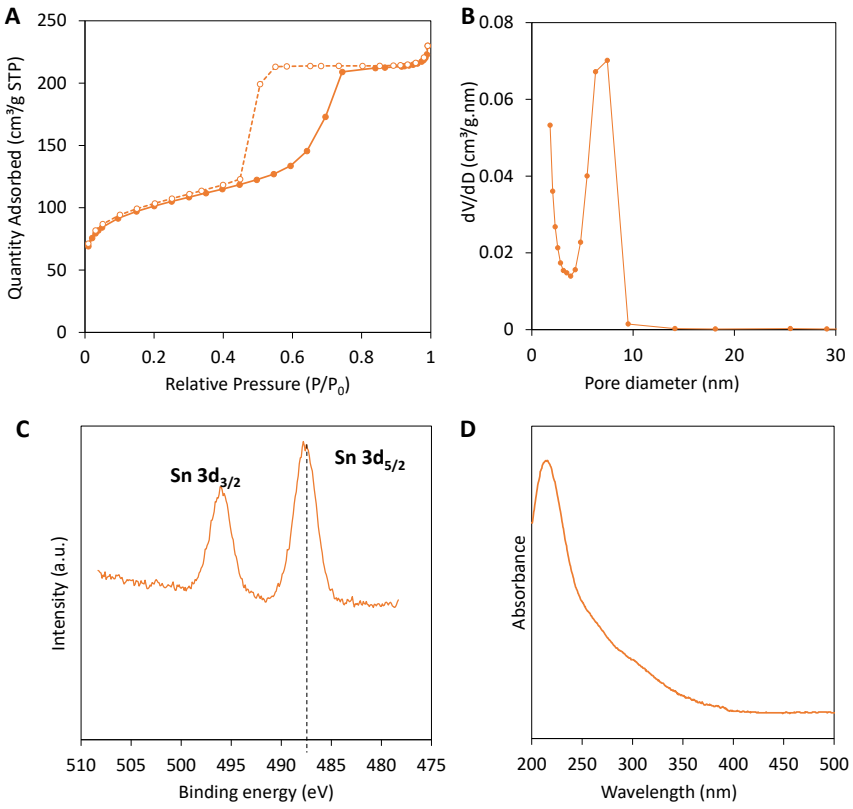

Figure 3.4. (A) Nitrogen adsorption (plain symbols) and desorption (empty symbols) isotherms of **$SnSiO_2$**. (B) BJH pore size distribution analysis obtained from the adsorption isotherm. (C) XPS spectra of the Sn3d region with indication (dotted line) of the theoretical binding energy of $Sn3d_{5/2}$ in Sn^{4+} state (487.2 eV)[297]. (D) Diffuse reflectance UV/Vis spectrum of **$SnSiO_2$**.

The chemical state of tin in the material was investigated by XPS. The Sn 3d spectra confirmed tin is in Sn^{4+} state, with a Sn $3d_{5/2}$ peak centered at a binding energy of 487.2 eV (Figure 3.4 C).[297–300] The surface atomic fraction Si/Sn reached the value of 70, which is very close to the nominal one (74), suggesting a homogeneous distribution of Sn in the silica matrix. Diffuse reflectance UV/Vis spectroscopy was used to further prove the successful insertion of Sn in the silica framework. The spectra show a broad absorption band at λ = 210-240 nm attesting for the presence of Sn^{4+} in tetrahedral coordination in the silica framework in this sample, while the minor contribution at λ ~ 280 nm indicates the presence of a small proportion of hexacoordinated polymeric Sn-O-Sn type species (Figure 3.4 D).[301,302] The insertion of Sn in the silica matrix was also studied by ^{119}Sn NMR spectroscopy under static conditions (Figure 3.5). The signal centered at δ = -695 ppm is characteristic of intra-framework Sn^{IV} in tetrahedral coordination, connected with 4 atoms of Si by oxygen bridges.[302] Although a minor amount of tin in extra-framework cannot be completely ruled out, significant amounts of SnO_2 were not detected. Overall, UV, XPS and NMR results prove the insertion of tin in the silica framework.

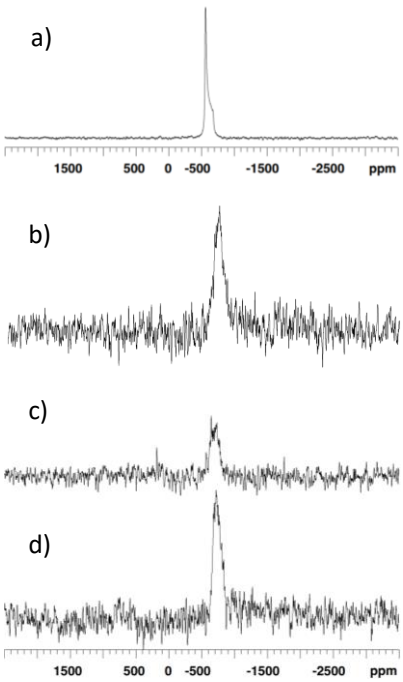

Figure 3.5. Solid state ^{119}Sn static NMR spectrum of (a) pure SnO_2, (b) Au(1)$SnSiO_2$ calcined, (c) fresh Au(1)$SnSiO_2$ and (d) $SnSiO_2$ calcined.

The acidity of the sample was assessed by pyridine adsorption and FTIR spectroscopy. The FTIR spectra are displayed in Figure 3.6. The band found at 1455 cm^{-1} is characteristic of Lewis acid sites and attests of the successful incorporation of Lewis acidity in this sample. The surface density of Lewis acid sites reached 36 $\mu mol.g^{-1}$. Small amount of Brønsted acidity was observed (band at 1545 cm^{-1}).

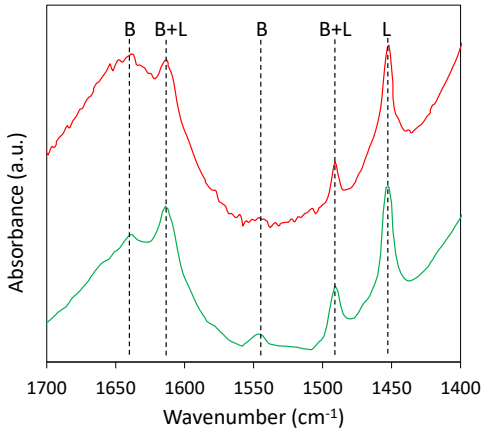

Figure 3.6. FTIR spectra after pyridine adsorption and desorption at 150 °C for 2 hours of **$SnSiO_2$** (bottom green curve) and **Au(1)$SnSiO_2$** (top red curve). B = band corresponding to Brønsted acid sites; L = band corresponding to Lewis acid sites.

Table 3.2. Experimental content of gold and tin at the surface and in the material

	Surface Au loading (wt. %)[a*]	Surface Si/Sn ratio[a]	Bulk Au loading (wt %)[b]	Bulk Si/Sn ratio[b]
$AuSiO_2$	0.13	/	0.79	/
$SnSiO_2$	/	70	/	73
Au(0.5)$SnSiO_2$	0.13	67	0.6	73
Au(1)$SnSiO_2$	0.26	82	1.1	72
Au(2)$SnSiO_2$	0.59	64	2	71

(a) Determined by XPS analysis, (b) Determined by ICP-OES analysis. *Calculated based on the surface atomic ratio of O, Si, Sn and Au.

The **$SnSiO_2$** catalyst was tested for the conversion of DHA to methyl lactate. In the conditions of the reaction (same as above), we verified that DHA was completely transformed in methyl lactate after 4 hours, with a selectivity of >99%. This excellent activity is crucial to the objective of this work, as we target the cascade reaction from glycerol to methyl lactate.

3.3.2. Cascade reaction with a physical mixture of $AuSiO_2$ and $SnSiO_2$

The physical mixture of **$AuSiO_2$** (1 wt.% of Au) and **$SnSiO_2$** (Si/Sn = 74) was used to perform the cascade reaction (Figure 3.7 A). After 8 hours glycerol conversion reached 70%, slightly higher than when using $AuSiO_2$ alone. No DHA was detected, most probably due to its rapid consumption by the tin catalyst. Overall, the yield to the final product of the cascade (Y_{ML} = 19%) was close to the yield of DHA obtained with $AuSiO_2$. The formation of by-products (formed in abundance via over-oxidation of DHA when **$AuSiO_2$** was used alone) could not be avoided. Over time, the conversion of glycerol remained around 70% and the methyl lactate yield plateaued at ~23%. These results show that – owing to the introduction of the effective **$SnSiO_2$** catalyst – the reaction can indeed be pushed from the formed DHA towards the final product (ML). Yet, the ML yield and selectivity remain modest (as dictated by the poorly selective first reaction on the gold catalyst).

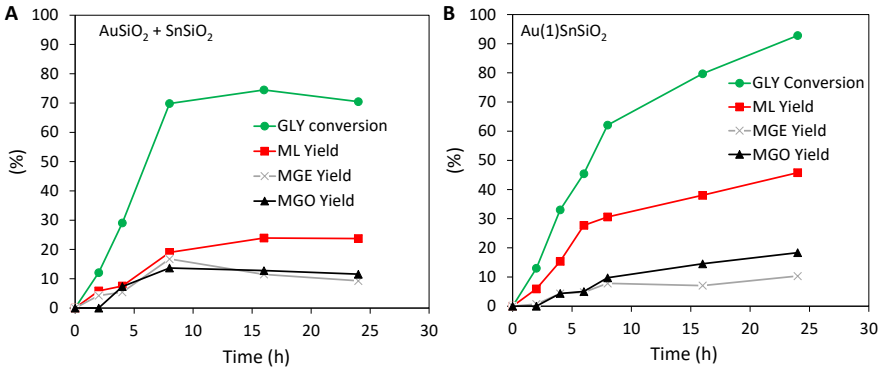

Figure 3.7. Kinetic study of the transformation glycerol (GLY) to methyl lactate (ML), methyl glycerate (MGE) and methyl glycolate (MGO) with (A) the mechanical mixture of **$AuSiO_2$** and **$SnSiO_2$**, (B) the bifunctional catalyst $AuSn(1)SiO_2$. Reaction conditions: T = 140°C, p_{air} = 30 bar, 0.25 M glycerol in methanol, and GLY/Catalyst ratio = 2.3 (w/w).

3.3.3. Bifunctional Au(x)SnSiO$_2$ catalysts

We reasoned that bifunctional materials bearing both the tin and the gold active species on the same solid particles would be primed to further boost the ML yield in the cascade reaction. Indeed, a facile substrate channeling between the two active sites could effectively drive the reaction to the desired methyl lactate. The synthesis of such bifunctional catalysts was attempted before (using multi-step preparation procedures involving sol-gel, colloidal immobilization, and deposition-precipitation),[185,196,198,205,206] but the resulting material showed impaired catalytic performance, mostly due to the difficulty to stabilize both the Au and the Sn species in their most active forms. Here, the aerosol-assisted sol-gel synthesis was exploited to synthesize bifunctional catalysts in one step (plus calcination). These samples were denoted **Au(x)SnSiO$_2$**, where "x" corresponds to the nominal Au loading. The Si/Sn ratio was kept the same in each catalyst (Si/Sn = 74).

Similar to the monometallic catalysts described above, the texture of the bifunctional catalysts was characterized by type IV isotherms featuring the typical H2 hysteresis loop (Figure 3.8 A) corresponding to ink-bottle neck pores. The BJH analysis performed on the adsorption branch of the isotherm showed a narrow pore size distribution centered on 5 nm. All bifunctional catalysts exhibited a high surface area and pore volume, similar to **AuSiO$_2$** and **SnSiO$_2$** (Table 3.1). As it was already observed in the previous chapters and for the Au- and Sn-SiO$_2$ catalysts, the desorption isotherms all exhibited a 'forced closure' caused by the TSE, attesting for the presence of smaller pores of 4 nm.

The crystallite size was measured employing X-ray diffraction (Figure 3.8 B). The addition of tin did not have an impact on the gold crystallites size as it remained very small (3.1 nm) and close to the Au NPs size in **AuSiO$_2$** (Table 3.3). Similarly, the size remained the same regardless of the gold loading engaged.

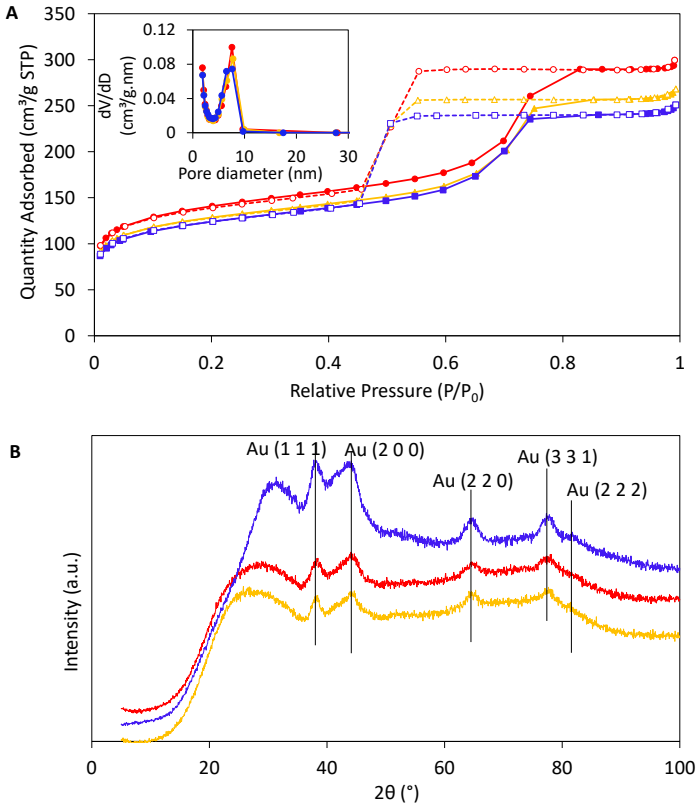

Figure 3.8. (A) Nitrogen adsorption (plain symbols) and desorption (empty symbols) isotherms of **Au(x)SnSiO₂**. Inserts show BJH pore size distribution analysis obtained from the adsorption isotherms. (B) X-ray diffractograms of **Au(x)SnSiO₂**. The color of the curve depends on the gold loading: 0.5% (▲), 1% (●), 2% (■).

Gold and tin contents in the different solids were verified to be very close to the targeted loadings (ICP-OES, Table 3.2). The Au 4f spectra for each bifunctional catalyst also showed the slight shift toward lower binding energy for the $Au4f_{7/2}$ peak (~83 eV), typically attributed to very small gold nanoparticles (Figure 3.9 A). Increasing the loading of gold in the catalysts led to a proportionally higher amount of gold found at the surface of the materials (Table 3.2). The Si/Sn surface ratio remained close to the nominal ratio (Si/Sn = 74) in all bifunctional catalysts, indicating that the Sn is homogeneously dispersed in the material and that the presence of gold and MPTMS did not impact tin dispersion. Exactly like in the case of **SnSiO₂**, Sn is inserted in the

silica matrix with a Sn $3d_{5/2}$ XPS peak centered at ~487 eV corresponding to Sn^{4+} state (Figure 3.9 B).

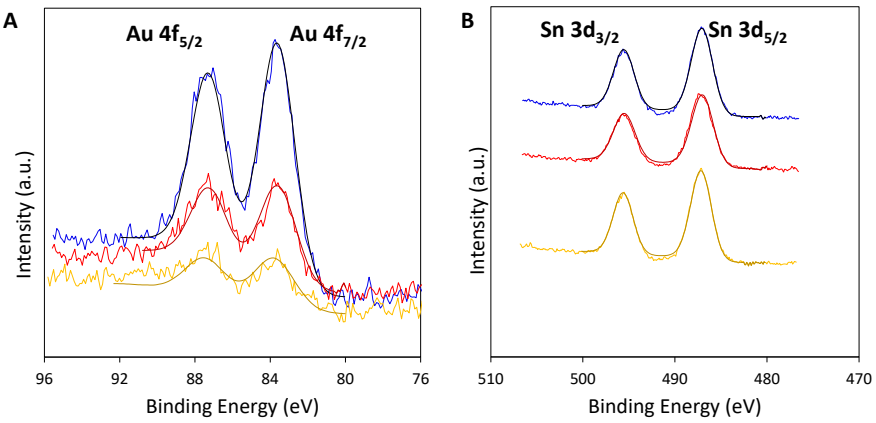

Figure 3.9. XPS spectra of the (A) the Au4f region and (B) Sn3d region of **Au(x)SnSiO$_2$** materials: 0.5% (●), 1% (●), 2% (●). The theoretical binding energy of $Au4f_{7/2}^0$ and $Sn3d_{5/2}$ in Sn^{4+} state are respectively 84.3 eV and 487.2 eV.

In the perspective of a cascade reaction with two different active species, it is important to verify that the two species are inserted in their appropriate state, and that the presence of one does not affect the chemical state of the other (for example via the formation of alloyed Au-Sn nanoparticles). Thus, **Au(1)SnSiO$_2$** was further investigated through XANES and EXAFS analyses, and compared to an Au foil as a reference sample, in order to get selective information about the gold environment. The XANES spectra of the sample and the reference foil are very similar suggesting that gold in the sample is in its metallic form maintaining the same environment to that of pure Au (Figure 3.10 A). This is confirmed by the comparison of the EXAFS interference functions and of corresponding FTs of the sample and the reference foil, which only show minor differences in the amplitudes of the oscillations and in the height of the peaks, respectively. This indicates that there is a strong similarity between the gold environment in **Au(1)SnSiO$_2$** and the gold reference foil (Figure 3.10 B-C), suggesting no chemical interaction between gold and tin. The reduced amplitudes of the oscillations and the lower FT peaks intensity of the sample with respect to the reference foil (Figure 3.10 B-C), are consistent with the small dimensions of the gold nanocrystals.

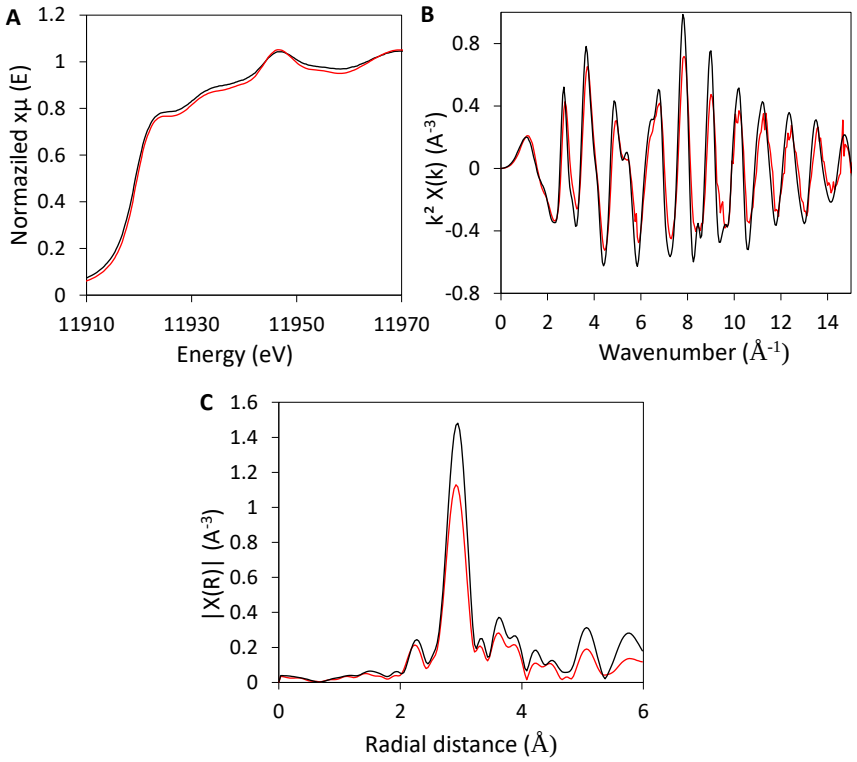

Figure 3.10. (A) normalized XANES spectra, (B) k2χ(k) EXAFS interference functions and (C) corresponding FTs moduli (phase shift corrected) of **Au(1)SnSiO₂** (red curves) and Au foil (black curves).

Table 3.3 Properties of gold in the different catalysts

	Gold dispersion (%)[a]	Gold crystallite size (nm)[b]
$AuSiO_2$	21	3.7
$Au(0.5)SnSiO_2$	13.5	3.1
$Au(1)SnSiO_2$	16	3.1
$Au(2)SnSiO_2$	8.5	3.2

[a] Measured by thiol titration
[b] Measured by XRD with Scherrer equation applied on the 38.1° peak.

The insertion of tin was investigated in the sample **Au(1)SnSiO$_2$** (fresh and after calcination) by ^{119}Sn NMR spectroscopy. The spectrum exhibited the same signal as in **SnSiO$_2$** centered at δ = -695 ppm, indicating the presence of intra-framework Sn^{IV} (Figure 3.5). This confirms that the addition of gold in the synthesis does not disrupt the proper insertion of tin in the silica framework. Similarly, the acidity of the sample **Au(1)SnSiO$_2$** was not impacted by the presence of gold in the material, with a surface density of Lewis acid sites reaching 38 µmol.g^{-1} (Figure 3.6).

The sample morphology was investigated by transmission electron microscopy (TEM). The **Au(x)SnSiO$_2$** samples consist of spherical shaped microspheres with 5-7 nm interconnected pores (Figure 3.11). The gold nanoparticle size distribution was estimated through TEM measurements on 200 nanoparticles. Whatever the gold loading, the materials exhibited overall a narrow gold nanoparticles size distribution centered at 3.5 nm, in good agreement with XRD results (Figure 3.12). Gold nanoparticles are homogeneously dispersed in the microspheres. EDX elemental mapping (Figure 3.11) allowed highlighting that tin and gold were effectively and homogeneously dispersed in the catalyst microspheres.

The dispersion measurements performed on the different samples showed that the dispersion is somewhat lower in the 2%, compared to the 0.5%, 1% bifunctional catalysts and to the 1% monofunctional **AuSiO$_2$** catalyst (Table 3.3). This result shows that the amount of gold actually surface-available in the 2% catalyst is close to the one found in the 1% material. Considering that the gold nanoparticle size remained similar in the two materials, the decreased dispersion suggests that some nanoparticles are partially embed inside the silica walls when the gold loading reached 2%.

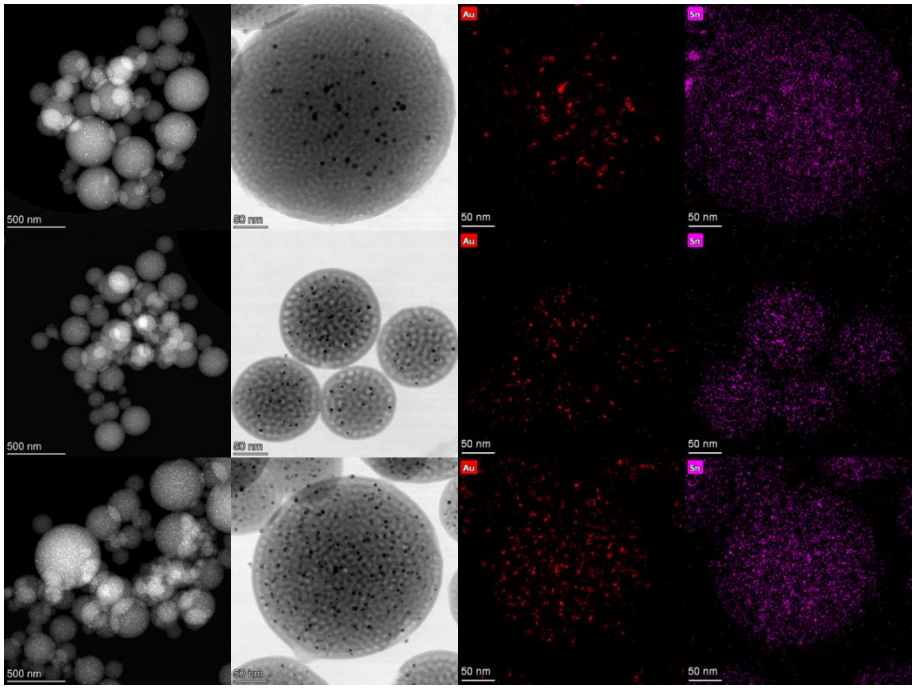

Figure 3.11. Transmission electron microscope analysis. Respectively from top to bottom: **Au(0.5)SnSiO$_2$**, **Au(1)SnSiO$_2$** and **Au(2)SnSiO$_2$**; from left to right: HAADF, STEM, STEM-EDX of Au and STEM-EDX of Sn. These images were measured with a FEI Tecnai F20 microscope.

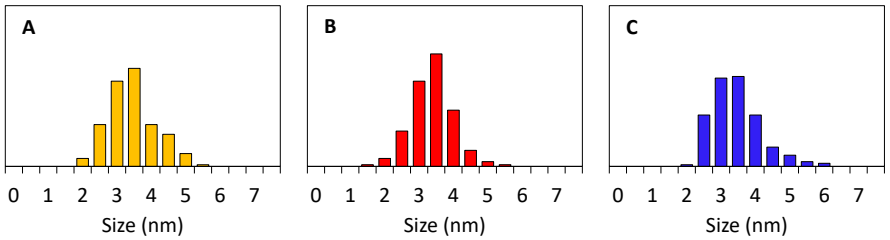

Figure 3.12. Gold nanoparticles size distribution of (A) **Au(0.5)SnSiO$_2$**, (B) **Au(1)SnSiO$_2$** and (C) **Au(2)SnSiO$_2$**. The size distribution was estimated on 200 nanoparticles.

3.3.4. Cascade reaction with bifunctional Au(1)$SnSiO_2$ catalysts

The bifunctional catalyst **Au(1)$SnSiO_2$** was tested in the one-pot transformation of glycerol to methyl lactate. The kinetic profile of glycerol conversion and ML yield with **Au(1)$SnSiO_2$** can be directly compared to the cascade performed with the mechanical mixture (**$AuSiO_2$** + **$SnSiO_2$**) with exactly the same amount of Sn and Au introduced in the reactor (Figure 3.7). Overall, the glycerol conversion was higher along the test with the bifunctional catalyst. Close to total conversion was achieved after 24 hours with the bifunctional catalyst while it remained stuck at 70% for the mechanical mixture. More interestingly, the ML selectivity was highly improved when using the bifunctional catalyst, resulting in a markedly higher ML yield. For example, at 4, 8, and 24h, the ML yield reached 8, 19, and 23% with the mechanical mixture of the two catalysts, but reached 15, 31, and 49% with the bifunctional catalyst.

This confirms that **Au(1)$SnSiO_2$** is intrinsically more active and selective toward ML. With the characterization and the catalytic results in hands, we reason that the bifunctional catalyst takes advantage of the proximity between tin and gold active sites to rapidly channel the intermediate DHA towards further conversion to ML, resulting in improved selectivity and overall yield. Overall, the formation of MGO and MGE by-products (resulting from the oxidation of DHA on gold nanoparticles) remained relatively low. As it was already mentioned, we cannot exclude that there might be some diffusional limitations in the microspheres due the shape of the pores formed during the aerosol process.

3.3.5. Optimization of the reaction conditions

With the high-performance bifunctional catalyst in hand, the reaction conditions were modified with the idea to further improve the ML selectivity and yield. While the temperature clearly had an important impact, with almost no catalytic activity at 120°C. Increasing the temperature from 140°C to 180°C highly improved the catalytic performance (Table 3.4). We decided to target higher selectivity and selected 160°C as the best temperature. Moving further, by varying the glycerol concentration and the air pressure, new optimized conditions were selected for the rest of this work (*vide infra*): at 160°C, under 15 bar of air and vigorous stirring. In these conditions a complete conversion of glycerol was obtained after 16 hours (Figure 3.13). More importantly, the ML yield could be improved to around 62% while maintaining the production of by-products (MGO and MGE) very low.

Table 3.4. Catalytic performance of **Au(1)SnSiO$_2$** on different reaction conditions. Each test was stopped after 6 hours.

Temperature (°C)	P_{air} (bar)	Gly/Au (w/w)	GLY conversion (%)	ML Selectivity (%)	ML Yield (%)
120	30	2.3	5	100	5
140	30	2.3	41	67	28
160	30	2.3	77	68	52
180	30	2.3	96	60	58
160	30	**0.575**	70	75	52
160	30	**1.15**	77	72	57
160	30	**4.6**	54	54	29
160	**15**	1.15	85	73.1	62.2

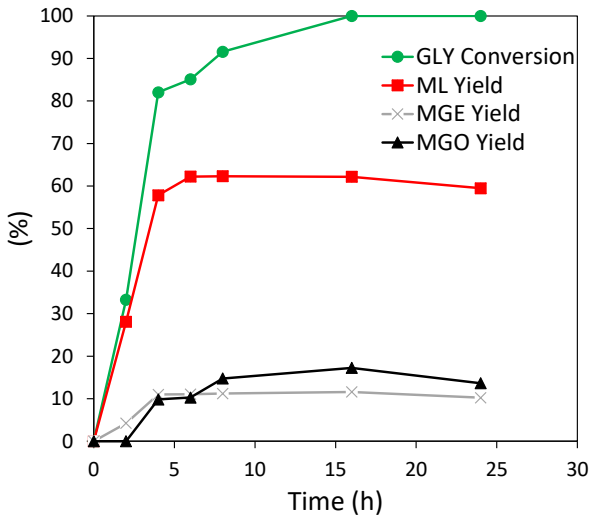

Figure 3.13. Kinetic study of the transformation glycerol (GLY) to methyl lactate (ML), methyl glycerate (MGE) and methyl glycolate (MGO) with **Au(1)SnSiO$_2$.** Reaction conditions: T = 160°C, p_{air} = 15 bar, 0.125 M glycerol in methanol, and GLY/Catalyst ratio = 1.15 (w/w).

The two catalysts **Au(0.5)SnSiO$_2$** and **Au(2)SnSiO$_2$** were also tested in the new reaction conditions to investigate the effect of the gold loading (Figure 3.14). The catalysts containing 0.5% of gold showed a glycerol conversion limited at 40% after 4 hours while the ML yield reached 33%. The lower conversion was attributed to the lower amount of gold in the material. On the other hand, the **Au(2)SnSiO$_2$** sample displayed higher glycerol conversion with a good ML selectivity. Although the dispersion in this material was lower (Table 3.3), the higher conversion at the beginning of the reaction was ascribed to the higher amount of gold detected at the catalyst surface by XPS. In both cases, methyl glycerate, the first product of the overoxidation of DHA, was detected. This product can actually act as a chelating agent on the gold nanoparticles, hindering the catalytic active sites. The rapid loss of catalytic activity in the two materials was attributed to the poisoning of the gold nanoparticles. Such deactivation was already observed when working with **AuSiO$_2$**, and we demonstrated that in order to recover its catalytic activity, a thermal treatment was required. The adsorption of undesired products on the catalytic species can also be responsible for the carbon loss sometimes observed during the reaction.

When comparing the **Au(1)SnSiO$_2$** and **Au(2)SnSiO$_2$** samples, it appeared that a higher loading of gold led to poorer catalytic performance (lower conversion and ML yield) over time. It is hypothesized that the larger amount of gold located at the surface of the microsphere in the Au 2% would lead to higher amount of methyl glycerate produced and then adsorbed, thus leading to a faster catalyst deactivation. Therefore, **Au(1)SnSiO$_2$** was selected as the best for further investigations.

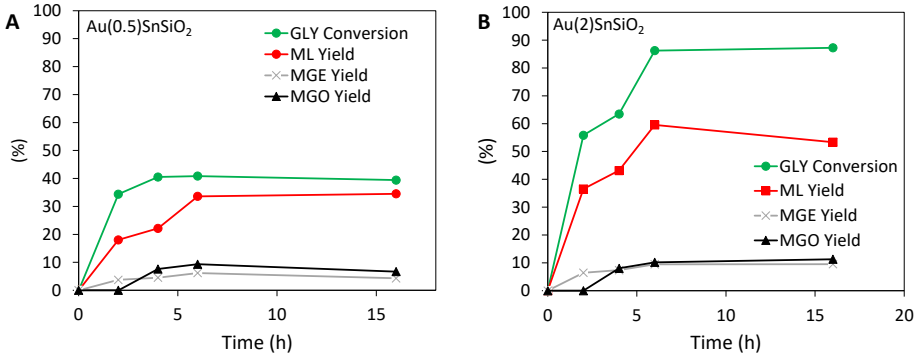

Figure 3.14. Kinetic study of the transformation glycerol (GLY) to methyl lactate (ML), methyl glycerate (MGE) and methyl glycolate (MGO) with (A) **Au(0.5)SnSiO$_2$** and (B)**Au(2)SnSiO$_2$**. Reaction conditions: T = 160°C, pair = 15 bar, 0.125 M glycerol in methanol, and GLY/Catalyst ratio = 1.15 (w/w). Each measure has an error of ± 5%.

The catalytic performance of this latter was compared to other catalytic systems described in the literature (Table 3.5). It is noteworthy to mention that such comparison can be complicated due to the reaction parameters (temperature, pression, glycerol/noble metal molar ratio) that differ in each report, and the fact that the transformation of glycerol to ML implies 2 consecutive reactions. In order to correctly calculate a turn-over frequency on the cascade reaction, it should be performed on the limiting step – the oxidation of the glycerol to DHA. However, it requires to know precisely the amount of noble metal that is actually performing the catalytic reaction. In our case, as the gold is not deposited but incorporated in one-pot, we suspect that part of our nanoparticles – although they are available in the pores – do not participate in the oxidation of glycerol due to some diffusion limitations. Therefore, we decided to not compare the catalytic systems based on the TOF of the first reaction. On the other hand, a TOF cannot be calculated on the second step of the reaction either as (i) this step is not limiting and (ii) the reactant (DHA) cannot be quantified as it is directly consumed.

Instead, we propose to compare the catalytic systems based on their methyl lactate yield, more precisely, their highest methyl lactate yield reached in the shortest time (Table 3.5). The best catalytic system should be the one achieving the highest ML yield in the shortest time, with a high glycerol/noble metal ratio, at the lowest temperature, while avoiding catalyst deactivation. It is for example interesting to see that the system working at the lowest temperature (Au/CuO + Snβ) reach good methyl lactate yield in a very short time, but however works with a very low glycerol/Noble metal molar ratio – thus implying the use of large amount of catalyst, which can be unattractive.

The catalytic system developed in the present work is showing good performance with ML yield in the range of other systems – although it did not outcompete the best catalysts (the zeolites). Importantly, we argue that the rapid and facile synthesis route developed here is also an important feature of our catalytic system.

Table 3.5. Comparison of the different catalytic systems developed in the literature.

Catalysts	T (°C)	t (h)	P (bar)	Noble metal loading (wt%)	Gly/Noble metal molar ratio	ML Yield (%)	Ref
Au-USY-600	160	5	30 (air)	0.35	1407	60	[194]
Au/SnUSY	160	1.75	5 (O_2)	1	98.5	72	[205]
Au/Sn(20)Mt	210	1	30 (air)	1	1407	43	[185]
2Au/CuO + Sn-MCM-41-XS	140	10	30 (air)	1.79	985	75	[196]
PtAu/C + Sn-MCM-41-XS	140	8	30 (air)	1	692.5	68	[197]
Au/CuO + Snβ	90	2	15 (air)	1	49.2	55	[198]
Au/SnβMS	140	4	5 (air)	1	98.5	90	[206]
Au(1)$SnSiO_2$	160	6	15 (air)	1	246	62	This work

Au(1)$SnSiO_2$ was further studied to shed light on its robustness. A "hot filtration test" confirmed that the activity was solely attributed to the solid catalyst (no leaching of active species acting in the homogeneous phase, see Figure 3.15 A). The recyclability of **Au(1)$SnSiO_2$** was investigated following the same reaction conditions. In a typical recycling experiment, the test was carried out for 2 hours (where conversion is still far from completion) before removing the catalyst by centrifugation. The catalyst was washed with methanol and regeneration was performed at 450°C under flowing air (100 $mL.min^{-1}$). The catalyst showed excellent recyclability with an overall stable ML yield over 4 cycles (Figure 3.15 B). The gold nanoparticles remained small (3.8 nm, measured by XRD) after the 4 cycles performed. It is noteworthy to mention that without applying a thermal treatment, the catalyst was no longer active in the cascade reaction, implying that the deactivation was indeed caused by the presence of products adsorbed on the active species.

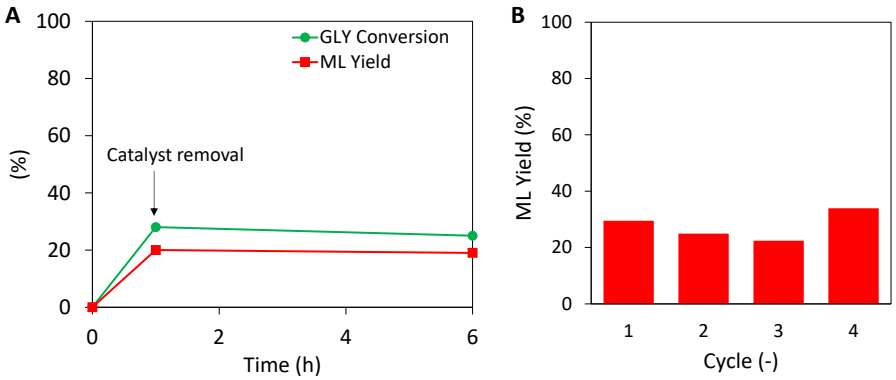

Figure 3.15. (A) Hot filtration test performed with Au(1)$SnSiO_2$, (B) Recycling test performed with Au(1)$SnSiO_2$. Reusability tests were performed keeping a glycerol/catalyst (w/w ratio) = 1.15 during the different cycles.

3.4. Conclusion

Bifunctional catalysts combining gold nanoparticles dispersed in mesoporous tin silicate microspheres (**$AuSnSiO_2$**) were prepared in one step by the aerosol-assisted sol-gel process. The materials displayed advantageous mesoporous texture (with large pore volume and high surface area), small surface-accessible gold nanoparticles, and highly dispersed tin species inserted in the silica framework generating abundant Lewis acid sites. Monofunctional **$AuSiO_2$** and **$SnSiO_2$** catalysts were used as benchmarks. In-depth characterization showed that the intrinsic properties of tin sites and gold sites were not mutually affected in the bifunctional catalyst. While the monofunctional $AuSiO_2$ catalyst showed moderate activity and poor selectivity in the oxidation of glycerol to DHA (producing large amounts of methyl glycerate), the bifunctional catalyst allowed running the cascade reaction glycerol > DHA > methyl lactate very effectively. In fact, the ML yield markedly surpasses the DHA yield observed when running only the first reaction. Thus, we evidenced that the combination of the two active sites boosts the catalytic performance, as the intermediate product is effectively funneled towards the second reaction (DHA rearrangement with methanol) occurring on tin sites. Importantly, higher selectivity and yield are observed for the bifunctional material, if compared with a corresponding mechanical mixture. This confirms the pivotal role of site proximity in the bifunctional catalysts. This work highlights the interest of bringing together in one unique material two catalytic

species to run efficiently a cascade reaction. In this context, the aerosol-assisted sol-gel preparation is shown as a key enabling technology that markedly facilitates the preparation of such bifunctional catalysts.

CHAPTER 4: Extending the MPTMS-stabilized synthesis strategy to Pd-Sn-, Pt-Sn- and AuPdSn-SiO_2 bifunctional catalysts

Abstract

Supported noble metals; such as Pt and Pd nanoparticles are reported as good candidates to perform the catalytic transformation of glycerol to DHA. On the other hand, AuPd bimetallic nanoparticle have gained a lot of interest in the field of catalysis and have been reported as excellent catalyst for the glycerol oxidation. By harnessing the diverse properties of both metals, bimetallic nanoparticles offer a versatile platform for designing catalysts with improved activity, stability, and selectivity compared to their monometallic counterparts. Once combined with a tin-silica mixed oxide, these metal nanoparticles could be used for the cascade transformation of glycerol to methyl lactate. However, the traditional protocols to synthesize supported Pt, Pd an bimetallic AuPd nanoparticles, especially on a silica support, suffers from a poor size and composition control. Here, we report the one-pot synthesis of various bifunctional materials, combining Pt, Pd and AuPd nanoparticles with Sn-SiO_2 mixed oxides leveraging of the aerosol-assisted sol-gel process. More precisely, we investigate the potential of using a stabilizer (MPTMS) in the aerosol synthesis. All the materials displayed advantageous textural properties, featuring small nanoparticles (2-8 nm *vs.* < 2 nm with MPTMS). In the absence of the stabilizer, the formation of intermetallic compounds (Pt_3Sn_2 and PdSn), which results in the reduction of active sites, was inevitable. However, the introduction of the stabilizer successfully prevented the formation of these compounds. The formation of bimetallic Au-Pd nanoparticles could not be demonstrated. All the bifunctional materials exhibited good catalytic activity with excellent selectivity, especially the Pt-based catalysts, in the cascade transformation of glycerol to methyl lactate. This chapter highlights the potential benefit of employing a stabilizer to preserve the intrinsic properties of each metal during the one-step synthesis of bifunctional materials using the AASG process.

4.1. Introduction

The catalytic conversion of glycerol, a renewable and abundant feedstock, into valuable chemicals such as methyl lactate has garnered significant interest due to its potential for more sustainable and greener synthesis. The two steps reaction – also called cascade reaction – requires two types of active sites. Noble metals such as gold (Au), platinum (Pt) and palladium (Pd) have demonstrated good catalytic activity in glycerol oxidation to dihydroxyacetone (DHA) while, as discussed in the introduction of this work, tin is the best candidate to subsequently transform DHA to methyl lactate.[14]

Notably, AuPd bimetallic nanoparticles were also reported by Tang *et al.* as an excellent candidate to perform the first step of the cascade reaction.[197] In fact the AuPd-based catalyst described in their study outperformed the Au- and the Pd-based catalysts. More broadly, in the field of catalysis, bimetallic formulations have gained significant interest due to the synergistic effect brought by the combination of the two metals.[303–306] The presence of a second metal can tune the electronic properties, the morphology and the stability of the nanoparticles, resulting in enhanced catalytic performance compared to their monometallic counterparts.[197] The physical and chemical characteristics of bimetallic nanoparticles are strongly influenced by the spatial organization, atomic arrangement, and the proportion of each atom. These properties can be finely tuned by adjusting the nanoparticles composition. Consequently, significant efforts have been dedicated to the synthesis of bimetallic nanocrystals with precisely defined structure.[307]

Numerous chemical techniques have been developed to synthesize supported bimetallic nanoparticles catalysts, offering various degrees of control over the formation of these metal interactions. Among these techniques, the most commons involve (i) the preformation of the bimetallic nanoparticles in solution following by their deposition on a support, and (ii) the impregnation of the precursor salts onto the support – either simultaneously (co-reduction) or as a sequence (successive reduction).[308] However, these techniques suffer from a limited control over the final nanoparticle composition and structure, resulting in a lack of homogeneity between the different particles.[309] Dash *et al.* for example reported the synthesis of AuPd(1:1)/TiO_2 by co-reduction of Au and Pd. [310] The final material exhibited nanoparticles with a non-uniform composition as gold was mainly found in the larger particles. Another significant drawback of these protocols is that they heavily rely on both the interactions between the support and the metals, and the surface characteristics of the support.[311] On the other hand, as it was stated and demonstrated previously, silica supports typically have poor affinity with

noble metals making the synthesis of supported bimetallic nanoparticles on silica even more challenging.

As shown by the work carried out in our laboratory for Au, Pt, Pd, and Cu (see Chapter 2 of this dissertation,[287] as well as Paris *et al.*[227] and Pampararo *et al.*[10]), it is possible to incorporate a metal salt directly into silica particles, while they are being formed by sol-gel reactions assisted by aerosol processing, and to subsequently provoke the controlled exsolution of the metal to form small metal nanoparticles strongly embedded in the silica matrix and yet surface-accessible for catalysis. Possibly, the metal can be located in the pores (in the surfactant micelles) or at the micelle-silica interface, as it is probably the case for MPTMS-stabilized synthesis of Au-SiO_2 as discussed above. In any case, these strategies are very different from those implying the impregnation, and evidence accumulate to show that resulting NPs properties (size, stability, activity) can be very different from what is obtained via more classical preparation methods.

The synthesis of bimetallic compounds using the aerosol processes was already reported in the literature.[312–314] However, reports of the synthesis of supported bimetallic nanoparticles, especially on silica, using this technique are scare. In their work, Wang *et al.* developed an innovative aerosol drying impregnation (ADI) method to support bimetallic nanoparticles of various metals on a suspension of pre-formed SiO_2 particles.[315] They relied on the rapid drying to minimize the aggregation and obtain uniform highly dispersed well-alloyed nanoparticles with ultra-small sizes (1.4-2.2 nm) . Their control over the composition and size of these nanoparticles was achieved by adjusting the precursor amount in the aerosol. However, in this study, the silica support was already preformed and the aerosol was actually used as an impregnation technique of the bimetallic compounds. Moving further, Hong *et al* demonstrated the one-pot aerosol synthesis (at 700°C) of CoFe bimetallic oxides embedded within SiO_2 microspheres – starting by a solution of their respective precursors.[316] Unfortunately, this material was not thoroughly studied as it was just used as a substrate for the further growth of N-doped carbon nanotubes and then removed.

In the last chapter of this work, we focused on the aerosol-assisted sol-gel synthesis method to prepare bifunctional catalysts combining bimetallic AuPd nanoparticles and Sn, targeting the cascade conversion of glycerol to methyl lactate. We also extended the strategy developed in the second chapter to study the formation of Pt and Pd nanoparticles – as they are less expensive metals than gold – in the AASG process in the presence of Sn. To the best of our knowledge, the one-pot of bimetallic nanoparticles embedded on a mixed

oxide – especially with SiO_2 – using the AASG process has never been reported.

4.2. Experimental section

The reader is directed to the EXPERIMENTAL SECTION (p. 54-59) for general procedures of characterization. Here, only the methods specifically implemented in this chapter are presented.

4.2.1. Catalyst preparation

Briefly, solution A was prepared by mixing 12 g of TEOS (or 95 mol.% TEOS and 5 mol.% of MPTMS when the sample was synthesized with MPTMS) with 20 g of acidified water (HCl, 0.01M). In a second vessel, 3.88 g of Pluronic F127 was dissolved in 45 g of absolute ethanol and 8 g of deionized water. The two solutions were kept overnight under stirring at room temperature. The metal precursors ($PdCl_2$ or $(NH_4)_2PtCl_4$, and then $SnCl_4 \cdot 5H_2O$) were then added to solution A to reach the targeted loading (noble metals: 1-2%, tin: Si/Sn ratio = 74). The resulting solution was stirred for 10 minutes between each addition and then added to solution B and stirred for another 30 minutes. The mixture was atomized with a 6-Jet 9306A atomizer from TSI (operating at 30 psi) and the droplets formed were dried by passing through a tubular quartz tube heated at 350°C. The powder was recovered on a cellulose nitrate filter (pore size: 0.45 µm) then dried at 80°C overnight. The resulting sample was calcined under flowing H_2(5%)/Ar (100 $mL.min^{-1}$) at 550°C for 6 h (1°$C.min^{-1}$). The successful removal of the surfactant under these conditions was confirmed by TGA analysis (See ANNEX 1, Figure A.1.2). When AuPdSn material was synthesized, the amount of Au and Pd were added to target a total loading of 1% (Au:Pd = 1:1).

4.2.2. Catalytic tests

Catalytic cascade tests for the transformation of glycerol to methyl lactate were performed in a 160 mL Parr stainless steel autoclave reactor equipped with a Teflon liner. In a typical experiment, a solution of glycerol in methanol (0.125 M, 20 mL) was loaded with 68 mg of dodecane (used as GC internal standard) and a chosen amount of catalysts. The reaction was performed under 15 bar of air (used as oxidant) under vigorous stirring at 160°C. After a

selected time, the reactor was cooled down in a cold bath and the reaction mixture was centrifuged to separate the catalyst.

4.3. Results and discussion

4.3.1. Pd- and Pt-$SnSiO_2$ bifunctional systems

Different catalysts were synthesized, maintaining a molar ratio for Si/Sn = 74, while Pt and Pd were incorporated to reach a 1 wt.% or 2 wt.% loading. For each material – as for the monometallic **$Pt(1)SiO_2$** and **$Pd(1)SiO_2$** presented in chapter 2 – two formulations were tested, one without MPTMS and one with 5 mol.% of MPTMS. As it was observed for the monometallic materials, the fresh **$PtSnSiO_2$** and **$PdSnSiO_2$** samples synthesized with MPTMS displayed yellow / orange color, corresponding to the color of the metal precursor used during the synthesis. This observation suggested that the nanoparticles were not yet formed at this stage of the synthesis. Once calcined, the powders became grey / black which led to think that metallic nanoparticles were formed. In contrast, when MPTMS was absent, the fresh powders already exhibited a dark color, indicating that the formation of metallic nanoparticles already occurred during the aerosol process.

ICP analyses were conducted to confirm the successful incorporation of metals (Pd or Pt and Sn) in the various synthesized materials (Table 4.1). The experimental metal content in each material closely matched the targeted loading, indicating a good incorporation during the aerosol synthesis. In the case of the Pt-based catalyst, there was a slight decrease in the metal content, which can be attributed to the decomposition of the Pt precursor during storage over time. Furthermore, the atomic bulk ratio of Si/Sn consistently achieved a reasonable value, close to the targeted nominal ratio (Si/Sn = 74). This result serves as evidence of the effective incorporation of metals in the catalysts during the aerosol process.

Table 4.1. Bulk and surface metal content in the bifunctional materials, measure by ICP and XPS.

	Bulk Pd or Pt content (wt.%)[a]	Bulk atomic Si/Sn ratio[a]	Surface Pt or Pd content (wt.%)[b]	Bulk atomic Si/Sn ratio[b]
Pd(1)$SnSiO_2$	1.28	87	0.72	70
Pd(1)$SnSiO_2$ MPTMS	1.31	81	0.69	70
Pt(1)$SnSiO_2$	0.77	79	0.86	36
Pt(1)$SnSiO_2$ MPTMS	0.81	75	0.38	55
Pt(2)$SnSiO_2$	1.60	80	1.44	32
Pt(2)$SnSiO_2$ MPTMS	1.58	73	0.72	98

[a] Measured by ICP
[b] Measured by XPS

The textural properties of the different materials were assessed by N_2-physisorption (Figure 4.1, Table 4.2). The BET surface area, as well as the pore size and the pore volume of the Pt-based catalysts remained stable between the different samples whether MPTMS is added in the synthesis or not. These values were comparable to those obtained for AuSn catalyst. Each catalyst displayed Type IV isotherms with H2-type hysteresis, indicating the presence of interconnected bottleneck pores. Additionally, all materials exhibited a narrow pore size distribution (Figure 4.1 inlet). These indicate that the nature of the metal, the metal loading or the presence of MPTMS did not have a significant impact on the successful formation of the Pluronic F127 micelles during the EISA phenomena in the aerosol process. When comparing these results to the ones obtained with the monometallic materials (Table 2.1), a small decrease of the pore volume is observed. Interestingly, in the bifunctional catalysts the shape of the isotherms of the bifunctional catalysts remained quite similar, whether the sample contained MPTMS or not, which was not the case with the monometallic materials (Figure 2.14). Moreover, while the BET surface area was higher for the MPTMS-containing samples in the monometallic materials, an opposite trend is observed in the bifunctional materials.

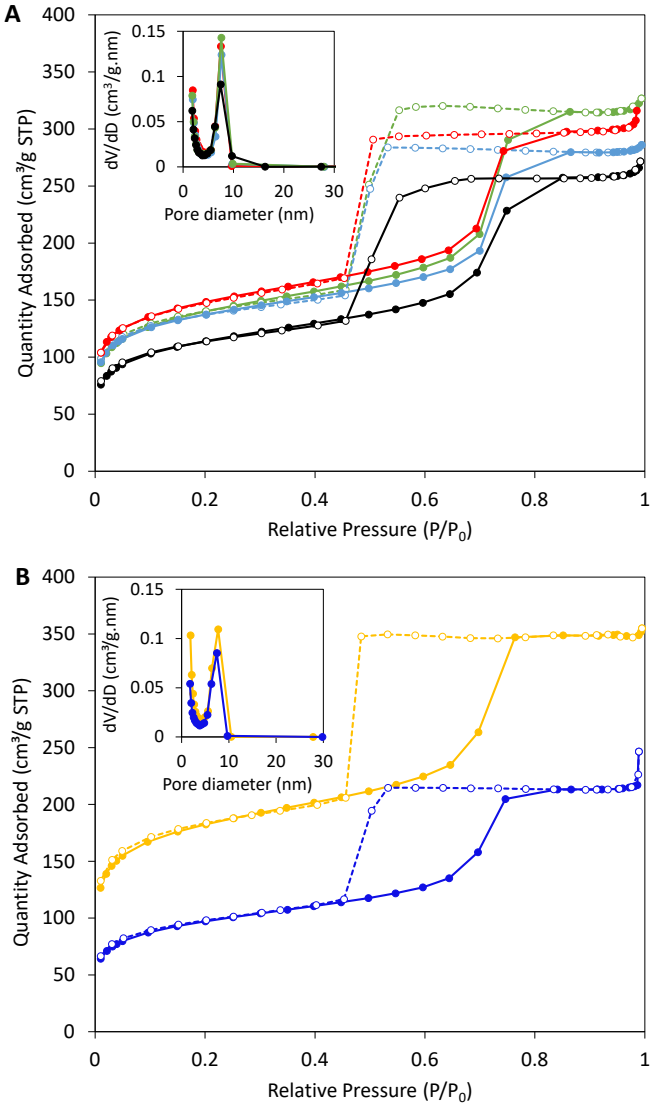

Figure 4.1. Nitrogen adsorption (plain symbols) and desorption (empty symbols) isotherms of (A) Pt catalysts: **Pt(1)SnSiO$_2$** (●), **Pt(1)SnSiO$_2$ MPTMS** (●), **Pt(2)SnSiO$_2$** (●) and **Pt(2)SnSiO$_2$ MPTMS** (●); and (B) Pd catalysts: **Pd(1)SnSiO$_2$** (●) and **Pd(1)SnSiO$_2$ MPTMS** (●). Inserts show BJH pore size distribution analysis obtained from the adsorption isotherms.

Table 4.2. Textural properties of the different bifunctional catalysts.

	BET surface area ($m^2.g^{-1}$)	BJH pore size (nm)	Pore volume ($cm^3.g^{-1}$)	Micropore volume ($cm^3.g^{-1}$)
Au(1)$SnSiO_2$ MPTMS	440	5	0.45	0.11
Pd(1)$SnSiO_2$	580	5	0.43	0.14
Pd(1)$SnSiO_2$ MPTMS	320	6	0.33	0.06
Pt(1)$SnSiO_2$	480	9	0.45	0.11
Pt(1)$SnSiO_2$ MPTMS	370	6	0.40	0.07
Pt(2)$SnSiO_2$	440	5	0.44	0.11
Pt(2)$SnSiO_2$ MPTMS	460	6	0.49	0.10
AuPd$SnSiO_2$ MPTMS	460	5	0.42	0.11

The samples were investigated by XRD to gain more insight on the nanoparticle's formation, their chemical composition and their crystallite structure. The diffractograms of the fresh catalysts (after the aerosol synthesis) and after calcination (at 550°C, $1°C.min^{-1}$) are displayed on Figure 4.2. For all the materials, as it was previously stated in the other chapters, the broad peak found from 2θ = 15° to 30° corresponds to the amorphous silica support. A light shift of this peak was observed after calcination in all samples, which was attributed to a small shrinkage of the silica structure after the micelles were removed and the porosity released. The two peaks observed in the silica peak of the fresh **Pt(1)$SnSiO_2$ MPTMS** came from the F127 surfactant.

Several characterizations were used to identify the nature of the nanoparticles in the different catalytic systems (XRD, EXAFS and XPS). For a better understanding, the results were divided in two sections: phase identification of Pd- and Pt-$SnSiO_2$ bifunctional systems synthesized without MPTMS and phase identification of Pd- and Pt-$SnSiO_2$ bifunctional systems synthesized with MPTMS. It is noteworthy to remind that the MPTMS was added in the aerosol synthesis to hopefully stabilize the Pd and Pt precursor and was removed during calcination.

Phase identification of Pd- and Pt-$SnSiO_2$ bifunctional systems synthesized without MPTMS

The fresh **Pd(1)$SnSiO_2$** XRD pattern (Figure 4.2) clearly presented the characteristic diffraction peaks of metallic palladium. The size of the metal nanoparticles, calculated on the 2θ = 40°, reached 4.5 nm which is actually

almost the same size measured on the fresh **Pd(1)SiO$_2$** sample. Similarly, in the fresh **Pt(2)SnSiO$_2$** diffractogram, the peaks corresponded to metallic Pt with a crystallite size of 2 nm. Interestingly, the diffractogram of these sample drastically changed after calcination. According to the identification software Diffrac.eva, and in good agreements with reports in the literature,[317–319] the peaks observed in calcined **Pd(1)SnSiO$_2$** corresponded to a Pd_3Sn_2 intermetallic phase. The intermetallic nanoparticles had a diameter of 7.7 nm (estimated on the 2θ = 58.2° peak), in the same range of the size obtained with the monometallic sample. **Pt(1)SnSiO$_2$** and **Pt(2)SnSiO$_2$** both exhibited a small and broad peak at 2θ = 41°, possibly related to hexagonal PtSn, although with uncertain identification. The very weak signal was attributed to the low Pt loading and the formation of very small nanoparticles due to the Pt enhanced resistance to sintering (Tammann temperature = 741°C). Unfortunately, the size of these crystallites could not be measured.

In the absence of MPTMS, it appeared that metallic Pd and Pt nanoparticles were already formed during the aerosol synthesis in the fresh catalysts. However, after calcination, the nature of the nanoparticles was completely changed to form intermetallic compound: Pd_3Sn_2 and PtSn. Their respective sizes were in good agreement with the results of the metallic nanoparticles Pd and Pt observed in the monometallic compounds.

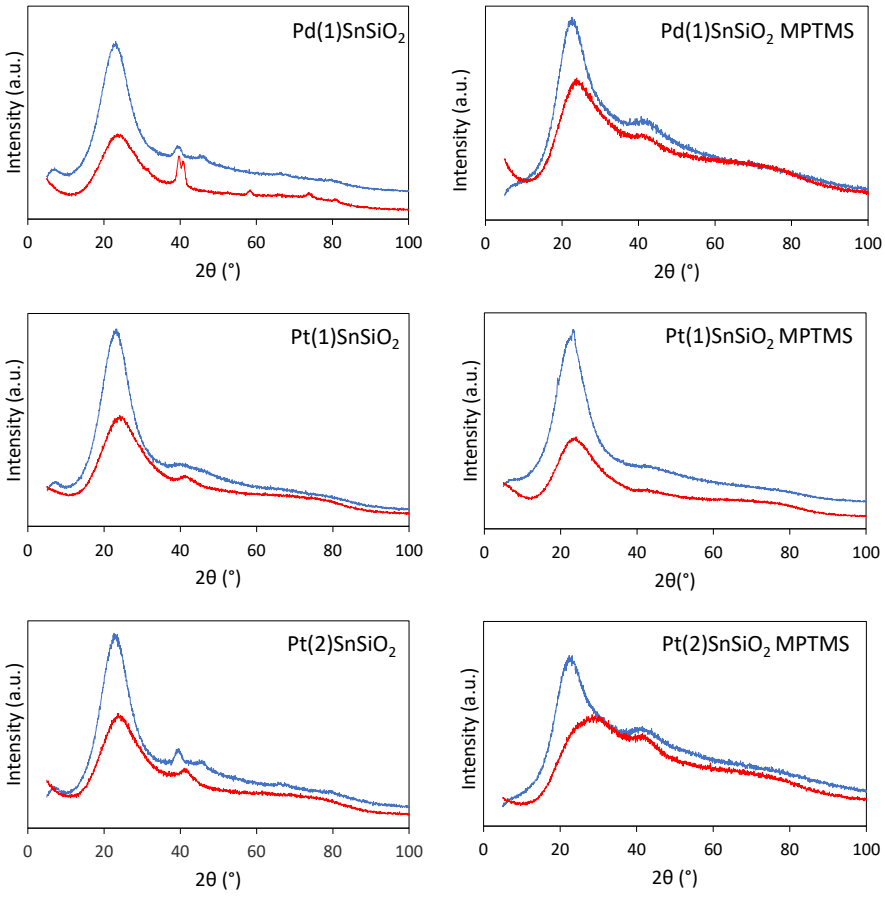

Figure 4.2. X-ray diffractogram of the different PtSn and PdSn catalysts with and without MPTMS. The blue curve corresponds to the fresh catalyst and the red curve to the calcined material.

XANES and EXAFS analyses were performed to better understand the XRD results and to get selective information about the Pd and Pt environment. Each calcined sample was therefore tested and compared to a Pd and Pt foil as a reference.

The normalized XANES spectra of the Pd-based samples and a Pd reference foil are displayed in Figure 4.3 A. The distinct XANES spectra of the **Pd(1)SnSiO$_2$** sample compared to the Pd reference foil suggested that the Pd environment differed from that of bulk Pd, with very reduced contributions from

Pd-Pd distances. Furthermore, notable differences were observed between the XANES spectra and EXAFS functions (Figure 4.3 B) of this sample and the Pd reference indicating variations in their respective Pd environments. It should be noted that the Sn-K-edge (See ANNEX 3) of **Pd(1)SnSiO$_2$** also exhibited a different behavior when compared to the other samples. There might be several contributions to take into account to explain these results, but it seemed reasonable to attribute the differences between the sample and the reference foil as due to the nanoparticles interacting with the Sn atoms. According to Chen *et al.*, the formation of the Pd_3Sn_2 intermetallic phase resulted in a shift of the XANES curve towards lower energy, which aligns with the results obtained with **Pd(1)SnSiO$_2$** and its corresponding X-ray diffractogram.[318]

Figure 4.4 shows the XANES and EXAFS analysis of the calcined Pt-Sn bifunctional catalysts and a Pt reference foil. As it was observed for Pd, the sample, XANES spectra are very different from the Pt reference foil, suggesting that the Pt environment in the samples were different to that of bulk Pt, with reduced contribution from Pt-Pt distances. In the work of Uemura *et al*, they mention the complexity to identify and separate Pt_3Sn_2 and PtSn and find a correct fitting with these intermetallics.[320] When comparing their results to the ones obtained in this work, the samples without MPTMS could correspond to a slightly oxidized PtSn phase.

To conclude, the XANES and EXAFS results gave more insight on the environment of the Pd and Pt atoms, and more particularly on the fact that the Pt-Pt and Pd-Pd contributions were very reduced, attesting the absence or the low amount of pure metallic nanoparticles formed – which confirmed the XRD results. It is reasonable to say that in the absence of MPTMS, intermetallic compound – Pd_3Sn_2 and PtSn – were formed

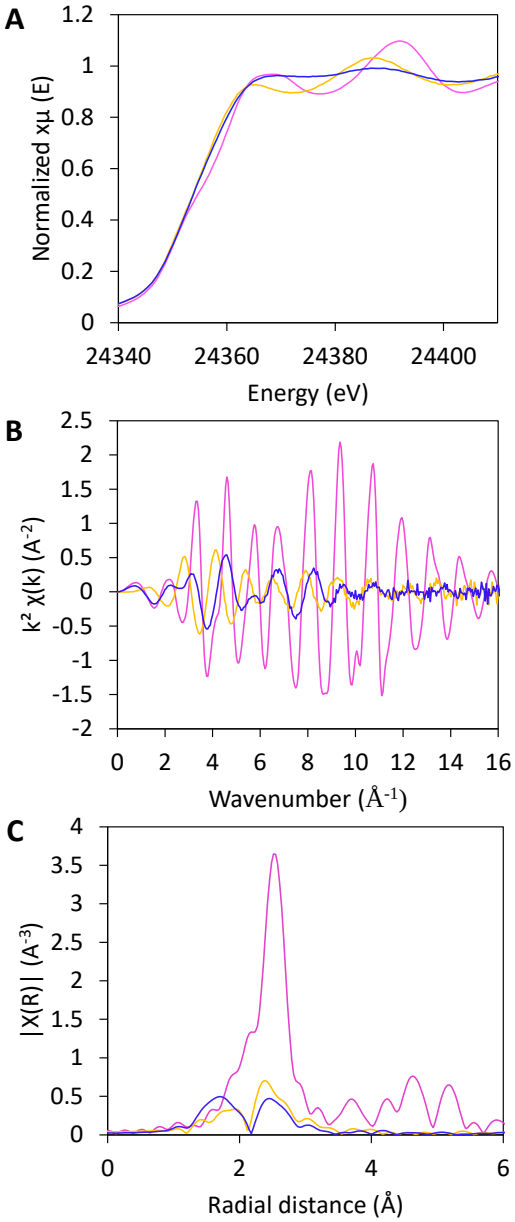

Figure 4.3. (A) normalized X-ray absorption near edge structure (XANES) spectra of Pd K edge, (B) k2χ(k) EXAFS interference functions and (C) corresponding FTs moduli (phase shift corrected) of Pd foil (pink curves) **Pd(1)SnSiO$_2$** (●) and **Pd(1)SnSiO$_2$ MPTMS** (●).

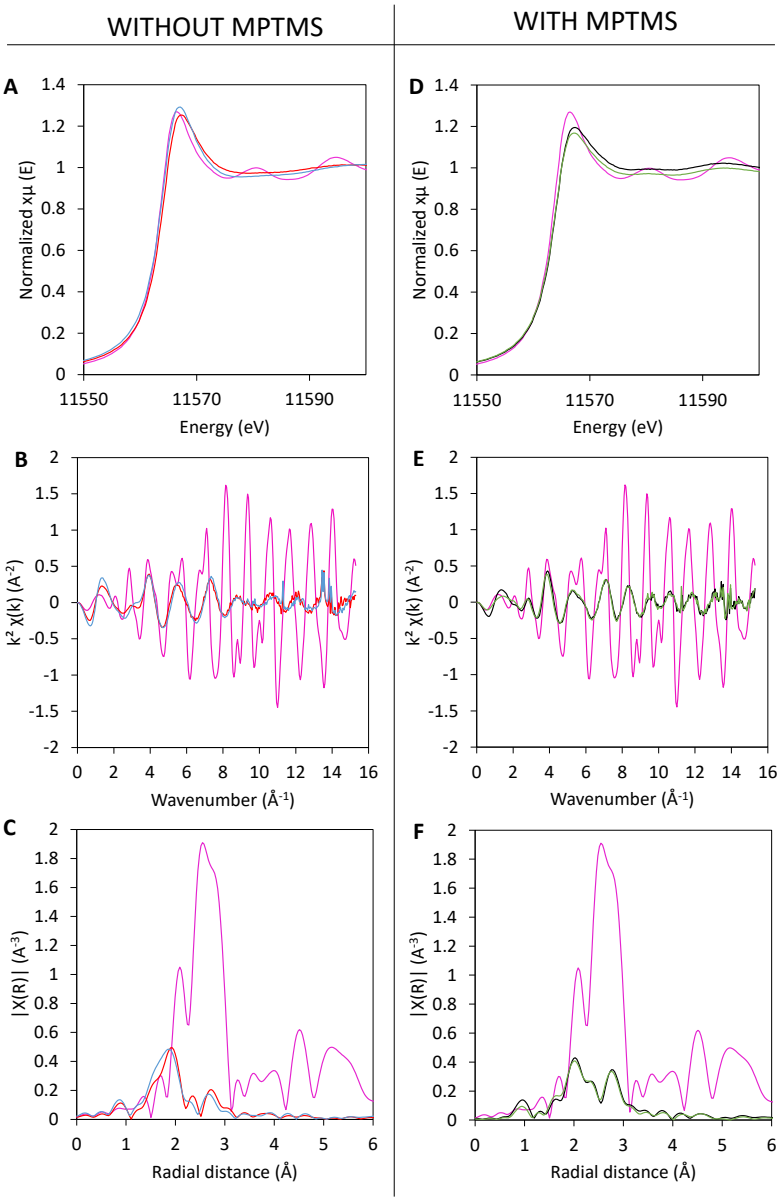

Figure 4.4. (A,D) normalized X-ray absorption near edge structure (XANES) spectra of Pt L_3 edge, (B,E) k2χ(k) EXAFS interference functions and (C,F) corresponding FTs moduli (phase shift corrected) of Pt foil (●), **Pt(1)SnSiO$_2$** (●), **Pt(1)SnSiO$_2$ MPTMS** (●), **Pt(2)SnSiO$_2$** (●) and **Pt(2)SnSiO$_2$ MPTMS (●).**

Following these results, XPS analysis were performed to study the surface composition, but also the chemical state of the different elements. (Figure 4.5, Table 4.3). The Sn3d, Pd3d and Pt4f regions were studied and the quantification was performed on their corresponding $Sn3d_{5/2}$, $Pd3d_{5/2}$ and $Pt4f_{7/2}$ peaks.

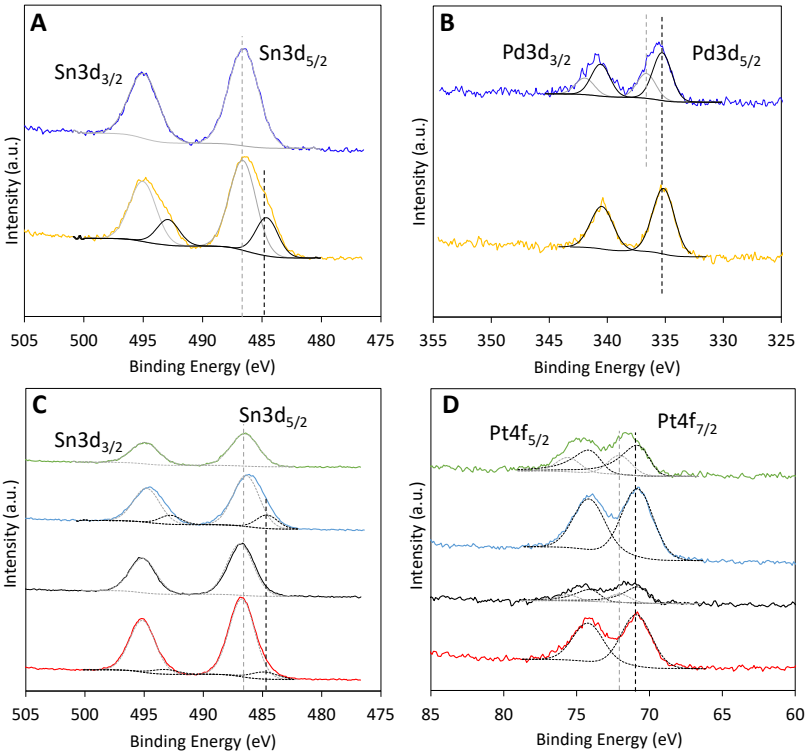

Figure 4.5. XPS spectra of the (A) the Sn3d region and (B) the Pd3d region of **Pd(1)SnSiO$_2$** (●) and **Pd(1)SnSiO$_2$ MPTMS** (●); and XPS spectra of (C) the Sn3d region and (D) the Pt4f region of **Pt(1)SnSiO$_2$** (●), **Pt(1)SnSiO$_2$ MPTMS** (●), **Pt(2)SnSiO$_2$** (●) and **Pt(2)SnSiO$_2$ MPTMS** (●). For all the different metals, the black dotted curves and lines are the deconvolution and theoretical value of metallic compounds while the grey dotted curves and lines stand for their corresponding oxides.

The Sn3d region of all the catalysts without MPTMS showed the same trend (i.e. an enlargement of the $Sn3d_{5/2}$) caused by the presence of two types of Sn – one metallic (BE ~ 485 eV) and one oxide (BE ~ 486.6 eV) – that were visible in Figure 4.5 A, C. While the component of oxidized Sn was attributed

to tin in Sn^{4+} state, hence incorporated in the silica framework, the presence of metallic tin was ascribed to the formation of Pd-Sn / Pt-Sn nanoparticles. It is noteworthy to mention that in the case of Pt-based materials, the metallic component of tin is limited. These results, aligned with the XRD and EXAFS analysis, confirm that when MPTMS is absent of the aerosol synthesis, the noble metal (Pd or Pt) formed intermetallic particles with Sn. These results are also consistent with reports found in the literature for PtSn and Pd_3Sn_2 species.[318,319,321–323] The Pd3d and Pt4f regions in these samples were only found in their metallic states (BE = 335.4 eV for Pd and BE = 71.1 eV for Pt) (Figure 4.5 B, D). The composition of the surface was calculated (Table 4.1) and reached a surface content of Pt and Pd close to the targeted loadings. For tin, the experimental surface ratio Si/Sn of **Pd(1)SnSiO$_2$** was also close to the nominal ratio. However, this ratio was highly reduced for the Pt-based materials. This meant that the amount of tin at the surface was higher in these catalysts. This result was attributed to the formation of the intermetallic compounds, leading to an inhomogeneous distribution of the Sn in the microspheres, with a higher amount at their surface.

Considering the XRD, EXAFS and XPS analysis, we have now a better insight on the nanoparticle's nature. While the **Pd(1)SnSiO$_2$** shows the presence of a Pd_3Sn_2 intermetallic phase, for the Pt(1) and **Pt(2)SnSiO$_2$**, the PtSn phase was formed

Phase identification of Pd- and Pt-SnSiO$_2$ bifunctional systems synthesized with MPTMS

The samples containing-MPTMS showed the same trend in their XRD results as it was observed for the monometallic samples (see Chapter 2, section 2.3.2) with almost no peaks visible in the fresh or the calcined materials (Figure 4.2). It is unclear if the small broad peak observed at 2θ ~ 40° in the fresh samples **Pd(1)SnSiO$_2$ MPTMS** and **Pt(2)SnSiO$_2$ MPTMS** corresponded to nanoparticles formed in these materials. After calcination, the same broad peak was observable in both samples, with no significant change in their positions or shapes. However, it was uncertain if they could be attributed to the metallic Pd or Pt, in the absence of other distinctive peaks. They may potentially correspond to the primary peak of the intermetallic compounds PdSn or PtSn, but with no evident certitude.[317,324] PdO might also be a suitable fit.[325] Overall, the X-ray diffractograms of the MPTMS containing samples did not give enough information to precisely determine the nanoparticle's nature. However, the nanoparticles formed were very small and highly dispersed, to the point that their size could not be measured.

XANES and EXAFS analysis were also performed on these samples (Figure 4.3 and Figure 4.4). When comparing the samples synthetized without MPTMS to the ones with MPTMS, differences among the samples were also noticeable indicating variations in their respective Pd and Pt environments. Since no evidence of Sn-Pd distances were evidenced at the Sn K-edge for **Pd(1)SnSiO$_2$ MPTMS** (See ANNEX 3), we considered that the formation of Pd-Sn intermetallic compounds was limited in this sample. Similar XANES spectra with peaks at slightly higher energy were found in the literature and were assigned to the formation of PdO species (Figure 4.3).[326–328] When considering the aforementioned results and the XRD, it became evident that the addition of MPTMS during synthesis hindered the formation of intermetallic Pd_3Sn_2 nanoparticles. Instead, it promotes the creation of significantly smaller nanoparticles, which could either be PdO nanoparticles or metallic Pd nanoparticles with PdO species at their surface.

For the Pt-based catalysts, unfortunately, no clear identification was found in the presence of MPTMS (Figure 4.4). More interestingly, the difference between the samples without and with MPTMS were also highlighted, with noticeable differences in the interactions of the metal atoms with Sn. Regarding the results observed for Pt-based materials explained above, and comparing them to the MPTMS-based materials, we believe that different phases might be coexisting. Since no evidence of Sn-Pt distances were demonstrated at the Sn K-edge (See ANNEX 3: Sn-K Edge XANES and EXAFS analyses) for any of the Pt containing samples, it is possible that only a very limited amount of Sn atoms interacts with Pt as the Sn atoms are in excess. Further analysis by EXAFS would be needed to get quantitative information, which can be done by fitting the data with suitable models.

Regarding the XPS analysis of the samples in which MPTMS was added during the aerosol synthesis, a completely different tendency was observed than for the MPTMS free catalysts (Figure 4.5). The Sn3d peak only exhibited one component – the one of Sn^{4+} – suggesting that in these samples, the tin was successfully and entirely incorporated in the silica framework (Figure 4.5 A, C). On the other hand, Pd and Pt were mainly found in their metallic state, but their respective peaks were also shifted, suggesting the presence of another chemical state (Figure 4.5 B, D). For the **Pd(1)SnSiO$_2$ MPTMS** catalyst, the other component was found at 336.4 eV, which corresponded to oxidized Pd. It is possible that in this sample, the Pd nanoparticles were partially oxidized, as it was previously hypothesized with the EXAFS and XRD results. Similar results were obtained for **Pt(1)SnSiO$_2$ MPTMS** and **Pt(2)SnSiO$_2$ MPTMS**, with the contribution of the PtO ~72 eV.[329] The quantification of the different metal at the surface showed that Pd and Pt experimental loadings were reduced when working with MPTMS (Table 4.1). Such results were already observed when working with gold. The Si/Sn ratio

in **Pd(1)SnSiO$_2$ MPTMS** reached a value close to the targeted one. However, this ratio in the Pt-catalysts was reduced.

Considering the XRD, EXAFS and XPS analysis, we concluded that the samples synthesized in the presence of MPTMS had low interactions between Pd or Pt and Sn, but rather formed metallic nanoparticles partially oxidized.

Acidity assessment

The sample's acidity, normally brought by the successful incorporation of tin in the silica as intra-framework Sn^{IV}, was evaluated through pyridine adsorption and FTIR spectroscopy. A standard **SnSiO$_2$** sample (Si/Sn = 74) synthesized by aerosol was also analyzed to have a better comparison with the bifunctional materials (Figure 4.6). The presence of a band at 1455 cm^{-1} in the spectra indicates the successful integration of Lewis acid sites, and consequently, tin active sites, in the samples. No Brønsted acidity was detected in any of the materials (no peaks found at 1545 cm^{-1}).

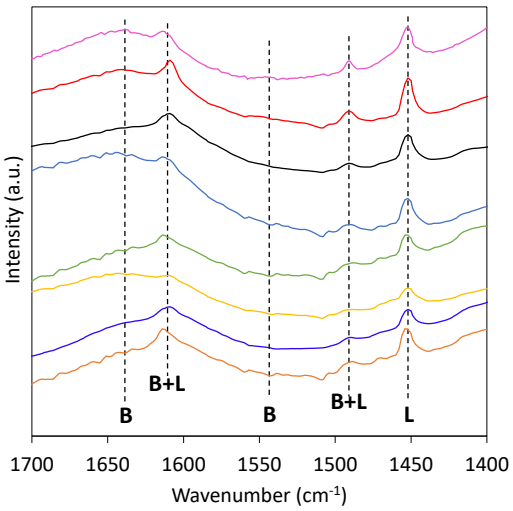

Figure 4.6. FTIR spectra after pyridine desorption at 150 °C for 2 hours of **SnSiO$_2$** (●), **Pt(1)SnSiO$_2$** (●), **Pt(1)SnSiO$_2$ MPTMS** (●), **Pt(2)SnSiO$_2$** (●) and **Pt(2)SnSiO$_2$ MPTMS** (●); and (B) Pd catalysts: **Pd(1)SnSiO$_2$** (●) and **Pd(1)SnSiO$_2$ MPTMS** (●); and **AuPdSnSiO2 MPTMS** (●). B = band corresponding to Brønsted acid sites; L = band corresponding to Lewis acid sites.

The amount of Lewis acid sites was calculated in the different materials based on the area of the band at 1455 cm^{-1} in the FTIR spectra corresponding to the amount of pyridine still adsorbed at the surface of the pellets after a desorption at 150°C (Table 4.3). **$SnSiO_2$**, as mentioned in Chapter 3, exhibited a surface density of Lewis acid sites of 36 $\mu mol.g^{-1}$. Surprisingly, in almost all the bifunctional materials, this value was reduced. In the Pd-Sn based catalysts, a significant reduction of approximately 42% of the amount of Lewis acid sites was observed, with almost no difference whether the sample contained MPTMS or not. For the Pt-Sn samples, a clear difference was observable when the samples contained MPTMS or not. In the absence of MPTMS, the surface density of Lewis acid sites was reduced when compared to **$SnSiO_2$**. On the other hand, the values calculated for **Pt(1)$SnSiO_2$ MPTMS** and **Pt(2)$SnSiO_2$** remained very close to our reference, implying that in these materials, the Sn was successfully incorporated in the framework rather than forming an intermetallic compound with the platinum in these materials.

These results were actually correlated with the results obtained by EXAFS and XPS analysis. Indeed, without MPTMS, the formation of the bimetallic compounds led to a reduction of the Sn responsible for the Lewis acid sites while when MPTMS was added to the synthesis process, the intermetallic formation was prevented and the tin was fully incorporated as part of the silica framework. The only sample that did not follow this trend is **Pd(1)$SnSiO_2$ MPTMS**. It was possible that the very small Pd NPs hindered the access of tin sites, reducing their accessibility.

Table 4.3. Lewis acidity measured via the FTIR spectra after pyridine desorption at 150°C.

Samples	Lewis acidity ($\mu mol.g^{-1}$)
$SnSiO_2$	36.0
Pd(1)$SnSiO_2$	21.2
Pd(1)$SnSiO_2$ MPTMS	20.8
Pt(1)$SnSiO_2$	29.4
Pt(1)$SnSiO_2$ MPTMS	37.9
Pt(2)$SnSiO_2$	23.2
Pt(2)$SnSiO_2$ MPTMS	29.5
AuPd$SnSiO_2$ MPTMS	33.2

Samples morphology

Transmission electron microscopy was used to have a better idea of the morphology and structure of the different catalysts (Figure 4.7). Image of the samples containing 1 wt.% of Pt could not be measured, but we strongly believe that their morphology should be close to the one of the 2 wt.%. All the materials consisted of the characteristic microspheres usually obtained with the aerosol-assisted sol-gel process (as it was already demonstrated in the previous chapters). The interconnected porosity, resulting from the removal of Pluronic F127 (i.e. the templating agent used in the synthesis) was observable in each sample.

The nanoparticles were observable for the samples synthesized without MPTMS – **Pd(1)SnSiO$_2$** and **Pt(2)SnSiO$_2$** – with a mean size of 6.5 and 3 nm respectively, which was consistent with the XRD results. As for the samples that were synthesized in the presence of MPTMS, the nanoparticles were very hard to observed. Some were found at the surface microsphere (as pointed with the red arrows in the pictures). In **Pd(1)SnSiO$_2$ MPTMS**, very small nanoparticles were observed (Figure 4.8, left image) with a diameter below 2 nm, confirming their formation, and the XRD results. We expect similar results for **Pt(2)SnSiO$_2$ MPTMS** but we could not manage to observe them during analysis.

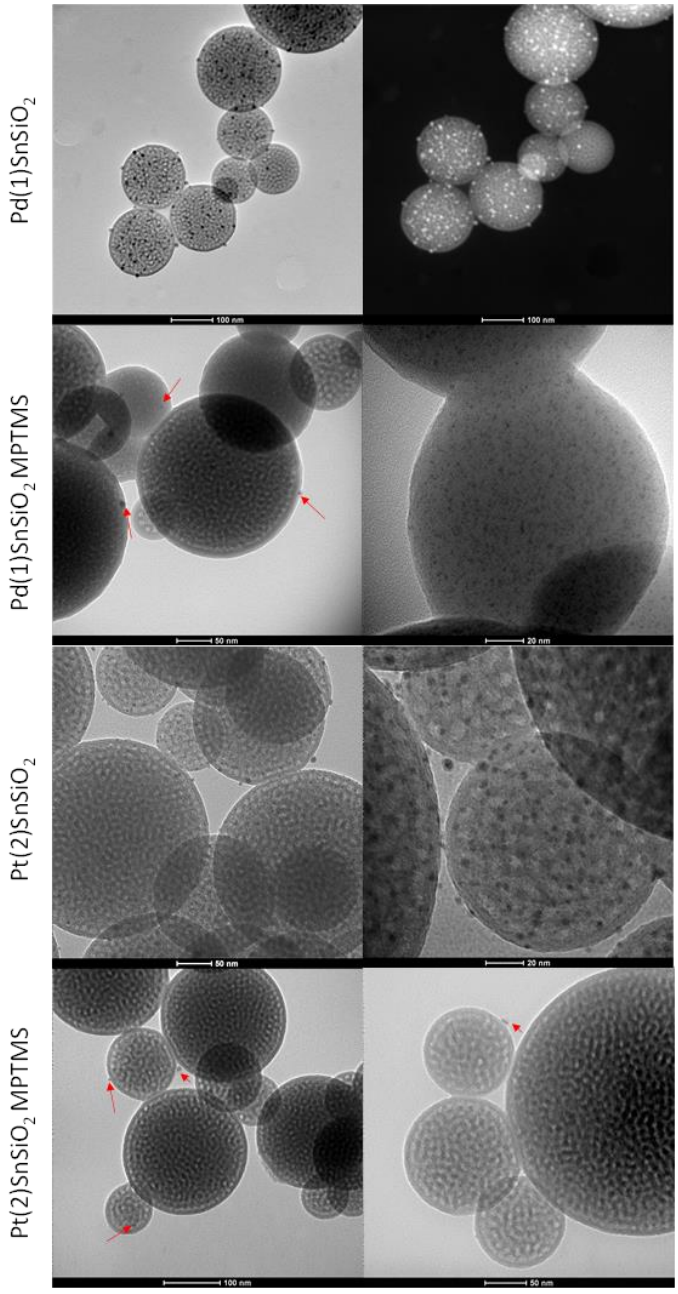

Figure 4.7. Transmission electron microscopy analysis of the different bifunctional materials and HAADF (top right picture) (measure with a Philips Tecnai 20). Nanoparticles are showed with red arrows.

4.3.2. AuPdSnSiO_2 system

Tang *et al* reported excellent catalytic performance in the cascade reaction when working with supported AuPd bimetallic nanoparticles and Sn-MCM-41-XS (see in the introduction, section 3.2. Mechanical mixture for the cascade reaction).[197] Based on these results, we decided to further complexify our material, with the idea to combine Au-Pd intermetallic nanoparticles as the active site for the reaction 1 and Sn-SiO_2 mixed oxide for the reaction 2. Such material was synthesized in one-pot, still using the AASG process. The two noble metal precursors (for Au and Pd) were added in the synthesis to reach a total metal loading of 1 wt.% (Au/Pd ratio 1:1), along with the Sn precursor (Si/Sn = 74). The resulting mixture was processed, dried and calcined under the same conditions as the other materials. Considering the challenge of stabilizing gold during synthesis (see Chapter 2), this material was only synthesized with the addition of MPTMS in the synthesis.

The elemental composition of this material could not be determined by ICP. However, based on the consistently successful incorporation of the various metals using the aerosol-assisted sol-gel process (as the many results presented in this work demonstrated), we anticipated that the experimental loading of Au, Pd, and Sn would be very close to the targeted loading.

The textural properties of this samples remained very close to the one of the other bifunctional materials (Figure 4.8 A, Table 4.2), demonstrating that the addition of a third metal in the synthesis did not impact the texture of this material. The XRD pattern of the fresh sample showed no peak, except for the broad peak of amorphous silica. When calcined, a small broad peak around $2\theta \sim 40°$ is visible, which could correspond to (111) facet of Au-Pd (Figure 4.8 B).[330] However, the absence of the other characteristic peaks made the identification rather difficult, and it could also be the diffraction of isolated Au and Pd nanoparticles. The observed X-ray diffractogram was actually very close to the one observed for Pd(1)SnSiO_2 MPTMS, so it is expected that the formation of very small nanoparticles highly dispersed in the microspheres as it was the case of this sample.

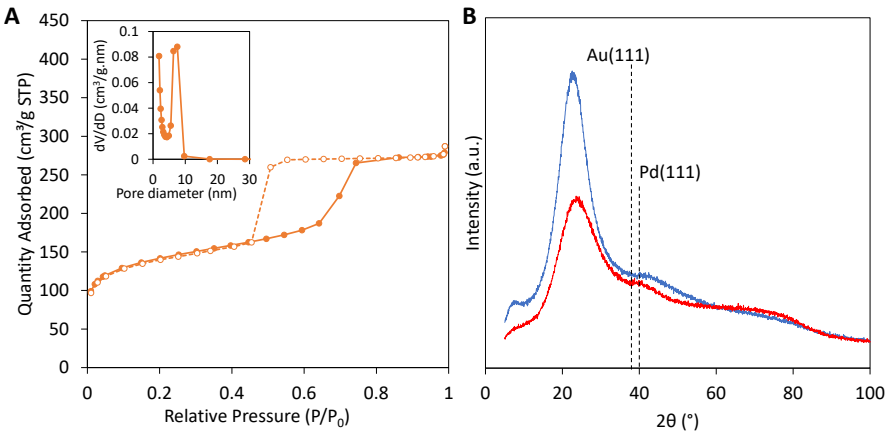

Figure 4.8. (A) Nitrogen adsorption (plain symbols) and desorption (empty symbols) isotherms of **$AuPdSnSiO_2$ MPTMS;** in inserts show BJH pore size distribution analysis obtained from the adsorption isotherms. X-ray diffractogram of fresh (blue curve) and calcined (red curve) **$AuPdSnSiO_2$ MPTMS.**

XPS analysis were performed to study the surface composition of **$AuPdSnSiO_2$ MPTMS.** The gold spectra exhibited two peaks at 83.7 and 87.4 eV corresponding to the $Au4f_{7/2}$ and $Au4f_{5/2}$ which corresponded to Au^0 oxidation state (Figure 4.9 A). Palladium was also detected in its metallic state, with the peaks $Pd3d_{5/2}$ and $Pd3d_{3/2}$ found at 335.5 and 340.8 eV (Figure 4.9 B). The presence of tin was observed solely in the Sn4+ chemical state (BE ~ 487 eV), confirming its incorporation in the silica framework (Figure 4.9 C). The small shift toward lower binding energy observed for gold might result from alloy formation.[197] However, it is difficult to conclude on the bimetallic character of the nanoparticles (or if they are present as isolated Au and Pd nanoparticles) due to the binding energy of Pd that was found precisely at the value of Pd^0 state. Interestingly, the addition gold in the aerosol synthesis seemed to prevent the presence of PdO species when compared to the **$Pd(1)SnSiO_2$ MPTMS** sample. The content of palladium and gold at the surface was estimated at 0.46 wt.% and 0.24 wt. respectively. While the value for Pd was very close to the nominal loading (0.5 wt.%), the one of gold was slightly decreased (0.5 wt.% targeted), attesting for a heterogeneous distribution of the gold compared to palladium in the microspheres. The Si/Sn atomic ratio at the surface reached 70 which was very close to the targeted ratio (Si/Sn = 74).

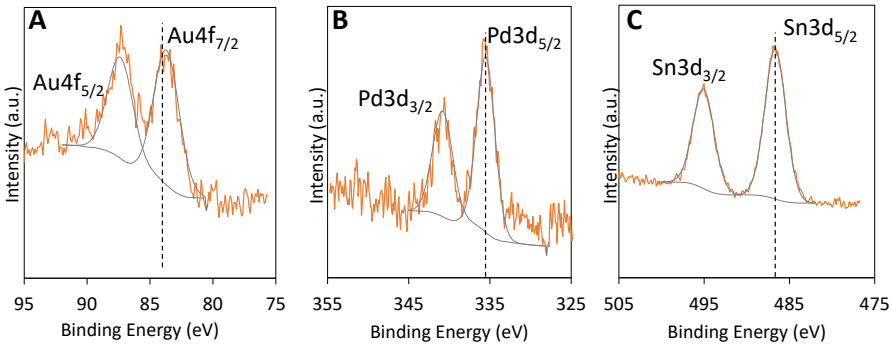

Figure 4.9. XPS spectra of the different region (A) Au4f, (B) Pd3d and (C)Sn3d of **$AuPdSnSiO_2$ MPTMS**. The theoretical binding energy of Au^0, Pd^0 and Sn^{4+} oxidation states are shown in with the black dotted lines.

In this material, the density of Lewis acid sites reached 33.2 µmol.g^{-1}, which was very close to the **$SnSiO_2$** value (Table.4.3, Figure 4.6). Combined with the XPS results, this strongly confirmed that all the tin was incorporated in the silica framework, bringing the Lewis acidity necessary for the second step of the cascade reaction. This also confirmed that the tin did not interact with any of the metal.

The morphology of the sample was analyzed by TEM (Figure 4.10). The structure of **$AuPdSnSiO_2$ MPTMS** was very similar to the one of the other bifunctional materials, consisting of well-defined microspheres with interconnected pores. Nanoparticles were observed at the surface of the microspheres with diameter of around 3.5 nm. However, considering the XRD results, we believe that smaller nanoparticles could also be found in the material (like it was observed for **Pd(1)$SnSiO_2$ MPTMS**).

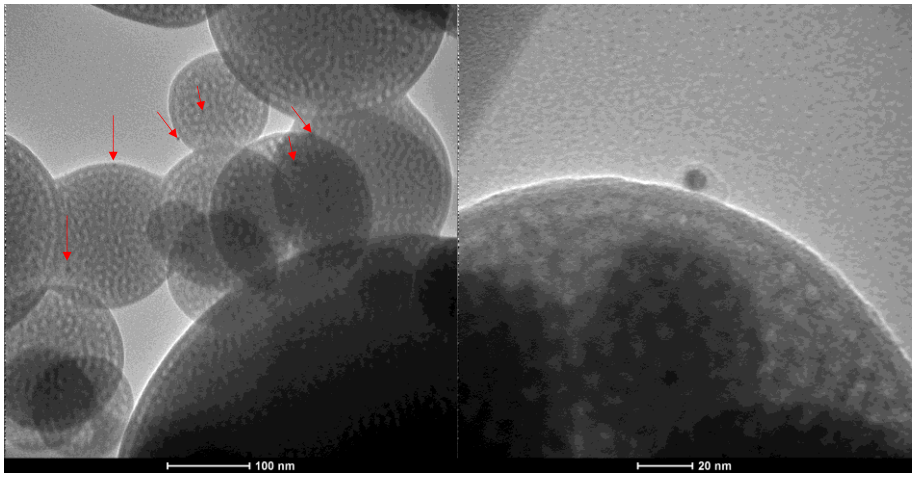

Figure 4.10. Transmission electron microscopy analysis of **AuPdSnSiO$_2$ MPTMS** (measured with a Philips Tecnai 20 microscope). Nanoparticles are showed with red arrows.

4.3.3. Catalytic test

The different materials were tested in the catalytic upgrading of glycerol to methyl lactate. The catalytic performances of the bifunctional catalysts were first compared after 2 hours to target the initial rate of the reaction Figure 4.11, top) and after 6 hours (Figure 4.11, bottom).

The Pd-based catalysts showed almost no difference of catalytic performance whether the sample contained MPTMS or not, and between 2 and 6 hours. Additionally, the conversion and yield toward ML were not improved when compared to the results obtained for the monometallic PdSiO$_2$ and **PdSiO$_2$ MPTMS** (Figure 2.17). Such observations were mainly attributed to the reduced amount of Lewis acid sites in these materials (Table 4.3), but also the presence of rather large Pt_3Sn_2 nanoparticles in **Pd(1)SnSiO$_2$** (ø = 7.7nm) and the presence of PdO in **Pd(1)SnSiO$_2$ MPTMS**.

When comparing the PtSn catalysts without MPTMS, the Pt(1)SnSiO$_2$ displayed very poor conversion, even after 6 hours of reaction. Increasing the amount of platinum in the sample to 2 wt.% highly improved the catalytic performance, reaching a glycerol conversion of 44% and a ML yield of 34% after 2 hours, increasing to 68% and 60% after 6 hours.

In the presence of MPTMS, **Pt(1)SnSiO$_2$ MPTMS** exhibited the best catalytic performance after 2 hours and good performance after 6 hours. Very good catalytic results were also obtained with **Pt(2)SnSiO$_2$ MPTMS** after 6 hours. However, increasing the amount of Pt in these materials did not improved the glycerol conversion and even impaired the ML yield. Such results were also observed for gold with a decrease of the selectivity and therefore the yield when the gold loading was higher, mostly due to higher overoxidation rate on the noble metal.

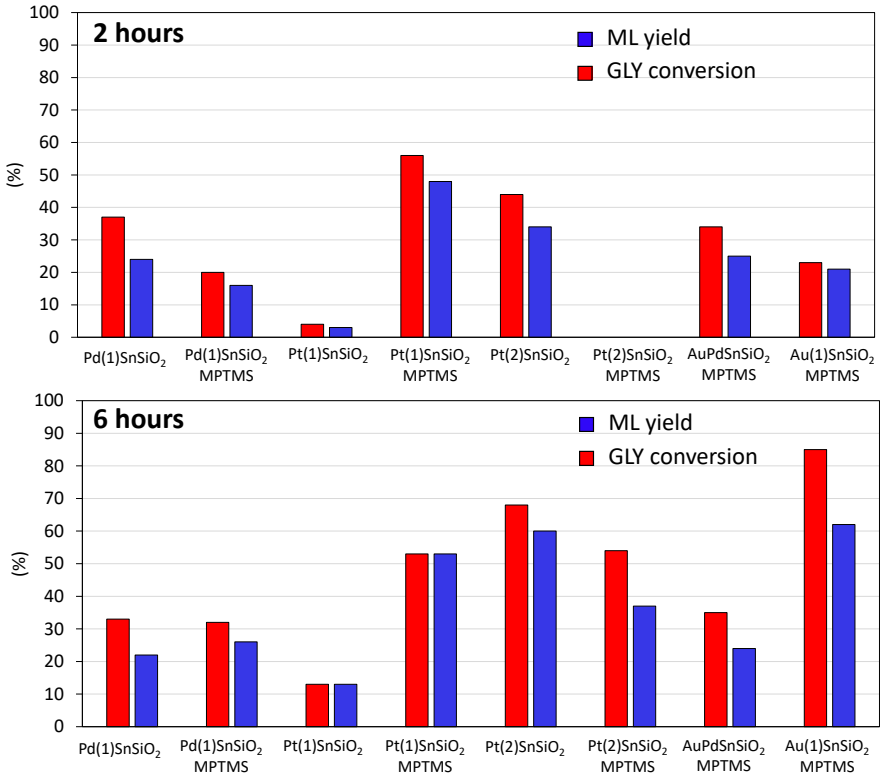

Figure 4.11. Catalytic performance of the different materials synthesized in this chapter. The data of Au(1)SnSiO$_2$ (MPTMS) were added to have a comparison. Reaction conditions: T = 160°C, pair = 15 bar, 0.125 M glycerol in methanol, and GLY/Catalyst ratio = 1.15 (w/w). Each measure has an error of ± 5%.

From a selectivity point of view, **Pt(1)SnSiO$_2$ MPTMS** and **Pt(2)SnSiO$_2$** were also the best catalysts with a selectivity > 85% and > 75% respectively. It is unclear why these two catalysts showed the best performance. Indeed,

these results cannot be related to the amount of Lewis acid sites (37.9 µmol.g^{-1} for **Pt(1)SnSiO$_2$ MPTMS** and 23.2 µmol.g^{-1} for **Pt(2)SnSiO$_2$**), the amount of Pt (1 and 2 wt.%); the nanoparticle's nature (Pt/Pt-O and PtSn) or their size. It is believed that it is a combination and a good balance of these different parameters that brought the better catalytic performance. However, other tests should be performed to have a deep understanding of these catalytic systems and these results.

The **AuPdSnSiO$_2$ MPTMS** catalyst did not show a significant improvement of the catalytic performance after 2 hours when compared to **Pd(1)SnSiO$_2$ MPTMS** or Au(1)SnSiO$_2$-MPTMS. The catalyst after 6 hours even showed no increase of the glycerol conversion, most probably due to the fast deactivation of the catalyst.

Overall, the bifunctional catalysts developed in this chapter displayed better initial catalytic activity (after 2 hours) than the one of Au(1)SnSiO$_2$. However, after 6 hours, this latter exhibited the best catalytic performance, suggesting a better resistance toward deactivation.

4.4. Conclusion

Bifunctional materials combining gold-palladium, palladium or platinum and tin silicate microspheres were synthesized in one step leveraging on the aerosol-assisted sol-gel process. The impacts of adding of a stabilizer – MPTMS – in the synthesis was thoroughly investigated in the Pt- and Pd-based materials. All the catalysis exhibited advantageous textural properties with high surface area and large pore volume. Interestingly, the nature of the nanoparticles formed in the different materials was highly impacted by the presence of the stabilizer. In its absence, the noble metal was prone to form intermetallic compound with tin (Pd_3Sn_2 and PtSn), resulting in the partial reduction of the density of Lewis acid sites (initially brought by the successful incorporation of Sn in the silica framework). On the other hand, the formation of partially oxidized Pt and Pd metallic nanoparticles and the insertion of tin species in the silica framework generating abundant Lewis acid sites was favored when the materials were synthesized with the stabilizer. The nanoparticles in these catalysts were very small (Ø < 2 nm) and highly dispersed in the tin-silicate microspheres. Thus, we evidenced the role of MPTMS to maintain the intrinsic properties of the two catalytic sites and prevent them from interacting. We demonstrated that even in the presence of a third metal in the aerosol synthesis to obtain AuPdSnSiO$_2$ MPTMS, the intrinsic properties of each metal were preserved. The bimetallic nature of the

AuPd nanoparticles could not be confirmed or excluded. The resulting catalysts were all active in the glycerol transformation to methyl lactate. Pt(1)$SnSiO_2$ MPTMS and Pt(2)$SnSiO_2$ displayed excellent catalytic activity in the cascade reaction, with an increased selectivity to ML when compared to the Au(1)$SnSiO_2$ MPTMS presented in Chapter 3. However, further catalytic tests should be performed to better understand the origin of this catalytic boost. While the chapter 2 highlighted the importance of using a stabilizer to prevent the formation of large gold nanoparticles, this chapter emphasizes its potential to maintain the intrinsic properties of each metal when synthesizing bifunctional materials in one step by AASG process.

GENERAL CONCLUSION

In this thesis, the design of bifunctional catalysts via the aerosol-assisted sol-gel (AASG) process for the direct conversion of glycerol to methyl lactate was investigated. Specifically, the synthesis of materials combining noble metal nanoparticles supported on metallosilicates was targeted. However, challenges arose from working with noble metal nanoparticles and silica, especially considering the difficulty to stabilize the metal at the silica surface. This often results in sintering, especially at elevated temperatures, due to the nanoparticles' high mobility on the surface of the silica. Therefore, these challenges needed to be addressed first. In this thesis, the following observations, conclusions and findings were made:

(i) The synthesis of gold-silica catalysts using the (AASG) process is possible. Their synthesis can be achieved by two different routes: (1) a two steps procedure implying the addition of colloidal gold in the aerosol process, or (2) a one-pot procedure where the gold precursor is directly added to the aerosol synthesis. During the two steps synthesis, the preformed gold nanoparticles rapidly sinter during the aerosol processing to form large nanoparticles, buried in the silica microspheres and therefore not available or active in catalysis. In the one-pot route, the gold precursor is directly decomposed during synthesis and form even larger nanoparticles, poorly dispersed in the silica microspheres. The stabilization of the preformed gold nanoparticles and the gold precursor during the aerosol processing is the key to prevent the formation of large nanoparticles. The stabilizer, a thiol-functionalized silane (MPTMS), is selected for its ability to incorporate the silica framework upon polycondensation in the aerosol process. As a result, it also acts as an anchoring point to reduce the mobility of the gold nanoparticles at the silica surface upon thermal treatment. The resulting catalysts display small nanoparticles (~3 nm) with strong resistance against sintering, uniformly distributed within the silica microspheres. The size of the gold nanoparticles could even be controlled by modulating the calcination temperature of the catalyst. The availability of the gold nanoparticles, which is an important parameter to control (especially during one-pot synthesis) is successfully achieved in the presence of the MPTMS. The resulting catalysts are both active in the oxidation of glycerol to dihydroxyacetone (DHA) in methanol, with good selectivity, markedly outcompeting the benchmark catalyst prepared by deposition-precipitation. It is noteworthy to mention that such transformation was never reported in the literature and that the catalytic performance of our materials could not be compared.

(ii) The addition of another catalytic species in the one-pot aerosol synthesis to obtain an Au-$SnSiO_2$ bifunctional catalyst does not impact the controlled formation of the gold nanoparticles. Similarly, the insertion of tin in the silica framework, generating Lewis acid sites, is not impaired by the presence of gold or MPTMS in the synthesis. The gold loading does not impact the physicochemical properties of the catalysts or the gold nanoparticles size. The bifunctional materials are highly active in the cascade transformation of glycerol to methyl lactate, with an optimum at 1wt.% of gold. The presence of the two catalytic sites on one unique solid further enhances the catalytic performance by efficiently directing the intermediate product (DHA) to the subsequent reaction to form methyl lactate. In fact, the yield toward methyl lactate significantly exceeds the yield of DHA observed when conducting only the first reaction. Importantly, higher selectivity and yield are observed for the bifunctional material, when compared with a corresponding mechanical mixture. This emphasizes the role of site proximity in bifunctional catalysts to efficiently run a cascade reaction.

(iii) The nature of the nanoparticles formed can be controlled by adjusting the formulations of the aerosol solution. The ability of palladium and platinum to form intermetallic compound with tin in the bifunctional catalysts is observed, leading to a loss of catalytically active species – as the reduction of the Lewis acid sites. The use of a stabilizer (MPTMS), as an anchoring point, actually prevents the two metals to interact and allow to main their intrinsic properties. In its presence, the active species are preserved. Even in the presence of a third metal in the one-pot aerosol process, no interactions between the metals is demonstrated. The different materials are catalytically active in the cascade reaction and are highly selectivity to methyl lactate.

(iv) Overall, the results obtained in this thesis dissertation are considered as valuable in the field of supported metal nanoparticles synthesis. The one-pot synthesis strategy developed using MPTMS has already demonstrated its effectiveness, not only with noble metals (Au, Pd and Pt) but also with non-noble metals (Ni, Cu, Co). Finally, the control over the nanoparticle's nature (monometallic, intermetallic), is also demonstrated, leveraging on the segregation of the metal by the use of the stabilizer. In this regard, the aerosol-assisted sol-gel technique stands out as a crucial technology that significantly simplifies the synthesis of such materials.

FUTURE WORK

A new one-pot synthesis route for stabilized silica-supported metal nanoparticles (*via* the use of MPTMS) and bifunctional materials has been developed in this work. Yet, some improvement could be provided at different levels in order to further improve the developed systems. The following section outlines both the potential opportunities and the challenges ahead.

Regarding the synthesis route developed for the first step of the cascade reaction, we showed that Au was achieving better catalytic performance than Pd or Pt (*Chapter 2*). To further improve the catalytic activity of these latter, we suggest introducing a dopant (such as Bi for example) to form an alloy with the noble metal nanoparticles. It was indeed reported that doping Pd and Pt nanoparticles by introducing π-electron donator could increase the DHA selectivity. The loading and nature of the dopant should be studied and optimized. This way, the use of precious metal – and their environmental impacts – could be reduced. Similarly, more in depth investigations on the possible formation of bimetallic nanoparticles with and without MPTMS should be performed and potentially extended to other formulations (Au-Pt, Pd-Ag, etc) on silica. The use of less expensive metals could also contribute to a significant reduction in the catalyst preparation expenses. While adding a second metal in the AASG process has already been widely reported, the control on the formation of the alloy or bimetallic nanoparticles during the aerosol process should first be studied to determine the feasibility and optimal synthesis conditions.

Although the catalytic transformation of glycerol to methyl lactate was successfully demonstrated, the catalytic performance could be improved to reach higher methyl lactate yield. Based on preliminary results, we emphasized that glycerol is mainly reacting with the gold nanoparticles located at the surface of the silica microspheres. First, the hypothesis that our systems suffer from diffusion limitations should be elucidated. One could use different templating agents (such as polymer beads, Brij-58) in the aerosol synthesis to form smaller or larger pores in the final material. Then, by performing the cascade reaction and studying the relation between the activity and the pores size, one could find the optimum synthesis parameter to maximize the methyl lactate yield. This way, the issue of gold nanoparticles availability, especially for the glycerol oxidation, could be resolved.

Concerning the synthesis of bimetallic compounds, one should compare the results obtained in Chapter 4 with benchmark catalysts prepared by a traditional method (impregnation of Pt or Pd onto an aerosol Sn-SiO_2) where

the formation of intermetallic is avoided. The Sn:Pd and Sn:Pt should also be adjusted while maximizing the catalytic performance.

From a broader perspective, the synthesis route for silica-supported metal nanoparticles developed in this work could be highly valuable, not only for catalysis but also other applications (in drug delivery, solar cells for example). Similarly, the synthesis of bifunctional materials with tailored and controlled properties in one unique step is of great interest in the realm of greener chemistry, and the ease of scaling-up aerosol processes is very attractive from an industrial point of view.

ANNEX 1: TGA ANALYSIS

The TGA analyses were conducted with the valuable assistance and expertise of Jean-François Statsyns.

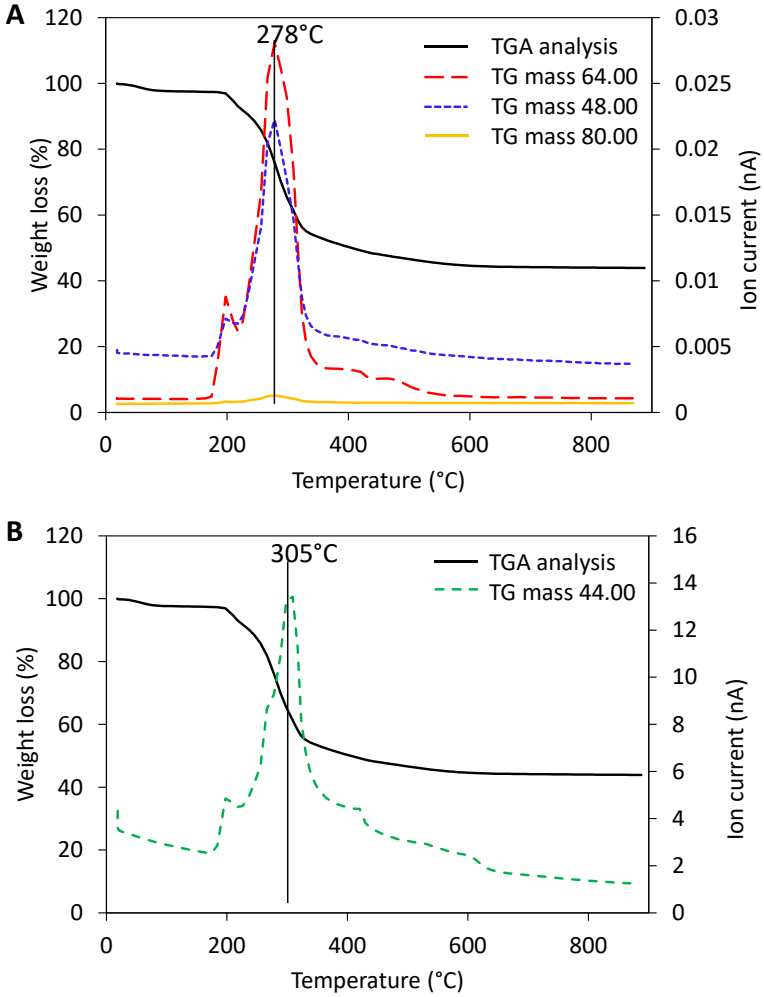

Figure A.1.1. TGA-MS analyses of fresh **AuSiO$_2$-MPTMS**. The decomposition of MPTMS is shown with the 80.00 (SO_3), 64.00 and 48.00 (SO_2) mass peaks (A) while the decomposition of the surfactant is attributed to the 44.00 (CO_2) mass peak (B). The decomposition of MPTMS happens few degrees before the decomposition of F127.

TGA analysis were also performed to make sure that the surfactant was successfully removed from the different materials synthesized in Chapter 4, even though the calcination was not performed under air. Two conditions were used to compare them: (i) calcination under air and (ii) calcination under H_2(5%)/Ar (Figure 4.1). It appeared that no matter the calcination conditions, similar mass losses are observed after 550°C (-52.5124 for the H_2/Ar *vs.* 53.024% under air), although the mass loss are not at the same temperature. Considering that we performed the calcination for 6 hours at 550°C, we estimated (and verified afterward) that the porosity was released either way.

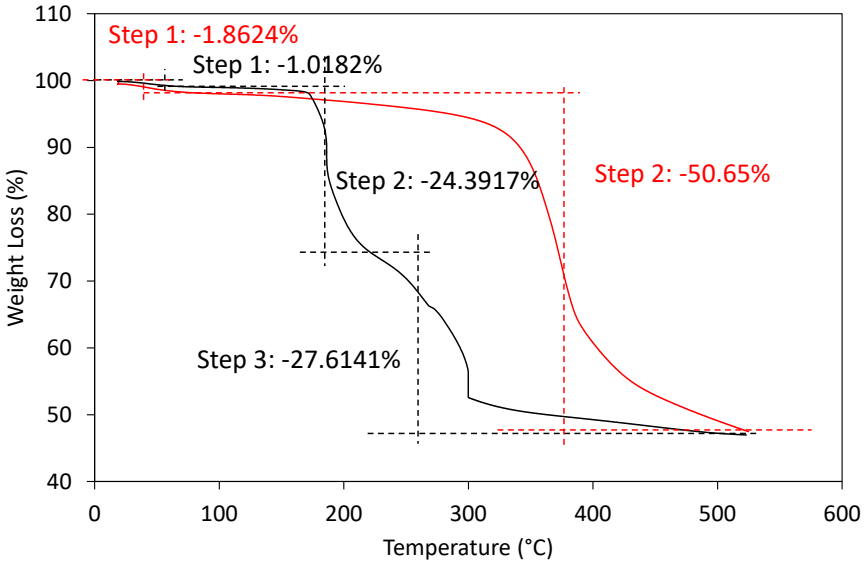

Figure A.1.2. TGA analyses of fresh **Pt(1)SnSiO$_2$ MPTMS**. The dark curve corresponds to the TGA performed under air while the red curve was performed under H_2(5%)/Ar.

ANNEX 2: THE MPTMS STRATEGY EXTENDED TO NON-NOBLE METALS

The results presented in this section were obtained during the master thesis of Sophie Coppens who investigated the potential of MPTMS-stabilization synthesis strategy with the AASG process (See Chapter 2)CHAPTER 2 on non-noble metals. Indeed, taking into consideration the scarcity and high cost of these metals,[331] the development of non-noble metals as substitute for noble metals are emerging in catalysis.[332] In this perspective, materials containing Ni, Cu, or Co nanoparticles on silica were investigated.

Experimental

The protocol used to synthesize the catalyst was already described in the Chapter 2 (2.2.1. Catalysts preparation; ***Synthesis by AASG***). The precursors added for the different metals (Co, Cu, and Ni) were respectively $Co(Cl_2).6H_2O$, $Cu(NO_3)_2.6H_2O$, or $Ni(NO_3)_2.6H_2O$) and were added to reach a nominal loading of 10 wt.%. The amount of MPTMS (and therefore of TEOS to keep a constant number of moles of Si) was adapted to have a molar ratio metal/MPTMS = 1 during the different synthesis. The calcination conditions were kept the same for each material (i.e. under static air, 550°C, $1°C.min^{-1}$). The materials were characterized by XRD, XPS and N_2-physisorption.

Results and discussion

Monometallic materials with a nominal loading of 10 wt.% of Co, Cu or Ni incorporated on a silica support were synthesized in one-pot leveraging on the AASG process. For each metal, two different samples were synthesized, without and with MPTMS. It is noteworthy to mention that the amount of MPTMS was adapted to reach a molar ratio MPTMS/Metal = 1. This way, each mole of metal is supposedly stabilized by one mole of thiol from MPTMS. Indeed, several tests were conducted to show that a molar ratio of MPTMS to Metal less than 1 had a negative impact on the effective stabilization of the metal, while a ratio equal to 1 proved sufficient for stabilizing the metal.

For each metal studied, the textural and structural properties of the catalysts was investigated with specific attention to the formation of metal nanoparticles (or metal oxide) depending on the presence/absence of MPTMS (3-mercaptopropyltrimethoxysilane). The metal catalysts were not tested in the glycerol oxidation – as they are known as inactive – but were successfully

tested in catalytic reactions (ethanol dehydrogenation and reforming, CO_2 methanation). Those results will however not be presented in this work.

The textural characteristics of the various materials remained quite similar to what was previously observed with pure silica, gold-silica, platinum-silica, and palladium-silica samples (Table A.2.1). The type IV isotherms, depicted in Figure A.2.1. A, showed the typical hysteresis of interconnected bottleneck pores. Each sample demonstrated a narrow pore size distribution (Figure A.2.1. B). Interestingly, the substantial metal content and the high amount of MPTMS in the material did not have a significant impact on the textural properties.

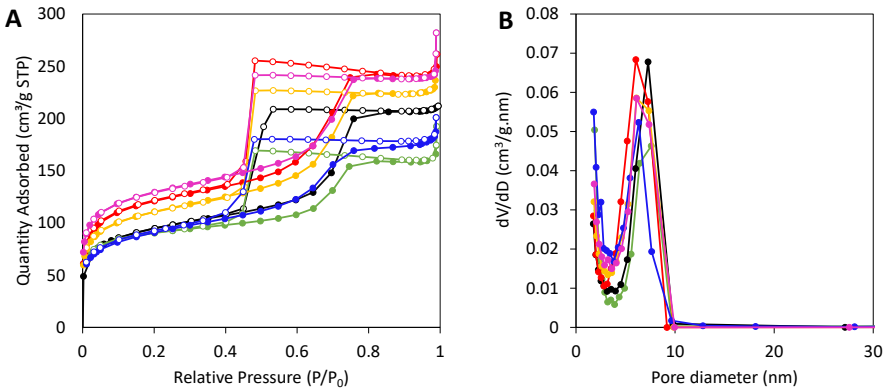

Figure A.2.1. (A) Nitrogen adsorption (plain symbols) and desorption (empty symbols) isotherms and (B) BJH pore size distribution analysis obtained from the adsorption isotherms of Co(10%)SiO_2 (●), Co(10%)SiO_2 MPTMS (●), Cu(10%)SiO_2 (●), Cu(10%)SiO_2 MPTMS (●), Ni(10%)SiO_2 (●) and Ni(10%)SiO_2 MPTMS (●).

Table A.2.1. Textural properties of the different materials.

	BET surface area ($m^2.g^{-1}$)	BJH pore size (nm)	Pore volume ($cm^3.g^{-1}$)	Micropore volume ($cm^3.g^{-1}$)
Co(10%)SiO_2	290	6	0.29	0.09
Co(10%)SiO_2 MPTMS	310	6	0.33	0.09
Cu(10%)SiO_2	370	9	0.35	0.11
Cu(10%)SiO_2 MPTMS	410	6	0.38	0.12
Ni(10%)SiO_2	440	6	0.37	0.14
Ni(10%)SiO_2 MPTMS	300	5	0.28	0.09

X-ray diffraction (XRD) analysis was used to investigate the chemical nature of the metal nanoparticles. In the fresh materials (right after synthesis) - shown as blue curves in Figure A.2.2 – no peaks were observed, indicating that the metal nanoparticles were not formed during the aerosol synthesis. This shows a good stability of the metal precursors in the synthesis conditions (aerosol furnace temperature = 350°C).

After subjecting the samples to calcination, sharp peaks became visible in all the materials without MPTMS, indicating the formation of nanoparticles in these materials. In the Co(10%)SiO_2 catalyst, the observed very sharp peaks are characteristic of Co_3O_4 species, and are suggesting the presence of very large nanoparticles. Their diameter was calculated using the Scherrer equation and reach the size of 57.4 nm (Table A.2.2). This indicates a significant aggregation phenomenon induced by the calcination conditions. Similarly, the Cu(10%)SiO_2 sample after calcination also showed sharp peaks, characteristic of CuO species, with an estimated size of 33 nm. The Ni(10%)SiO_2 sample, on the other hand, exhibited larger peaks, characteristic of nickel oxide, suggesting the formation of smaller nanoparticles. Their diameter actually reached 8 nm. Looking at the Tammann temperature (i.e. the temperature at which the solid material become sufficiently mobile to diffuse and consequently is susceptible to sintering). of these metal species, the different sintering and size observed can be better understood. Indeed, the Tammann temperature of the metal species can be ordered as followed Co_3O_4 < CuO < NiO (339°C < 526°C < 841°C), which follows the is correlated to the trend of the nanoparticles size (57.4 nm > 33 nm > 8 nm).[289] The calcination, performed at 550°C, highly increases the mobility of the CuO and Co_3O_4 nanoparticles, leading to their sintering. Furthermore, operating at a high metal loading (10 wt.%) also increases the likelihood of nanoparticles contact, leading to their sintering. The formation of oxide species is explained by the calcination operated under static air.

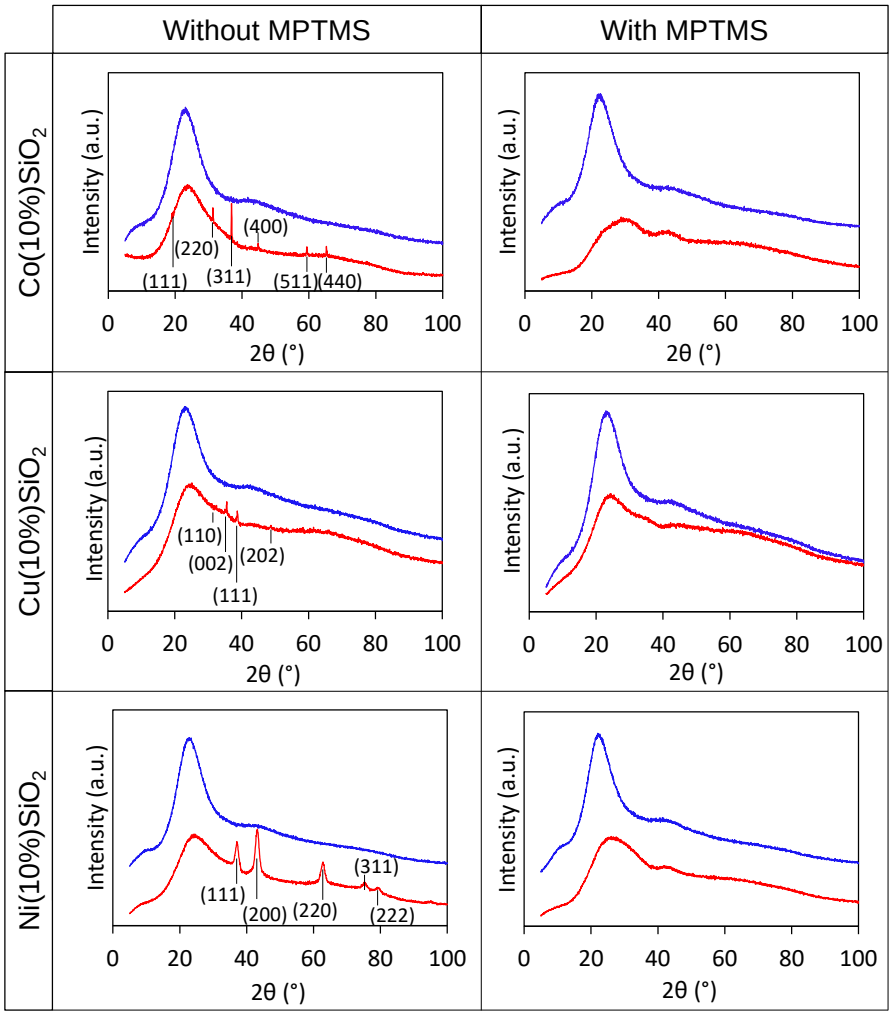

Figure A.2.2. X-ray diffractograms of the different materials with and without MPTMS. The blue curves correspond to the fresh catalyst (after aerosol synthesis) while the red curves correspond to the calcined catalysts. The different phases (Co_3O_4 for Co(10%)SiO_2, CuO for Cu(10%)SiO_2 and NiO for Ni(10%)SiO_2) are identified in each diffractograms.

The absence of peaks when MPTMS is added in the synthesis is indicating the limitation of the sintering phenomenon. It is also important to note the presence of a shift and the appearance of a broad band, suggesting a modification of the silica matrix following the addition of MPTMS. The

nanoparticles size could not be calculated. This either indicates that the nanoparticles are not formed, or that they are very small and highly dispersed in the microspheres.

The presence of the metal nanoparticles at the surface was investigated by XPS (Table A.2.2.). In each material, the presence of the corresponding metal as confirmed (Figure A.2.3).

Table A.2.2. Characteristics of the metal nanoparticles and location.

	Metal nanoparticle size (nm)	Surface metal content (wt.%)
$Co(10\%)SiO_2$	57.4	6
$Co(10\%)SiO_2$ MPTMS	Not measurable	9
$Cu(10\%)SiO_2$	33	8.8
$Cu(10\%)SiO_2$ MPTMS	Not measurable	11
$Ni(10\%)SiO_2$	7.7	4.6
$Ni(10\%)SiO_2$ MPTMS	Not measurable	7.2

Overall, the sample containing MPTMS exhibited a higher surface loading of their corresponding metal. This can be attributed to a combination of the very small nanoparticles size with MPTMS – which is highly dispersed at the silica surface – or the action of the MPTMS that acts as an anchoring point at the surface of the material. The resulting surface metal content is very close to the nominal loading.

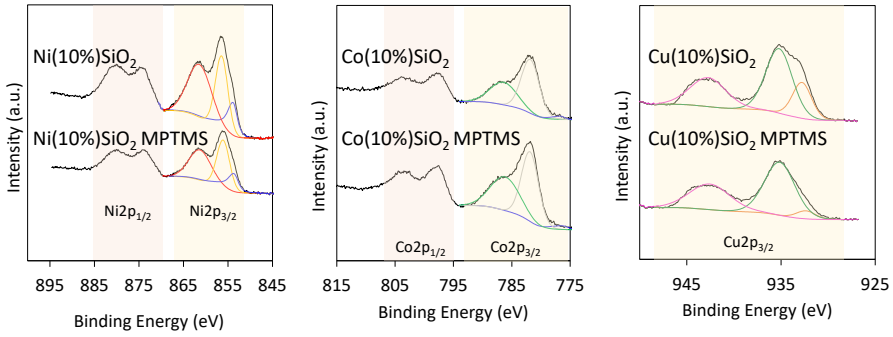

Figure A.2.3. XPS spectra of the different materials. The different components are indicated as follow (i) Ni[0] (●), Ni[II] (●) and Ni[II]satellite (●); (ii) Co[0] (●), Co[II] (●) and Co[III] (●); (iii) Cu[0] (●), Cu[II] (●) and Cu[II] satellite (●).

As for the chemical state of the metal at the surface, the XPS results confirmed the presence of metal oxides. The presence or absence of the MPTMS did not significantly change the distribution of the different chemical state in each metal.

Conclusion

In this study, we investigated the impact of adding MPTMS during the one-pot synthesis of catalysts based on non-noble metal nanoparticles. N_2-physisorption revealed that the stabilizer had no apparent impact on the textural properties of the silica support. Through X-ray diffraction (XRD) analysis, we confirmed the stabilizer's influence on Ni, Cu, and Co metals, leading to good dispersion and a high reduction in nanoparticle size. The stabilizing effect of MPTMS on less noble metals than gold was demonstrated in this study, resulting in catalytic improvement for certain synthesized materials. Further fundamental research to understand the interactions between MPTMS thiol groups and each metal would be beneficial to gain a better understanding of these systems. To the best of our knowledge, interactions between those metals to stabilize them have never been reported in the literature.

To gain a deeper understanding of the stabilization mechanism, additional characterization is required. Furthermore, it remains uncertain whether the nanoparticles are readily accessible for catalytic purposes and to what degree. Consequently, conducting TEM, ICP, and dispersion measurements is essential to obtain a more comprehensive insight into the material morphologies.

ANNEX 3: Sn-K Edge XANES and EXAFS analyses

Experimental

The X-ray absorption spectra were recorded on the B18 beamline at the DIAMOND synchrotron (Oxfordshire, UK). The samples, in form of powder, were diluted with polyvinylpyrrolidone (PVP) and pressed to form pellets. Due to the low concentration of absorbing atom spectra at the Sn K-edge was collected at room temperature in fluorescence mode, using a Si(311) monochromator. A reference sample of SnO_2 was collected in transmission mode. The monochromator energy scale was calibrated collecting data of a reference foil of the pure element for each edge, at the same time as each sample. The data analysis was performed using the ATHENA.[1] With ATHENA, the XANES spectra are normalised; in the EXAFS region the position of the absorption edge, E_0, is determined, and the absorption due to the isolated atom is subtracted, by fitting the pre-edge and post-edge regions, to obtain the EXAFS function $\chi(k)$. This is multiplied by k^2 to enhance the oscillations at high k, and then the corresponding Fourier Transforms (FTs) are calculated. FTs show the radial distances around the absorbing element, noting that there is a shift with respect to the real distances due to a phase-shift effect, which is typical in EXAFS. Real distances are 0.3-0.5 Å longer than the position of the FTs maxima if no phase-shift correction is applied, as in the case of this preliminary report.

Results and discussion

The Figure A.3.1 below shows the normalised XANES spectra measured on the $SnSiO_2$ matrix with no NPs and on all the samples containing NPs (Au, Pt and Pd). Data were also collected on a Sn reference foil (to calibrate the energy scale, but also working as a reference) and on a sample of SnO_2. These are not shown below since for a qualitative comparison it was sufficient to compare the samples with the NPs to the matrix with no NPs. A shift has been applied to the spectra to avoid superposing too many spectra, even if this makes it more difficult to notice differences among the samples. Overall all the XANES spectra are quite similar to each other, indicating that the Sn environment should be quite similar in all samples regardless of the presence of NPs.

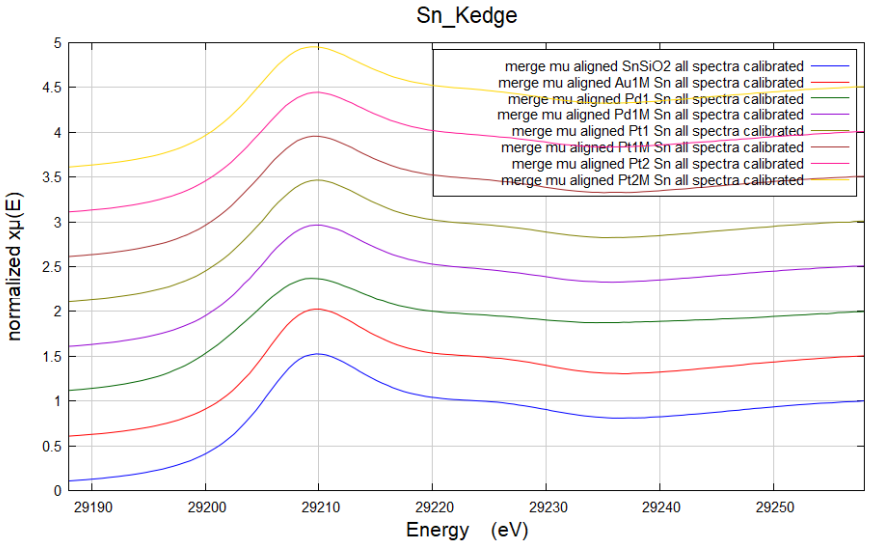

Figure A.3.1. XANES spectra of the bifunctional materials measured on the Sn-K edge.

The EXAFS functions and corresponding FTs for the $SnSiO_2$ matrix with no NPs and on all the samples containing NPs are displayed in Figure A.3.2. The overall similarity among the matrix and all the samples was confirmed also in the EXAFS region, but one sample – Pd(1)$SnSiO_2$ – did show some more evident differences with respect to the other samples and to the matrix. This can be better appreciated in the FTs, where Pd(1)$SnSiO_2$ sample showed a peak at longer distances that is likely due to Sn-Pd distances.

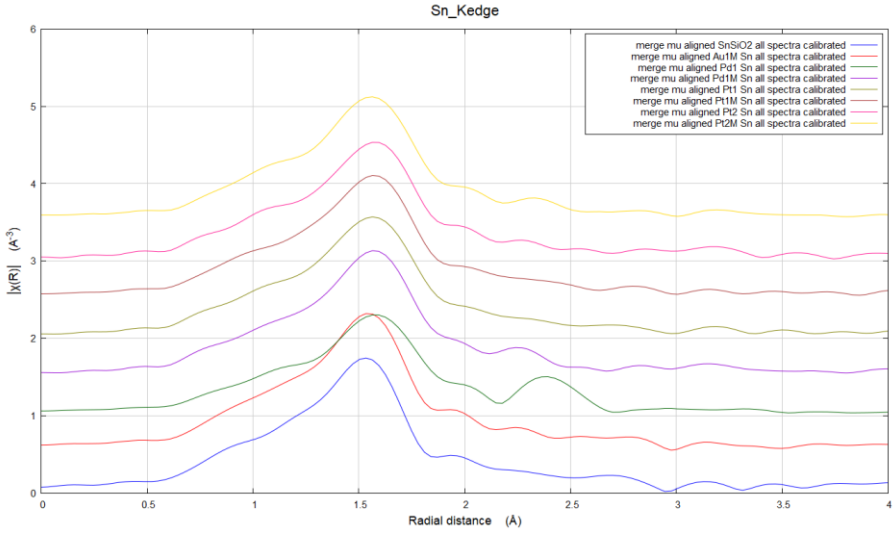

Figure A.3.2. k2χ(k) EXAFS interference functions of the different bifunctional materials and $SnSiO_2$.

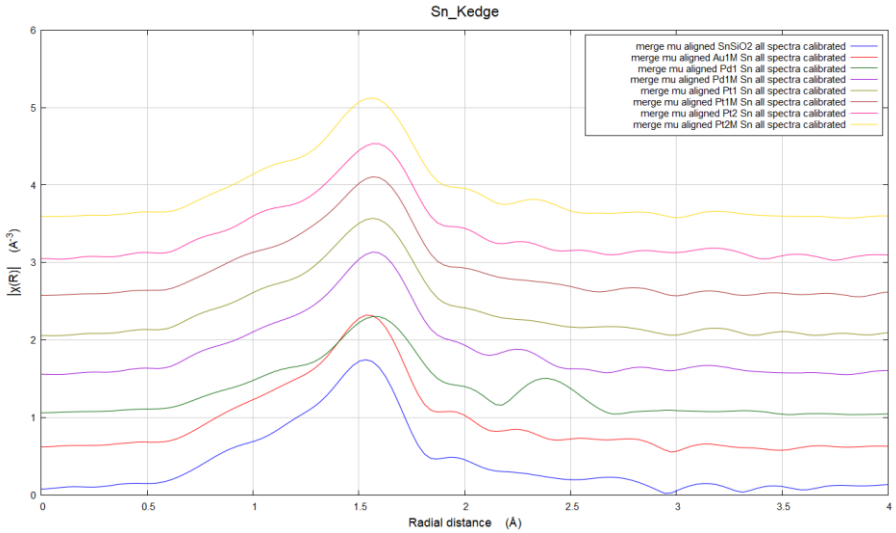

Figure A.3.3. Corresponding FTs moduli (phase shift corrected) of the different bifunctional materials and $SnSiO_2$.

REFERENCES

1. Anastas, P. & Eghbali, N. Green Chemistry: Principles and Practice. *Chem Soc Rev* **39**, 301–312 (2010).
2. Bagnato, G., Iulianelli, A., Sanna, A. & Basile, A. Glycerol Production and Transformation: A Critical Review with Particular Emphasis on Glycerol Reforming Reaction for Producing Hydrogen in Conventional and Membrane Reactors. *Membranes* **7**, 17 (2017).
3. Peppler, H. J. A Bacteriological Comparison between Synthetic and Natural Glycerol. *J. Bacteriol.* **44**, 233–236 (1942).
4. Vivek, N. *et al.* Recent advances in the production of value-added chemicals and lipids utilizing biodiesel industry generated crude glycerol as a substrate – Metabolic aspects, challenges and possibilities: An overview. *Bioresour. Technol.* **239**, 507–517 (2017).
5. Kaur, J., Sarma, A. K., Jha, M. K. & Gera, P. Valorisation of crude glycerol to value-added products: Perspectives of process technology, economics and environmental issues. *Biotechnol. Rep.* **27**, e00487 (2020).
6. Banković-Ilić, I. B., Stamenković, O. S. & Veljković, V. B. Biodiesel production from non-edible plant oils. *Renew. Sustain. Energy Rev.* **16**, 3621–3647 (2012).
7. Abdul Hakim Shaah, M. *et al.* A review on non-edible oil as a potential feedstock for biodiesel: physicochemical properties and production technologies. *RSC Adv.* **11**, 25018–25037 (2021).
8. Romano, U. & Ricci, M. Industrial Applications. in *Liquid Phase Oxidation via Heterogeneous Catalysis* 451–506 (John Wiley & Sons, Ltd, 2013).
9. Leung, D. Y. C., Koo, B. C. P. & Guo, Y. Degradation of biodiesel under different storage conditions. *Bioresour. Technol.* **97**, 250–256 (2006).
10. Pampararo, G. & Debecker, D. P. Sodium Aluminate-Catalyzed Biodiesel Synthesis. *ACS Sustain. Chem. Eng.* **11**, 10413–10421 (2023).
11. Balat, M. & Balat, H. Progress in biodiesel processing. *Appl. Energy* **87**, 1815–1835 (2010).
12. Skrzyńska, E., Wondołowska-Grabowska, A., Capron, M. & Dumeignil, F. Crude glycerol as a raw material for the liquid phase oxidation reaction. *Appl. Catal. Gen.* **482**, 245–257 (2014).
13. Stojković, I. J., Stamenković, O. S., Povrenović, D. S. & Veljković, V. B. Purification technologies for crude biodiesel obtained by alkali-catalyzed transesterification. *Renew. Sustain. Energy Rev.* **32**, 1–15 (2014).
14. Walgode, P. M., Faria, R. P. V. & Rodrigues, A. E. A review of aerobic glycerol oxidation processes using heterogeneous catalysts: a sustainable pathway for the production of dihydroxyacetone. *Catal. Rev.* 1–90 (2020).

15. OECD & Food Nations. OECD-FAO Agricultural Outlook 2018-2027. (2018).
16. Agency, I. E. *World Energy Outlook 2018* IEA Paris (2018).
17. Transport & Environment. *10 years of EU fuels policy increased EU's reliance on unsustainable biofuel*. (2021).
18. Meng, Y. *et al.* Activating molecular oxygen by Au/ZnO to selectively oxidize glycerol to dihydroxyacetone. *Catal. Sci. Technol.* **8**, 2524–2528 (2018).
19. Nanda, M. R. *et al.* Catalytic conversion of glycerol for sustainable production of solketal as a fuel additive: A review. *Renew. Sustain. Energy Rev.* **56**, 1022–1031 (2016).
20. Quispe, C. A. G., Coronado, C. J. R. & Carvalho Jr., J. A. Glycerol: Production, consumption, prices, characterization and new trends in combustion. *Renew. Sustain. Energy Rev.* **27**, 475–493 (2013).
21. Kazmi, A. & Clark, J. Biomass to Chemicals. in *Comprehensive Renewable Energy* 395–410 (Elsevier, 2012).
22. Ravichandiran, P. & Gu, Y. Glycerol as Eco-Efficient Solvent of Organic Transformation. in *Bio-based solvents* 1–28 (2017).
23. Liu, Y., Zhong, B. & Lawal, A. Recovery and utilization of crude glycerol, a biodiesel byproduct. *RSC Adv.* **12**, 27997–28008 (2022).
24. Carlucci, C. A Focus on the Transformation Processes for the Valorization of Glycerol Derived from the Production Cycle of Biofuels. *Catalysts* **11**, 280 (2021).
25. Len, C. & Luque, R. Continuous flow transformations of glycerol to valuable products: an overview. *Sustain. Chem. Process.* **2**, (2014).
26. US Glycerol prices, Available on https://www.selinawamucii.com/insights/prices/united-states-of-america/glycerol/.
27. Chilakamarry, C. R., Sakinah, A. M. M., Zularisam, A. W. & Pandey, A. Glycerol waste to value added products and its potential applications. *Syst. Microbiol. Biomanufacturing* **1**, 378–396 (2021).
28. Mizugaki, T., Arundhathi, R., Mitsudome, T., Jitsukawa, K. & Kaneda, K. Highly Efficient and Selective Transformations of Glycerol Using Reusable Heterogeneous Catalysts. *ACS Sustain. Chem. Eng.* **2**, 574–578 (2014).
29. Ramesh, S. & Debecker, D. P. Room temperature synthesis of glycerol carbonate catalyzed by spray dried sodium aluminate microspheres. *Catal. Commun.* **97**, 102–105 (2017).
30. Ramesh, S., Amoura, M. & Debecker, D. P. Highly basic solid catalysts obtained by spray drying of a $NaAlO_2$ and boehmite suspension for the upgrading of glycerol to acetins. *Sustain. Energy Fuels* **4**, 3546–3551 (2020).
31. Ramesh, S., Devred, F., van den Biggelaar, L. & Debecker, D. P. Hydrotalcites Promoted by $NaAlO_2$ as Strongly Basic Catalysts with Record Activity in Glycerol Carbonate Synthesis. *ChemCatChem* **10**, 1398–1405 (2018).

32. Soumoy, L. *et al.* Hafnium-doped silica nanotubes for the upgrading of glycerol into solketal: Enhanced performances and in-depth structure-activity correlation. *J. Catal.* **411**, 41–53 (2022).
33. Vivian, A. *et al.* Surface-functionalized mesoporous gallosilicate catalysts for the efficient and sustainable upgrading of glycerol to solketal. *Green Chem.* **23**, 354–366 (2021).
34. Pham, P. D., Monge, S., Lapinte, V., Raoul, Y. & Robin, J. J. Various radical polymerizations of glycerol-based monomers. *Eur. J. Lipid Sci. Technol.* **115**, 28–40 (2013).
35. Priya Samudrala, S. Glycerol Transformation to Value-Added 1,3-Propanediol Production: A Paradigm for a Sustainable Biorefinery Process. in *Glycerine Production and Transformation - An Innovative Platform for Sustainable Biorefinery and Energy* (eds. Frediani, M., Bartoli, M. & Rosi, L.) (IntechOpen, 2019).
36. Pala Rosas, I., Luis Contreras Larios, J., Zeifert, B. & Salmones Blásquez, J. Catalytic Dehydration of Glycerine to Acrolein. in *Glycerine Production and Transformation - An Innovative Platform for Sustainable Biorefinery and Energy* (eds. Frediani, M., Bartoli, M. & Rosi, L.) (IntechOpen, 2019).
37. Sahani, S., Upadhyay, S. N. & Sharma, Y. C. Critical Review on Production of Glycerol Carbonate from Byproduct Glycerol through Transesterification. *Ind. Eng. Chem. Res.* **60**, 67–88 (2021).
38. Ayoub, M. *et al.* Glycerol Conversion to Diglycerol via Etherification under Microwave Irradiation. in *Apolipoproteins, Triglycerides and Cholesterol* (eds. Y. Waisundara, V. & Z. Jovandaric, M.) (IntechOpen, 2020).
39. Ciriminna, R., Fidalgo, A., Ilharco, L. M. & Pagliaro, M. Dihydroxyacetone: An Updated Insight into an Important Bioproduct. *ChemistryOpen* **7**, 233–236 (2018).
40. Global Dihydroxyacetone (CAS 96-26-4) industry research report, competitive landscape, market size, regional status and prospect, https://www.360marketupdates.com/global-dihydroxyacetone-cas-96-26-4-industry-research-report-competitive-landscape-market-21404382.
41. Zeng, W., Shan, X., Liu, L. & Zhou, J. Efficient 1,3-dihydroxyacetone biosynthesis in Gluconobacter oxydans using metabolic engineering and a fed-batch strategy. *Bioresour. Bioprocess.* **9**, 121 (2022).
42. El Roz, A., Fongarland, P., Dumeignil, F. & Capron, M. Glycerol to Glyceraldehyde Oxidation Reaction Over Pt-Based Catalysts Under Base-Free Conditions. *Front. Chem.* **7**, (2019).
43. Behr, A., Eilting, J., Irawadi, K., Leschinski, J. & Lindner, F. Improved utilisation of renewable resources: New important derivatives of glycerol. *Green Chem* **10**, 13–30 (2008).
44. Ketchie, W. C., Murayama, M. & Davis, R. J. Promotional effect of hydroxyl on the aqueous phase oxidation of carbon monoxide and glycerol over supported Au catalysts. *Top. Catal.* **44**, 307–317 (2007).

45. Demirel-Gülen, S., Lucas, M. & Claus, P. Liquid phase oxidation of glycerol over carbon supported gold catalysts. *Catal. Today* **102**–**103**, 166–172 (2005).
46. Villa, A., Veith, G. M. & Prati, L. Selective Oxidation of Glycerol under Acidic Conditions Using Gold Catalysts. *Angew. Chem. Int. Ed.* **49**, 4499–4502 (2010).
47. Liu, S.-S., Sun, K.-Q. & Xu, B.-Q. Specific Selectivity of Au-Catalyzed Oxidation of Glycerol and Other C3-Polyols in Water without the Presence of a Base. *ACS Catal.* **4**, 2226–2230 (2014).
48. Carrettin, S., McMorn, P., Johnston, P., Griffin, K. & Hutchings, G. J. Selective oxidation of glycerol to glyceric acid using a gold catalyst in aqueous sodium hydroxide. *Chem. Commun.* 696–697 (2002).
49. Villa, A., Wang, D., Su, D. S. & Prati, L. Gold Sols as Catalysts for Glycerol Oxidation: The Role of Stabilizer. *ChemCatChem* **1**, 510–514 (2009).
50. Villa, A. *et al.* Glycerol Oxidation Using Gold-Containing Catalysts. *Acc. Chem. Res.* **48**, 1403–1412 (2015).
51. Rodrigues, E. G. *et al.* Gold supported on carbon nanotubes for the selective oxidation of glycerol. *J. Catal.* **285**, 83–91 (2012).
52. Zope, B. N., Hibbitts, D. D., Neurock, M. & Davis, R. J. Reactivity of the Gold/Water Interface During Selective Oxidation Catalysis. *Science* **330**, 74–78 (2010).
53. Hutchings, G. J. *et al.* New approaches to designing selective oxidation catalysts: Au/C a versatile catalyst. *Top. Catal.* **38**, 223–230 (2006).
54. Liang, D. *et al.* Selective oxidation of glycerol in a base-free aqueous solution over different sized Pt catalysts. *Catal. Commun.* **10**, 1586–1590 (2009).
55. Yuan, Z., Gao, Z. & Xu, B.-Q. Acid-base property of the supporting material controls the selectivity of Au catalyst for glycerol oxidation in base-free water. *Chin. J. Catal.* **36**, 1543–1551 (2015).
56. Wang, Y. *et al.* Selective Oxidation of Glycerol to Dihydroxyacetone over $Au/Cu_x Zr_{1-x}O_y$ Catalysts in Base-Free Conditions. *ACS Appl. Mater. Interfaces* **11**, 44058–44068 (2019).
57. Kimura, H. Selective oxidation of glycerol on a platinum-bismuth catalyst by using a fixed bed reactor. *Appl. Catal. Gen.* **105**, 147–158 (1993).
58. Kimura, H., Tsuto, K., Wakisaka, T., Kazumi, Y. & Inaya, Y. Selective oxidation of glycerol on a platinum-bismuth catalyst. *Appl. Catal. Gen.* **96**, 217–228 (1993).
59. Dou, J. *et al.* Carbon supported Pt9Sn1 nanoparticles as an efficient nanocatalyst for glycerol oxidation. *Appl. Catal. B Environ.* **180**, 78–85 (2016).
60. Garcia, R., Besson, M. & Gallezot, P. Chemoselective catalytic oxidation of glycerol with air on platinum metals. *Appl. Catal. Gen.* **127**, 165–176 (1995).

61. Hirasawa, S., Nakagawa, Y. & Tomishige, K. Selective oxidation of glycerol to dihydroxyacetone over a Pd–Ag catalyst. *Catal. Sci. Technol.* **2**, 1150 (2012).
62. Dimitratos, N. *et al.* Effect of Particle Size on Monometallic and Bimetallic (Au,Pd)/C on the Liquid Phase Oxidation of Glycerol. *Catal. Lett.* **108**, 147–153 (2006).
63. Brett, G. L. *et al.* Selective Oxidation of Glycerol by Highly Active Bimetallic Catalysts at Ambient Temperature under Base-Free Conditions. *Angew. Chem. Int. Ed.* **50**, 10136–10139 (2011).
64. Zhao, Z. *et al.* Volcano-shape glycerol oxidation activity of palladium-decorated gold nanoparticles. *Chem Sci* **5**, 3715–3728 (2014).
65. Hirasawa, S., Nakagawa, Y. & Tomishige, K. Selective oxidation of glycerol to dihydroxyacetone over a Pd–Ag catalyst. *Catal. Sci. Technol.* **2**, 1150 (2012).
66. Hirasawa, S., Watanabe, H., Kizuka, T., Nakagawa, Y. & Tomishige, K. Performance, structure and mechanism of Pd–Ag alloy catalyst for selective oxidation of glycerol to dihydroxyacetone. *J. Catal.* **300**, 205–216 (2013).
67. Davis, S. E., Ide, M. S. & Davis, R. J. Selective oxidation of alcohols and aldehydes over supported metal nanoparticles. *Green Chem* **15**, 17–45 (2013).
68. Katryniok, B. *et al.* Selective catalytic oxidation of glycerol: perspectives for high value chemicals. *Green Chem.* **13**, 1960 (2011).
69. Shen, Y., Li, Y. & Liu, H. Base-free aerobic oxidation of glycerol on TiO_2 -supported bimetallic Au–Pt catalysts. *J. Energy Chem.* **24**, 669–673 (2015).
70. Ning, X. *et al.* Promoting role of bismuth and antimony on Pt catalysts for the selective oxidation of glycerol to dihydroxyacetone. *J. Catal.* **335**, 95–104 (2016).
71. Prati, L. & Rossi, M. Gold on Carbon as a New Catalyst for Selective Liquid Phase Oxidation of Diols. *J. Catal.* **176**, 552–560 (1998).
72. Dorofeeva, O. V. *et al.* Molecular Structure and Conformational Composition of 1,3-Dihydroxyacetone Studied by Combined Analysis of Gas-Phase Electron Diffraction Data, Rotational Constants, and Results of Theoretical Calculations. Ideal Gas Thermodynamic Properties of 1,3-Dihydroxyacetone. *J. Phys. Chem. A* **111**, 6434–6442 (2007).
73. Ribeiro, L. S. *et al.* Pd, Pt, and Pt–Cu Catalysts Supported on Carbon Nanotube (CNT) for the Selective Oxidation of Glycerol in Alkaline and Base-Free Conditions. *Ind. Eng. Chem. Res.* **55**, 8548–8556 (2016).
74. Kwon, Y., Birdja, Y., Spanos, I., Rodriguez, P. & Koper, M. T. M. Highly Selective Electro-Oxidation of Glycerol to Dihydroxyacetone on Platinum in the Presence of Bismuth. *ACS Catal.* **2**, 759–764 (2012).
75. Verma, A. M., Laverdure, L., Melander, M. M. & Honkala, K. Mechanistic Origins of the pH Dependency in Au-Catalyzed Glycerol Electro-oxidation: Insight from First-Principles Calculations. *ACS Catal.* **12**, 662–675 (2022).

76. Zhou, Y., Shen, Y., Xi, J. & Luo, X. Selective Electro-Oxidation of Glycerol to Dihydroxyacetone by PtAg Skeletons. *ACS Appl. Mater. Interfaces* **11**, 28953–28959 (2019).
77. Garcia, A. C., Birdja, Y. Y., Tremiliosi-Filho, G. & Koper, M. T. M. Glycerol electro-oxidation on bismuth-modified platinum single crystals. *J. Catal.* **346**, 117–124 (2017).
78. Lee, S. *et al.* Highly selective transformation of glycerol to dihydroxyacetone without using oxidants by a PtSb/C-catalyzed electrooxidation process. *Green Chem.* **18**, 2877–2887 (2016).
79. Villa, A. *et al.* Tailoring the selectivity of glycerol oxidation by tuning the acid–base properties of Au catalysts. *Catal. Sci. Technol.* **5**, 1126–1132 (2015).
80. Pan, Y., Wu, G., He, Y., Feng, J. & Li, D. Identification of the Au/ZnO interface as the specific active site for the selective oxidation of the secondary alcohol group in glycerol. *J. Catal.* **369**, 222–232 (2019).
81. Hu, W., Knight, D., Lowry, B. & Varma, A. Selective Oxidation of Glycerol to Dihydroxyacetone over Pt−Bi/C Catalyst: Optimization of Catalyst and Reaction Conditions. *Ind. Eng. Chem. Res.* **49**, 10876–10882 (2010).
82. Yang, L., Li, X., Chen, P. & Hou, Z. Selective oxidation of glycerol in a base-free aqueous solution: A short review. *Chin. J. Catal.* **40**, 1020–1034 (2019).
83. Taarning, E. *et al.* Zeolite-Catalyzed Isomerization of Triose Sugars. *ChemSusChem* **2**, 625–627 (2009).
84. Della Pina, C., Falletta, E. & Rossi, M. Highly selective oxidation of benzyl alcohol to benzaldehyde catalyzed by bimetallic gold–copper catalyst. *J. Catal.* **260**, 384–386 (2008).
85. Ouyang, G., Wang, C. X. & Yang, G. W. Surface Energy of Nanostructural Materials with Negative Curvature and Related Size Effects. *Chem. Rev.* **109**, 4221–4247 (2009).
86. Belyakova, O. A. & Slovokhotov, Y. L. Structures of large transition metal clusters. *Russ. Chem. Bull.* **52**, 2299–2327 (2003).
87. Quinson, J. Surfactant-Free Precious Metal Colloidal Nanoparticles for Catalysis. *Front. Nanotechnol.* **3**, 770281 (2021).
88. Ndolomingo, M. J., Bingwa, N. & Meijboom, R. Review of supported metal nanoparticles: synthesis methodologies, advantages and application as catalysts. *J. Mater. Sci.* **55**, 6195–6241 (2020).
89. Sápi, A. *et al.* Metallic Nanoparticles in Heterogeneous Catalysis. *Catal. Lett.* **151**, 2153–2175 (2021).
90. An, K. & Somorjai, G. A. Size and Shape Control of Metal Nanoparticles for Reaction Selectivity in Catalysis. *ChemCatChem* **4**, 1512–1524 (2012).
91. Haruta, M., Kobayashi, T., Sano, H. & Yamada, N. Novel Gold Catalysts for the Oxidation of Carbon Monoxide at a Temperature far Below 0 °C. *Chem. Lett.* **16**, 405–408 (1987).

92. Farias, M. J. S. & Feliu, J. M. Determination of Specific Electrocatalytic Sites in the Oxidation of Small Molecules on Crystalline Metal Surfaces. *Top. Curr. Chem.* **377**, (2019).
93. Hansen, T. W., DeLaRiva, A. T., Challa, S. R. & Datye, A. K. Sintering of Catalytic Nanoparticles: Particle Migration or Ostwald Ripening? *Acc. Chem. Res.* **46**, 1720–1730 (2013).
94. Wu, N., Lu, X., An, R. & Ji, X. Thermodynamic analysis and modification of Gibbs–Thomson equation for melting point depression of metal nanoparticles. *Chin. J. Chem. Eng.* **31**, 198–205 (2021).
95. He, B. J.-J., Wang, C.-X., Zheng, T.-T. & Zhao, Y.-K. Thermally Induced Deactivation and the Corresponding Strategies for Improving Durability in Automotive Three-Way Catalysts. *Johns. Matthey Technol. Rev.* **60**, 196–203 (2016).
96. Turba, T., Norton, M. G., Niraula, I. & McIlroy, D. N. Ripening of nanowire-supported gold nanoparticles. *J. Nanoparticle Res.* **11**, 2137–2143 (2009).
97. Ruiz Puigdollers, A., Schlexer, P., Tosoni, S. & Pacchioni, G. Increasing Oxide Reducibility: The Role of Metal/Oxide Interfaces in the Formation of Oxygen Vacancies. *ACS Catal.* **7**, 6493–6513 (2017).
98. Song, J. *et al.* Dispersion and support dictated properties and activities of Pt/metal oxide catalysts in heterogeneous CO oxidation. *Nano Res.* **14**, 4841–4847 (2021).
99. Shinde, P. S. *et al.* A Brief Overview of Recent Progress in Porous Silica as Catalyst Supports. *J. Compos. Sci.* **5**, 75 (2021).
100. Wei, Y., Yang, W. & Yang, Z. An excellent universal catalyst support-mesoporous silica: Preparation, modification and applications in energy-related reactions. *Int. J. Hydrog. Energy* **47**, 9537–9565 (2022).
101. Zhao, Y., Girelli, V., Ersen, O. & Debecker, D. P. CO_2 methanation with high-loading mesoporous Ni/SiO_2 catalysts: Toward high specific activity and new mechanistic insights. *J. Catal.* **426**, 283–293 (2023).
102. Kumar, S., Malik, M. M. & Purohit, R. Synthesis Methods of Mesoporous Silica Materials. *Mater. Today Proc.* **4**, 350–357 (2017).
103. Dhiman, M., Singh, B. & Polshettiwar, V. Silica-Supported Nanoparticles as Heterogeneous Catalysts. in *Nanoparticles in Catalysis* (eds. Philippot, K. & Roucoux, A.) 215–238 (Wiley, 2021).
104. Okumura, M. *et al.* Chemical vapor deposition of gold on Al_2O_3, SiO_2, and TiO_2 for the oxidation of CO and of H2. *Catal. Lett.* **51**, 53–58 (1998).
105. Min, B. ., Santra, A. . & Goodman, D. . Understanding silica-supported metal catalysts: Pd/silica as a case study. *Catal. Today* **85**, 113–124 (2003).
106. Pan, X. & Bao, X. Reactions over catalysts confined in carbon nanotubes. *Chem. Commun.* 6271 (2008).
107. Astruc, D., Lu, F. & Aranzaes, J. R. Nanopartikel als regenerierbare Katalysatoren: an der Nahtstelle zwischen homogener und heterogener Katalyse. *Angew. Chem.* **117**, 8062–8083 (2005).

108. Gabaldon, J. P., Bore, M. & Datye, A. K. Mesoporous silica supports for improved thermal stability in supported Au catalysts. *Top. Catal.* **44**, 253–262 (2007).
109. Lu, J. *et al.* Coking- and Sintering-Resistant Palladium Catalysts Achieved Through Atomic Layer Deposition. *Science* **335**, 1205–1208 (2012).
110. Cao, A., Lu, R. & Veser, G. Stabilizing metal nanoparticles for heterogeneous catalysis. *Phys. Chem. Chem. Phys.* **12**, 13499 (2010).
111. Rashkeev, S. N., Dai, S. & Overbury, S. H. Modification of Au/TiO_2 Nanosystems by SiO_2 Monolayers: Toward the Control of the Catalyst Activity and Stability. *J. Phys. Chem. C* **114**, 2996–3002 (2010).
112. Merkel, T. J. *et al.* Scalable, Shape-Specific, Top-Down Fabrication Methods for the Synthesis of Engineered Colloidal Particles. *Langmuir* **26**, 13086–13096 (2010).
113. Wang, X., Zhuang, J., Peng, Q. & Li, Y. A general strategy for nanocrystal synthesis. *Nature* **437**, 121–124 (2005).
114. Chrouda, A., Mahmoud Ali Ahmed, S. & Babiker Elamin, M. Preparation of Nanocatalysts Using Deposition Precipitation with Urea: Mechanism, Advantages and Results. *ChemBioEng Rev.* **9**, 248–264 (2022).
115. van der Lee, M. K., van Dillen, J., Bitter, J. H. & de Jong, K. P. Deposition Precipitation for the Preparation of Carbon Nanofiber Supported Nickel Catalysts. *J. Am. Chem. Soc.* **127**, 13573–13582 (2005).
116. Zanella, R., Giorgio, S., Henry, C. R. & Louis, C. Alternative Methods for the Preparation of Gold Nanoparticles Supported on TiO_2. *J. Phys. Chem. B* **106**, 7634–7642 (2002).
117. Mäki-Arvela, P. & Murzin, D. Y. Effect of catalyst synthesis parameters on the metal particle size. *Appl. Catal. Gen.* **451**, 251–281 (2013).
118. Corma, A. & Garcia, H. Supported gold nanoparticles as catalysts for organic reactions. *Chem. Soc. Rev.* **37**, 2096 (2008).
119. Haruta, M. *et al.* Low-Temperature Oxidation of CO over Gold Supported on TiO_2, α-Fe_2O_3, and Co_3O_4. *J. Catal.* **144**, 175–192 (1993).
120. Delannoy, L. *et al.* Preparation of Supported Gold Nanoparticles by a Modified Incipient Wetness Impregnation Method. *J. Phys. Chem. B* **110**, 22471–22478 (2006).
121. Kim, H. *et al.* Noble Metal-Based Multimetallic Nanoparticles for Electrocatalytic Applications. *Adv. Sci.* **9**, 2104054 (2022).
122. Wu, M.-C. *et al.* Nitrogen-Doped Anatase Nanofibers Decorated with Noble Metal Nanoparticles for Photocatalytic Production of Hydrogen. *ACS Nano* **5**, 5025–5030 (2011).
123. Penkova, A. *et al.* Gold nanoparticles on silica monospheres modified by amino groups. *Microporous Mesoporous Mater.* **117**, 530–534 (2009).
124. Cho, J., Xu, L., Jo, C. & Ryoo, R. Highly monodisperse supported metal nanoparticles by basic ammonium functionalization of mesopore walls for industrially relevant catalysis. *Chem. Commun.* **53**, 3810–3813 (2017).

125. Bore, M. T., Mokhonoana, M. P., Ward, T. L., Coville, N. J. & Datye, A. K. Synthesis and reactivity of gold nanoparticles supported on transition metal doped mesoporous silica. *Microporous Mesoporous Mater.* **95**, 118–125 (2006).
126. Davidson, M. *et al.* Hybrid Mesoporous Silica/Noble-Metal Nanoparticle Materials—Synthesis and Catalytic Applications. *ACS Appl. Nano Mater.* **1**, 4386–4400 (2018).
127. Qu, Z., Zhang, X., Yu, F. & Jia, J. A simple one pot synthesis of mesoporous silica hosted silver catalyst and its low-temperature CO oxidation. *Microporous Mesoporous Mater.* **188**, 1–7 (2014).
128. Li, H. *et al.* Immobilization of glucose oxidase and platinum on mesoporous silica nanoparticles for the fabrication of glucose biosensor. *Electrochimica Acta* **56**, 2960–2965 (2011).
129. Alshammari, K., Niu, Y., Palmer, R. E. & Dimitratos, N. Optimization of sol-immobilized bimetallic Au–Pd/TiO_2 catalysts: reduction of 4-nitrophenol to 4-aminophenol for wastewater remediation. *Philos. Trans. R. Soc. Math. Phys. Eng. Sci.* **378**, 20200057 (2020).
130. Villa, A., Wang, D., Veith, G. M., Vindigni, F. & Prati, L. Sol immobilization technique: a delicate balance between activity, selectivity and stability of gold catalysts. *Catal. Sci. Technol.* **3**, 3036 (2013).
131. Murphy, E. F. *et al.* Nondestructive Sol−Gel Immobilization of Metal(salen) Catalysts in Silica Aerogels and Xerogels. *Chem. Mater.* **13**, 1296–1304 (2001).
132. Gedanken, A. Using sonochemistry for the fabrication of nanomaterials. *Ultrason. Sonochem.* **11**, 47–55 (2004).
133. Campelo, J. M. *et al.* Microwave facile preparation of highly active and dispersed SBA-12 supported metal nanoparticles. *Green Chem.* **10**, 853 (2008).
134. Zhang, Y. & Erkey, C. Preparation of supported metallic nanoparticles using supercritical fluids: A review. *J. Supercrit. Fluids* **38**, 252–267 (2006).
135. Savastenko, N., Volpp, H.-R., Gerlach, O. & Strehlau, W. Synthesis of nanostructured lean-NO x catalysts by direct laser deposition of monometallic Pt-, Rh- and bimetallic PtRh-nanoparticles on SiO_2 support. *J. Nanoparticle Res.* **10**, 277–287 (2008).
136. Legrand, J.-C. *et al.* Application of a dihydrogen afterglow to the preparation of zeolite-supported metallic nanoparticles. *Catal. Today* **89**, 177–182 (2004).
137. Campelo, J. M., Luna, D., Luque, R., Marinas, J. M. & Romero, A. A. Sustainable Preparation of Supported Metal Nanoparticles and Their Applications in Catalysis. *ChemSusChem* **2**, 18–45 (2009).
138. White, R. J., Luque, R., Budarin, V. L., Clark, J. H. & Macquarrie, D. J. Supported metal nanoparticles on porous materials. Methods and applications. *Chem Soc Rev* **38**, 481–494 (2009).
139. Jamkhande, P. G., Ghule, N. W., Bamer, A. H. & Kalaskar, M. G. Metal nanoparticles synthesis: An overview on methods of preparation,

advantages and disadvantages, and applications. *J. Drug Deliv. Sci. Technol.* **53**, 101174 (2019).
140. Komesu, A., Oliveira, J. A. R. de, Martins, L. H. da S., Wolf Maciel, M. R. & Maciel Filho, R. Lactic Acid Production to Purification: A Review. *BioResources* **12**, 4364–4383 (2017).
141. Casalini, T., Rossi, F., Castrovinci, A. & Perale, G. A Perspective on Polylactic Acid-Based Polymers Use for Nanoparticles Synthesis and Applications. *Front. Bioeng. Biotechnol.* **7**, 259 (2019).
142. Singhvi, M. S., Zinjarde, S. S. & Gokhale, D. V. Polylactic acid: synthesis and biomedical applications. *J. Appl. Microbiol.* **127**, 1612–1626 (2019).
143. Okolie, J. A. *et al.* Waste biomass valorization for the production of biofuels and value-added products: A comprehensive review of thermochemical, biological and integrated processes. *Process Saf. Environ. Prot.* **159**, 323–344 (2022).
144. Ojo, A. O. & de Smidt, O. Lactic Acid: A Comprehensive Review of Production to Purification. *Processes* **11**, 688 (2023).
145. Kasinathan, P., Hwang, D. W., Lee, U., Hwang, Y. K. & Chang, J.-S. Effect of solvent and impurity on synthesis of ethyl lactate from fermentation-derived ammonium lactate. *Chem. Eng. Sci.* **66**, 4549–4554 (2011).
146. Kasinathan, P. *et al.* Synthesis of ethyl lactate from ammonium lactate solution by coupling solvent extraction with esterification. *Sep. Purif. Technol.* **76**, 1–7 (2010).
147. Datta, R. & Henry, M. Lactic acid: recent advances in products, processes and technologies — a review. *J. Chem. Technol. Biotechnol.* **81**, 1119–1129 (2006).
148. Upare, P. P., Hwang, Y. K., Chang, J.-S. & Hwang, D. W. Synthesis of Lactide from Alkyl Lactate via a Prepolymer Route. *Ind. Eng. Chem. Res.* **51**, 4837–4842 (2012).
149. Ren, S., Ye, X. P. & Ayers, P. D. Tandem catalytic conversion of glycerol using solid catalysts followed by transesterification to produce alkyl lactate. *RSC Adv.* **5**, 53230–53239 (2015).
150. Lasprilla, A. J. R., Martinez, G. A. R., Lunelli, B. H., Jardini, A. L. & Filho, R. M. Poly-lactic acid synthesis for application in biomedical devices — A review. *Biotechnol. Adv.* **30**, 321–328 (2012).
151. de Clippel, F. *et al.* Fast and Selective Sugar Conversion to Alkyl Lactate and Lactic Acid with Bifunctional Carbon–Silica Catalysts. *J. Am. Chem. Soc.* **134**, 10089–10101 (2012).
152. Pescarmona, P. P. *et al.* Zeolite-catalysed conversion of C3 sugars to alkyl lactates. *Green Chem.* **12**, 1083 (2010).
153. Mäki-Arvela, P., Aho, A. & Murzin, D. Y. Heterogeneous Catalytic Synthesis of Methyl Lactate and Lactic Acid from Sugars and Their Derivatives. *ChemSusChem* **13**, 4833–4855 (2020).
154. Zhang, H. *et al.* Chemocatalytic Production of Lactates from Biomass-Derived Sugars. *Int. J. Chem. Eng.* **2018**, 1–18 (2018).

155. Kim, K. D., Wang, Z., Jiang, Y., Hunger, M. & Huang, J. The cooperative effect of Lewis and Brønsted acid sites on Sn-MCM-41 catalysts for the conversion of 1,3-dihydroxyacetone to ethyl lactate. *Green Chem.* **21**, 3383–3393 (2019).
156. Bicker, M., Endres, S., Ott, L. & Vogel, H. Catalytical conversion of carbohydrates in subcritical water: A new chemical process for lactic acid production. *J. Mol. Catal. Chem.* **239**, 151–157 (2005).
157. Hayashi, Y. & Sasaki, Y. Tin-catalyzed conversion of trioses to alkyl lactates in alcohol solution. *Chem. Commun.* 2716 (2005).
158. Abreu, F. R. *et al.* New metal catalysts for soybean oil transesterification. *J. Am. Oil Chem. Soc.* **80**, 601–604 (2003).
159. Román-Leshkov, Y. & Davis, M. E. Activation of Carbonyl-Containing Molecules with Solid Lewis Acids in Aqueous Media. *ACS Catal.* **1**, 1566–1580 (2011).
160. Yang, X. *et al.* Conversion of dihydroxyacetone to methyl lactate catalyzed by highly active hierarchical Sn-USY at room temperature. *Catal. Sci. Technol.* **6**, 1757–1763 (2016).
161. Jimenez-Martin, J. M. *et al.* Efficient Conversion of Glucose to Methyl Lactate with Sn-USY: Retro-aldol Activity Promotion by Controlled Ion Exchange. *ACS Sustain. Chem. Eng.* **10**, 8885–8896 (2022).
162. Feliczak-Guzik, A., Sprynskyy, M., Nowak, I. & Buszewski, B. Catalytic Isomerization of Dihydroxyacetone to Lactic Acid and Alkyl Lactates over Hierarchical Zeolites Containing Tin. *Catalysts* **8**, 31 (2018).
163. West, R. M. *et al.* Zeolite H-USY for the production of lactic acid and methyl lactate from C3-sugars. *J. Catal.* **269**, 122–130 (2010).
164. Corma, A., Nemeth, L. T., Renz, M. & Valencia, S. Sn-zeolite beta as a heterogeneous chemoselective catalyst for Baeyer–Villiger oxidations. *Nature* **412**, 423–425 (2001).
165. Tolborg, S. *et al.* Incorporation of tin affects crystallization, morphology, and crystal composition of Sn-Beta. *J Mater Chem A* **2**, 20252–20262 (2014).
166. Hammond, C., Conrad, S. & Hermans, I. Simple and Scalable Preparation of Highly Active Lewis Acidic Sn-β. *Angew. Chem. Int. Ed.* **51**, 11736–11739 (2012).
167. Guo, Q. *et al.* Highly Active and Recyclable Sn-MWW Zeolite Catalyst for Sugar Conversion to Methyl Lactate and Lactic Acid. *ChemSusChem* **6**, 1352–1356 (2013).
168. Li, L. *et al.* Extra-small porous Sn-silicate nanoparticles as catalysts for the synthesis of lactates. *J. Catal.* **314**, 56–65 (2014).
169. Li, L. *et al.* Selective conversion of trioses to lactates over Lewis acid heterogeneous catalysts. *Green Chem.* **13**, 1175 (2011).
170. Osmundsen, C. M., Holm, M. S., Dahl, S. & Taarning, E. Tin-containing silicates: structure–activity relations. *Proc. R. Soc. Math. Phys. Eng. Sci.* **468**, 2000–2016 (2012).

171. Pizzolitto, C. *et al.* Acid sites modulation of siliceous-based mesoporous material by post synthesis methods. *Microporous Mesoporous Mater.* **328**, 111459 (2021).
172. Ferrini, P. *et al.* Lewis acid catalysis on single site Sn centers incorporated into silica hosts. *Coord. Chem. Rev.* **343**, 220–255 (2017).
173. Kilos, B., Nowak, I., Ziolek, M., Tuel, A. & Volta, J. C. Transition metal containing (Nb, V, Mo) SBA-15 molecular sieves —synthesis, characteristic and catalytic activity in gas and liquid phase oxidation. in *Studies in Surface Science and Catalysis* vol. 158 1461–1468 (Elsevier, 2005).
174. Xing, S. *et al.* Direct synthesis and characterization of pore-broadened Al-SBA-15. *Microporous Mesoporous Mater.* **239**, 316–327 (2017).
175. Das, T. K., Chaudhari, K., Chandwadkar, A. J. & Sivasanker, S. Synthesis and catalytic properties of mesoporous tin silicate molecular sieves. *J. Chem. Soc. Chem. Commun.* 2495 (1995).
176. Rajalakshmi, R., Srinivasan, V. V., Pachamuthu, M. P. & Maheswari, R. Characterizations of tin (SnO_2) doped KIT-5 by direct synthesis. *Mater. Chem. Phys.* **154**, 164–169 (2015).
177. Ho, S.-T., Dinh, Q.-K., Tran, T.-H., Nguyen, H.-P. & Nguyen, T.-D. One-step synthesis of ordered Sn-substituted SBA-16 mesoporous materials using prepared silica source of rice husk and their selectively catalytic activity. *Can. J. Chem. Eng.* **91**, 34–46 (2013).
178. Chaudhari, K. *et al.* Synthesis, Characterization, and Catalytic Properties of Mesoporous Tin-Containing Analogs of MCM-41. *J. Catal.* **183**, 281–291 (1999).
179. Nekoksová, I., ilková, N., Zukal, A. & Čejka, J. Introduction of tin into mesoporous molecular sieves for oxidation of adamantanone. in *Studies in Surface Science and Catalysis* vol. 156 779–786 (Elsevier, 2005).
180. Navas, D., Fuentes, S., Castro-Alvarez, A. & Chavez-Angel, E. Review on Sol-Gel Synthesis of Perovskite and Oxide Nanomaterials. *Gels* **7**, 275 (2021).
181. Shah, P., Ramaswamy, A. V., Lazar, K. & Ramaswamy, V. Synthesis and characterization of tin oxide-modified mesoporous SBA-15 molecular sieves and catalytic activity in trans-esterification reaction. *Appl. Catal. Gen.* **273**, 239–248 (2004).
182. Wang, X. *et al.* Characterization and catalytic properties of tin-containing mesoporous silicas prepared by different methods. *J. Mol. Catal. Chem.* **238**, 185–191 (2005).
183. Ballivet-Tkatchenko, D., Bernard, F., Demoisson, F., Plasseraud, L. & Sanapureddy, S. R. Tin-Based Mesoporous Silica for the Conversion of CO_2 into Dimethyl Carbonate. *ChemSusChem* **4**, 1316–1322 (2011).
184. Nishiyama, N., Yamaguchi, M., Nishiyama, Y., Egashira, Y. & Ueyama, K. Enhancement of structural stability of mesoporous silica via infiltration of SnCl4 vapor. *J. Non-Cryst. Solids* **351**, 3218–3224 (2005).

185. Li, J., Li, D., Liu, C., Xu, C. & Dong, W. The conversion of glycerol to methyl lactate catalyzed by tin-exchanged montmorillonite-supported gold catalysts. *J. Chem. Technol. Biotechnol.* **94**, 1958–1967 (2019).
186. Dhakshinamoorthy, A. & Garcia, H. Cascade Reactions Catalyzed by Metal Organic Frameworks. *ChemSusChem* **7**, 2392–2410 (2014).
187. Filice, M. & Palomo, J. M. Cascade Reactions Catalyzed by Bionanostructures. *ACS Catal.* **4**, 1588–1598 (2014).
188. Kasipandi, S. & Bae, J. W. Recent Advances in Direct Synthesis of Value-Added Aromatic Chemicals from Syngas by Cascade Reactions over Bifunctional Catalysts. *Adv. Mater.* **31**, 1803390 (2019).
189. Cho, H. J., Chang, C.-C. & Fan, W. Base free, one-pot synthesis of lactic acid from glycerol using a bifunctional Pt/Sn-MFI catalyst. *Green Chem* **16**, 3428–3433 (2014).
190. Razali, N. & Abdullah, A. Z. Production of lactic acid from glycerol via chemical conversion using solid catalyst: A review. *Appl. Catal. Gen.* **543**, 234–246 (2017).
191. Sharninghausen, L. S., Campos, J., Manas, M. G. & Crabtree, R. H. Efficient selective and atom economic catalytic conversion of glycerol to lactic acid. *Nat. Commun.* **5**, 5084 (2014).
192. Kano, E. *et al.* Continuous Production of Lactic Acid from Glycerol over Bifunctional Catalysts under Base-Free Conditions Using a Liquid-Phase Flow Reactor. *ACS Sustain. Chem. Eng.* **10**, 12072–12081 (2022).
193. Tao, M., Dan Zhang, Guan, H., Huang, G. & Wang, X. Designation of highly efficient catalysts for one pot conversion of glycerol to lactic acid. *Sci. Rep.* **6**, (2016).
194. Pazhavelikkakath Purushothaman, R. K., van Haveren, J., Melián-Cabrera, I., van Eck, E. R. H. & Heeres, H. J. Base-Free, One-Pot Chemocatalytic Conversion of Glycerol to Methyl Lactate using Supported Gold Catalysts. *ChemSusChem* **7**, 1140–1147 (2014).
195. An efficient one pot conversion of glycerol to lactic acid using bimetallic gold-platinum catalysts on a nanocrystalline CeO_2 support. *Appl. Catal. B Environ.* **147**, 92–100 (2014).
196. Tang, Z., Fiorilli, S. L., Heeres, H. J. & Pescarmona, P. P. Multifunctional Heterogeneous Catalysts for the Selective Conversion of Glycerol into Methyl Lactate. *ACS Sustain. Chem. Eng.* **6**, 10923–10933 (2018).
197. Tang, Z. *et al.* Base-free conversion of glycerol to methyl lactate using a multifunctional catalytic system consisting of Au–Pd nanoparticles on carbon nanotubes and Sn-MCM-41-XS. *Green Chem.* **21**, 4115–4126 (2019).
198. Zhou, L., Xu, Y., Yang, X., Lu, T. & Han, L. Utilization of biodiesel byproduct glycerol: Production of methyl lactate over Au/CuO and Sn-Beta binary catalyst under mild reaction conditions. *Energy Convers. Manag.* **196**, 277–285 (2019).

199. De, S., Dutta, S. & Saha, B. Critical design of heterogeneous catalysts for biomass valorization: current thrust and emerging prospects. *Catal. Sci. Technol.* **6**, 7364–7385 (2016).
200. Murzin, D. Y. On Spatial Control in Heterogeneous Multifunctional Catalysts. *Catal. Lett.* **147**, 613–621 (2017).
201. Huang, Y.-B., Liang, J., Wang, X.-S. & Cao, R. Multifunctional metal–organic framework catalysts: synergistic catalysis and tandem reactions. *Chem. Soc. Rev.* **46**, 126–157 (2017).
202. Cai, Z. *et al.* Unlocking Bifunctional Electrocatalytic Activity for CO_2 Reduction Reaction by Win-Win Metal–Oxide Cooperation. *ACS Energy Lett.* **3**, 2816–2822 (2018).
203. Ramli, A. *et al.* Bifunctional Heterogeneous Catalysts for Biodiesel Production using Low Cost Feedstocks: A Future Perspective. in *Frontiers in Bioenergy and Biofuels* (eds. Jacob-Lopes, E. & Zepka, L. Q.) (InTech, 2017).
204. Ma, D. *et al.* Bifunctional MOF heterogeneous catalysts based on the synergy of dual functional sites for efficient conversion of CO_2 under mild and co-catalyst free conditions. *J. Mater. Chem. A* **3**, 23136–23142 (2015).
205. Lu, T. *et al.* Promotion Effect of Sn on Au/Sn-USY Catalysts for One-Pot Conversion of Glycerol to Methyl Lactate. *ACS Catal.* **7**, 7274–7284 (2017).
206. Tang, B. *et al.* Constructing core-shell structured Au/Snβ@mesosilica composite for one-pot base-free conversion of glycerol to methyl lactate. *Microporous Mesoporous Mater.* **347**, 112348 (2023).
207. Debecker, D. P. Innovative Sol-Gel Routes for the Bottom-Up Preparation of Heterogeneous Catalysts. *Chem. Rec.* **18**, 662–675 (2018).
208. Sanchez, C. *et al.* “Chimie douce”: A land of opportunities for the designed construction of functional inorganic and hybrid organic-inorganic nanomaterials. *Comptes Rendus Chim.* **13**, 3–39 (2010).
209. Arpagaus, C., Collenberg, A., Ruetti, D., Assadpour, E. & Mahdi Jafari, S. Nano Spray Drying for Encapsulation of Pharmaceuticals. *Int. J. Pharm.* **546**, (2018).
210. Sosnik, A. & Seremeta, K. P. Advantages and challenges of the spray-drying technology for the production of pure drug particles and drug-loaded polymeric carriers. *Adv. Colloid Interface Sci.* **223**, 40–54 (2015).
211. Debecker, D. P., Bras, S. L., Boissière, C., Chaumonnot, A. & Sanchez, C. Aerosol processing: a wind of innovation in the field of advanced heterogeneous catalysts. *Chem. Soc. Rev.* **47**, 4112–4155 (2018).
212. Faustini, M., Grosso, D., Boissière, C., Backov, R. & Sanchez, C. “Integrative sol–gel chemistry”: a nanofoundry for materials science. *J. Sol-Gel Sci. Technol.* **70**, 216–226 (2014).
213. Vivian, A., Fusaro, L., Debecker, D. P. & Aprile, C. Mesoporous Methyl-Functionalized Sn-Silicates Generated by the Aerosol Process for the

Sustainable Production of Ethyl Lactate. *ACS Sustain. Chem. Eng.* **6**, 14095–14103 (2018).
214. Smeets, V. *et al.* Aerosol Route to TiO_2–SiO_2 Catalysts with Tailored Pore Architecture and High Epoxidation Activity. *Chem. Mater.* **31**, 1610–1619 (2019).
215. Kim, A. *et al.* Mesoporous TiO_2 Support Materials for Ru-Based CO_2 Methanation Catalysts. *ACS Appl. Nano Mater.* **2**, 3220–3230 (2019).
216. Maksasithorn, S., Praserthdam, P., Suriye, K. & Debecker, D. P. Preparation of super-microporous WO_3–SiO_2 olefin metathesis catalysts by the aerosol-assisted sol–gel process. *Microporous Mesoporous Mater.* **213**, 125–133 (2015).
217. Godard, N. *et al.* High-Yield Synthesis of Ethyl Lactate with Mesoporous Tin Silicate Catalysts Prepared by an Aerosol-Assisted Sol–Gel Process. *ChemCatChem* **9**, 2211–2218 (2017).
218. Ramesh, S., Indukuri, K., Riant, O. & Debecker, D. P. Synthesis of Carbonate Esters by Carboxymethylation Using $NaAlO_2$ as a Highly Active Heterogeneous Catalyst. *Org. Process Res. Dev.* **22**, 1846–1851 (2018).
219. Smeets, V. *et al.* Hollow zeolite microspheres as a nest for enzymes: a new route to hybrid heterogeneous catalysts. *Chem. Sci.* **11**, 954–961 (2020).
220. Van der Verren, M., Smeets, V., vander Straeten, A., Dupont-Gillain, C. & Debecker, D. P. Hybrid chemoenzymatic heterogeneous catalyst prepared in one step from zeolite nanocrystals and enzyme–polyelectrolyte complexes. *Nanoscale Adv.* **3**, 1646–1655 (2021).
221. Gabaldon, J. P., Bore, M. & Datye, A. K. Mesoporous silica supports for improved thermal stability in supported Au catalysts. *Top. Catal.* **44**, 253–262 (2007).
222. Kan, E., Kuai, L., Wang, W. & Geng, B. Delivery of Highly Active Noble-Metal Nanoparticles into Microspherical Supports by an Aerosol-Spray Method. *Chem. - Eur. J.* **21**, 13291–13296 (2015).
223. Kuai, L. *et al.* Titania supported synergistic palladium single atoms and nanoparticles for room temperature ketone and aldehydes hydrogenation. *Nat. Commun.* **11**, 48 (2020).
224. Hampsey, J. E., Arsenault, S., Hu, Q. & Lu, Y. One-Step Synthesis of Mesoporous Metal−SiO_2 Particles by an Aerosol-Assisted Self-assembly Process. *Chem. Mater.* **17**, 2475–2480 (2005).
225. Zhu, Y., Free, M. L., Woolam, R. & Durnie, W. A review of surfactants as corrosion inhibitors and associated modeling. *Prog. Mater. Sci.* **90**, 159–223 (2017).
226. Jin, Z., Xiao, M., Bao, Z., Wang, P. & Wang, J. A General Approach to Mesoporous Metal Oxide Microspheres Loaded with Noble Metal Nanoparticles. *Angew. Chem. Int. Ed.* **51**, 6406–6410 (2012).
227. Paris, C. *et al.* CO_2 Hydrogenation to Methanol with Ga- and Zn-Doped Mesoporous Cu/SiO_2 Catalysts Prepared by the Aerosol-Assisted Sol-Gel Process. *ChemSusChem* **13**, 6409–6417 (2020).

228. Sachse, A. *et al.* Efficient mesoporous silica–titania catalysts from colloidal self-assembly. *Chem. Commun.* **48**, 10648 (2012).
229. Vivian, A. *et al.* The high activity of mesoporous Ga-SiO_2 catalysts in the upgrading of glycerol to solketal explained by in-depth characterization. *J. Catal.* **400**, 83–92 (2021).
230. Zhang, J. *et al.* Significant promotion effect of carbon nanotubes on the electrocatalytic activity of supported Pd NPs for ethanol oxidation reaction of fuel cells: the role of inner tubes. *Chem Commun* **50**, 13732–13734 (2014).
231. Pieta, I. S., Ishaq, M., Wells, P. P. & Anderson, J. A. Quantitative determination of acid sites on silica-alumina. *Appl. Catal. Gen.* **390**, 127–134 (2010).
232. Panthi, B. *et al.* Using Thiol Adsorption on Supported Au Nanoparticle Catalysts to Evaluate Au Dispersion and the Number of Active Sites for Benzyl Alcohol Oxidation. *ACS Catal.* **5**, 2232–2241 (2015).
233. Ravel, B. & Newville, M. *ATHENA*, *ARTEMIS*, *HEPHAESTUS*: data analysis for X-ray absorption spectroscopy using *IFEFFIT*. *J. Synchrotron Radiat.* **12**, 537–541 (2005).
234. Sardar, R., Funston, A. M., Mulvaney, P. & Murray, R. W. Gold Nanoparticles: Past, Present, and Future. *Langmuir* **25**, 13840–13851 (2009).
235. Ishida, T., Murayama, T., Taketoshi, A. & Haruta, M. Importance of Size and Contact Structure of Gold Nanoparticles for the Genesis of Unique Catalytic Processes. *Chem. Rev.* **120**, 464–525 (2020).
236. Daruich De Souza, C., Ribeiro Nogueira, B. & Rostelato, M. E. C. M. Review of the methodologies used in the synthesis gold nanoparticles by chemical reduction. *J. Alloys Compd.* **798**, 714–740 (2019).
237. Mallick, K., Wang, Z. L. & Pal, T. Seed-mediated successive growth of gold particles accomplished by UV irradiation: a photochemical approach for size-controlled synthesis. *J. Photochem. Photobiol. Chem.* **140**, 75–80 (2001).
238. Takahashi, F., Yamamoto, N., Todoriki, M. & Jin, J. Sonochemical preparation of gold nanoparticles for sensitive colorimetric determination of nereistoxin insecticides in environmental samples. *Talanta* **188**, 651–657 (2018).
239. Hujjatul Islam, M., Paul, M. T. Y., Burheim, O. S. & Pollet, B. G. Recent developments in the sonoelectrochemical synthesis of nanomaterials. *Ultrason. Sonochem.* **59**, 104711 (2019).
240. Zhang, S., Leem, G., Srisombat, L. & Lee, T. R. Rationally Designed Ligands that Inhibit the Aggregation of Large Gold Nanoparticles in Solution. *J. Am. Chem. Soc.* **130**, 113–120 (2008).
241. F. Y. Alzoubi, J. Y. Alzouby, M. K. Alqadi, H. A. Alshboul & K. M. Aljarrah. Synthesis and Characterization of Colloidal Gold Nanoparticles Controlled by the pH and Ionic Strength. *Chin. J. Phys.* **53**, (2015).
242. Cortie, M. B. & van der Lingen, E. Catalytic Gold Nanoparticles. *Mater. Forum* **26**, 1–14 (2002).

243. Chakraborty, S., Ansar, S. M., Stroud, J. G. & Kitchens, C. L. Comparison of Colloidal versus Supported Gold Nanoparticle Catalysis. *J. Phys. Chem. C* **122**, 7749–7758 (2018).
244. Peng, S. *et al.* A facile synthesis of monodisperse Au nanoparticles and their catalysis of CO oxidation. *Nano Res.* **1**, 229–234 (2008).
245. Fafarman, A. T. *et al.* Thiocyanate-Capped Nanocrystal Colloids: Vibrational Reporter of Surface Chemistry and Solution-Based Route to Enhanced Coupling in Nanocrystal Solids. *J. Am. Chem. Soc.* **133**, 15753–15761 (2011).
246. Mozaffari, S. *et al.* The role of nanoparticle size and ligand coverage in size focusing of colloidal metal nanoparticles. *Nanoscale Adv.* **1**, 4052–4066 (2019).
247. Gao, J., Huang, X., Liu, H., Zan, F. & Ren, J. Colloidal Stability of Gold Nanoparticles Modified with Thiol Compounds: Bioconjugation and Application in Cancer Cell Imaging. *Langmuir* **28**, 4464–4471 (2012).
248. Hofmann, A., Schmiel, P., Stein, B. & Graf, C. Controlled Formation of Gold Nanoparticle Dimers Using Multivalent Thiol Ligands. *Langmuir* **27**, 15165–15175 (2011).
249. Woehrle, G. H., Brown, L. O. & Hutchison, J. E. Thiol-Functionalized, 1.5-nm Gold Nanoparticles through Ligand Exchange Reactions: Scope and Mechanism of Ligand Exchange. *J. Am. Chem. Soc.* **127**, 2172–2183 (2005).
250. Chen, X., Wei, M., Jiang, S. & Förster, S. Two Growth Mechanisms of Thiol-Capped Gold Nanoparticles Controlled by Ligand Chemistry. *Langmuir* **35**, 12130–12138 (2019).
251. Fang, Y. *et al.* Gold on thiol-functionalized magnetic mesoporous silica sphere catalyst for the aerobic oxidation of olefins. *J. Mol. Catal. Chem.* **392**, 16–21 (2014).
252. Meng, J. *et al.* Gold nanoparticles self-assemble on the thiol-functionalized fibrous silica microspheres to produce a robust catalyst. *J. Phys. Chem. Solids* **174**, 111190 (2023).
253. Nakamura, T., Yamada, Y. & Yano, K. Direct synthesis of monodispersed thiol-functionalized nanoporous silica spheres and their application to a colloidal crystal embedded with gold nanoparticles. *J. Mater. Chem.* **17**, 3726 (2007).
254. Groen, J. C., Peffer, L. A. A. & Pérez-Ramírez, J. Pore size determination in modified micro- and mesoporous materials. Pitfalls and limitations in gas adsorption data analysis. *Microporous Mesoporous Mater.* **60**, 1–17 (2003).
255. Waseem, M. *et al.* Synthesis and characterization of silica by sol-gel method. *J Pak Mater Soc* **3**, 19–21 (2009).
256. Baker, R. The relationship between particle motion on a graphite surface and Tammann temperature. *J. Catal.* **78**, 473–476 (1982).
257. Turba, T. F. *Thermal Stability of Supported Gold Nanoparticles*. (2011).

258. Solsona, B. *et al.* Deep oxidation of pollutants using gold deposited on a high surface area cobalt oxide prepared by a nanocasting route. *J. Hazard. Mater.* **187**, 544–552 (2011).
259. Scirè, S. & Liotta, L. F. Supported gold catalysts for the total oxidation of volatile organic compounds. *Appl. Catal. B Environ.* **125**, 222–246 (2012).
260. He, C. *et al.* Recent Advances in the Catalytic Oxidation of Volatile Organic Compounds: A Review Based on Pollutant Sorts and Sources. *Chem. Rev.* **119**, 4471–4568 (2019).
261. Rodrigues, E. G., Delgado, J. J., Chen, X., Pereira, M. F. R. & Órfão, J. J. M. Selective Oxidation of Glycerol Catalyzed by Gold Supported on Multiwalled Carbon Nanotubes with Different Surface Chemistries. *Ind. Eng. Chem. Res.* **51**, 15884–15894 (2012).
262. Pakrieva, E. *et al.* Glycerol Oxidation over Supported Gold Catalysts: The Combined Effect of Au Particle Size and Basicity of Support. *Processes* **8**, 1016 (2020).
263. Mallat, T. & Baiker, A. Oxidation of alcohols with molecular oxygen on platinum metal catalysts in aqueous solutions. *Catal. Today* **19**, 247–283 (1994).
264. Ballarin, B. *et al.* Functionalization of silica through thiol-yne radical chemistry: a catalytic system based on gold nanoparticles supported on amino-sulfide-branched silica. *RSC Adv.* **6**, 25780–25788 (2016).
265. Ballarin, B. *et al.* Supported Gold Nanoparticles for Alcohols Oxidation in Continuous-Flow Heterogeneous Systems. *ACS Sustain. Chem. Eng.* **5**, 4746–4756 (2017).
266. Fazzini, S. *et al.* Novel Synthesis of Gold Nanoparticles Supported on Alkyne-Functionalized Nanosilica. *J. Phys. Chem. C* **118**, 24538–24547 (2014).
267. Gu, J., Fan, W., Shimojima, A. & Okubo, T. Microwave-induced synthesis of highly dispersed gold nanoparticles within the pore channels of mesoporous silica. *J. Solid State Chem.* **181**, 957–963 (2008).
268. Shah, K. W. & Zheng, L. Microwave-assisted Synthesis of Hexagonal Gold Nanoparticles Reduced by Organosilane (3-Mercaptopropyl)trimethoxysilane. *Materials* **12**, 1680 (2019).
269. Veith, G. M. *et al.* Thermal stability and catalytic activity of gold nanoparticles supported on silica. *J. Catal.* **262**, 92–101 (2009).
270. Pol, V. G., Gedanken, A. & Calderon-Moreno, J. Deposition of Gold Nanoparticles on Silica Spheres: A Sonochemical Approach. *Chem. Mater.* **15**, 1111–1118 (2003).
271. Chen, L., Hu, J., Qi, Z., Fang, Y. & Richards, R. Gold Nanoparticles Intercalated into the Walls of Mesoporous Silica as a Versatile Redox Catalyst. *Ind. Eng. Chem. Res.* **50**, 13642–13649 (2011).
272. Wang, C., Chen, L. & Qi, Z. One-pot synthesis of gold nanoparticles embedded in silica for cyclohexane oxidation. *Catal. Sci. Technol.* **3**, 1123 (2013).

273. Sunil Sekhar, A. C., Sivaranjani, K., Gopinath, C. S. & Vinod, C. P. A simple one pot synthesis of nano gold–mesoporous silica and its oxidation catalysis. *Catal. Today* **198**, 92–97 (2012).
274. Ogundare, O. D., Akinribide, O. J., Adetunji, A. R., Adeoye, M. O. & Olubambi, P. A. Crystallite size determination of thermally deposited Gold Nanoparticles. *Procedia Manuf.* **30**, 173–179 (2019).
275. Radnik, J., Mohr, C. & Claus, P. On the origin of binding energy shifts of core levels of supported gold nanoparticles and dependence of pretreatment and material synthesis. *Phys. Chem. Chem. Phys.* **5**, 172–177 (2003).
276. Reinecke, B. N. *et al.* Elucidating the electronic structure of supported gold nanoparticles and its relevance to catalysis by means of hard X-ray photoelectron spectroscopy. *Surf. Sci.* **650**, 24–33 (2016).
277. Wu, P., Bai, P., Yan, Z. & Zhao, G. X. S. Gold nanoparticles supported on mesoporous silica: origin of high activity and role of Au NPs in selective oxidation of cyclohexane. *Sci. Rep.* **6**, (2016).
278. Otto, K., Oja Acik, I., Krunks, M., Tõnsuaadu, K. & Mere, A. Thermal decomposition study of $HAuCl_4 \cdot 3H_2O$ and $AgNO_3$ as precursors for plasmonic metal nanoparticles. *J. Therm. Anal. Calorim.* **118**, 1065–1072 (2014).
279. Buining, P. A., Humbel, B. M., Philipse, A. P. & Verkleij, A. J. Preparation of Functional Silane-Stabilized Gold Colloids in the (Sub)nanometer Size Range. *Langmuir* **13**, 3921–3926 (1997).
280. Ventura-Espinosa, D., Martín, S., García, H. & Mata, J. A. Ligand effects in the stabilization of gold nanoparticles anchored on the surface of graphene: Implications in catalysis. *J. Catal.* **394**, 113–120 (2021).
281. Vericat, C. *et al.* Surface characterization of sulfur and alkanethiol self-assembled monolayers on Au(111). *J. Phys. Condens. Matter* **18**, R867–R900 (2006).
282. Bergeret, G. & Gallezot, P. Particle Size and Dispersion Measurements. *Handb. Heterog. Catal.* **2**, 738–765.
283. Laoufi, I. *et al.* Size and Catalytic Activity of Supported Gold Nanoparticles: An in Operando Study during CO Oxidation. *J. Phys. Chem. C* **115**, 4673–4679 (2011).
284. Valden, M., Lai, X. & Goodman, D. W. Onset of Catalytic Activity of Gold Clusters on Titania with the Appearance of Nonmetallic Properties. *Science* **281**, 1647–1650 (1998).
285. The oxidative esterification of glycerol to methyl glycerate in methanol using gold on oxidic supports: an insight in product selectivity. *Green Chem.* **14**, 2031 (2012).
286. Worz, N., Brandner, A. & Claus, P. Platinum−Bismuth-Catalyzed Oxidation of Glycerol: Kinetics and the Origin of Selective Deactivation. *J. Phys. Chem. C* **114**, 1164–1172 (2010).
287. Van der Verren, M. *et al.* Airborne Preparation of Small Gold Nanoparticles Dispersed on Mesoporous Silica for the Catalytic

Oxidation of Glycerol to Dihydroxyacetone. *ACS Appl. Nano Mater.* **5**, 18977–18985 (2022).
288. Thommes, M. *et al.* Physisorption of gases, with special reference to the evaluation of surface area and pore size distribution (IUPAC Technical Report). *Pure Appl. Chem.* **87**, 1051–1069 (2015).
289. Argyle, M. & Bartholomew, C. Heterogeneous Catalyst Deactivation and Regeneration: A Review. *Catalysts* **5**, 145–269 (2015).
290. Ning, P. *et al.* Recent advances in the valorization of plant biomass. *Biotechnol. Biofuels* **14**, 102 (2021).
291. Dochain, D., Van Den Daelen, A., Styskalik, A., Vykoukal, V. & Debecker, D. P. Aerosol-assisted sol-gel synthesis of mesoporous Ag-Ta-SiO_2 catalysts for the direct upgrading of ethanol to butadiene. *RSC Sustain.* 10.1039.D2SU00080F (2023).
292. De Marco, M. L. *et al.* High-Entropy-Alloy Nanocrystal Based Macro- and Mesoporous Materials. *ACS Nano* **16**, 15837–15849 (2022).
293. Busto, G. *et al.* Raspberry Colloid Templated Catalysts Fabricated Using Spray Drying Method. *Catalysts* **13**, 60 (2022).
294. Mitsuka, Y. *et al.* Fabrication of Integrated Copper-Based Nanoparticles/Amorphous Metal–Organic Framework by a Facile Spray-Drying Method: Highly Enhanced CO_2 Hydrogenation Activity for Methanol Synthesis. *Angew. Chem. Int. Ed.* **60**, 22283–22288 (2021).
295. Urruchurto, C. M., Carriazo, J. G., Osorio, C., Moreno, S. & Molina, R. A. Spray-drying for the preparation of Al–Co–Cu pillared clays: A comparison with the conventional hot-drying method. *Powder Technol.* **239**, 451–457 (2013).
296. Wang, N., Wei, Y., Chang, M., Liu, J. & Wang, J.-X. Macro-Meso-Microporous Metal–Organic Frameworks: Template-Assisted Spray Drying Synthesis and Enhanced Catalysis. *ACS Appl. Mater. Interfaces* **14**, 10712–10720 (2022).
297. Peeters, E. *et al.* Highly Dispersed Sn-beta Zeolites as Active Catalysts for Baeyer–Villiger Oxidation: The Role of Mobile, *In Situ* Sn(II)O Species in Solid-State Stannation. *ACS Catal.* **11**, 5984–5998 (2021).
298. Kwoka, M. *et al.* XPS study of the surface chemistry of L-CVD SnO_2 thin films after oxidation. *Thin Solid Films* **490**, 36–42 (2005).
299. Kwoka, M. *et al.* Surface properties of SnO_2 nanolayers prepared by spin-coating and thermal oxidation. *Nanotechnology* **31**, 315714 (2020).
300. Shen, Z. *et al.* Surface amino-functionalization of Sn-Beta zeolite catalyst for lactic acid production from glucose. *RSC Adv.* **9**, 18989–18995 (2019).
301. Alarcón, E. A., Villa, A. L. & Correa, C. M. de. Characterization of Sn- and Zn-loaded MCM-41 catalysts for nopol synthesis. *Microporous Mesoporous Mater.* **122**, 208–215 (2009).
302. Chaudhari, K. *et al.* Synthesis, Characterization, and Catalytic Properties of Mesoporous Tin-Containing Analogs of MCM-41. *J. Catal.* **183**, 281–291 (1999).

303. Hatta, A. H. *et al.* A review on recent bimetallic catalyst development for synthetic natural gas production via CO methanation. *Int. J. Hydrog. Energy* **47**, 30981–31002 (2022).
304. Especel, C., Lafaye, G. & Epron, F. Bimetallic Catalysts for Sustainable Chemistry: Surface Redox Reactions For Tuning The Catalytic Surface Composition. *ChemCatChem* **15**, (2023).
305. Das, P. *et al.* Biocompatible functionalized AuPd bimetallic nanoparticles decorated on reduced graphene oxide sheets for photothermal therapy of targeted cancer cells. *J. Photochem. Photobiol. B* **212**, 112028 (2020).
306. Zulkepli, S. *et al.* Synergistic effect of bimetallic Fe-Ni supported on hexagonal mesoporous silica for production of hydrocarbon-like biofuels via deoxygenation under hydrogen-free condition. *Energy Convers. Manag.* **273**, 116371 (2022).
307. Huang, H. *et al.* Aqueous Synthesis of Pd–M (M = Pd, Pt, and Au) Decahedra with Concave Facets for Catalytic Applications. *Top. Catal.* **63**, 664–672 (2020).
308. Toshima, N. & Yonezawa, T. Bimetallic nanoparticles—novel materials for chemical and physical applications. *New J. Chem.* **22**, 1179–1201 (1998).
309. da Silva, A. G. M., Rodrigues, T. S., Haigh, S. J. & Camargo, P. H. C. Galvanic replacement reaction: recent developments for engineering metal nanostructures towards catalytic applications. *Chem. Commun.* **53**, 7135–7148 (2017).
310. Dash, P. & Scott, R. W. J. Towards the Rational Design of Supported-Bimetallic Nanoparticle Catalysts. *MRS Proc.* **1217**, (2009).
311. Wang, A., Liu, X. Y., Mou, C.-Y. & Zhang, T. Understanding the synergistic effects of gold bimetallic catalysts. *J. Catal.* **308**, 258–271 (2013).
312. Majerič, P., Jenko, D., Friedrich, B. & Rudolf, R. Formation of Bimetallic Fe/Au Submicron Particles with Ultrasonic Spray Pyrolysis. *Metals* **8**, 278 (2018).
313. Halevi, B. *et al.* Aerosol-Derived Bimetallic Alloy Powders: Bridging the Gap. *J. Phys. Chem. C* **114**, 17181–17190 (2010).
314. Byeon, J. H. & Kim, Y.-W. An aerosol-seed-assisted hybrid chemical route to synthesize anisotropic bimetallic nanoparticles. *Nanoscale* **4**, 6726 (2012).
315. Wang, H. *et al.* Aerosol Spray Drying Guided Synthesis of Ultrasmall Alloyed Bimetallic Nanoparticles Supported on Silica for Catalytic Semihydrogenation. *Small* 2204744 (2022).
316. Hong, J. H., Park, G. D. & Kang, Y. C. Aerosol-assisted synthesis of bimetallic nanoparticle-loaded bamboo-like N-doped carbon nanotubes as an efficient bifunctional oxygen catalyst for Zn-air batteries. *Int. J. Energy Res.* **46**, 5215–5225 (2022).

317. Pei, Y. *et al.* Pairwise semi-hydrogenation of alkyne to *cis* -alkene on platinum-tin intermetallic compounds. *Nanoscale* **12**, 8519–8524 (2020).
318. Chen, M. *et al.* Thermal Unequilibrium of PdSn Intermetallic Nanocatalysts: From In Situ Tailored Synthesis to Unexpected Hydrogenation Selectivity. *Angew. Chem. Int. Ed.* **60**, 18309–18317 (2021).
319. Li, F. *et al.* Formic acid decomposition-inhibited intermetallic Pd3Sn2 nanonetworks for efficient formic acid electrooxidation. *J. Power Sources* **450**, 227615 (2020).
320. Uemura, Y. *et al.* In situ time-resolved XAFS study on the structural transformation and phase separation of Pt3Sn and PtSn alloy nanoparticles on carbon in the oxidation process. *Phys. Chem. Chem. Phys.* **13**, 15833 (2011).
321. Bueno, S. L. A., Zhan, X., Wolfe, J., Chatterjee, K. & Skrabalak, S. E. Phase-Controlled Synthesis of Pd–Sn Nanocrystal Catalysts of Defined Size and Shape. *ACS Appl. Mater. Interfaces* **13**, 51876–51885 (2021).
322. Wang, K. *et al.* Palygorskite promoted PtSn/carbon catalysts and their intrinsic catalytic activity for ethanol oxidation. *Electrochimica Acta* **70**, 394–401 (2012).
323. Faroppa, M. L. *et al.* Oxidation of Glycerol in Base-Free Aqueous Solution Using Carbon-Supported Pt and PtSn Catalyst. *Catalysts* **13**, 1071 (2023).
324. Ramachandran, R. K. *et al.* Size- and composition-controlled Pt–Sn bimetallic nanoparticles prepared by atomic layer deposition. *RSC Adv.* **7**, 20201–20205 (2017).
325. Seok, S., Hussain, M. A., Park, K. J., Kim, J. W. & Kim, D. H. Sonochemical synthesis of PdO@silica as a nanocatalyst for selective aerobic alcohol oxidation. *Ultrason. Sonochem.* **28**, 178–184 (2016).
326. Watanabe, S. *et al.* Spectroscopic and first-principles calculation studies of the chemical forms of palladium ion in nitric acid solution for development of disposal of high-level radioactive nuclear wastes. *AIP Adv.* **8**, 045221 (2018).
327. Decarolis, D. *et al.* Spatial Profiling of a Pd/Al_2O_3 Catalyst during Selective Ammonia Oxidation. *ACS Catal.* **11**, 2141–2149 (2021).
328. Martin, D. J., Decarolis, D., Tucoulou, R., Martínez-Criado, G. & M. Beale, A. Towards the interrogation of the behaviour of a single nanoparticle under realistic catalytic reaction conditions. *Catal. Struct. React.* **3**, 63–70 (2017).
329. Tseng, J.-Y. *et al.* Memory characteristics of Pt nanocrystals self-assembledfrom reduction of an embedded PtOx ultrathin film in metal-oxide-semiconductor structures. *Appl. Phys. Lett.* **85**, 2595–2597 (2004).
330. Yang, M., Wang, Z., Wang, W. & Liu, C. Synthesis of AuPd alloyed nanoparticles via room-temperature electron reduction with argon glow discharge as electron source. *Nanoscale Res. Lett.* **9**, (2014).

331. Zhang, F. *et al.* Noble-metal single-atoms in thermocatalysis, electrocatalysis, and photocatalysis. *Energy Environ. Sci.* **14**, 2954–3009 (2021).
332. Liu, L. & Corma, A. Metal Catalysts for Heterogeneous Catalysis: From Single Atoms to Nanoclusters and Nanoparticles. *Chem. Rev.* **118**, 4981–5079 (2018).

LIST OF PUBLICATIONS, COMMUNICATIONS AND AWARDS

PUBLICATIONS

Published articles

1. Hybrid chemoenzymatic heterogeneous catalyst prepared in one step from zeolite nanocrystals and enzyme–polyelectrolyte complexes

Margot Van der Verren, Valentin Smeets, Aurélien Vander Straeten, Chistine Dupont-Gillain, Damien P. Debecker

Nanoscale Advances 3 (6), 1646-1655, 2021.

2. Hybrid chemoenzymatic heterogeneous catalysts

Damien P. Debecker, Valentin Smeets, Margot Van der Verren, Hippolyte Meersseman Arango, Marty Kinnaer, François Devred

Current Opinion in Green and Sustainable Chemistry 28, 100437, 2021.

3. Airborne Preparation of Small Gold Nanoparticles Dispersed on Mesoporous Silica for the Catalytic Oxidation of Glycerol to Dihydroxyacetone

Margot Van der Verren, Vit Vykoukal, Ales Styskalik, Ali Shan Malik, Carmela Aprile, and Damien P. Debecker

ACS Applied Nano Materials 5 (12), 18977–18985, 2022.

Submitted articles

1. Bifunctional Au-Sn-SiO_2 catalysts promote the direct upgrading of glycerol to lactates

Margot Van der Verren, Anna Corrias, Vit Vykoukal, Ales Styskalik, Carmela Aprile, Damien P. Debecker

2. Hafnosilicate Microspheres as Effective Catalysts for the Conversion of Dihydroxyacetone to Ethyl Lactate

Ali Shan Malik, Margot Van der Verren, Damien P. Debecker, Carmela Aprile

COMMUNICATIONS

Oral communications

1. Novel pathway for the preparation of a hybrid chemoenzymatic heterogeneous catalyst combining enzyme-polyelectrolyte complexes and zeolite nanocrystals

Margot Van der Verren, Valentin Smeets, Aurélien vander Straeten, Christine C. Dupont-Gillain and Damien P. Debecker

Oral presentation at the 1st Next Generation of Biocatalysis, in Bern (Switzerland), May 27-28, 2021.

2. Innovative Au-Sn-SiO_2 bifunctional material for the upgrading of glycerol to methyl lactate

Margot Van der Verren, Carmela Aprile and Damien Debecker

Oral presentation at the PhD Day 2022, in Louvain-la-Neuve (Belgium), May 25, 2022.

3. Highly dispersed gold silica catalyst prepared in one step by the aerosol-assisted sol-gel process

Margot Van der Verren, Carmela Aprile and Damien Debecker

Oral presentation at the SOL-GEL 2022, in Lyon (France), July 24-29, 2022.

4. Novel one-pot synthesis of highly dispersed gold silica catalyst for glycerol oxidation

Margot Van der Verren, Carmela Aprile and Damien Debecker

Oral presentation at the 9th World Congress on Oxidation Catalysis Oxidation for a Sustainable Future and Clean Environment, in Cardiff (Wales), September 4-8, 2022.

5. Innovative Au-Sn-SiO2 bifunctional material for the upgrading of glycerol to methyl lactate

Margot Van der Verren, Carmela Aprile and Damien Debecker

Oral presentation at the CRF-ChemCYS 2022, in Blankenberge (Belgium), October 12-14, 2022.

Poster communications

1. Development of bifunctional heterogeneous catalysts for the upgrading of bio-based glycerol toward methyl lactate

Margot Van der Verren, Damien Debecker

Poster presentation at the PhD Day 2023, in Louvain-la-Neuve (Belgium), May 26, 2022.

AWARDS

1. Best oral presentation Award at the Next Generation of Biocatalysis in Bern (Switzerland), May 27-28, 2021.

2. Best oral presentation Award at the PhD Day 2022, in Louvain-la-Neuve (Belgium), May 25, 2022.